Ultrasensitive Nonlinear Vibrational Spectroscopy of Complex Molecular Systems

ISBN 978-94-6233-571-4

Cover design: Oleg Selig

Ultrasensitive Nonlinear Vibrational Spectroscopy of Complex Molecular Systems

ACADEMISCH PROEFSCHRIFT

ter verkrijging van de graad van doctor
aan de Universiteit van Amsterdam
op gezag van de Rector Magnificus
prof. dr. ir. K. I. J. Maex
ten overstaan van een door het College voor Promoties
ingestelde commissie,
in het openbaar te verdedigen in de Agnietenkapel
op donderdag 30 maart 2017, te 14:00 uur

door

Oleg Selig

geboren te Alma-Ata, Kazachstan

PROMOTIECOMMISSIE

promotor:	prof. dr. H. J. Bakker	Universiteit van Amsterdam
copromotor:	dr. Y. L. A. Rezus	AMOLF
overige leden:	prof. dr. W. J. Buma	Universiteit van Amsterdam
	prof. dr. A. M. Brouwer	Universiteit van Amsterdam
	prof. dr. A. F. Koenderink	Universiteit van Amsterdam
	prof. dr. M. L. Groot	Vrije Universiteit Amsterdam
	dr. M. S. Pchenitchnikov	Rijksuniversiteit Groningen
	dr. E. C. Garnett	AMOLF

Faculteit der Natuurwetenschappen, Wiskunde en Informatica

The work described in this thesis was performed at the FOM Institute AMOLF, Science Park 104, 1098 XG Amsterdam, The Netherlands. This work is part of the research programme of the *Stichting Fundamenteel Onderzoek der Materie* (FOM), which is financially supported by the *Nederlandse Organisatie voor Wetenschappelijk Onderzoek* (NWO).

Publications covered in this thesis

Oleg Selig, Ana V. Cunha, Mark van Eldijk, Jan C.M. van Hest, Thomas L.C. Jansen, Huib J. Bakker, Yves L.A. Rezus
Temperature-induced collapse of elastin-like peptides studied by 2DIR spectroscopy
In preparation

O. Selig, R. Siffels and Y.L.A. Rezus
Ultrasensitive ultrafast vibrational spectroscopy employing the near field of gold nanoantennas
Phys. Rev. Lett. **111**, 23:233004:1–5 (2015)

Yves L.A. Rezus and Oleg Selig
Impact of local-field effects on the plasmonic enhancement of vibrational signals by infrared nanoantennas
Opt. Express **24**, 2202–2227 (2016)

Artem A. Bakulin, Oleg Selig, Huib J. Bakker, Yves L.A. Rezus, Christian Müller, Tobias Glaser, Robert Lovrincic, Zhengua Sun, Zhuoying Chen, Aron Walsh, Jarvist M. Frost and Thomas L.C. Jansen
Real-time observation of organic cation reorientation in methylammonium lead iodide perovskites
J. Phys. Chem. Lett. **6**, 3663–3669 (2015)

Oleg Selig, Aditya Sadhanala, Christian Müller, Robert Lovrincic, Zhuoying Chen, Yves L.A. Rezus, Jarvist M. Frost, Thomas L.C. Jansen, Artem A. Bakulin
Organic cation rotation and immobilisation in pure and mixed methylammonium Lead-Halide Perovskites
Submitted

Other publications

Artem A. Bakulin, Robert Lovrincic, Yu Xi, Oleg Selig, Huib J. Bakker, Yves L.A. Rezus, Pabitra K. Bayak, Alexandr Fonari, Veaceslav Coropceanu, Jean-Luc Bredas and David Cahen
Mode-selective vibrational modulation of charge transport in organic electronic devices
Nature Commun. **6**, 7880:1–8 (2015)

Contents

CHAPTER 1

INTRODUCTION

1.1 HISTORY OF SPECTROSCOPY

1.1.1 OPTICAL SPECTROSCOPY

Optical spectroscopy is one of the most important and influential instruments in the toolbox of a scientist. It provides a unique possibility to link a macroscopic observation, dispersed light, to microscopic properties such as the atomic composition, the presence of specific chemical groups and even the molecular structure.

Newton is often referred to as the first spectroscopist[1,2] since he coined the term spectrum. Additionally, he demonstrated that sunlight is composed of multiple colors by dispersing a ray into its rainbow spectrum and recombining it again using a set of prisms.[3] In the beginning of the 19th century Wollaston improved Newtons approach and was the first to discover that, upon close inspection, the continuous spectrum of the sun is interrupted by sharp dark bands.[4] Although the precise origin of these (Fraunhofer) lines remained a mystery for another hundred years, their presence hinted at a way of distinguishing light sources with a similar appearance, like stars, by characterizing their spectrum. In 1822 Herschel observed that different substances burn at distinct colors and noted that even extremely "minute" quantities of certain elements can be detected by the hue of the flame.[5] Bunsen and Kirchhoff combined the previous two observations by demonstrating that the low pressure gas of a substance absorbs and emits light of exactly the same color.[6] After cataloging the absorption lines of most of the alkali and earth alkali metals, they went on and used their new realization to prove the existences of cesium and rubidium[7] by identifying, until then, unassigned emission lines in water from the village Dürkheim and in the mineral lepidolite.

Kirchhoff's rules established the possibility to describe the atomic composition of stars, light years away, by matching their absorption lines with the cataloged emission lines of all known elements. Equipped with this knowledge, Jules Jansen and Norman Lockyer proved the existence of helium in 1868 by observing the sun spectrum and identifying a so far unclassified sharp yellow line.[8] This was the first

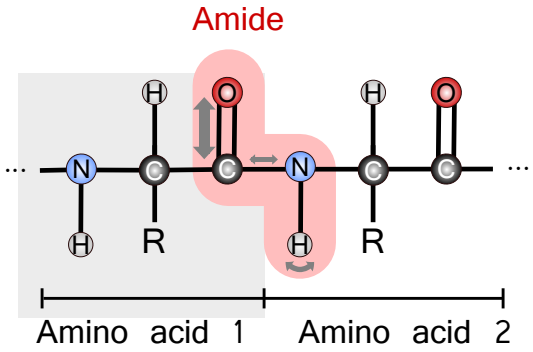

FIGURE 1.1. Two linked amino acids. The amide I mode involves the amide group (highlighted in red) and arises mainly from the C=O-stretching vibration with contributions from the C–N-stretching and N–H-bending vibration.[9]

time that an element was discovered on a celestial body other than the earth. Since then, the discovery of most elements has either been led or confirmed by means of optical spectroscopy.

1.1.2 INFRARED SPECTROSCOPY

The electromagnetic spectrum has more to offer than just the visible. Herschel showed already in 1800 that there is invisible radiation beyond the red part of the solar spectrum (the infrared), carrying enough energy to heat thermometers above room temperature.[10] Nevertheless, it took almost a century until the exploration of this new invisible part of the spectrum began. In 1882, Abney and Festing invented a new photographic compound which was sensitive in the near infrared (<1.2 μm). They studied different organic compounds and discovered extinction lines similar to the ones found in the visible. These lines were highly correlated with the presence of certain chemical groups which led to initial speculations that infrared spectroscopy is less sensitive to the presence of specific elements but instead rather interacts with the collective motion of atoms.[11] This theory was confirmed by Coblentz who can be seen as the father of infrared spectroscopy. Not only was he the first to measure more than a hundred organic compounds in the whole mid-infrared range (1-15 μm) and to coin the term mid-infrared; but he was also the first to provide experimental evidence for the connection between fundamental vibrations and molecular structure.[12] Only years later Rose published a paper where he concisely stated that the structural groups of hydrocarbons have a specific absorption frequency and a fixed cross section independent of the compound they are part of. This laid the foundation for the qualitative and quantitative analysis of arbitrary samples using infrared spectroscopy.[13,14] In the 1940s the American petroleum and rubber industry became intensely interested in a fast and efficient method to identify,

monitor and distinguish compounds with very similar atomic composition but a different chemical structure such as crude oil and its refined derivatives. They chose infrared spectroscopy which by then showed very promising indications of being chemically specific and capable of identifying chemical bonds and groups, and even capable of providing some structural information such as the distinction of various structural isomers. The industrial application fueled the development of new, easy to use spectrometers, which led to the dispersion of infrared spectroscopy into other industries and academic research.

1.1.3 PROTEIN SPECTROSCOPY

Arguably one of the most powerful applications of infrared spectroscopy is the investigation of the three-dimensional structure of proteins. Proteins and peptides are the molecular machines in our bodies and they orchestrate almost every biological process from DNA replication[15] to mood regulation.[16,17] The key aspect to their functionality is their three-dimensional form.[18] Small variations in their structure can already have severe impact on their efficiency or, even worse, result in diseases, such as sickle-cell anemia[19] or progeria syndrome[20a]. Therefore, the precise knowledge of the (correctly folded) protein structure is of key interest, not only for medical purposes, but for a fundamental understanding of biology.

One way by which infrared spectroscopy can provide information about the protein structure is via the spectrum of the amide I vibration. The amide I vibration is one of the characteristic modes of the peptide bonds inside proteins. It mainly corresponds to the stretching of the backbone carbonyl group (C=O, ∼80%) with additional contributions from the C–N-stretching and N–H in-plane bending vibration (see Figure 1.1).[9] This mode has a rather large infrared extinction coefficient, absorbing at ∼1650 cm^{-1}, and is extremely sensitive to changes in the backbone environment, such as hydrogen bonding. In principle, a protein which consists of n amino acid residues contains $n-1$ amide I oscillators. The spectrum of a well-structured protein usually looks very different from the spectrum of an isolated amide I vibration. The reason for this difference is the coupling between the individual amide groups inside a protein, which leads to collective oscillations of the involved amide I vibrations. The frequencies of these collective oscillations depend sensitively on the three-dimensional organization of the residues inside the protein, and therefore on the secondary structure.[21]

Figure 1.2 shows how the amide I spectra can be used to distinguish between the three most common secondary-structure motifs: random coil, α-helices and β-sheets. Usually, unstructured domains (random coils) show a broad featureless band at 1639–1654 cm^{-1}, α-helices a relatively narrow band at 1642–1660 cm^{-1} and β-sheets mostly show two distinct resonances, with one intense peak around 1630 cm^{-1} and a weak one at ∼1680 cm^{-1}.[21] These spectral signatures allow not only a qualitative but also a quantitative analysis of the protein architecture.[22,23]

[a] premature aging

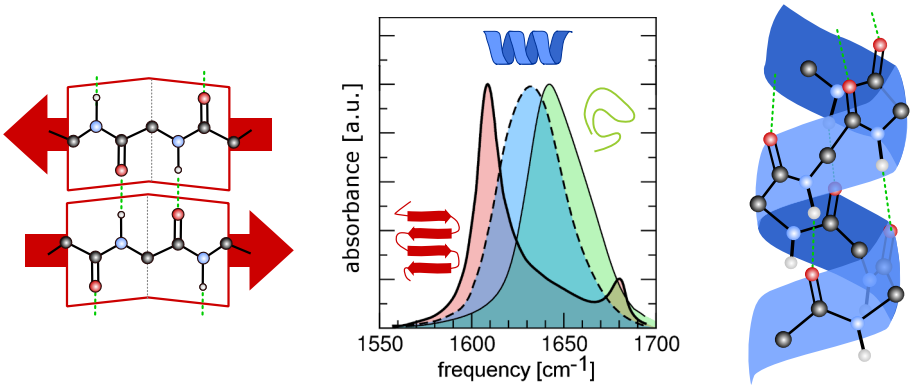

FIGURE 1.2. Infrared spectra of the amide I region. Spectrum (center) of the same peptide (poly-l-lysine) in three distinct secondary structure conformations (spectra adapted from[24]). The different spectral shapes of β-sheets (red, left) and α-helices (blue, right) originate from distinct hydrogen bonding patterns and phase relations of the involved amide groups.

1.2 NOVEL DEVELOPMENTS IN PROTEIN INFRARED SPECTROSCOPY

1.2.1 TWO-DIMENSIONAL INFRARED SPECTROSCOPY

One limitation of infrared spectroscopy is that information-rich spectral windows, like the amide I region, are often crowded with absorption bands originating from various chemical groups and/or different secondary structure motifs. This overlap of many resonances can result in hard to interpret, featureless and broad lineshapes. A second limitation is that although most chemical groups have an infrared signature, it is very difficult to obtain information about the spatial organization of the groups from the linear spectrum. In other words, the linear spectrum does not allow one to unambiguously determine how different vibrational modes are coupled to each other.

Both shortcomings can be lifted by moving from steady state linear infrared spectroscopy to ultrafast two-dimensional infrared (2DIR) spectroscopy. In 2DIR spectroscopy ultra-short laser pulses are used to excite molecular vibrations and to follow their relaxation dynamics. The excitation acts like a short-term tag which labels an oscillator and allows to track it on a femtosecond timescale. Similar to nuclear magnetic resonance (NMR) spectroscopy, the spectra in 2DIR spectroscopy are spread along two dimensions where one axis marks the excitation and the other the detection frequency. This frequency dispersion by itself can greatly simplify the assignment of the observed vibrational bands. Furthermore, interacting chemical groups give rise to distinct spectral features, i.e. cross-peaks, which carry information about the underlying coupling mechanism and the relative orientation of the involved

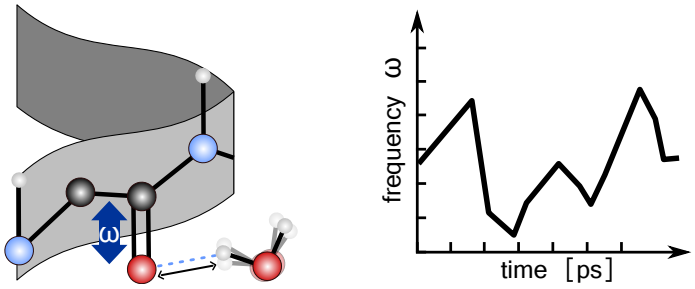

FIGURE 1.3. Rapid motions of solvent molecules in close vicinity of the peptide backbone cause the amide I vibrational frequency ω to fluctuate. 2DIR spectroscopy can be used to access the timescale of these fluctuations, and thereby the solvent exposure, by monitoring the time-dependent lineshapes (Section 2.5.4).

vibrational modes.

Many studies have demonstrated that 2DIR spectroscopy is capable of extracting direct structural information about the investigated system. In one of the earliest 2DIR experiments, Woutersen and Hamm used polarization-resolved 2DIR to study the spatial structure of the model peptide trialanine.[25] By studying the polarization dependence of the cross-peaks between the alanines and assuming a planar geometry for the amide units, they could determine the absolute angles between the three residues. In a different set of studies the group of Rubtsov looked at the picosecond dynamics of cross-peaks in various molecules and demonstrated that the time-dependence of the cross-peak intensity can be used to measure the atomic distance between chemical groups with angstrom precision.[26]

In addition to providing structural information, 2DIR is extremely sensitive to protein-solvent interactions. The rapid motions of solvent molecules close to the protein cause fluctuations in the amide I vibrational frequency (Fig. 1.3) resulting in inhomogeneous broadening of the spectrum. Since the time resolution of 2DIR spectroscopy is higher than the timescale of most solvent motions, also the solvent-induced spectral diffusion can be followed in real time. The group of Hochstrasser used a combination of isotope-labelling and 2DIR to study the time scale of the frequency variation of most of the amide I vibrations in β-amyloid fibrils. Fast variations were only observed for a small subset of residues, which they assigned to the presence of mobile water molecules inside the otherwise dry protein[27](Fig. 1.4). These results indicate that 2DIR is capable of detecting individual, structurally significant water molecules in the vicinity of the protein backbone.

Intrinsically disordered peptides In recent years, it became increasingly obvious that many proteins are not perfectly well structured. On the contrary, it is currently assumed that 35% of the proteins in the human proteome contain extended intrinsically disordered domains.[28] These unstructured regions allow the proteins to display a large conformational diversity, and thereby scaffold and bind with numerous interaction sites. Furthermore, the high flexibility often leads to a

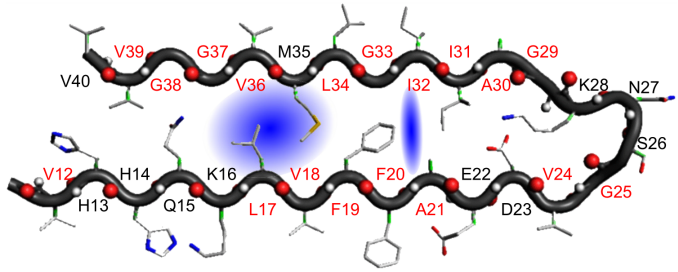

FIGURE 1.4. Schematic representation of one monomer unit of Aβ40 fibril. The measurement of the frequency fluctuations of individually labeled residues (red) with 2DIR suggested the presence of individual water atoms (blue), contained inside the otherwise dry protein.[27]

low binding affinity resulting in fast interprotein interactions, making proteins containing intrinsically disordered domains a key element in many cellular signal-processing pathways.[29] Malfunction of intrinsically disordered proteins (IDP) has been linked to a variety of human maladies including diabetes, cardiovascular and neurodegenerative diseases and most cancer varieties.[30,31] Oftentimes the reason for the malfunction originates in misfolding of the proteins into a nonfunctional, insoluble aggregate. A detailed understanding of the aggregation process and, in general, the physiochemical properties of the unstructured domains, is essential for the development of possible cures. Unfortunately, fast progress has been limited due the extreme flexibility of these proteins.

Most IDPs occupy a large and fairly flat energetic landscape which allows them to rapidly interconvert between different conformations and which prevent high quality crystal formation. This makes them an extremely difficult subject for conventional experimental methods to study protein structure, such as x-ray crystallography and NMR spectroscopy.[32] Therefore, ultrafast experimental methods can be very useful to extract direct structural information.

Elastin-like polypeptides (ELPs) were proposed as a minimal model system for the investigation of IDPs since they possess many physical, chemical and biological properties common to IDPs.[33] ELPs are intrinsically disordered biopolymeres which can undergo a temperature-induced and aggregation-like phase transition. In Chapter 4 we will employ the structural specificity and picosecond time-resolution of two-dimensional infrared spectroscopy to investigate the inverse-temperature transition of ELPs and to identify residual structural elements.

1.2.2 EFFORTS TO ENHANCE IR SENSITIVITY

Although infrared absorption spectroscopy provides a powerful tool to study biomolecules in solution, it is severely limited when it comes to the investigation of nanometer-sized samples, like self-assembled monolayers, supported lipid bilayers (and possibly anchored membrane proteins), or in general ultrathin films. The origin for this limitation is twofold: most chemical groups have a relatively small

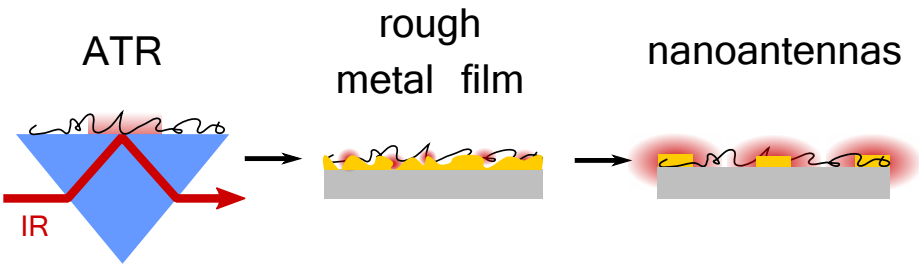

FIGURE 1.5. Efforts to enhance the infrared absorption of (ultra-)thin films (see text for discussion).

absorption cross-section in the infrared and the high solvent-to-film ratio causes significant background absorption.

A common approach to mitigate these problems is to employ attenuated total reflection infrared spectroscopy (ATR-IR). In ATR-IR the infrared light is passed through an optically dense crystal and internally reflected from a surface onto which the sample is deposited. The reflection is accompanied by an evanescent field which extends into the sample volume. The resulting short optical path lengths of around 0.5–3 μm allows one to study samples with a strong solvent absorption[34] . In addition, the optical path length is highly reproducible (because it does not rely on the use of a sample spacer), so that the solvent background can be subtracted very accurately. Although this method can greatly boost the sensitivity for adsorbed thin films, it is generally insufficient to achieve monolayer detection. In 1974, Fleischman et al. showed that monolayer sensitivity can be obtained in Raman scattering experiments by attaching the studied molecules to a roughened silver film, introducing the new method of surface enhanced Raman spectroscopy (SERS).[35] Half a decade later, it was demonstrated that similar results can be achieved in infrared spectroscopy by adsorbing molecules to a metal film deposited on top of an infrared transparent substrate,[36] although with significantly less signal enhancement. The signal enhancement in surface enhanced infrared absorption spectroscopy (SEIRA) originates from nanometer sized features and the strong curvature of the roughened metal film which leads to strong local electric fields.

In recent years, nanofabrication methods became commonly available which allowed the replacement of the metal films with specifically engineered metal nanostructures. These resonant nanoantennas act like little lenses, strongly focusing the infrared light into subwavelength volumes, thereby strongly enhancing the vibrational signals from molecules adsorbed to the nanoantennas. The current generation of SEIRA can thus achieve zeptomolar sensitivity[37,38] and has been incorporated in 'on-chip' designs paving the way for a new class of biological sensors.[39]

Despite these advances, most studies so far have been limited to exploring surface enhancement in linear infrared spectroscopy. Obviously, it would be highly beneficial to also apply these surface-enhancement techniques for increasing the sensitivity of nonlinear infrared spectroscopy. This would, for example, make it possible to study the structure of membrane proteins that are embedded in surface-attached

membranes. A large part of this thesis is dedicated to the development of the technique of Nanoantenna Enhanced Nonlinear Infrared Spectroscopy (NENIS).

1.3 OUTLINE OF THE THESIS

Chapter 2 presents the theory on which the experiments described in this thesis are based. The first part of the chapter deals with the theory of surface plasmons. In the second part of the chapter non-linear light conversion is discussed, and the fundamentals of linear and nonlinear infrared spectroscopy are introduced. The last part of the chapter introduces the experimental observables of 2DIR spectroscopy and discusses the information they provide. In Chapter 3 the experimental setup that has been used to collect data for this thesis is described. In Chapter 4 the inverse temperature transition of elastin-like peptides is studied with time resolved 2DIR. Chapter 5 introduces a novel method to perform nonlinear vibrational spectroscopy on nanoscale volumes with the assistance of infrared nanoantennas. The capabilities of this method are demonstrated by recording the 2DIR spectrum of a 5 nm thick film of polymethylmethacrylate. In Chapter 6 an analytical model for nanoantenna enhanced vibrational spectroscopy is introduced and the implications of local-field effects are discussed. In Chapter 7 we use 2DIR spectroscopy to study the molecular motion of the organic cation in methylammonium lead iodide perovskites, and in Chapter 8 we investigate how this motion is affected by the substitution of the halide anions in the material.

CHAPTER 2

THEORY

2.1 MACROSCOPIC ELECTRODYNAMICS

2.1.1 MAXWELL'S EQUATIONS

The basis for describing electric and magnetic fields and their interaction with matter is given by Maxwell's equations, which were published by their namesake James Clerk Maxwell in 1861. In 1884 Oliver Heaviside reformulated the equations to their nowadays well-known form. The macroscopic Maxwell equations in their differential form in SI units read (e.g.[40]):

$$\nabla \cdot \vec{D}(\vec{r},t) = \rho(\vec{r},t) \tag{2.1a}$$

$$\nabla \cdot \vec{B}(\vec{r},t) = 0 \tag{2.1b}$$

$$\nabla \times \vec{E}(\vec{r},t) = -\frac{\partial \vec{B}(\vec{r},t)}{\partial t} \tag{2.1c}$$

$$\nabla \times \vec{H}(\vec{r},t) = \frac{\partial \vec{D}(\vec{r},t)}{\partial t} + \vec{j}(\vec{r},t), \tag{2.1d}$$

where $\vec{j}$ and ρ are the current and charge densities, $\vec{E}$ is the electric field, $\vec{D}$ the electric displacement, $\vec{H}$ the magnetic field and $\vec{B}$ the magnetic induction. Since the materials investigated in this thesis are nonmagnetic ($\mu_r = 1$), we will focus on describing the interaction of matter with the electric field. The presence of an external electric field can induce electric dipoles $\vec{\mu}$ inside the volume V of medium resulting in a macroscopic polarization $\vec{P}(\vec{r},t) = 1/V \sum_{i=1}^{n} \vec{\mu}_i(\vec{r},t)$. If the applied electric field strength is small, the polarization increases linearly with the field:

$$\vec{P} = \varepsilon_0 \chi_e \vec{E}, \tag{2.2}$$

where χ_e is the electric susceptibility. For a monochromatic electric field, the electric displacement field inside a material is given by:

$$\vec{D} = \varepsilon_0 \vec{E} + \vec{P} = (1+\chi_e)\varepsilon_0 \vec{E} = \varepsilon_r \varepsilon_0 \vec{E}, \tag{2.3}$$

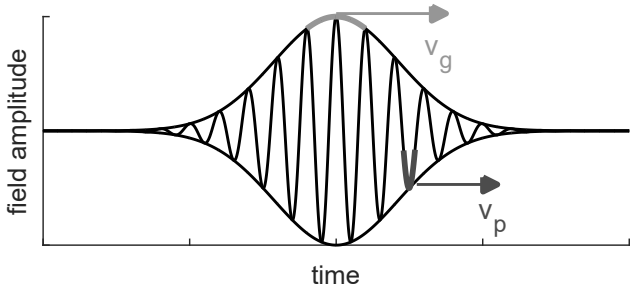

FIGURE 2.1. Field amplitude of a propagating (polychromatic) light pulse with indicated group (v_g) and phase velocity (v_p).

where ε_0 is the vacuum permittivity. From the last equation follows that the displacement field also increases linearly with the electric field where ε_r, the material permittivity, is the proportionality constant. It is worth noting that χ_e and ε_r are complex tensors in general and only reduce to scalars for isotropic media and small electric field strengths.
The propagation of electromagnetic fields is described by the wave equation which can be derived by taking the curl of Eq. (2.1c), assuming a source-free medium ($\rho = 0$, $\vec{j} = 0$), and making use of Eq. (2.1d) and Eq. (2.3):

$$\left(\nabla^2 - \frac{1}{c^2}\frac{\partial^2}{\partial t^2}\right)\vec{E} = \mu_0 \frac{\partial^2}{\partial t^2}\vec{P}, \tag{2.4}$$

where $c = \sqrt{(\varepsilon_0 \mu_0)^{-1}}$ is the speed of light in vacuum, and μ_0 the vacuum permeability.

2.1.2 THE REFRACTIVE INDEX n

To describe the propagation of light inside a material it is convenient to introduce the material specific refractive index. By assuming a nonmagnetic material $\mu_r = 1$ we can relate the refractive index n, the dielectric function, and the susceptibility via:

$$n = \sqrt{\varepsilon_r \mu_r} \approx \sqrt{1 + \chi} = \tilde{n} + i\kappa. \tag{2.5}$$

In the last equation we have written the refractive index as sum of the real ($\tilde{n}$) and imaginary (κ) part of n. To understand the properties of the refractive index, it is insightful to investigate the implication for a monochromatic plane wave with frequency ω traveling through the material:

$$E = E_0 e^{i(kx - \omega t)} + c.c.. \tag{2.6}$$

Here k denotes the wave vector, and $c.c.$ refers to the complex conjugate. The wave vector is defined as[41]

$$k = \frac{n(\omega)\omega}{c} \tag{2.7}$$

and is in general complex valued due to its dependence on $n(\omega)$. Combining the last two equations leads to:

$$E = E_0 e^{i\omega(\frac{\tilde{n}}{c}x-t)} \cdot e^{-\omega\frac{\kappa}{c}x} + c.c., \tag{2.8}$$

where we have separated the exponent into an oscillating contribution depending on $\tilde{n}$ and an exponentially decaying contribution depending on κ. Thus, a nonvanishing imaginary part of n leads to a decrease of the amplitude as the wave travels through the medium. We can quantify the amount of attenuation by inspecting the light intensity of a plane wave inside the material, which is given by:[42]

$$I = \frac{1}{2}c\sqrt{\varepsilon_r}\mathscr{R}e\{E \cdot E^*\} = \frac{1}{2}c\sqrt{\varepsilon_r}e^{-2\omega\frac{\kappa}{c}x}|E_0^2|, \tag{2.9}$$

where the asterisk denotes the complex conjugate. By comparing the last equation to the Lambert-Beer law:

$$I = I_0 e^{-\alpha x}, \tag{2.10}$$

we see that the absorption coefficient α is related to the imaginary part of the refractive index by:

$$\alpha = 2\frac{\kappa}{c}\omega. \tag{2.11}$$

Next, we look at the influence of the real part of the refractive index $\tilde{n}$ on the oscillating part of the electric field which governs the velocity of the wave. Monochromatic plane waves (see Eq. (2.8)) propagate at the phase velocity:

$$v_p(\omega) = \frac{c}{\tilde{n}(\omega)} \tag{2.12}$$

through the medium. Therefore, the real part of the refractive index determines the speed of light inside a material (relative to the speed of light in vacuum). If $\tilde{n}$ is frequency dependent ($\frac{\partial\tilde{n}}{\partial\omega} \neq 0$), then the medium is often referred to be dispersive. In this thesis we employ ultrashort light pulses, consisting of multiple frequency components, to study the molecular dynamics of bulk samples. The envelope of the light pulses, will travel at a constant group velocity:[41]

$$v_g = \frac{c}{\tilde{n} + \omega\frac{d\tilde{n}}{d\omega}}. \tag{2.13}$$

If the group velocity is also frequency dependent, then the pulse will spread with propagation time. Figure 2.2 shows the real and imaginary part of the refractive index close to a resonance. The lineshape of the real part extends over a much broader frequency region than the imaginary part, which implies that severe pulse elongation can occur even though the medium is transparent ($\kappa \approx 0$).

2.1.3 MODELS FOR THE REFRACTIVE INDEX

To describe the frequency dependence of the refractive index, we assume that an electric field $\vec{E} = \vec{E}_0 e^{-i\omega t}$ inside a material can displace charges, like electrons,

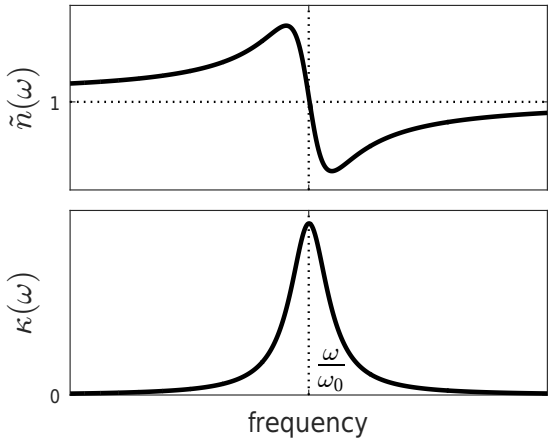

FIGURE 2.2. Frequency dependence of the real $\tilde{n}$ and imaginary κ part of the refractive index n in vicinity of a resonance at ω_0.

ions[43].[44] For small electric field strengths the bound charges with effective mass m and charge q will experience a restoring force with spring constant k. In addition, the movement of the charges will be damped by a general friction term Γ due to, among others, radiative damping.[42] Summing over all presented terms allows us to write the equation of motion:

$$m\frac{\partial^2\vec{x}}{\partial t^2} = F_{restore} + F_{damp} + F_{drive} \tag{2.14}$$

$$= -k\vec{x} - m\Gamma\frac{\partial\vec{x}}{\partial t} + q\vec{E}_0 e^{-i\omega t}. \tag{2.15}$$

This differential equation can be solved by using the ansatz $\vec{x} = \vec{x}_0 e^{-i\omega t}$ which leads to:

$$\vec{x}_0 = \frac{q\vec{E}_0}{m}\cdot\frac{1}{\omega_0^2 - \omega^2 - i\Gamma\omega}, \tag{2.16}$$

where we have introduced the fundamental frequency $\omega_0 = \sqrt{\frac{k}{m}}$ of the oscillator. Since the oscillators inside the medium can have different properties (like friction terms), and experience different local environments, we can divide them into ensembles i with the oscillator densities N_i, local friction terms Γ_i and fundamental frequencies ω_i. By combining the expression for the displacement of the charge $\vec{x}$, with the definition for the microscopic dipole $\vec{\mu} = q\vec{x}$ and Eq. (2.3) we can express the dielectric function as:

$$\varepsilon_r(\omega) = 1 + \sum_i \frac{q^2}{m_i\varepsilon_0}\frac{N_i}{\omega_i^2 - \omega^2 - i\Gamma_i\omega}. \tag{2.17}$$

Figure 2.2 shows the dielectric function close to a resonance.
Equation 2.17 (Lorentz model[42]) provides a general approach for charge displacement

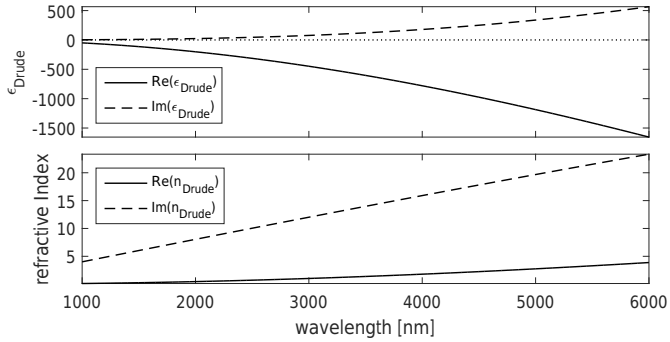

FIGURE 2.3. Dielectric function (top) and refractive index (bottom) of gold calculated with the Drude model ($\Gamma = 17.1 \cdot 10^{12}$ s^{-1}, $\omega_p = 2.15 \cdot 10^{15}$ s^{-1}[46]).

and offers an accurate description for a wide range of phenomena including bound electrons, dielectrics and molecular vibrations.

For (noble) metals at visible and infrared frequencies where the majority of the accessible charges originate from free electrons, the Lorentz model reduces to the Drude model.[45] In this special case, the restoring force vanishes ($k = 0$) and we can substitute the electron mass m_e, charge $q = -e$ and density n into Eq. (2.17) and arrive at:

$$\varepsilon_r(\omega) = 1 + \frac{e^2 n}{m_e \varepsilon_0} \frac{1}{-\omega^2 - i\Gamma\omega} = 1 - \frac{\omega_p^2}{\omega^2 + i\Gamma\omega}, \tag{2.18}$$

where we have introduced the material specific plasma frequency $\omega_p = \sqrt{\frac{e^2 n}{m_e \varepsilon_0}}$.

Figure 2.3 shows the real and imaginary part of the dielectric function of gold calculated with literature values for Γ and ω_p.[46] With increasing wavelength the real part of ε_r decreases monotonically and the imaginary part increases monotonically. The Drude model reproduces the experimental data of noble metals, like gold, very well in the infrared, but it breaks down in the visible and ultraviolet frequency range where interband transition from bound electrons becomes a dominant contribution to the dielectric function.[47]

Since for most metals the friction term is significantly smaller than the plasma frequency ($\Gamma \ll \omega_p$), the dielectric function can be further simplified to:

$$\varepsilon_r \approx 1 - \frac{\omega_p^2}{\omega^2}. \tag{2.19}$$

Using the Fresnel equation to determine the reflectivity, one can show that materials with a negative real part act as good reflectors. However, for $\omega > \omega_p$ ε_r becomes positive and the material becomes transparent.[41] The plasma frequency of most metals is in the ultraviolet, explaining why they are good mirrors in the visible and the infrared.

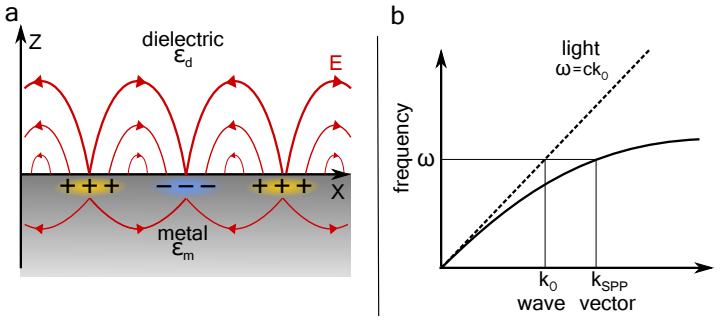

FIGURE 2.4. a) Charge density and electric field of a surface-plasmon-polariton (SPP) at the metal-dielectric interface. b) Dispersion relation of a plane wave in vacuum (dashed) and a SPP (straight).

2.2 PLASMONICS

Plasmonic nanoantennas have the ability to localize energy from the free radiation field to their direct vicinity (see Fig. 2.6). In Chapter 5 and Chapter 6 we will show how the near-field enhancement associated with this process can be exploited to greatly increase the signals in nonlinear infrared spectroscopy.
The following section will provide some theoretical background. We will first introduce the surface-plasmon-polariton as a solution to Maxwell's equations at the plane metal-dielectric interface. In the second part we will make the connection with nanoantennas by considering sub-wavelength particles. Nanoantennas can be resonantly driven by the external light field leading to strongly localized particle-plasmon-polaritons (PPP). We will introduce two intuitive models to explain the origin of the resonance condition of the PPPs and show how it is affected by the antenna geometry.

2.2.1 SURFACE PLASMON POLARITONS

Figure 2.4a shows a schematic representation of a surface-plasmon-polariton (SPP) which is the charge density oscillation and the accompanying electromagnetic wave at the interface of a dielectric and a material with (close to) free electrons, like most noble metals.[48]
To show that SPPs are solutions of Maxwell's equations it is sufficient to look at a two dimensional system (x-z-plane) where the dielectric and the metal form an interface along the x-axis, and the materials have respective dielectric constants ε_d and ε_m. Here we assume that both dielectric constants are real. We will use a p-polarized wave which propagates along the x-axis in the x-y-plane and has wave vector components parallel $k_{||}$ and perpendicular $k_{\perp}$ to the interface. Since SPPs are bound to the interface, the electric field has to decay exponentially into both media. Therefore, the perpendicular component of the wave vector $k_{\perp}$ has to be imaginary. We are assuming that the plasmon propagates along the interface (x-direction). Therefore,

the wave vector component parallel to the interface $k_{||}$ has to have a real part. Hence, the electric field inside the metal (m) and dielectric (d) are given by:

$$\vec{E}_l = \begin{pmatrix} E_{||} \\ 0 \\ E_{\perp} \end{pmatrix} e^{i(k_{||,l}x-\omega t)} e^{ik_{\perp,l}z} \quad l = m, d. \tag{2.20}$$

Because we consider a material without any excess charge carriers, $\nabla \cdot \vec{D} = 0$ we find that

$$k_{||,l}E_{||,l} + k_{\perp,l}E_{\perp,l} = 0 \quad l = m, d. \tag{2.21}$$

Next we use the standard electromagnetic boundary conditions at a charge-free interface:[40]

$$E_{||,m} - E_{||,d} = 0 \tag{2.22}$$

$$\varepsilon_m E_{\perp,m} - \varepsilon_d E_{\perp,d} = 0. \tag{2.23}$$

The last four equations only have a nontrivial solution for

$$\varepsilon_m k_{\perp,d} - \varepsilon_d k_{\perp,m} = 0. \tag{2.24}$$

Lastly, we use the dispersion relation of a homogeneous medium:[40,41]

$$\varepsilon_l k^2 = k_{\perp,l}^2 + k_{||,l}^2 \quad l = d, m, \tag{2.25}$$

where k is the wave vector in vacuum. Combining Eq. (2.24) and Eq 2.25, and using the fact that the parallel component of the wave vector has to be conserved,[41] we find for the components of the wave vector:

$$k_{||} = \sqrt{\frac{\varepsilon_m \varepsilon_d}{\varepsilon_m + \varepsilon_d}} \frac{\omega}{c} \tag{2.26}$$

$$k_{\perp,l} = \sqrt{\frac{\varepsilon_l^2}{\varepsilon_m + \varepsilon_d}} \frac{\omega}{c} \quad l = m, d. \tag{2.27}$$

Electric fields that are confined to an interface decay exponentially into both media. Therefore, it follows from Eq. (2.27) that the sum of the dielectric functions has to be negative. Demanding a real solution for $k_{||}$ also requires the product of the dielectric functions to be negative, therefore:

$$\varepsilon_d \cdot \varepsilon_m < 0 \tag{2.28}$$

$$\varepsilon_d + \varepsilon_m < 0. \tag{2.29}$$

It is easy to find material pairs that fulfil these requirements. As was shown in Section 2.1.3, the dielectric function of noble metals is mainly composed of a large, negative real part at visible and infrared frequencies, and dielectrics like air, glass or

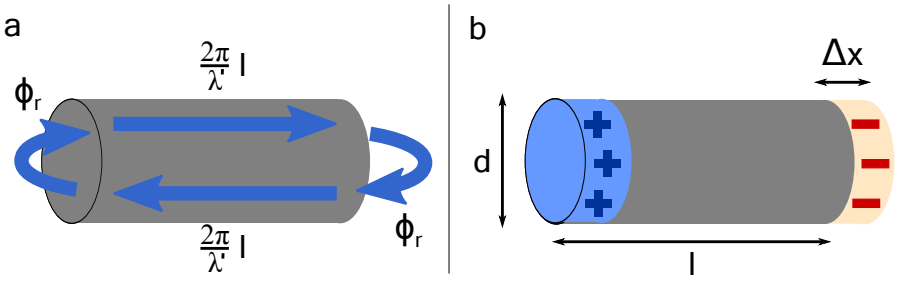

FIGURE 2.5. a) Fabry-Perot-model of a single nanowire. A wave traveling along the wire acquires a phase $\phi = \frac{2\pi}{\lambda} l$ and upon reflection at the caps an additional factor of ϕ_r. b) Mass-spring-model of a single nanowire, where the free electron gas is displaced by Δx inducing net charges at the ends.

CaF_2 have a small, positive and real ε_r in the same frequency range. Having found possible material pairs, the remaining question is how to excite surface-plasmon-polaritons. Figure 2.4 shows the dispersion relation for the parallel component of the wave vector of a plane wave in free space and for a SPP at a air-metal interface. Energy and momentum conservation dictates that excitation of the plasmon happens at the intersection of the two curves. Since no such crossing point exists (different momentum at every energy), it is not possible to directly excite SPPs with plane-wave illumination.

2.2.2 PARTICLE PLASMONS

In contrast to plane interfaces, it is possible to directly (by plane-wave illumination) excite surface plasmons on particles much smaller than the wavelength.[49] Imagine, for example, a small metal wire with a diameter of 10–100 nm, so that the penetration depth (skin depth) of the electric field is of the same order as the radius[a]. Combined with the strong curvature of the wire, this leads to a broad distribution of differently oriented wave vectors at the interface, of which some match the dispersion relation of the plasmon.

The excited surface plasmons are strongly localized on the wire and in the simplest case propagate as rotationally symmetric waves along the structure.[49,50] If we are dealing with a wire of finite length, like a rod, the ends act as discontinuities which can be described as mirrors at which the propagating wave is reflected with a phase jump Φ_r.[49] It is easy to imagine that we can find wavelengths λ' for a given length d of the metal rod where the phase difference δ between consecutive round trips is an integer n multiple of 2π, resulting in constructive interference:

$$\delta = 2(\frac{2\pi}{\lambda'} l + \Phi_r) = 2n\pi \quad n = 0, 1, 2, \ldots. \tag{2.30}$$

[a]Using Equation 2.11 we can estimate the skin depth (decay of the field magnitude to $1/e$) of gold ($\kappa \approx 38$) at 6 μm to be 13 nm.

Thus, a localized particle-plasmon-polariton (PPP) can be described as a standing electromagnetic wave on a metal nanorod.[51] This Fabry-Pérot model, besides providing an intuitive model for the plasmon resonance, also correctly captures the higher-order modes which have been observed in near-field probing experiments[51] (see also Fig 2.6). It is worth noting that the wavelength λ' of this PPP is smaller than the corresponding vacuum wavelength λ_0. Using the Drude model and assuming a subwavelength metal rod one can show that:

$$\lambda' = a + b\,\lambda_0, \tag{2.31}$$

where a and b are frequency independent parameters which are given by the geometry of the rod and end caps.[52]
It is instructive to introduce an alternative description where the localized surface plasmon is treated as the resonant displacement of the free electrons of the metal (mass-spring-model). We describe the nanorod as a cylinder with base $A = \pi(d/2)^2$ and length l (see Fig. 2.5). If the electron distribution of this rod is displaced by Δx relative to the lattice, net charges $\pm q$ accumulate at the ends. This charge accumulation is strongly dependent on the electron density n and leads to a Coulomb potential of the form:

$$V(\Delta x) = \frac{1}{4\pi\varepsilon_0}\frac{q^2}{d} = \frac{1}{4\pi\varepsilon_0}\frac{(neA)^2}{l}\Delta x^2, \tag{2.32}$$

where e is the electron charge. By expressing the spring constant as $D = \omega_{Res}^2 m$ where $m = m_e nAl$ represents the collective mass of all electrons, the restoring force can be written as:

$$F(\Delta x) = -\frac{\partial V}{\partial \Delta x} = -\frac{n^2e^2}{2\pi\varepsilon_0}\frac{A^2}{l}\Delta x = -D\Delta x, \tag{2.33}$$

which allows us to determine the resonance frequency

$$\omega_{Res} = \frac{\omega_p}{2\sqrt{2}}\frac{d}{l}, \tag{2.34}$$

where $\omega_p = \sqrt{\frac{ne^2}{\varepsilon_0 m_e}}$ is the material specific plasma frequency. Although this model disregards higher-order resonances and does not accurately predict the precise spectral position of the plasmon resonance, it provides an intuitive picture for the resonance condition, and works very well for capturing general trends. Among others, it correctly predicts the scaling of the resonance frequency with the inverse of the aspect ratio $R = d/l$,[53] as well as the dependency of ω_{Res} on the charge carrier density (i.e. the metal used).[54]

2.3 NONLINEAR POLARIZATION

Most experiments in this thesis deal with the ultrafast dynamics of vibrational modes that are resonant in the mid-infrared, e.g. the amide I (6 μm) and the NH_3^+-bending

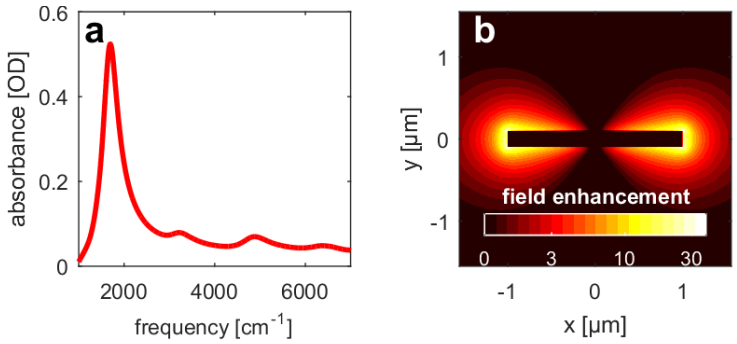

FIGURE 2.6. a) Linear infrared spectrum of gold nanorods on a CaF_2 substrate. In addition to the fundamental resonance at 1700 cm^{-1}, higher-order modes can be seen at ~3300 cm^{-1}, ~4900 cm^{-1}, ~6400 cm^{-1}. b) Finite-difference time-domain simulations of one gold nanorod (black bar in the center) on a CaF_2 substrate. The color scale shows the enhancement of the incident electric field at the resonance frequency of the nanoantenna.

vibration (7 µm). Unfortunately, there are no ultrafast, tunable laser systems which access this wavelength range directly. Instead, one usually starts with an intense light source in the visible or near-infrared (0.5–1.2 µm) and exploits the nonlinearity of the light-matter interaction to generate infrared wavelengths. Modern pulsed laser sources in the visible can generate electric field strengths of more than 10^9 V/m for which in many materials the linear relationship between the polarization and the electric field does not hold anymore. In this case we can express the induced polarization as a power series in the electric field $\vec{E}$[55]

$$P_i = \varepsilon_0 \left(\sum_{j=1}^{3} \chi_{ij}^{(1)} E_j + \sum_{j,k=1}^{3} \chi_{ijk}^{(2)} E_j E_k + \sum_{j,k,l=1}^{3} \chi_{ijkl}^{(3)} E_j E_k E_l + \dots \right), \tag{2.35}$$

where the tensors $\chi^{(n)}$ are the various expansion orders of χ with rank $n+1$. By writing the products in Equation 2.35 we are assuming that all orders of χ are real, i.e. that the material reacts instantaneously to the applied electric field.[56] For light-conversion applications involving $\chi^{(2)}$ this is mostly valid since the involved crystals are transparent and can be assumed lossless in the frequency regions of interest. By expressing every expansion order n by a symbol $\vec{P}^{(n)}$ we can rewrite Equation 2.35 as a sum of linear $P^{(1)} = P^L$ and nonlinear terms P^{NL}:

$$\vec{P} = \vec{P}^{(1)} + \vec{P}^{(2)} + \vec{P}^{(3)} + \dots = \vec{P}^L + \vec{P}^{NL}. \tag{2.36}$$

The magnitude of the different susceptibility tensor elements strongly depends on the material and symmetry of the medium. For instance, the second order polarization vanishes inside the bulk of a centrosymmetric material. Therefore a non-vanishing second order polarization can only arise at the interface of a material or inside the bulk of a non-centrosymmetric material.[55,56]

For the following discussion we will drop the vectorial nature of the electric field and the polarization and consider $P^{(2)}$ for a noncentrosymmetric, nonlinear medium

in the presence of two monochromatic, linearly polarized plane waves propagating in the z-direction. We can write the total electric field as a superposition of the two scalar input fields, with $\omega_1 > \omega_2$:

$$E(t,z) = A_1 \cos(k_1 z - \omega_1 t) + A_2 \cos(k_2 z - \omega_2 t), \tag{2.37}$$

where A_n is the amplitude, k_n the wave vector and ω_n the frequency of the respective field. Inserting Equation 2.37 into the second order polarization $P^{(2)}$ yields:

$$\begin{aligned} P^{(2)} = \varepsilon_0 \chi^{(2)} E^2 = \varepsilon_0 \chi^{(2)} \big(& 0.5 A_1^2 \cos(2(k_1 z - \omega_1 t)) && \text{(SHG)} && (2.38)\\ & + 0.5 A_2^2 \cos(2(k_2 z - \omega_2 t)) && \text{(SHG)} && (2.39)\\ & + A_1 A_2 \cos((k_1 + k_2) z - (\omega_1 + \omega_2) t) && \text{(SFG)} && (2.40)\\ & + A_1 A_2 \cos((k_1 - k_2) z - (\omega_1 - \omega_2) t) && \text{(DFG)} && (2.41)\\ & + 0.5 (A_1^2 + A_2^2) \big). && \text{(OR)} && (2.42) \end{aligned}$$

This equation shows that the nonlinear polarization has new frequency components which were not present in the input fields. Specifically, the first two terms represent second harmonic generation (SHG) or the doubling of ω_1 and ω_2, the third term is the sum frequency (SFG) and the fourth term the difference frequency of the two input frequencies. The last term is constant in time and corresponds to a static polarization of the medium (optical rectification).

To simplify the discussion, we assume that the most dominant contribution originates from the DFG-term (Eq. (2.41)) where the ordering of the frequencies is given by: $\omega_1 > \omega_2 \geq \omega_3$. In general, all of the above frequency mixing processes are present, but by manipulating magnitude of the wave vectors of the input fields and the generated field, the conversion efficiency of specific processes can be selected, as will be shown below.

To investigate the light conversion process inside the nonlinear material, we insert the nonlinear polarization into the wave equation Eq. 2.4:

$$\frac{\partial^2 E(t,z)}{\partial z^2} - \frac{\varepsilon_r}{c^2} \frac{\partial^2 E(t,z)}{\partial t^2} = \mu_0 \frac{\partial^2 P^{NL}(t)}{\partial t^2}. \tag{2.43}$$

The nonlinear polarization acts as a source term which oscillates at ω_3:

$$P^{NL}(t,z) = P^{NL}(z) e^{-i\omega_3 t} + c.c., \tag{2.44}$$

which in turn drives an electric field with amplitude $\tilde{A}(z)$:

$$E(t,z) = \tilde{A}(z) e^{-i\omega_3 t} + c.c. \tag{2.45}$$

at the same frequency. We assume that the field amplitudes $\tilde{A}$, A_1 and A_2 are time-independent. By executing the time derivative we can remove the time-dependence from Eq. (2.43):

$$\frac{\partial^2 \tilde{A}(z)}{\partial z^2} + \frac{\varepsilon_r \omega_3^2}{c^2} \tilde{A}(z) = -\mu_0 \omega_3^2 P^{NL}(z). \tag{2.46}$$

The amplitude of the generated electric field is explicitly dependent on the position, since it will increase or decrease as the input fields propagate through the material. We make the assumption that the higher-order terms of the expansion in Eq. 2.36 only contribute a small correction to the linear term. Therefore, it is expected that the amplitude will vary slowly over multiple optical cycles. This is called the slowly varying envelope approximation[55,56] and it allows us to separate the amplitude $\tilde{A}(z) = A(z)e^{ikz}$ of the generated field into a rapidly varying component e^{ikz} and a slowly evolving envelope $\tilde{A}(z)$. With this we can simplify the first term in Eq. (2.43):

$$\frac{\partial^2 A(z)e^{ikz}}{\partial z^2} = \left(-k^2 A(z) + 2ik\frac{\partial A(z)}{\partial z} + \frac{\partial^2 A(z)}{\partial z^2}\right)e^{ikz} \tag{2.47}$$

$$\approx \left(-k^2 A(z) + 2ik\frac{\partial A(z)}{\partial z}\right)e^{ikz} \tag{2.48}$$

by assuming $\left|ik\frac{\partial A(z)}{\partial z}\right| \gg \left|\frac{\partial^2 A(z)}{\partial z^2}\right|$. Combining Eq. (2.44) and Eq. (2.48) we can rewrite the wave equation Eq. (2.43) in its general form:

$$2ik\frac{\partial A}{\partial z}e^{ikz} = \mu_0 \omega^2 P^{NL}. \tag{2.49}$$

By replacing the nonlinear polarization with the DFG-term from Eq. (2.42), we arrive at:

$$2ik\frac{\partial A_3}{\partial z}e^{ik_3 z} = -\frac{2\omega_3^2}{c^2}\chi^{(2)}A_1 A_2 e^{i(k_1 - k_2)z}. \tag{2.50}$$

The right-hand side of the equation can be interpreted as the spatially modulated polarization, with wavelength $2\pi/(k_1 - k_2)$, driving an electric field; and the left hand side is the generated electric field with wavelength $2\pi/k_3$. The efficiency of the nonlinear light conversion is dictated by the wave vector mismatch $\Delta k = k_1 - k_2 - k_3$ between the polarization and the wave front of the generated field. This means, that as long as Δk is non-vanishing, there exists a point $l_c = \pi/\Delta k$ at which the generated field has a phase shift of π relative to the field generated at $z = 0$. This destructive interference results in an energy flow from E_3 back to E_1 and E_2. The coherence length l_c defines the maximum path length up to which the amplitude of the generated field increases.

Under most conditions, even when employing materials with strong optical nonlinearity, the build up of E_3 will be negligible, since $\Delta k \neq 0$. To understand why $\Delta k \neq 0$ we can rewrite the wave vector mismatch:

$$\Delta k = \frac{n_1\omega_1}{c} - \frac{n_2\omega_2}{c} - \frac{n_3\omega_3}{c} \tag{2.51}$$

$$\Delta k = \frac{1}{c}(\omega_2(n_1 - n_2) + \omega_3(n_1 - n_2)). \tag{2.52}$$

In the absence of a resonance, most materials exhibit normal dispersion ($n(\omega_1) > n(\omega_2)$ for all $\omega_1 > \omega_2$), in which case the wave vector mismatch in the last equation is always greater than zero. It is, nevertheless, possible to achieve $\Delta k = 0$ by using

a technique called phase-matching, which employs a class of materials which are nonlinear and birefringent. In these materials, the refractive index strongly depends on the polarization and propagation direction of the electric field. Therefore, perfect phase-matching can be achieved by adjusting the beam polarization and choosing the correct crystal orientation.[55,56] In our setup, we use this approach to effectively convert 800 nm light to the mid-infrared (Section 3.1).

2.4 NONLINEAR INFRARED SPECTROSCOPY

Most of the experiments presented in this thesis involve nonlinear infrared spectroscopy. In this section we will introduce the theoretical foundation for infrared light-absorption, discuss the basic principles of pump-probe spectroscopy and show how it can be used to explore ultrafast molecular dynamics.

2.4.1 INFRARED ABSORPTION

Molecular vibrations can be described as quantum mechanical harmonic oscillators.[57–59] The time-independent Hamiltonian of an oscillator with mass m and spring constant k is given by:

$$\hat{H}_0 = \frac{\hat{p}^2}{2m} + \frac{1}{2}k\hat{x}^2, \tag{2.53}$$

where $\hat{p}$ and $\hat{x}$ refer to the momentum and position operator, respectively. The energies E_ν for the allowed states $|\Psi\rangle$ of the system can be found by solving the time-independent Schrödinger equation:[60,61]

$$\hat{H}_0 |\Psi\rangle = \hat{E} |\Psi\rangle . \tag{2.54}$$

By determining the eigenvalues of the equation one can find the state energies:

$$E_\nu = \hbar\omega_0(\nu + \frac{1}{2}), \tag{2.55}$$

where ν is the vibrational quantum number and $\omega_0 = \sqrt{k/m}$ the fundamental frequency of the oscillator. The system described so far is stationary, and it will not undergo state transitions because the Hamiltonian is independent of time. A time-dependent perturbation $V(t)$ of the static Hamiltonian:

$$\hat{H}(t) = \hat{H}_0 + \hat{V}(t) \tag{2.56}$$

is necessary to induce a state transition. In spectroscopy, the perturbation is given by an oscillating electric field which acts on the dipole moment (operator) $\vec{\hat{\mu}}$ of the molecule:[57]

$$\hat{V}(t) = -\frac{1}{2}\vec{\hat{\mu}} \cdot \vec{E}(t) = -\frac{1}{2}\vec{\hat{\mu}}\vec{E}_0\left(e^{-i\omega t} + e^{i\omega t}\right). \tag{2.57}$$

Here we have used the electric dipole approximation which assumes that the spatial extent of the electromagnetic wave is much larger than the size of the oscillator:

$e^{i\vec{k}\vec{x}-i\omega t} \approx e^{-i\omega t}$. The temporal evolution of the wave function $|\Psi\rangle$ is described by the time-dependent Schrödinger equation:[60,61]

$$i\hbar\frac{\partial}{\partial t}|\Psi\rangle = \hat{H}(t)|\Psi\rangle. \tag{2.58}$$

For a small perturbation, the transition rate R_{es} per unit time from an initial state $|s\rangle$ with energy E_s to a final state $|e\rangle$ with energy E_e is in first order given by Fermi's golden rule:[60,61]s

$$R_{es} = \frac{2\pi}{\hbar^2}|\langle e|\,\hat{V}(t)\,|s\rangle|^2(\delta(\omega_{es}-\omega)+\delta(\omega_{es}+\omega)), \tag{2.59}$$

where $\omega_{es} = (E_s - E_e)/\hbar$. Substituting the perturbation from the light field and writing the inner product $\vec{\hat{\mu}}\cdot\vec{E}$ in terms of the angle θ between $\vec{E}$ and $\vec{\hat{\mu}}$, we can reformulate the transition rate to:

$$R_{es} = \frac{\pi}{2\hbar^2}|E_0|^2\cos^2(\theta)\Big(\delta(\omega_{es}-\omega)+\delta(\omega_{es}+\omega)\Big)|\langle e|\,\hat{\mu}\,|s\rangle|^2. \tag{2.60}$$

Equation 2.60 provides much information about light absorption. The $\cos^2(\theta)$ factor implies that the relative orientation of the transition dipole moment and the electric field dictates the absorption. The two Dirac-δ functions ensure energy conservation: the amount of energy extracted ($\delta(\omega_{es}-\omega)$) from or provided ($\delta(\omega_{es}+\omega)$) to the electric field has to be exactly the energy difference between two states.

To evaluate the last factor in Eq. 2.60, it is convenient to expand $\vec{\hat{\mu}}(x)$ in a Taylor series around the equilibrium $x = x_0$:

$$\langle e|\,\vec{\hat{\mu}}(x)\,|s\rangle\Big|_{x\approx x_0} = \underbrace{\vec{\mu}(x_0)\langle e|s\rangle - \frac{\partial\vec{\mu}(x_0)}{\partial x}x_0\langle e|s\rangle}_{0\,for\,e\neq s} + \frac{\partial\vec{\mu}(x_0)}{\partial x}\langle e|\,\hat{x}\,|s\rangle\ldots \quad . \tag{2.61}$$

The first two terms are zero for state transitions, due to the orthogonality of the vibrational states. By using only the first order of the Taylor expansion, the selection rules are limited to $e = s \pm 1$. To also capture multi-quantum absorption, like overtones and combination bands, higher-order terms of the potential (anharmonicity) or the expansion of $\vec{\hat{\mu}}$ need to be included. Although it is possible to excite such higher-order transitions, their cross section usually rapidly decreases with the number of vibrational quanta involved[b]!

Lastly, the $\frac{\partial}{\partial x}\vec{\mu}$ term implies that for a mode to be excitable by the electric field, the transition dipole moment of the molecule has to change as a result of the vibrational motion. This explains why the symmetric stretch vibration of H_2O has an infrared absorption but the same vibration in CO_2 does not.

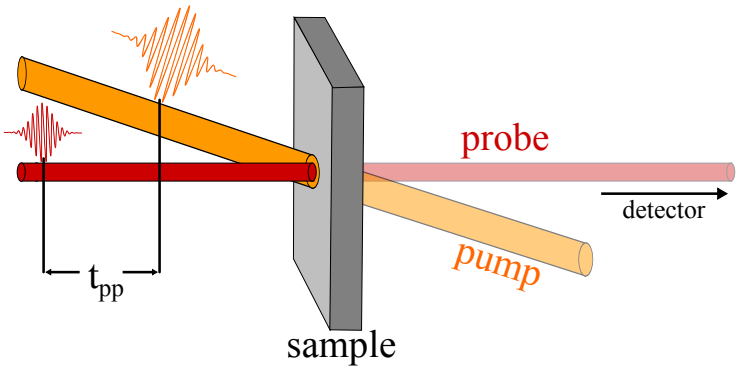

FIGURE 2.7. Pump-probe experiment. An intense pump pulse excites a significant amount of molecules in its focal spot (in the sample). The excited molecules are monitored by a weak probe pulse which interrogates the sample at a time delay t_{pp} after the pump pulse.

2.4.2 ANHARMONIC OSCILLATOR

It is easy to see that the harmonic potential used in the previous section is not a realistic representation of a vibration.The repulsive force should become infinitely large as the distance between two atoms (or chemical groups) vanishes due to electrostatic repulsion; for $x \to \infty$, the restoring force should become zero upon dissociation. For a more realistic representation, one can expand the vibrational potential to include higher-order terms:

$$\hat{H} = \underbrace{\frac{1}{2m}\hat{p}^2 + \frac{1}{2}k\hat{x}^2}_{H_0} + \underbrace{c\hat{x}^3 + d\hat{x}^4}_{\hat{H}'}, \tag{2.62}$$

where c and d are expansion coefficients. In the last equation we have also rewritten the harmonic Hamiltonian $\hat{H}_0$ as a function of the ladder operators:[60,61]

$$\hat{x} = \sqrt{\frac{\hbar}{2m\omega}}(\hat{a}^\dagger + \hat{a}) \qquad \hat{p} = i\sqrt{\frac{\hbar m\omega}{2}}(\hat{a}^\dagger - \hat{a}). \tag{2.63}$$

These operators simplify the calculation of the energy eigenvalues, since they essentially increase or decrease the energy of the oscillator by one quantum when they operate on the energy eigenstate $|n\rangle$:

$$\hat{a}^\dagger |n\rangle = \sqrt{n-1}\,|n+1\rangle \tag{2.64}$$

$$\hat{a}\,|n\rangle = \sqrt{n}\,|n-1\rangle\,. \tag{2.65}$$

It is straightforward to show that the expectation value of the cubic term ($\langle n|\hat{x}^3|n\rangle$) always equates to zero since all terms in the expansion of x^3 have an uneven number

[b]Some of these transitions can still be observed. For example, for long optical path lengths H_2O has a blueish color relative to D_2O which originates from a four-quantum transition (~760 nm).

of creation $\hat{a}$ and annihilation $\hat{a}^\dagger$ operators and therefore are not quantum conserving. Using perturbation theory to first order, the energy levels corresponding to $\hat{H}$ can be written as[57,60]

$$E_n = E_n^{(0)} + d\left\langle n^{(0)}\middle|\hat{x}^4\middle|n^{(0)}\right\rangle \tag{2.66}$$

$$= \hbar\omega\left(n+\frac{1}{2}\right) + \frac{3d\hbar^2}{2m^2\omega^2}\left(n^2+n+\frac{1}{2}\right), \tag{2.67}$$

where $n^{(0)}$ and $E_n^{(0)}$ are the states and the corresponding eigenenergies of the harmonic oscillator (zeroth order). Since the restoring force becomes weaker with increasing displacement, d has to be negative, resulting in lower energy eigenvalues than for the harmonic oscillator. Furthermore, the quartic term in the Hamiltonian leads to **non**equally spaced energy levels. This has very important consequences for pump-probe spectroscopy, where we simultaneously investigate the $|0\rangle \rightarrow |1\rangle$-transition and the $|1\rangle \rightarrow |2\rangle$-transition. For the harmonic case, both transitions have the same frequency.

For the following sections it is important to understand which energy states are usually accessible under normal lab conditions (room temperature). The probability for a mode to be thermally excited at a temperature T from state $|s\rangle$ to $|e\rangle$ is given by Boltzmann statistics:

$$\propto e^{-\frac{E_e-E_s}{k_B T}}, \tag{2.68}$$

where k_B is the Boltzmann constant. As an example, let us consider the $NH_3{}^+$ bending vibration which will be studied in Chapters 7 and 8 ($\omega \approx 1470$ cm^{-1}). From this frequency we can estimate that the excited state population of this vibration is only 0.1% at room temperature. Since all modes considered in this thesis are of similar or even higher frequency (>1470cm^{-1}), we will assume that their population manly occupies the ground state.

2.4.3 PUMP-PROBE SPECTROSCOPY

Linear infrared spectroscopy provies structural information about the interrogated molecules. For example, it provides information on the functional chemical groups present inside the molecules, on the strength of their hydrogen bonds, and, in the case of proteins, on their secondary structure. By extending the experiments to the nonlinear regime, we can gain additional information about dynamic processes, such as vibrational relaxation and molecular reorientation, and about the coupling between different vibrational modes.

In infrared pump-probe spectroscopy, an intense pump pulse is used to saturate a vibration and to prepare a nonequilibrium state. A subsequent weak probe pulse is used to interrogate the excited system. In the following chapters we are going to look at the amide I' and the symmetric NH_3-bend vibrations, which have a decay rate of ~1 ps. The ultrafast processes involving these mode can be observed by introducing a very well-defined time delay t_{pp} between the pump and probe pulses, which can be scanned with high precision over multiple orders of magnitude (fs–ns).

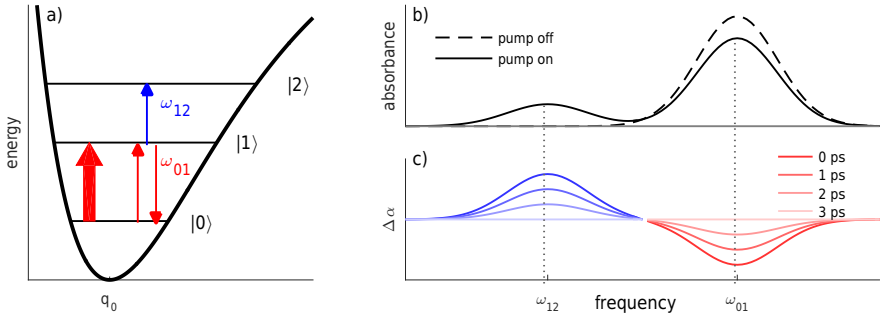

FIGURE 2.8. a) First three levels of an anharmonic vibrational potential. The pump (bold red arrow) excites part of the ground-state $|0\rangle$ population to the first excited state $|1\rangle$. Shortly thereafter the probe pulse exhibits a decreased absorption at the fundamental frequency ω_{01} due to the pump-induced ground-state depletion and stimulated emission from $|1\rangle$. In addition, the probe is absorbed more at ω_{12} because $|1\rangle$ oscillators can be excited to $|2\rangle$. b) shows the linear spectrum measured with and without the preceding pump interaction. c) Pump-probe delay dependent absorption change $\Delta\alpha$.

In practice, an absorption change is measured by comparing the absorption of the probe by the sample in the presence and absence of a pump excitation:

$$\Delta\alpha^{probe} = \alpha^{probe}_{pump_{on}} - \alpha^{probe}_{pump_{off}}. \tag{2.69}$$

For clarity, we will omit the superscript in the following. The second term is just the linear absorption of the probe:

$$\alpha(\omega) = n\sigma_{01}(\omega), \tag{2.70}$$

where n is the concentration of molecules per unit area and σ_{01} the spectrum of the ground state absorption ($|0\rangle \rightarrow |1\rangle$). The interaction with the pump leads to three effects:

1. **ground-state depletion:** The probe light is absorbed less at the fundamental transition $\sigma_{01}(\omega)$ since a fraction of the oscillators N are excited to the first excited state $|1\rangle$.

2. **stimulated emission:** The fraction of excited molecules N can be stimulated to the ground state by emitting a photon. This can also be interpreted as a decrease in absorption at the transition σ_{01}, since more photons are leaving the sample than have entered.

3. **excited-state absorption:** The fraction of excited molecules N can be excited further to the second excited state leading to absorption at slightly lower frequencies ω_{12} due to the anharmonicity of the vibrational potential.

Over time the excited molecules will relax from the excited state to the ground state:

$$N(t) = N(0)e^{-\frac{t}{\tau}}, \tag{2.71}$$

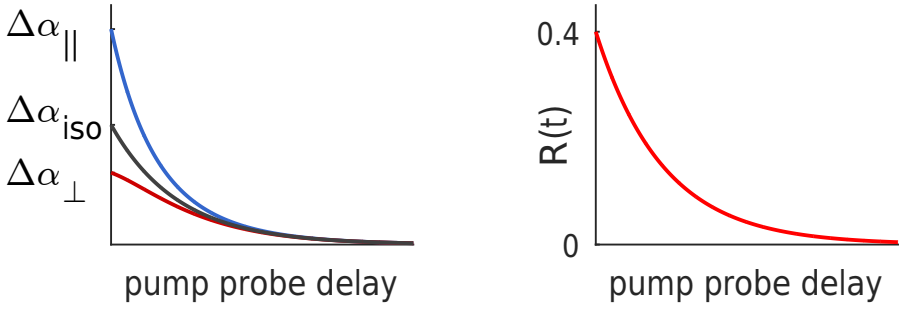

FIGURE 2.9. Polarization-dependent absorption change. By measuring the absorption change in parallel $\Delta\alpha_{||}$ and perpendicular $\Delta\alpha_{\perp}$ polarization, relative to the pump polarization, the isotropic $\Delta\alpha_{iso}$ and anisotropic $R(t)$ signal can be constructed.

where we have assumed a direct decay to the ground state with relaxation time τ. Hence, we can write for the pump induced absorption change:

$$\Delta\alpha(\omega,t) = (n - N(t))\sigma_{01}(\omega) - N(t)\sigma_{01}(\omega) + N(t)\sigma_{12}(\omega) - n\sigma_{01}(\omega) \tag{2.72}$$

$$= \Big(\underbrace{\sigma_{12}(\omega)}_{ESA} - \underbrace{2\sigma_{01}(\omega)}_{bleach}\Big)N(0)e^{-\frac{t}{\tau}}. \tag{2.73}$$

One usually refers to the negative terms of the absorption change as bleach and to the positive term as excited state absorption (ESA). Figure 2.8 summarizes this section in a schematic way.

2.4.4 POLARIZATION DEPENDENCE

One of the key pieces of information that we can access with pump-probe spectroscopy is the vibrational relaxation rate. Ideally, one would just need to monitor the amplitude of the pump-probe signal as a function of delay time to determine the excited-state population and, thereby, the vibrational lifetime. However, a complication arises because (in addition to the excited state population) there are other factors that can affect the amplitude of the pump-probe signal, for example reorientation (rotation) of the excited molecule. In a polarization-resolved pump-probe experiment, where all pulses are linearly polarized, we can construct the isotropic signal:

$$\Delta\alpha(t)_{iso} = \frac{\Delta\alpha(t)_{||} + 2\Delta\alpha(t)_{\perp}}{3}, \tag{2.74}$$

which only depends on the number of excited molecules.[62] Here, $\Delta\alpha_{||}$ and $\Delta\alpha_{\perp}$ are the absorption changes measured with a probe polarization parallel and orthogonal to the pump polarization, respectively.[c] It is important to realize that, due to the

[c]The factor of 2 enters due to the azimuthal symmetry of the excited dipole. If the pump beam linearly polarized (e.g. E_z), there are two different probing polarizations which result in the same absorption change (i.e. E_x and E_y).

$\cos^2\theta$ excitation dependency, the absorption change directly after excitation is highly anisotropic ($\Delta\alpha_{||} > \Delta\alpha_{\perp}$). By keeping track of the degree of anisotropy, we gain access to the average transition dipole orientation of the excited molecules, relative to the pump polarization as a function of delay time. This information can, for example, be used to determine the reorientation time of small molecules like water[d]. The time-dependent anisotropy can be constructed as:[62]

$$R(t) = \frac{\Delta\alpha_{||}(t) - \Delta\alpha_{\perp}(t)}{\Delta\alpha_{||}(t) + 2\Delta\alpha_{\perp}(t)}. \tag{2.75}$$

This definition removes the contribution of the vibrational relaxation to the anisotropy by normalizing to the isotropic signal. The experimental anisotropy provides a measure for the orientation correlation function of the transition dipole moment. More precisely, the anisotropy is related to the angular displacement of the transition dipole moment during the pump-probe delay via:

$$R(t) = \frac{2}{5}\langle P_2(\vec{\mu}(0)\cdot\vec{\mu}(t))\rangle \tag{2.76}$$

$$= \frac{2}{5}\left\langle \frac{1}{2}\left(3\cos^2\theta - 1\right)\right\rangle, \tag{2.77}$$

where $\langle ...\rangle$ is the ensemble average and $P(x)_2 = (3x^2 - 1)/2$ is the second order Legendre polynomial. It is insightful to look at the limiting cases of Equation 2.77 for an isotropic sample.

If $\mu(0)$ and $\mu(t)$ are parallel $R(t)$ is $\frac{2}{5}$. That is, the detected molecules have exactly the same orientation as the exited ones which is, for example, the case directly after excitation ($t_{pp} \sim 0$ ps) since there was not enough time yet for the molecules to undergo any kind of motion. Shortly after excitation, the molecules will undergo (rotational) diffusion and possibly transfer energy to other oscillators. Thus, for long pump-probe delays the molecular ensemble will approach an isotropic distribution with $\left\langle\cos^2\theta\right\rangle = 1/3$ and the anisotropy will decay to $R(t) = 0$. If $\mu(0)$ and $\mu(t)$ are perpendicular, $R(t)$ is $-\frac{1}{5}$.

In a polarization-resolved experiment we usually measure the decay of the anisotropy. The decay mechanism strongly depends on the system. In water, for example, both the reorientation of the individual molecules (~1–5 ps[63,64]) but also resonant energy transfer (<200 fs[65,66]) contribute to the decay of the anisotropy. In big molecules like proteins the anisotropy tends to stay close to 0.4 within the probed time interval since the rotational diffusion is slow compared to the vibrational lifetime.

2.5 TWO-DIMENSIONAL INFRARED SPECTROSCOPY

Two-dimensional infrared spectroscopy (2DIR) provides several advantages over conventional pump-probe spectroscopy. 2DIR can be seen as a pump-probe

[d]For example, the reorientation time of OD vibration of HOD in H_2O is 2.5 ps.[63]

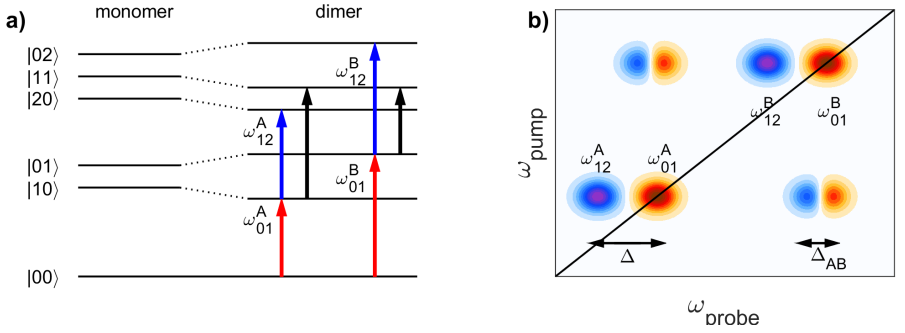

FIGURE 2.10. Coupling in 2DIR. a) level diagram of two vibrational modes in the monomer and weakly coupled configuration. $|ij\rangle$ represent states with i quanta in mode A and j quanta in mode B, and the associated line represents the energy level. Red arrows indicate ω_{01} transitions (bleach), blue arrows the ω_{12} transitions (ESA) and black arrows cross excitation. b) corresponding 2DIR map.

experiment resolved both along the probe and the pump frequency. The additional resolution along the pump axis gives more detailed access to the time evolution of spectral lineshapes (spectral diffusion), and it allows us to identify and characterize anharmonic coupling between vibrations.

Figure 2.10 shows the energy levels for two coupled vibrations and the corresponding 2DIR spectrum. The spectrum can roughly be divided into two parts: peak pairs along the diagonal consisting of a negative bleach ($|0\rangle \rightarrow |1\rangle$) and a positive excited state ($|1\rangle \rightarrow |2\rangle$) absorption of the individual vibrational modes; peak-pairs on the off-diagonal (cross-peaks) which also consist of a positive and a negative part. The appearance of cross-peaks means that excitation of vibration A induces a transient signal from vibration B. Therefore, the mere presence of cross-peaks is a very valuable piece of information since it directly implies coupling between two vibrational modes. By investigating the dynamics of the cross-peaks we can discriminate between different coupling mechanisms, such as anharmonic interaction or energy transfer. In addition, by analyzing the cross-peak anharmonicity (bleach-induced absorption splitting) we can get an indication about the coupling strength, and by looking at the cross-peak anisotropy one can extract the angle between the coupled transition dipoles.

The lineshape of every resonance provides insight into the local environment of the respective vibrational mode. In contrast to linear infrared spectroscopy, in 2DIR it is possible to directly disentangle contributions from homogeneous and inhomogeneous line broadening by inspecting the lineshapes at early t_{pp}-delays. By following the spectral evolution of a peak, one gains access to the timescale of the local fluctuations, which for molecules in solutions often can be related to the solvation dynamics.

2.5.1 ANHARMONIC INTERACTION

Next, we are going to inspect the coupling between two vibrational modes where, for simplicity, we will focus on a weakly coupled dimer and provide a flavor for the general information content accessible by 2DIR. The coupling between two vibrations, which we describe in their respective local mode coordinates, $\hat{q}_A$ and $\hat{q}_B$, is determined by the potential energy surface. Expanding the potential around the local mode coordinates q_i and keeping only the bilinear term yields the following expression for the coupling term:[67]

$$\hat{V}(\hat{q}_A, \hat{q}_B) \approx 2\beta_{AB}\hat{q}_A\hat{q}_B, \tag{2.78}$$

where β_{AB} is the coupling constant. Rewriting the potential in terms of ladder operators $\hat{q}_i = 1/\sqrt{2}(\hat{b}_i^\dagger + \hat{b}_i)$ and keeping only the quantum conserving terms leads to

$$\hat{V}_{AB} = \beta_{AB}(\hat{b}_A^\dagger\hat{b}_B + \hat{b}_B^\dagger\hat{b}_A). \tag{2.79}$$

We will describe the energy of the second excited state by:

$$E_{A,B}^{(2)} = 2E_{A,B}^{(1)} - \Delta_{A,B}, \tag{2.80}$$

where $\Delta_{A,B}$ is the correction term used to account for anharmonicity of the potential. For simplicity, we are going to assume equal diagonal anharmonicies $\Delta = \Delta_A = \Delta_B$ for both vibrational modes. With this, we can write the Hamiltonian for two weakly coupled anharmonic oscillators:[67]

$$\begin{aligned}\hat{H} = \hbar\omega_A\hat{b}_A^\dagger\hat{b}_A + \hbar\omega_B\hat{b}_B^\dagger\hat{b}_B - \frac{\Delta}{2}\hat{b}_A^\dagger\hat{b}_A^\dagger\hat{b}_A\hat{b}_A - \frac{\Delta}{2}\hat{b}_B^\dagger\hat{b}_B^\dagger\hat{b}_B\hat{b}_B \\ +\beta_{AB}(\hat{b}_A^\dagger\hat{b}_B + \hat{b}_B^\dagger\hat{b}_A)\end{aligned}, \tag{2.81}$$

where we have ignored the zero-point energies. The first two terms represent the harmonic-oscillator Hamiltonian for two independent oscillators A and B. The third and fourth terms are phenomenological correction terms needed to account for the anharmonic character of both oscillators. Finally the last term represents the coupling between the two oscillators. Since 2DIR (third-order) spectroscopy can only access states up to two quantum excitations, we work with a reduced basis set $\{|ij\rangle\} = \{|00\rangle, |01\rangle, |10\rangle, |02\rangle, |20\rangle, |11\rangle\}$, where i and j represent the number of excitation on site A and B, respectively. The Hamiltonian matrix in this basis is given by:[67,68]

$$\hat{H} = \begin{pmatrix} 0 & & & & & \\ & \hbar\omega_A & \beta_{AB} & & & \\ & \beta_{AB} & \hbar\omega_B & & & \\ & & & 2\hbar\omega_A - \Delta & 0 & \sqrt{2}\beta_{AB} \\ & & & 0 & 2\hbar\omega_B - \Delta & \sqrt{2}\beta_{AB} \\ & & & \sqrt{2}\beta_{AB} & \sqrt{2}\beta_{AB} & \hbar\omega_A + \hbar\omega_B \end{pmatrix}. \tag{2.82}$$

The Hamiltonian consists of three blocks corresponding to zero, one, and two quanta of excitation. The energies of the coupled states can be found by diagonalizing this Hamiltonian. Since the matrix is block diagonal, the sub-matrices can be diagonalized independently. For the one-quantum case the energies are given by:

$$E^{(1)}_{A,B} = 0.5\left(\hbar\omega_A + \hbar\omega_B \mp \sqrt{4\beta_{AB} + (\hbar\omega_B - \hbar\omega_A)^2}\right). \tag{2.83}$$

In the limit of weak coupling, $|\beta_{AB}| \ll |\hbar\omega_A - \hbar\omega_B|$, the excitation is mainly localized on one of the modes. The corresponding energies are given by the monomer energies slightly shifted by the coupling term:

$$E^{(1)}_{A,B} \approx \hbar\omega_{A,B} \mp \frac{2\beta^2_{AB}}{\hbar\omega_B - \hbar\omega_A}. \tag{2.84}$$

In the other extreme, when both oscillators are strongly coupled $|\beta_{AB}| \gg |\hbar\omega_A - \hbar\omega_B|$, the excitation is delocalized over both modes. In this case, the energies are given by the mean value of the energies of the uncoupled oscillators shifted by the coupling interaction:

$$E^{(1)}_{A,B} \approx 0.5(\hbar\omega_A + \hbar\omega_B) \mp \beta_{AB}. \tag{2.85}$$

Lastly, the energy for the simultaneous excitation of both sites is given by:

$$E^{(2)}_{AB} = E^{(1)}_A + E^{(1)}_B - \Delta_{AB}, \tag{2.86}$$

where Δ_{AB} is the off-diagonal anharmonicity. The last equation can be interpreted as a shift of the spectrum of one vibration, upon excitation of the other. Finding an analytical expression for Δ_{AB} is only possible for the degenerate case $\omega_A = \omega_B$.[67] However, by assuming weak coupling, one can use second order perturbation theory and show that the energy correction:[69]

$$\Delta_{AB} = \frac{4\Delta\beta^2_{AB}}{(\hbar\omega_A - \hbar\omega_B)^2} \tag{2.87}$$

is directly dependent on the coupling term β_{AB}, the energy gap between the two modes, and the diagonal anharmonicity. The seperation between the bleach and the induced absoption of a cross-peak are dictated by the off-diagonal anharmonicity. Hence, it is possible to extract Δ_{AB} and thereby the coupling term β_{AB} from the 2DIR spectrum.

In this context, it is interesting to note that diagonal anharmonicity is essential to observe any peak (doublets) in 2DIR, since without it the bleach and excited state absorption of every peak (diagonal and cross) would perfectly overlap and cancel each other out exactly. Finally, it should be noted that the coupling strength β_{AB} is not directly accessible in linear spectroscopy but it can be extracted from a 2DIR spectrum at one pump-probe delay.[25,68,70]

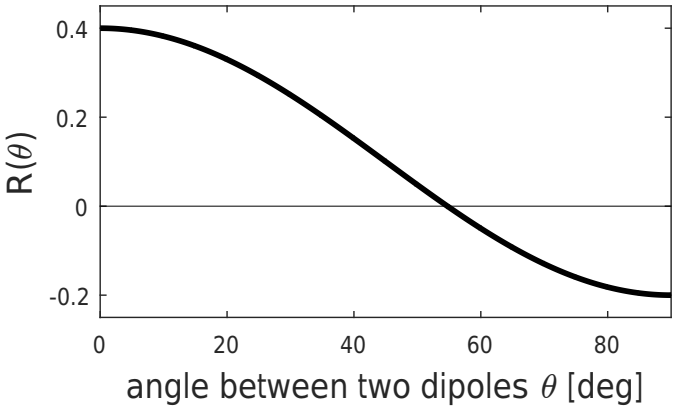

FIGURE 2.11. Cross-peak anisotropy as function of the angle-between the two involved vibrations.

2.5.2 ANISOTROPY OF CROSS-PEAKS

In Section 2.4.4 we saw that anisotropy measurements provide information abouth the orientational motion of (the transition dipole moment of) a molecular vibration. In a very similar manner, the anisotropy of a cross-peak can be used to deduce the relative orientation of two different molecular vibrations (i.e. the angle between their transition dipole moments).
Let us assume that we are inspecting two spectrally separated but still coupled vibrations. In a narrow band excitation experiment where the pump only overlaps with one of the vibrational modes the angle dependence of the anisotropy is the same as for the diagonal peaks:

$$R(\theta) = \frac{2}{5}\langle P_2(\theta)\rangle \quad \text{with} \quad P_2(\theta) = \frac{1}{2}\left(3\cos^2(\theta) - 1\right), \tag{2.88}$$

where θ denotes the angle between the transition dipoles. Therefore, by measuring the anisotropy of the cross-peak and using Eq. (2.88) we can directly extract the relative orientation of the two vibrational modes. In addition, the time-dependence of the cross-peak ansisotropy can provide information about the persistence time of a given configuration. For an extended description of polarization dependence of cross peaks in different experimental geometries and their delay time dependence the reader is referred to Ref.[71] and.[67]

2.5.3 ENERGY TRANSFER

The previous section discussed how cross-peaks can arise from an anharmonic interaction. In this section it will be shown that energy or population transfer can also lead to cross-peaks. Cross-peaks which originate from energy or population transfer can be identified by a delayed ingrowth of their amplitudes since the exchange happens on a timescale longer than the pulse duration ($\sim$100 fs). For most systems

the energy transfer is mediated by a constantly changing local environment. This pulling and pushing of the molecules results in fluctuations of the local side energies $E_i(t) = \bar{E}_i + \delta E_i$ and of the coupling terms $\beta(t) = \bar{\beta} + \delta\beta(t)$. Here $\delta E_i(t)$ and $\delta\beta(t)$ stand for the fluctuating parts of $E_i(t)$ and $\beta(t)$. We gain insight into the effect of these fluctuations by extending the previously introduced one-quantum Hamiltonian (Eq. (2.82)) for a coupled dimer:[72]

$$H(t) = \begin{pmatrix} \bar{E}_A + \delta E_A(t) & \bar{\beta}_{AB} + \delta\beta(t) \\ \bar{\beta}_{AB} + \delta\beta(t) & \bar{E}_B + \delta E_B(t) \end{pmatrix}. \tag{2.89}$$

Using the perturbative expansion to zeroth order, and assuming the weak coupling limit ($\beta \ll \Delta E = |\bar{E}_B - \bar{E}_A|$), one can diagonalize the Hamiltonian with respect to its time average and use Fermi's golden rule ($P_{ij} = k_{ij}T$) to express the cross-relaxation rate as:[72]

$$k_{ij} = \frac{1}{\hbar^2}\int_{-\infty}^{+\infty}\Big(\langle\delta\beta(0)\delta\beta(t)\rangle + \frac{2\beta}{\Delta E}\langle\delta\beta(0)\delta\Delta E(t)\rangle + \Big(\frac{\beta}{\Delta E}\Big)^2\langle\delta\Delta E(0)\delta\Delta E(t)\rangle\Big)e^{\frac{i}{\hbar}\Delta E t}dt \tag{2.90}$$

Here $\langle ...\rangle$ denotes the ensemble average, and $\delta\Delta E = \delta E_B(t) - \delta E_A(t)$. Since we assumed weak coupling, we discard the last two terms ($\frac{\beta}{\Delta E} \ll 1$). If the coupling fluctuations are Gaussian and Markovian[e], Kubo showed that the ensemble average can be written as[73]

$$\langle\delta\beta(0)\delta\beta(t)\rangle = d^2 e^{-\frac{t}{\tau}}, \tag{2.91}$$

where d is the amplitude of the fluctuation and τ the correlation time. Combining Eq. (2.90) and Eq. (2.91) we can find an expression for the transfer rate:

$$k = \frac{2d^2\tau}{\hbar^{-2} + \Delta E^2\tau^2}. \tag{2.92}$$

The last equation shows that the transfer rate is about inversely proportional to the correlation time and directly proportional to the square of the fluctuation amplitude d. Since local fluctuations often originate from the dynamics of the solvent, the choice of the solvent can be used to enhance or decrease the transfer rate between two modes. Lastly, we remark that it may seem that there is an inconsistency in this treatment as energy does not appear to be conserved, i.e., there is an energy mismatch between the initial and the final state. This apparent inconsistency is, however, resolved if one realizes that the energy mismatch is taken up by the low-frequency solvent modes that are responsible for the fluctuations $\delta\beta(t)$.[69,74]

2.5.4 SPECTRAL DIFFUSION

In the previous section we have shown how fluctuations of the coupling term ($\delta\beta$) can induce energy transfer between two modes. In this section we will

[e]The future state only depends on the present state of the system and not on the past.

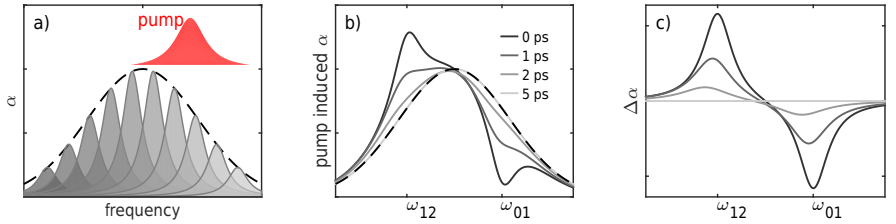

FIGURE 2.12. Hole burning experiment. a) Illustration of an inhomogeneously broadened vibrational mode. By using a narrowband pump pulse only a subensemble of all oscillators is excited, resulting in a narrowband dip in the absorption spectrum (b)). Over time,spectral diffusion takes place, which leads to an increasingly shallower and broader dip in the absorption spectrum. c) The transient spectrum corresponding to b).

discuss the spectral diffusion of a mode which is induced by fluctuations of the site energies (δE). In case these fluctuations occur relatively slowly they lead to an inhomogeneously broadened spectrum. The presence of a strongly inhomogeous broadening mechanism can sometimes be directly inferred by linear spectroscopy, since in most cases, it leads to Gaussian lineshapes in contrast to Lorentzian lineshapes for isolated (homogeneously broadened) vibrations. In general, it is not always possible to use the linear spectrum to determine which broadening mechanism is dominant since other close-by modes may obscure the lineshape or the inhomogeneity may be small relative to the natural linewidth.

In pump-probe spectroscopy this distinction is straightforward. Figure 2.12 demonstrates the principle of a hole-burning experiment where a narrowband pump pulse is used to excite a subband of an inhomogeneously broadened ensemble of oscillators. At short time delays, the pump will have bleached a relatively narrow hole into the absorption spectrum. With increasing pump-probe delay, all oscillators of the inhomogeneous distribution will interconvert, resulting in an increasingly broader and shallower hole. It is worth noting that the mere fact that one is able to bleach a hole in the absorption peak provides a direct confirmation that the transition in question is inhomogeneously broadened. In addition, the rate of the broadening (of the bleached hole) provides direct access to the timescale of the frequency fluctuations exhibited by the oscillators.

The frequency-frequency correlation function (FFCF) is proportional to the probability that an oscillator of a given frequency still has the same frequency after a certain period of time. Hence, by measuring the FFCF one can quantify the spectral diffusion of a given system. For an inhomogeneous ensemble of molecular vibrations, this can be achieved by performing a hole-burning experiment at different frequency positions within the corresponding absorption peak. In fact, if we stack all these hole-burning experiments on top of each other for a certain pump-probe delay we obtain a 2DIR spectrum. We can follow the spectral diffusion dynamics by monitoring the 2DIR lineshapes as a function of the pump-probe delay.

For short pump-probe delays all oscillators will be detected at the same frequency at which they were excited, resulting in diagonally elongated, elliptical 2DIR lineshapes

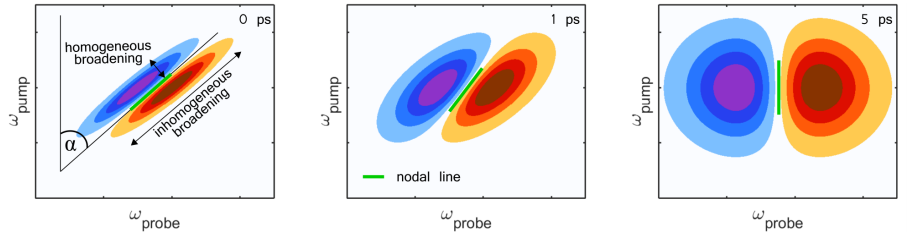

FIGURE 2.13. Measuring the inverse nodal line slope (INLS). All panels show the bleach (red) and ESA (blue) of a vibrational mode at different pump-probe delays. Directly after excitation, the diagonal width indicates the degree of inhomogeneous broadening and the anti-diagonal width the degree of homogeneous broadening. The anti-diagonal width increases with increasing time delay resulting in increasingly circular lineshapes and an increased slope of the nodal line (green).

(Fig. 2.13 left). With increasing delay time, the local environment of most oscillators will vary, which in turn changes their frequency. The frequency redistribution of the excited vibrations can be observed as the reshaping of the 2DIR lineshape with delay time (Fig. 2.13 right).

Similar to the previous section, we describe the frequency-frequency-correlation as $FFCF(t) = \langle \delta\omega(0)\delta\omega(t)\rangle$, where $\delta\omega$ denotes the instantaneous deviation from the fundamental transition frequency ω. Assuming random Gaussian fluctuations of the fundamental frequencies, it can be shown that to good approximation the FFCF decays exponentially:[73]

$$FFCF(t) = \langle \delta\omega(0)\delta\omega(t)\rangle = \Delta\omega^2 e^{-\frac{|t|}{\tau_c}}, \tag{2.93}$$

where τ_c is the decay constant of the correlation and $\Delta\omega$ the amplitude of the fluctuation.

There are various methods to extract the FFCF from the time-dependent 2DIR spectrum.[75,76] One of these methods uses the slope of the nodal line (green line in Figure 2.13) as it was shown that the inverse of this parameter is approximately proportional to the FFCF.[76] By plotting the decay of the inverse nodal line slope verses delay time one obtains the FFCF, which provides direct access to the timescale of the spectral diffusion. In general, however, the fluctuation of the vibrational frequency of a molecular vibration mostly result from the fast (orientational) motions of close-by solvent molecules (see Fig. 1.3). In Chapter 4, we will show how spectral diffusion measurements can yield insight into the solvent exposure of the amide groups of specific amino acids in peptides and proteins.

CHAPTER 3

EXPERIMENT

This chapter will present the pump-probe and 2DIR setup used for the experiments in this thesis. In addition, some aspects of the data acquisition and data processing will be discussed in detail.

3.1 LIGHT GENERATION

In our experiments the wavelengths of the pump and probe pulses can be tuned independently in the range 1.1–10 μm. In order to generate these pulses we start with a regeneratively amplified femtosecond laser system, after which a number of nonlinear conversion steps are used to reach the midinfrared wavelength region.

3.1.1 LASER SYSTEM

The starting point of the laser system is a Ti:Sapphire oscillator (Coherent, Mantis-5) which generates pulses at 811 nm (bandwidth > 80 nm) at a repetition rate of 80 MHz

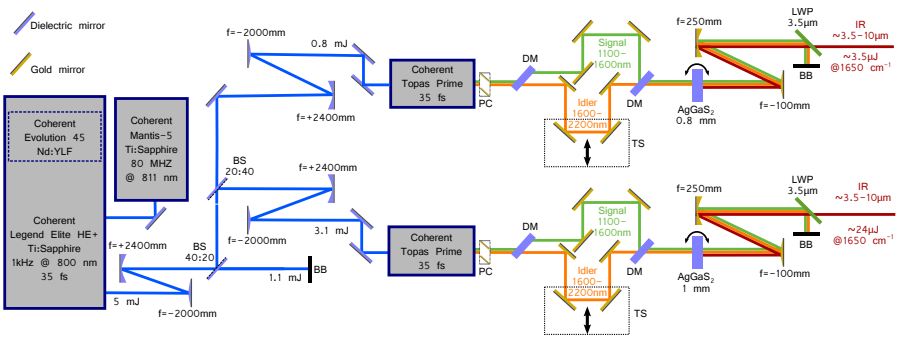

FIGURE 3.1. Generation of mid-infrared femtosecond pulses. BS: beam splitter. DM: dichroic mirror. $AgGaS_2$: silver-gallium-disulfide crystal with indicated thickness. LWP: longwave pass filter. BB: beam block. TS: translation stage. PC: periscope.

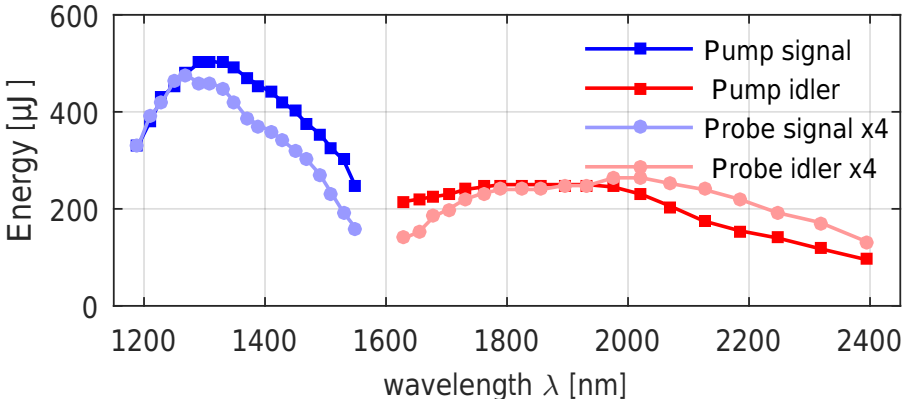

FIGURE 3.2. Signal and idler energies of the pump and probe OPAs as a function of wavelength.

with an output power of ∼ 580 mW. The output from the oscillator is used to seed a Ti:sapphire regenerative amplifier (Coherent, Legend Elite-USP-1K-HE+). The crystal in the amplifier is pumped by an internal ND:YLF laser (Coherent, Evolution 45, 1 kHz, 28 mJ) with a wavelength of 527 nm. After entering the amplifier, the seed pulse is stretched by a pair of gratings to reduce its peak intensity. 1 out of 80 000 seed pulses is coupled into the cavity of the amplifier via a Pockels cell. After 10 round trips through the pumped Ti:Sapphire crystal the amplified pulse is extracted using a second Pockels cell, and lastly, recompressed using a second set of gratings. The amplifier yields p-polarized 35 fs pulses (∼5 mJ) at 800 nm with a repetition rate of 1 kHz.
In order to reduce the power density on the following dielectric optics the diameter of the 800 nm beam is expanded by a factor 1.2 using a telescope. Next, two 80:20 beam splitters are used to split the 800 nm beam into three beams: a ∼0.8 mJ beam for the probe path, a ∼3.2 mJ beam for the pump path and an additional ∼1.1 mJ beam. The diameter of the beams for the pump and probe path are decreased using telescopes (factor: 1.2), and the beams are guided into two commercial optical parametric amplifiers (OPA; Coherent, TOPAS Prime).

3.1.2 OPTICAL PARAMETRIC AMPLIFIERS

The two OPAs constitute the first light conversion steps, and they each generate two output beams—signal (1.1-1.6
textmu m, s-polarized) and idler (1.6-2.2 μm, p-polarized)—with a power conversion efficiency of ∼ 30%[a]. The OPAs operate in two stages. In the first stage, two beams, each containing a small fraction (∼5%) of 800 nm light are split off. The first beam is focused into a sapphire crystal to generate a white-light continuum (WLC) and is consecutively frequency mixed with the delayed second beam inside a β-barium-borate (BBO) crystal. By choosing the delay between the strongly chirped WLC and

[a] ((signal+idler)/input)

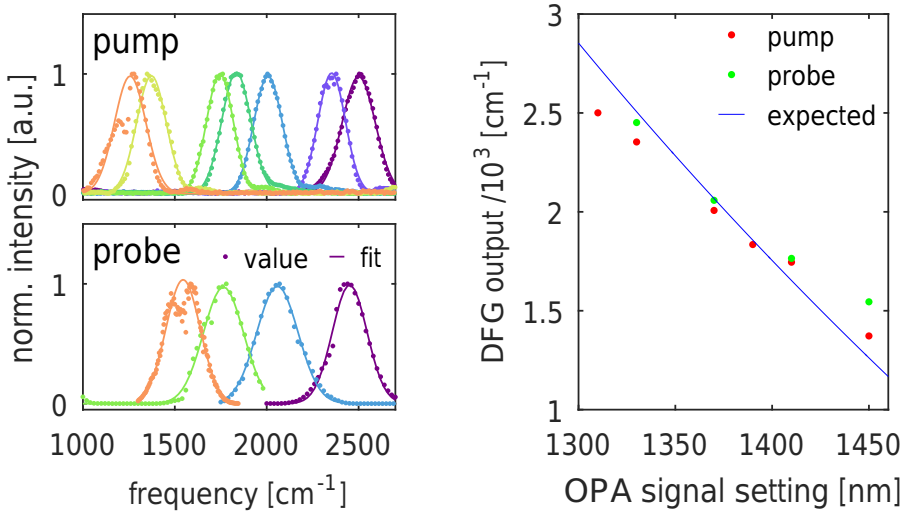

FIGURE 3.3. left: Example spectra of the infrared light generated by frequency mixing signal and idler beams in silver-gallium-disulfide for the pump and probe path. right: Center frequency of the infrared light generated by the difference frequency mixing process as a function of the selected OPA signal wavelength (red and green dots) compared to the expected values (blue line).

the 800 nm beam and the angle of the BBO-crystal, a specific frequency component can be selected and amplified. The amplified signal[b] beam is spatially isolated and used as a seed beam for the second stage. In the second stage the seed (signal) is combined with the remaining 800 nm light (∼90%) in a second BBO-crystal to generate the actual two output beams of the OPA.
The wavelength of the two output beams is set by four parameters: the angle of the BBO crystal in the first and second stage, the delay between the white-light and the 800 nm beam in the first stage, and the delay between the first and the second stage. All parameters can be set by computer controlled translation and rotation motors. After initial calibration of all motors, the wavelengths of signal and idler can directly be selected via a software interface. Figure 3.2 shows the measured energies for signal and idler as a function of frequency for both OPAs.

3.1.3 DIFFERENCE-FREQUENCY GENERATION

To arrive at wavelengths in the mid-infrared (3-10 μm) an additional nonlinear light conversion step is necessary. The conversion efficiency strongly depends on the quality of the temporal and spatial overlap of the signal and idler beams. Since both beams exit the OPA almost collinearly with a small time separation, they are initially separated onto two independent optical paths by a dichroic mirror, guided over a

[b]The three beams involved in difference frequency generation referred to as pump, signal, idler with the frequency ordering $\omega_{pump} > \omega_{signal} > \omega_{idler}$

retroreflector, and subsequently recombined onto a common path using a second dichroic mirror. The retroreflector in the idler path is mounted on a mechanical translation stage which allows to adjust the time delay between both paths. Lastly, the beams are difference-frequency mixed using a silver-gallium-disulfide (AGS, $AgGaS_2$) crystal. The generated p-polarized infrared beam is isolated by a germanium-based long-wave-pass filter (LWP, $\lambda > 3.4$ μm), and the signal and idler pulses are discarded onto a beam block (BB). Lastly, telescopes are used in the pump and probe paths to expand the beam size to ⌀3.8 mm and ⌀5.0 mm, respectively. Figure 3.3 shows example spectra of the generated infrared light and compares their center frequencies with expected values for the selected signal wavelengths.

3.2 PUMP-PROBE EXPERIMENT

Having described the generation of the infrared light, we will next discuss the implementation of the pump-probe experiment in this section. To this end, we will first summarize the working principle of the experiment, then present the experimental realization and, lastly, have an extended look at the detection of the infrared light with an MCT-detector.

3.2.1 OPERATING PRINCIPLE

During a pump-probe (pp) experiment we use the probe pulse to measure the pump-induced absorption change $\Delta\alpha$ of the sample. To this end, the transmission spectrum of the probe pulse is normalized to the reference spectrum ($T = \frac{I_{probe}(\nu)}{I_{ref}(\nu)}$) and measured in the presence and absence of a pump pulse. The normalization to the reference spectrum I_{ref} serves to compensate for fluctuations in the laser spectrum. This normalization results in a significant increase in the signal-to-noise ratio.[67] The pump-induced absorption change is given by:

$$\Delta\alpha(\nu) = -\log_{10}\left(\frac{T_{pump}(\nu)}{T_0(\nu)}\right) = -\log_{10}\left(\frac{I_{probe,pump}(\nu)\cdot I_{ref,0}(\nu)}{I_{probe,0}(\nu)\cdot I_{ref,pump}(\nu)}\right) \tag{3.1}$$

where the subscripts 0 and $pump$ refer to a measurement in the absence or presence of the pump pulse. To measure the dynamic processes inside the sample, e.g. to monitor the vibrational relaxation, the time t_{pp} between the pump and probe pulse is varied. Performing polarization-resolved experiments allows us to disentangle the measured absorption change into an isotropic contribution ($\Delta\alpha_{iso}$) which reflects the decay of the excited state population, and an anisotropic contribution ($R(t)$) which provides information about the orientational motion of the transition dipole moment that is probed (see Section 2.4.4).

3.2.2 SETUP: OPTICS

The description of the pump-probe experiment is presented in three parts: pump, probe and detection path. Figure 3.4 shows an overview of all three parts.

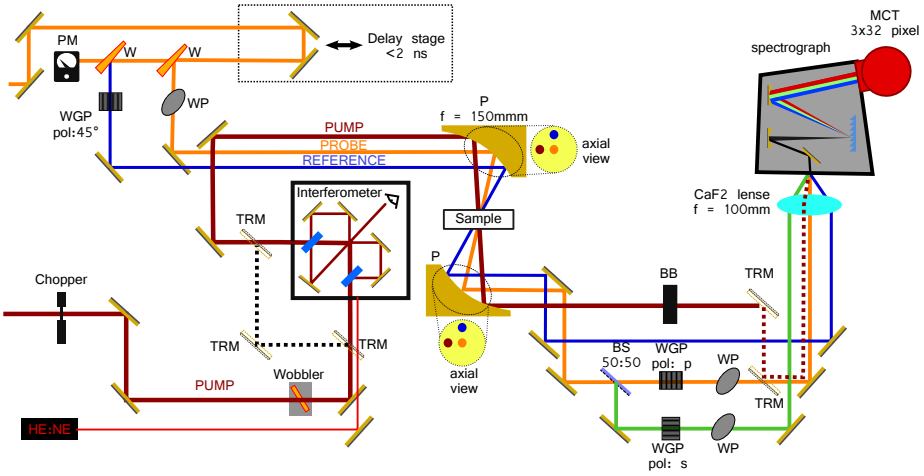

FIGURE 3.4. Pump-probe and 2DIR setup. PM: power meter. WGP: wiregrid polarizer. WP: waveplate. P: parabolic mirrors. BB: beam block. TRM: temporary routing mirror. W: ZnSe wedge. BS: beam splitter.

PUMP PATH

The pump beam first passes through a chopper (Thorlabs, MC2000). The chopper is synchronized to the laser, operates at 500 Hz, and blocks every other shot during a pump-probe experiment. Next, the beam is guided through a wobbling ZnSe-window (wobbler, AMOLF). The wobbler is used to minimize artifacts in the nonlinear signal which originate from pump-light (scattering) reaching the detector (see Section 3.4). For the 2DIR experiments, the beam is coupled into a Mach-Zehnder interferometer which allows for modulation of the pump spectrum (Section 3.3). Conveniently the interferometer can also be used to monitor the pump spectrum. For the pump-probe experiments the interferometer is bypassed by inserting temporary routing mirrors (TRM) into the beam path.

PROBE PATH

The probe beam is first guided over a retroreflector mounted on top of a computer-controlled translation stage (PI, M-414.3pd) with a travel range of 30 cm, which allows a precise control of the time delay between the pump and probe pulse from ∼10 fs up to 2 ns. Next, two ZnSe-wedges (45°, $R \approx 10\%$) are used to split off two reflections from the beam, so that the actual probe (∼200 nJ) and reference (∼200 nJ) are generated. The polarization of the probe beam is set to 45° relative to the pump beam polarization (and the normal of the table), which allows for simultaneous detection of $\Delta\alpha_{\parallel}$ and $\Delta\alpha_{\perp}$ (see below).

DETECTION PATH

Next, all three beams—pump, probe and reference—are focused into the sample using an off-axis gold parabolic mirror (90°, f = 15 cm). Pump and probe overlap spatially while the reference beam is displaced by a small distance. Behind the

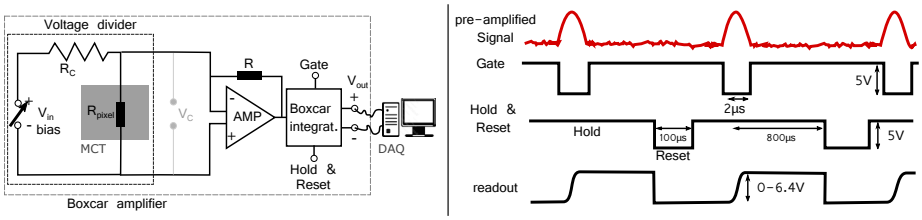

FIGURE 3.5. left: simplified detection circuit. An adjustable input voltage V_{in} is divided over a fix resistor R_c and the photoresistor R_{pixel}. The change in the extracted voltage V_c upon illumination, is amplified by an operation amplifier (AMP) and integrated using a boxcar integrator to yield the output V_{out}. right: Boxcar integration timing. The integration window of the pre-amplified signal is defined by a gate pulse (TTL, 2 µs). The integrated voltage is held for readout until an additional pulse (TTL, 100 µs) resets the integrators ∼ 100 µs before the next pulse arrives.

sample, the three beams are recollimated using an identical parabolic mirror. After the second parabolic mirror, the pump beam is discarded onto a beam block (during the experiments). Alternatively, it can be guided to the detector (for alignment purposes) using a flip mirror along the probe path.
Behind the sample, the probe beam is split into two independent paths, by a nonpolarizing 50:50 beamsplitter. In each path one polarization component is selected, either parallel (p) or perpendicular (s) to the pump polarization, using wire-grid polarizers. Both probe beams and the reference beam are coupled into a spectrograph (Oriel, MS260i). The beams are detected by a liquid-nitrogen-cooled mercury-cadmium-telluride detector (MCT, Infrared associates, 3x32 pixel).

3.2.3 SETUP: ELECTRONICS

INFRARED DETECTION

During the experiment three spectra (reference, probe$_{||}$, probe$_{\perp}$) are recorded simultaneously. In order to read, save and process the infrared signal the intensity of the incident light needs to be converted into a voltage. This is achieved by using three hardware components for each spectrum: one line of the MCT detector (32 pixel), one boxcar integrator (AMOLF), and one data acquisition card (DAQ-card, National Instruments, PXI-6225).
Figure 3.5 shows a schematic representation of the detection circuit. Every MCT pixel is a photoresistor ($R_{MCT} \sim 100\Omega$) which changes its resistance upon illumination ($\Delta R \sim 1/10\Omega$). The resistance change is converted into a voltage change by a voltage-dividing circuit consisting of an adjustable power source (V_{in}, bias), a reference resistor $R_c = 100\Omega$ and the MCT pixel. The voltage change is first amplified by an operational amplifier and then integrated using a gated boxcar integrator. The response of the amplified voltage divider to an infrared pulse has a temporal width of ∼ 1.5 µs. By choosing the integration window slightly broader (2 µs), one can minimize the noise originating from jitter in the laser timing (Figure 3.6a). Lastly, the integrated signal is digitized by the DAQ-cards (16 bits). The

maximum readout voltage of the boxcar integrators is around 6.4 V and it is fixed by the circuit design. Therefore, the dynamic range of the voltage measurement is determined by the resolution of the DAQ-card and the maximum voltage. One can, however, adjust the gain between incident light and generated voltage by choosing the width and timing of the gate pulse, and/or by choosing the bias current. It is advantageous to maximize the dynamic range of the optical measurement[cd] to increase the signal-to-noise ratio (see below) and prevent artifacts originating from the voltage discretization by the DAQ-cards.

Special care must be taken when increasing the bias current since, as a side effect, it can also increase the noise of the detection circuit. Figure 3.6 shows the measured dark noise of the complete detection circuit as a function of the applied bias current. This dark noise σ_{det} is completely random, and therefore it is the ultimate factor that limits the maximally achievable signal-to-noise ratio. Assuming perfect alignment, i.e. the fluctuations of the laser spectrum are completely compensated for by reference normalization, one can propagate the error of the voltage measurement (V_{ref}, V_{probe}) to estimate the relative noise in the transmission measurement $\frac{\sigma_T}{T}$ and in the absorption change $\frac{\sigma_{\Delta\alpha}}{\Delta\alpha}$ to:

$$\frac{\sigma_T}{T} = \sqrt{\left(\frac{\sigma_{det}}{V_{probe}}\right)^2 + \left(\frac{\sigma_{det}}{V_{ref}}\right)^2} \approx \sqrt{2}\frac{\sigma_{det}}{V_{probe}} \approx 0.07\% \tag{3.2}$$

$$\frac{\sigma_{\Delta\alpha}}{\Delta\alpha} \approx 2\frac{\sigma_{det}}{V_{probe}} \approx 0.1\% \tag{3.3}$$

where 1.5 mV and 3 V was used for σ_{det} and V_{probe} respectively. The difference of $\sqrt{2}$ between the two equations originates form the fact that $\Delta\alpha$ is computed as the ratio of two transmission measurements.

In summary, one should aim at having the highest possible readout voltage while simultaneously keeping the bias current as low as possible.

DETECTOR CALIBRATION

Figure 3.6d shows that the detected voltage does not scale perfectly linearly with the light intensity. This nonlinearity can have a severe impact on the measured transient spectrum, especially for samples for which absorption varies strongly over the spectrum. Therefore, it is necessary to first linearize the detector signal before using it to compute the transient spectrum. To this end, we use a calibration function $C(V, pix)$ to convert the measured voltage V into a quantity which depends linearly on the light intensity. In order to construct the calibration function, we first record the response of every pixel as a function of the light intensity $V(I, pix)$. This is achieved with the help of two polarizers in the probe path which act as a variable attenuator for the three detected beams. The relative light intensity I is determined (up to an arbitrary scaling factor) with the help of a calibrated pyroelectric detector

[c] largest intensity difference/ smallest intensity difference

[d] In a typical pump-probe measurement the absorption of the band of interest is adjusted to $\alpha \approx 1$ OD and the absorption change is detected to better than $\Delta\alpha \approx 0.5$ mOD

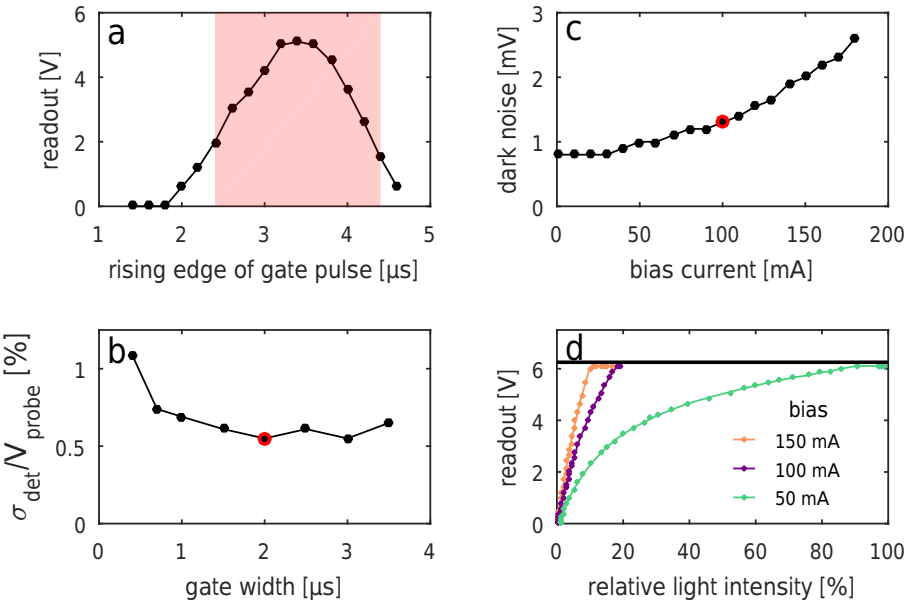

FIGURE 3.6. a: Pre-amplified voltage obtained by scanning the gate pulse (bias 100 mA per 16 pixel). Red shaded area indicates the gate pulse. b: Relative noise for a given readout Voltage (3 V) and bias current (100 mA per 16 pixel) as a function of gate width. c: Dark noise for one pixel (100 mA per 16 pixel, gate 2 µs). d: Voltage as a function of illumination for different bias currents (gate 2 µs). Red marks indicate the values used for the experiments in this thesis.

placed behind one of the ZnSe wedges in the setup (Figure 3.4). Typically, the voltage of a pixel $V(I, pix)$ saturates asymptotically as a function of the light intensity (see Figure 3.6d), and this functional dependence was found to be very well described by:

$$V(I, pix) = \frac{a_2 I}{a_1 + I}. \tag{3.4}$$

By inverting $V(I, pix)$, we find the correction function $C(V, pix)$ to be given by:

$$C(V, pix) = \frac{V a_1(pix)}{a_2(pix) - V} \tag{3.5}$$

where $a_2(pix)$ is the saturation voltage (at $I = \infty$) and $a_1(pix)$ is an arbitrary scaling factor which reflects the sensitivity of the pixel. By fitting V as a function of I we find $a_1(pix)$ and $a_2(pix)$ and hence the correction function $C(V, pix)$. This allows us to convert the recorded voltage of every pixel into a signal that is proportional to the incident light intensity.

At this point, the detector is calibrated, so that it is possible to correctly measure pump-probe and 2DIR signals. A final issue that needs to be addressed is the fact that the sensitivities of the individual pixels vary greatly (i.e. a_2/a_1 is different for

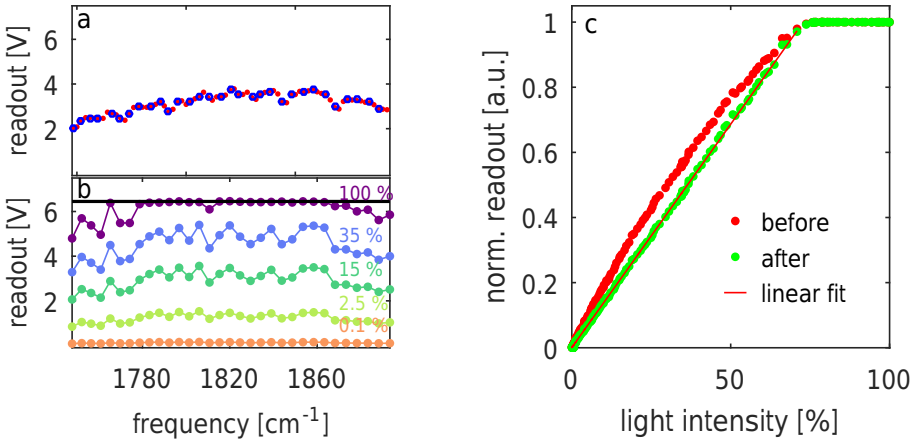

FIGURE 3.7. a: Spectrum obtained by scanning the spectrometer grating and recording the voltage for one pixel. Blue circles indicate values which were selected to match the pixels in the intensity series. b: Light intensity series. Shown is the voltage spectrum at a given relative illumination for the 32 pixels of the probe array. c: Normalized voltage as a function of light intensity for one pixel of the probe array before and after calibration. The plateau at a relative light intensity above 80 % originates from (electronic) saturation of the detector.

every pixel). Fortunately, this problem can be solved straightforwardly by scaling the parameters $a_1(pix)$ with respect to each other. The scaling factors are found by using the array detector to measure the spectrum of a light pulse and comparing this to a measurement in which a single pixel is used while the grating is scanned. While this variation does not affect the transient signal (which is independent of the absolute pixel sensitivity), it poses problems when the array is used to measure the intensity spectrum of a light pulse. Figure 3.7 shows the response for one pixel before and after calibration.

3.3 2DIR EXPERIMENT

The first 2DIR measurements were performed in the pump-probe geometry with an etalon (Fabry-Perot) placed in the pump beam to produce a narrow-band pump pulse ($\sim$15 cm^{-1}).[77] The two dimensional spectrum was generated by scanning the center frequency of the pump pulse and recording a transient spectrum for a range of pump frequencies. Although this frequency-domain approach is straightforward in its implementation and still widely used today, it comes at the cost of limited time resolution since it generates pump pulses with a duration of 0.5 — 1.0 ps.
All 2DIR spectra in this thesis are measured in the time-domain by employing a Mach-Zehnder (MZ) interferometer (Figure 3.13). As in the Fabry-Perot approach, the experiment is performed in the pump-probe geometry, but now the etalon is replaced by an MZ interferometer (see Figure 3.4). The advantages of the Mach-Zehnder method are that ultrashort pulses (<0.5 ps) can be used to obtain a high frequency resolution, and that the absorption change is measured simultaneously at all pump frequencies. In addition, one has the possibility to perform experiments where the two pump pulses have different polarizations. This offers certain advantages by providing additional experimental freedom and is obviously not possible with the Fabry-Perot approach.[78]
In the following section we will first discuss some general principles common to all Fourier transform spectroscopic techniques, such as the influence of the window function and the accessible resolution. In the second part we will describe the acquisition and processing of time-domain 2DIR spectra.

3.3.1 GENERAL PRINCIPLES OF FOURIER TRANSFORM SPECTROSCOPY

There are three main advantages of Fourier transform spectrometers (FTS) compared to dispersive spectrometers:[79]

- **Fellgett advantage** (multiplexing): In a dispersive spectrometer all wavelengths are collected consecutively, whereas in an FTS all wavelengths are collected simultaneously, resulting in a faster acquisition of the complete spectrum.

- **Jacquinot advantage** (throughput): The power throughput of a dispersive spectrometer is lower compared to the FTS due to the need of entrance and exit slits. This results in higher signal-to-noise when measuring with an FTS with the same experimental parameters (such as acquisition time, spectral range, resolution).

- **Connes advantage** (frequency calibration): The frequency axis of a dispersive spectrometer is defined by calibration (e.g with samples with well known absorption lines). In a FTS the frequency axis is derived from a (very well known) reference laser (mostly HeNe), resulting in much better long-term stability.

INTERFEROMETRY

Figure 3.8 shows a Michelson interferometer, where the light propagates from the

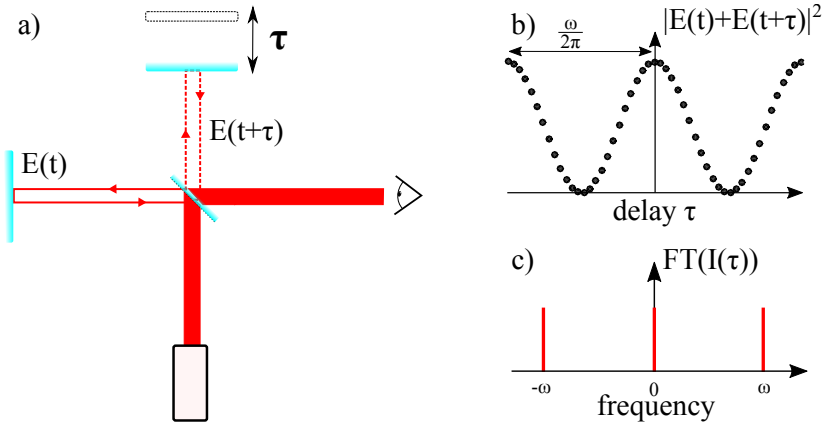

FIGURE 3.8. a) Michelson Interferometer: Light is split and recombined using a beamsplitter and measured by a slow photodetector. The end mirror of one arm can be moved to introduce a time delay τ. b) Measured intensity signal $I(\tau)$ as a function of displacement τ of a monochromatic light source. c) Fourier transform of $I(\tau)$

source to a 50:50 beamsplitter, is split up into two arms, reflected by end-mirrors in each arm, recombined by the same beamsplitter and lastly observed by a detector. One of the end-mirrors can be moved to introduce a path length difference, between the two arms:

$$\Delta x = 0.5\tau c. \tag{3.6}$$

Here τ is the time difference between the two paths and c the speed of light. For now, we assume that the electric field emitted by the light source is a monochromatic plane wave of the form:

$$E(t) = E_0 \exp^{i(k_0 x - \omega_0 t)} + c.c. \tag{3.7}$$

with real amplitude E_0. The total electric field E_{tot} at the position of the detector ($x = 0$) is given by the sum of the fields from the static $E(t)$ and the dynamic arm $E(t+\tau)$:

$$E_{tot}(t,\tau) = E(t) + E(t+\tau) = E(t)\left(1 + e^{-i\omega_0\tau}\right) + c.c. \tag{3.8}$$

Since most detectors (e.g. MCT, eye) are slow relative to the fast oscillating electric field, only the time averaged intensity over a time period T which is much longer than one light cycle can be measured:[80]

$$I(\tau) = 0.5 c\epsilon_0 \left\langle E_{tot}^2 \right\rangle_T = \frac{c\epsilon_0}{2T} \int_{t'}^{t'+T} dt' \, \mathcal{R}e\left(E_{tot}(t',\tau) E(t',\tau)^*_{tot}\right) \tag{3.9}$$

$$= c\epsilon_0 E_0^2 (1 + \cos(\omega_0 \tau)) \tag{3.10}$$

where the asterisk denotes the complex conjugate. Fourier transformation[e] of Equation 3.10 yields:

$$I(\omega) = \mathscr{F}(I(\tau)) \tag{3.11}$$

$$= c\epsilon_0 E_0^2 \left(\int_{-\infty}^{\infty} e^{-i\omega\tau} d\tau + \int_{-\infty}^{\infty} \cos(\omega_0\tau) e^{-i\omega\tau} d\tau \right) \tag{3.12}$$

$$= 0.5 c\epsilon_0 E_0^2 (2\delta(0) + \delta(\omega_0 - \omega) + \delta(\omega_0 + \omega)) \tag{3.13}$$

The first term originates from the constant offset (dc), the second and third term carry the frequency of the modulation.
If the electric field consist of a linear combination of two or more frequencies, then the interferogram $I(\tau)$ is given by a linear combination of frequency dependent cos-terms, since all other cross-terms vanish in Eq. 3.13. Therefore, it is straightforward to extend the discussion above to polychromatic light:

$$E(t) = \int_{-\infty}^{+\infty} E(\omega) e^{-i\omega t} d\omega + c.c. \tag{3.14}$$

$$I(\tau) = c\epsilon_0 \int_{-\infty}^{\infty} E^2(\omega)(1 + \cos(\omega\tau))\, d\omega \tag{3.15}$$

$$I(\omega) = \int_{-\infty}^{\infty} I(\tau) e^{-i\omega\tau} d\tau. \tag{3.16}$$

Here $E(\omega)$ is the spectral distribution. In reality, τ can neither be measured continuously nor varied until infinity. The implications of these limitations will be discussed in the following sections.

RESOLUTION

In any spectroscopic experiment, it is important to be aware of the resolution, i.e. the minimum frequency spacing that two spectral lines need to have in order to be distinguishable as separate lines. To estimate the resolution in FTS, we first recall the *convolution theorem*:[81]

$$\mathscr{F}(f(t) \cdot g(t)) = \mathscr{F}(f(t)) * \mathscr{F}(g(t)) \tag{3.17}$$

which states that the Fourier transform of the product of two functions equals the convolution of their Fourier transforms. It is important to realize that there is at least one product in any interferometric experiment. Even in the simple case of monochromatic light, we are limited by a finite scan length L which can be described as an infinitely long interferogram multiplied by a finite rectangular window (boxcar)

[e] Throughout the text we will use $\mathscr{F}(f(t)) = \int_{-\infty}^{\infty} f(t) e^{-i\omega t}$ for the Fourier transform and $\mathscr{F}(f(\omega)) = \frac{1}{2\pi} \int_{-\infty}^{\infty} f(\omega) e^{i\omega t}$ for the inverse Fourier transform.

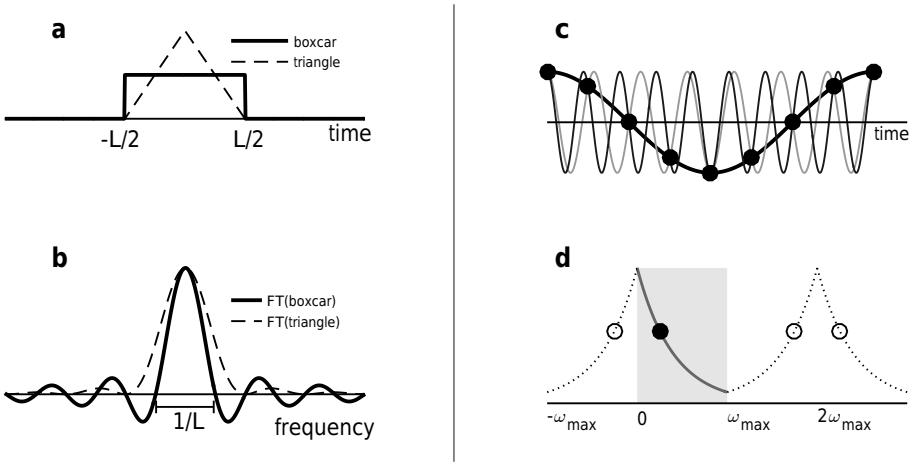

FIGURE 3.9. Apodization and Backfolding a) Two common window functions: boxcar (finite interferogram) and triangular function. b) The respective Fourier transforms: sinc and sinc^2. c) A sampled (dots) sine wave signal S (bold line), and sine waves with higher frequency perfectly matching the same sampling points. d) Unique frequency window (gray) $[0;\omega_{max}]$ for a given sampling rate. Filled circle corresponds to the frequency of the signal S (the bold line in c)) and the empty circles represent sine waves with high frequency matching the same sampling points.

function:

$$D(t) = 1 \quad \text{for} \quad t < |\frac{L}{2}| \tag{3.18}$$

$$= 0 \quad \text{for} \quad t > |\frac{L}{2}| \tag{3.19}$$

with the corresponding Fourier transform:[82]

$$\tilde{D}(\omega) = L\frac{\sin\left(\frac{\omega L}{2}\right)}{\frac{\omega L}{2}} \equiv L\,\mathrm{sinc}\left(\frac{\omega L}{2}\right) \tag{3.20}$$

Due to the convolution, the resulting spectrum will have a finite linewidth in the frequency domain even if we had a perfectly monochromatic source (δ-peaks). From Equation 3.20 one can see that in this case *the width of the spectral line is solely determined by the scanned distance L*.

One common criterion to define resolution is: two peaks are resolved if the two maxima are separated by a dip with an amplitude of 20% of the maximum amplitude. In the case of a square window function and perfectly sharp frequencies (monochromatic), the frequency resolution ω_{res} is given by:[79]

$$\omega_{res} \approx 0.75\frac{4\pi c}{L} \tag{3.21}$$

Of course, in a real experiment we do not measure infinitely sharp spectral lines. Therefore Equation 3.21 provides an upper limit for the best possible resolution at a given scan distance. It is important, however, to realize that the used window function (so far boxcar) influences the observed lineshapes via the convolution theorem (Eqn. 3.17).

In general, one can multiply the time-domain signal with any arbitrary function. This process is called apodization and is essentially equivalent to choosing the lineshape function (LSF) in the frequency domain. Figure 3.9 shows, as an example, the comparison between the square and triangular window function in the time and frequency domain. Ideally we would like to choose an apodization function which is infinitely narrow in the frequency domain, and therefore does not result in line broadening; and which does not have any sidelobes which could potentially be mistaken for real spectral features (peaks)[f]. However, there are certain limitations to the choice. The LSF can be characterized by two parameters: the full width at half maximum (FWHM) and the height of the largest secondary maximum. Norton and Beer found an empirical limit for how small the FWHM can get for a given side lobe magnitude[g].[83] This means, it is up to the experimenter to choose between LSFs which conserve narrow lines, or have low side lobes, or are the ideal compromise of the two for a given experiment.

SAMPLING

In the previous section it was shown that the choice of the scan length and window function have a severe impact on the observed spectral lineshapes. However, it is not yet clear how finely the time-domain data need to be sampled between the start and end position. Since the application of a Fourier transform implicitly assumes that the given data set is periodic, this question can be reformulated to: how many data points per period are needed to uniquely define a sine wave. Unfortunately, this question cannot be answered without additional information, since for every sampling frequency $1/\Delta\tau$ of a sine wave, there exist an infinite amount of sine waves with higher frequencies which exactly fit the same sampling points (see Figure 3.9c, d).

Hence, we impose that the measured signal is bandwidth-limited, i.e. there exists a maximum frequency component ω_{max} in the signal, and all higher frequency components are zero. The sampling of a continuous time domain signal $f(\tau)$ at every time step $\Delta\tau$ can be described, by the multiplication of $f(\tau)$ with a Dirac-comb

[f] The magnitude of the first minimum of the sinc function is about 22% of the magnitude of its absolute maximum.

[g] The empirical limit determined by Norton and Beer is

$$\log_{10}\frac{h}{h_0} \approx 1.939 - 1.401\left(\frac{W}{W_0}\right) - 0.597\left(\frac{W}{W_0}\right)^2 \tag{3.22}$$

where h/h_0 is the size of the first sidelobe of the apodization function relative to the sinc-function, and (W/W_0) the ratio of the widths.[83]

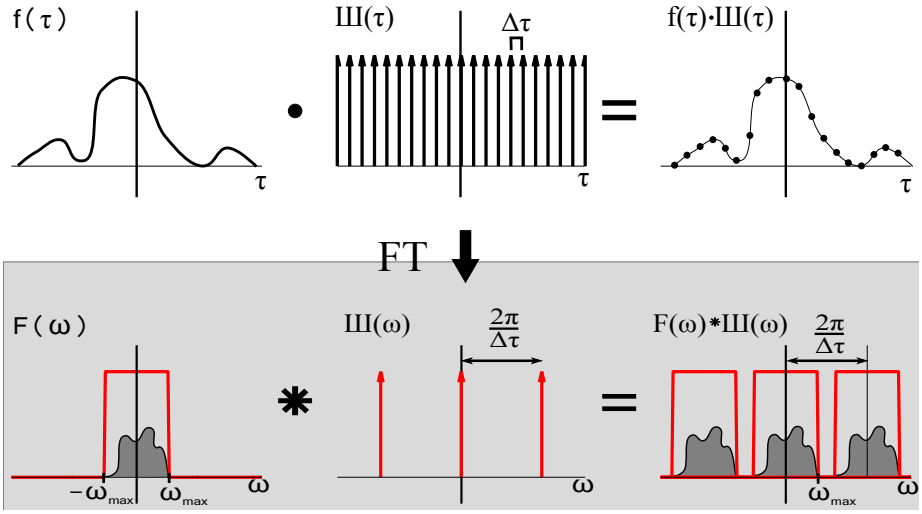

FIGURE 3.10. Fourier transform of a bandwidth limited, sampled, time domain signal. A time-domain signal which is sampled at every $\Delta\tau$ is given by the product of a continuous function $f(\tau)$ (here: sinc-function) and a Dirac-comb $\text{Ш}(\tau)$ (top). The product in time domain results in a convolution in frequency domain, leading to replication of the spectrum at a period of $2\pi\Delta\tau$.

(Fig. 3.10):

$$f^*(\tau) = f(\tau)\text{Ш}_{\Delta\tau}(\tau) \tag{3.23}$$

$$\text{Ш}_{\Delta\tau}(\tau) = \sum_{n=-\infty}^{+\infty} \delta(\tau - n\Delta\tau) \tag{3.24}$$

The Dirac-comb $\text{Ш}_{\Delta\tau}(\tau)$ is defined as the sum of an infinite number of equally spaced Dirac-deltas δ, and its subscript indicates the sampling step. Since the Dirac-comb is a periodic function it can also be written as a Fourier series:

$$\text{Ш}_{\Delta\tau}(\tau) = \frac{1}{\Delta\tau} \sum_{n=-\infty}^{+\infty} e^{in\omega_0\tau} \quad \text{with} \quad \omega_0 = \frac{2\pi}{\Delta\tau} \tag{3.25}$$

This allows us to calculate the Fourier transform of the sampled function $f^*(\tau)$ by invoking the convolution theorem (Eqn. 3.17):

$$F^*(\omega) = \mathscr{F}(f(\tau)\text{Ш}_{\Delta\tau}(\tau)) \tag{3.26}$$

$$= \frac{1}{\Delta\tau}\sum_{n=-\infty}^{\infty} \mathscr{F}(f(\tau)) * \mathscr{F}(e^{in\omega_0\tau}) \tag{3.27}$$

$$= \frac{1}{\Delta\tau}F(\omega) * (\sum_{n=-\infty}^{\infty} \delta(\omega - n\omega_0)) \tag{3.28}$$

$$= \frac{1}{\Delta\tau}F(\omega) * \text{Ш}_{\frac{2\pi}{\Delta\tau}}(\omega) \tag{3.29}$$

$$\tag{3.30}$$

The last equation shows that the Fourier transform of a sampled function $f^*(\tau)$ results in the spectrum of the continuous function $f(\omega)$ convoluted with a Dirac-comb, i.e. the spectrum repeats itself in the frequency domain with the period $\frac{2\pi}{\Delta\tau}$ (Figure 3.10). Therefore, as long as these spectral copies do not overlap, we can uniquely identify every frequency component of the signal. This is exactly the case when the bandwidth of the signal ($2 \times \omega_{max}$[h]) is smaller than the distance between two spectral copies:

$$\Delta\tau < \frac{2\pi}{2\omega_{max}} \tag{3.31}$$

$$\Delta\tau < \frac{1}{2f_{max}} \tag{3.32}$$

The minimum sampling rate $f_{Nyq} = 1/(\Delta\tau)$ at which ω_{max} can uniquely be identified is known as the Nyquist frequency. It is important to note that the above discussion only holds for bandwidth limited signals. Otherwise, there exists a possible overlap between the replica of the spectrum. Therefore, frequencies higher than ω_{max} will be present in the observation window $[0, \omega_{max}]$. This backfolding can only be prevented by limiting the time domain signal to the expected frequency range with the help of optical and/or electronic filters.

A similar line of thought can be invoked to show that the frequency sampling $\Delta\omega$ is given by:

$$\Delta\omega = \frac{\pi}{\tau_{max}} \tag{3.33}$$

Thus, the frequency sampling $\Delta\omega$ (not the resolution) is given by the maximum retardation L. Lastly, representing the frequency in units of wavenumbers ($\nu = \omega/(2\pi c)$ in cm^{-1}), provides a convenient relation between retardation x and

[h] The information content of the spectrum at negative frequencies is identical to the content at positive frequencies. Both halves of the spectrum can be interconverted as long as the time domain signal is known.

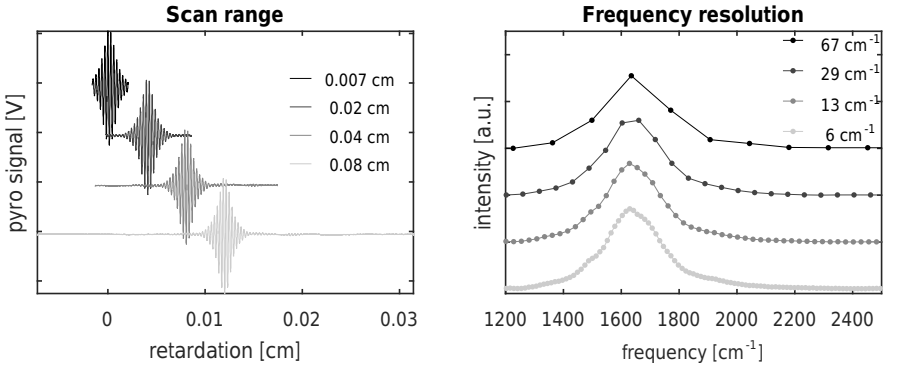

FIGURE 3.11. Interferograms with increasing scan range (left) and the corresponding spectra with increasing frequency resolution (right).

frequency sampling:

$$\Delta\nu[cm^{-1}] = \frac{1}{2x_{max}[cm]} \tag{3.34}$$

$$\nu_{max}[cm^{-1}] = \frac{1}{2\Delta x[cm]} \tag{3.35}$$

Next, we inspect the impact of scan range and sampling rate to provide some examples for the topics discussed in the previous section. Figure 3.11 shows interferograms with increasing scan range and the corresponding interferograms, and it demonstrates the inverse proportionality between maximum retardation and resolution (Eq. 3.33). Figure 3.12a shows the same interferogram sampled with different time steps and Figure 3.12b shows the corresponding spectra. Not only does this figure illustrate the effect of sampling rate on the maximal resolvable frequency, it also shows the effect of backfolding when the spectral features of interest are above the Nyquist frequency.

3.3.2 HARDWARE IMPLEMENTATION: MACH-ZEHNDER INTERFEROMETER

Figure 3.13 shows the design of the Mach-Zehnder interferometer, which was adapted from Ref.[78] The small footprint (15 x 15 cm) of the implementation allows for a flexible placement in the experimental setup. In the interferometer, the input beam is split into two using a 50:50 beamsplitter. The resulting beams are guided over two retroreflectors, after which they are recombined on a second beamsplitter. One of the retroreflectors is static while the other is mounted on a computer-controlled translation stage (PI, M-111.DG). The Mach-Zehnder interferometer provides two accessible output beams[i], with interference patterns that are each others opposites.

[i] in contrast to the Michelson interferometer, where one output beam is colinear with the input.

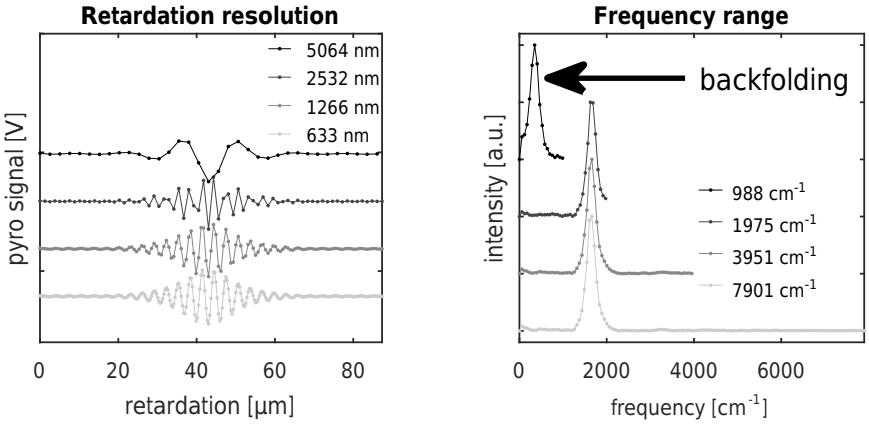

FIGURE 3.12. Interferograms with decreasing sampling step sizes (left) and the corresponding spectra with increasing maximum frequency (right). The black arrow indicates backfolding of the spectrum due to undersampling of the interferogram.

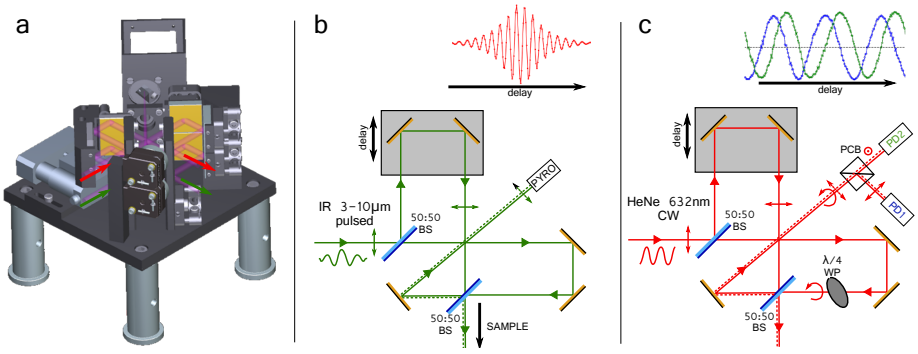

FIGURE 3.13. Mach-Zehnder interferometer geometry. a: Three-dimensional rendering of the bread board design. b: Schematic representation of the infrared beam path and interference pattern measured by the pyroelectric detector (inset, top). c: Schematic representation of the HeNe beam path and interference pattern measured by the photodiods (inset, top). Arrows indicate the polarization and the propagation direction. PD: photodiode. PCB: polarizing cube beamsplitter. WP: waveplate. BS: beam splitter.

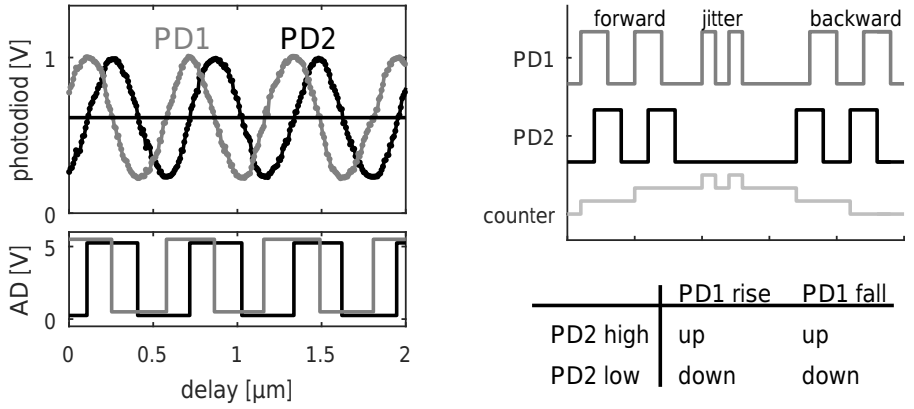

FIGURE 3.14. Delay distance sampling via counting interference fringes. Left: Raw photodiode signal (top) and corresponding digital TTL signal (bottom, offset for clarity). Right: Counting logic (bottom) and example signals for both photodiods and the corresponding counter values.

Our interferometer is, in fact, a double interferometer with two almost identical beam paths (an infrared beam path and a visible HeNe beam path) stacked on top of each other. The infrared beam path (Fig. 3.13b) serves to generate a pair of pump pulses while the HeNe beam path (Fig. 3.13b) is used to precisely determine the delay between the two infrared pulses by counting the HeNe interference fringes.

The counting of the HeNe fringes is implemented using a so-called quadrature counting scheme, as is explained in Figure 3.14. In this scheme two HeNe interferograms with a phase difference of 90° are generated (Figure 3.13). This makes it possible to distinguish between movements of the dynamic arm in the forward and backward direction. In order to create two out-of-phase HeNe interferograms a $\lambda/4$ plate is placed in one of the interferometer arms, thereby converting the linear polarization of the light to circular. The circularly polarized light from the first arm is recombined with the linearly polarized light from the second arm, after which the recombined beam is again split into two beams with the help of a polarizing cube beam splitter (oriented at 45° with respect to the linearly polarized input beam). The interference fringes in these two output beams are exactly 90° out-of-phase with respect to each other, and they are recorded using two photodiodes. The photodiode outputs are converted to binary signals using analog-to-digital converters (AMOLF) and fed into the quadrature counter integrated in the DAQ-cards. Figure 3.14 summarizes the counting procedure.
The quadrature counter method provides several advantages:

- The scanned delay is intrinsically measured on an equidistant grid (defined by the HeNe wavelength) which is necessary for the Fourier transformation of the interferogram.
- The displacement of the dynamic arm can be determined very accurately ($< \lambda_{HeNe}/2$) because the measurement is not affected by the limitations of the

translation stage, such as backlash ($\sim$2 μm) and unidirectional repeatability (0.1 μm).

- Using the quadrature-counting scheme the direction of the movement can be determined, which is not possible with a single-photodiode fringe counting.
- The combination of the above points allows for measurements with very fast scan rates ($>$0.3 mm/s).

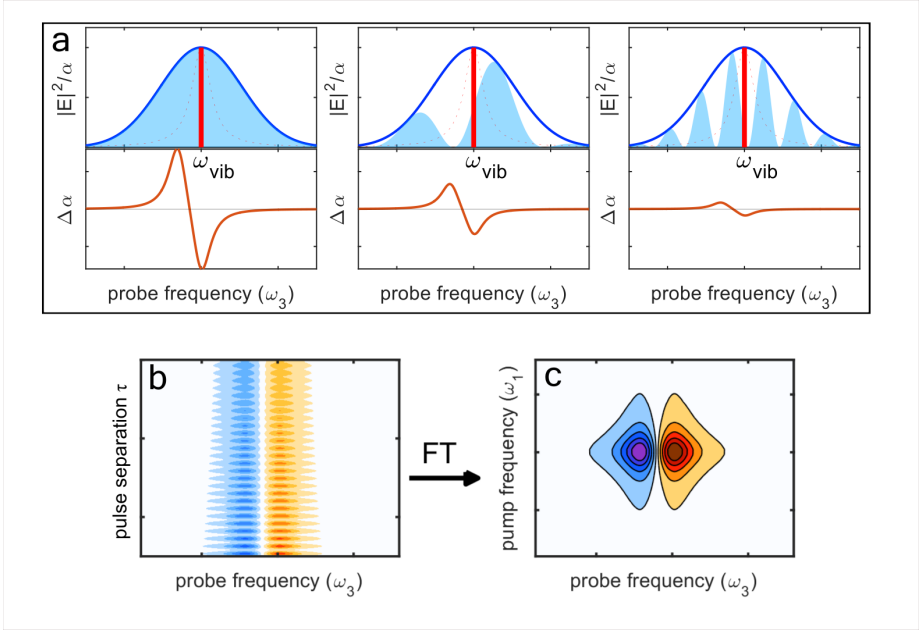

FIGURE 3.15. Generating a 2DIR spectrum.
a) Pump-probe spectra at different retardation times τ. The excitation efficiency of a vibration at ω_{vib} (top, red line) and therefore the amplitude of the generated pump-probe signal (bottom) depends on the overlap of the spectral density of the pump spectrum (top, blue area) and the spectrum of the vibration. The blue line (top) shows the envelope of the pump spectrum. b) 2DIR signal as a function of pump pulse separation τ and c) as a function of pump frequency ω_1.

3.3.3 PRINCIPLES OF FOURIER TRANSFORM 2DIR SPECTROSCOPY

To understand how a 2DIR spectrum is measured in the time-domain, we first need to understand how the Mach-Zehnder interferometer modifies the pump spectrum and, second, what influence this modified pump spectrum has on the resulting nonlinear signal.
The MZ interferometer converts the pump pulse into a pulse-pair with an adjustable time separation τ. The electric field of the pump at the sample position is given by:

$$E(t,\tau)_{pump} = E_{stat}(t) + E_{dyn}(t) = E_{stat}(t) + E_{stat}(t+\tau) \tag{3.36}$$

where E_{stat} and E_{dyn} refer to the electric field from the dynamic ($E(t+\tau)$) and the static arm ($E(t)$) of the interferometer, respectively. The corresponding pump spectrum after the interferometer is given by:

$$I(\omega,\tau) = 2|E_{stat}(\omega)|^2(1+\cos(\omega\tau)) \tag{3.37}$$

This equation shows that the effect of the MZ interferometer is to modulate the spectrum of the original pump pulse by interference fringes. These intensity

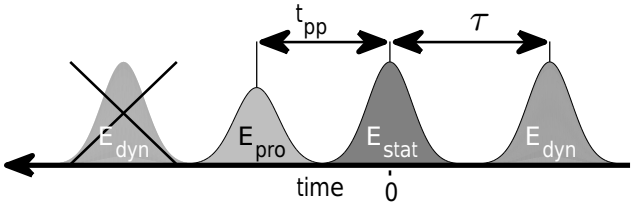

FIGURE 3.16. Pulse sequence in a 2DIR experiment.

oscillations originate from the cosine-term, and the frequency spacing between two fringes is determined by the time delay τ.
In the following, we take a phenomenological approach and examine the absorption change generated by the interaction of the pump pulse pair with a molecular vibration (characterized by a resonance frequency ω_{vib}) at a fixed pump-probe delay t_{pp} (Fig. 3.15). The excitation efficiency of the molecular vibration, and hence the amplitude of the pump-probe signal, is given by the spectral density of the pump pulse pair at the fundamental frequency ω_{vib}. This means that, if the retardation τ is scanned, the amplitude of the pump-probe signal will oscillate with a frequency ω_{vib}. Recording the absorption change as a function of τ (Fig. 3.15a) results in a two-dimensional time-frequency map $\Delta\alpha(\tau, t_{pp}, \omega_3)$ (Fig. 3.15b). Fourier transformation of $\Delta\alpha(\tau, t_{pp}, \omega_3)$ along τ yields a frequency-frequency correlation plot $\Delta\alpha(\omega_1, t_{pp}, \omega_3)$, or in other words the 2DIR spectrum (Fig. 3.15c).

3.3.4 DATA TREATMENT

This section discusses some additional steps that need to be taken after acquiring the time-domain signal to prevent introducing artifacts and to achieve 2DIR spectra with the highest possible resolution. In a FTIR measurement one usually records a symmetric double-sided interferogram by scanning the retardation τ from $-\tau_{max}$ to $+\tau_{max}$. In 2DIR spectroscopy this approach does not work because the signal is not symmetric around $\tau = 0$ (due to the presence of the probe pulse). We solve this issue by scanning the pulse from the dynamic arm of the interferometer E_{dyn} only in one direction, which is away from the probe pulse (see Figure 3.16). Hence, the time-domain signal in FT-2DIR is defined on the domain $\tau \in [0, \infty)$. Practically, a slightly larger τ-range is measured during the experiment, and the data set is truncated afterwards to only contain points where $\tau \geq 0$. Unfortunately, one cannot easily find the point where $\tau = 0$ by simply inspecting the nonlinear signal. That is because there is also a nonlinear signal at negative values of τ (which can be seen as artifact in the current context). The problem is that missing the point $\tau = 0$, by even as little as one sampling point, leads to lineshape distortions in the frequency domain as is illustrated in Figure 3.17. Since the time-domain 2DIR signal represents a single-sided interferogram (i.e. $\tau \geq 0$), its Fourier transform yields complex valued lineshapes. The highest possible spectral resolution is achieved by selecting the real part of the frequency-domain signal since it provides absorptive lineshapes, which have the

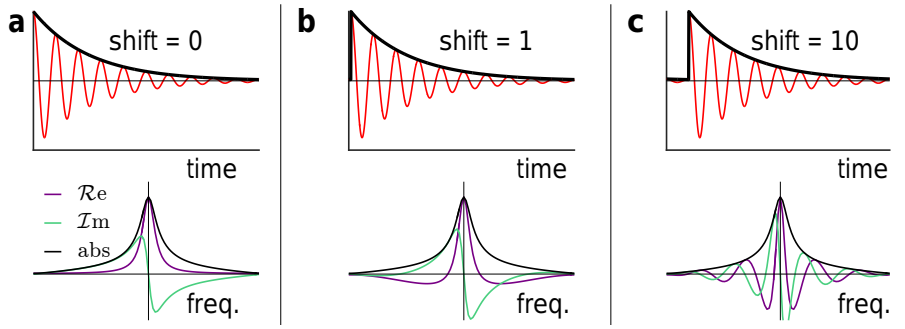

FIGURE 3.17. Single-sided exponential and its Fourier transform at a circular permutation (shift) of 0 (a), 1 (b), 10 (c) data points.

narrowest possible linewidth. Misjudging (shifting) the origin of the retardation axes by δ in the time-domain signal $A(\tau)$ introduces a linear phase ϕ_δ:

$$\mathcal{F}\{A(\tau+\delta)\} = \mathcal{F}\{A(\tau)\} \cdot e^{-i2\pi\delta\omega} \tag{3.38}$$

$$= A(\omega) \cdot e^{-i\phi_\delta(\omega)} \tag{3.39}$$

that mixes the real and imaginary part of the spectrum resulting in the aforementioned lineshape distortions.

The solution for this phasing problem is built into the Mach-Zehnder interferometer. One of its output beams is used to excite the sample, and the other to simultaneously record an interferogram of the pump pulse (Fig. 3.18a,b) which is totally symmetric around the point $\tau = 0$. In principle, we could find the sampling point closest to $\tau = 0$ by taking the minimum of the pump interferogram. However, it turns out that we need to determine $\tau = 0$ more precisely than one sampling point. This is achieved by the following approach. As follows from Eq. 3.39, the 2DIR signal can be completely compensated for the shift of the origin by multiplying the frequency domain signal with the correct phase function before taking the real part. The correct phase function is the function that minimizes the imaginary part of the pump spectrum. This follows from the fact that, contrary to the 2DIR response, the pump interferogram is a symmetric function of τ. Figure 3.19 shows a 2DIR spectrum with and without applying the phase correction.

ZERO PADDING

In Fourier transform spectroscopy, zero padding refers to the refinement of the frequency grid, by appending zeros to the time-domain data. In general, if the signal $I(\tau)$ has decayed completely at its last sampling point $N-1$, appending zeros does not change the informational content, but effectively increases the length of the data set. Since the frequency spacing $\Delta\omega$ after Fourier transformation is inversely proportional to the acquisition length τ_{max}:

$$\Delta\omega \propto \frac{1}{\tau_{max}} \tag{3.40}$$

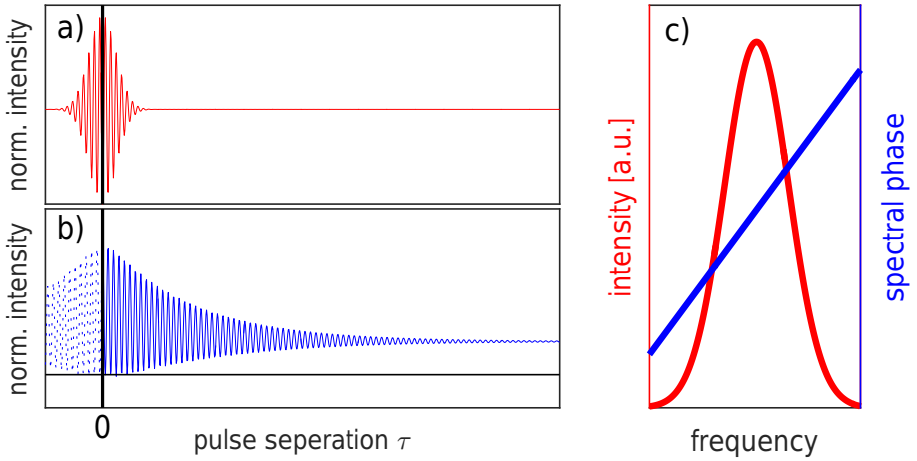

FIGURE 3.18. Phase correction of the 2DIR spectrum. Panel a) shows the interferogram of the pump acquired with the pyroelectric detector inside the Mach-Zehnder interferometer, and panel b) shows the simultaneously acquired time-domain 2DIR signal (for one frequency). Fourier transformation of the pyro signal (panel c) allows to extract the spectral phase which in turn can be used to both, remove data points in the 2DIR spectrum acquired for negative time delays ($\tau < 0$, dotted line in panel b), and to compensate for the spectral phase of the Fourier transform 2DIR time-domain data.

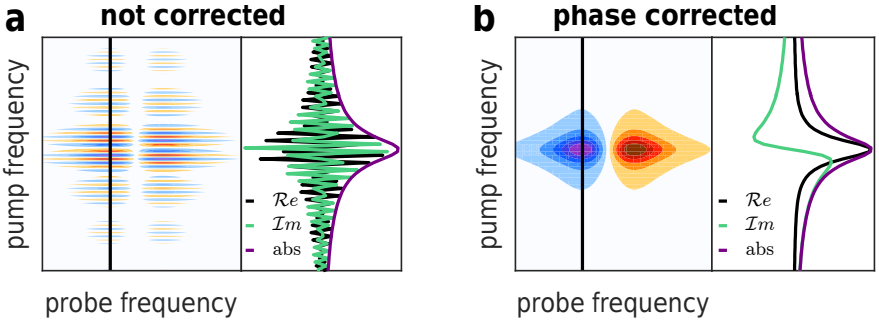

FIGURE 3.19. Effect of phase correction on the 2DIR spectrum. Panel a) shows the real part of $\Delta\alpha_{2D}(\omega_1, t_{pp}, \omega_3)$ without phase correction, and panel b) the phase corrected 2DIR spectrum. The right side of each panel shows the real and imaginary part and the absolute value for one probe frequency (black line) of the 2DIR spectrum.

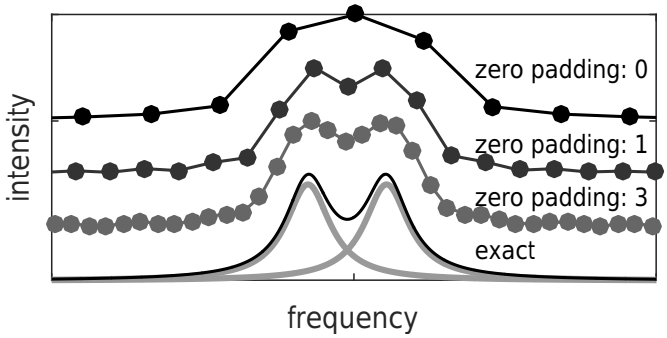

FIGURE 3.20. Zero-padding the Fourier transform of a single-sided function. A function consisting of two single-sided oscillating terms, which are close in frequency, was Fourier transformed with no zeros padded; the same amount of zeros added as used data points; and three times the amount of data points. The exact Fourier transform is shown as a comparison.

the addition of zeros at the end of the data set leads to an increase of the frequency sampling rate. This procedure, does not increase the resolution, instead it results in a trigonometric interpolation of the frequency domain data.[81]
In contrast, as is well known in NMR spectroscopy, the situation is different for a single-sided time-domain function. In this case one can actually achieve a resolution enhancement of at most a factor of two in the spectrum by zero padding the time-domain data. As was shown in ref.[84] this can intuitively be understood by the fact that zero padding (by a factor of two) effectively adds the information content of the imaginary part of the spectrum to the real part of the spectrum (which is the part we usually inspect). Further zero padding only results in an additional interpolation of the spectrum. Figure 3.20 demonstrates that zero padding a single-sided function which contains two oscillating terms which are close in period can can result in a distinction of the two peaks in the frequency domain.

3.3.5 CHOPPER STATE AND INTERFEROMETER SPEED

In the previous sections, the measurement of a 2DIR time-frequency map $\Delta\alpha(\tau, t_{pp}, \omega_3)$ was described as an acquisition of a pump-probe spectrum for every pump pulse separation τ. To this end, one needs to perform a transmission measurement for at least two laser shots per retardation step: one in the presence (T) and one in the absence (T_0) of the pump pulse. Although this is a valid approach, it is not strictly necessary in time-domain 2DIR because the modulation as a function of τ allows us to extract $\Delta\alpha_{2D}$ via the Fourier transform. Therefore, it is possible to skip the measurement of T_0 (the not-pumped spectrum) which results in a reduction in measurement time of a factor of 2 for the same signal-to-noise ratio. Figure 3.21 demonstrates this by comparing two 2DIR measurements, performed under the same conditions, with and without the usage of a chopper. The figure also shows that the noise in the measurements without chopper is almost independent of the speed of

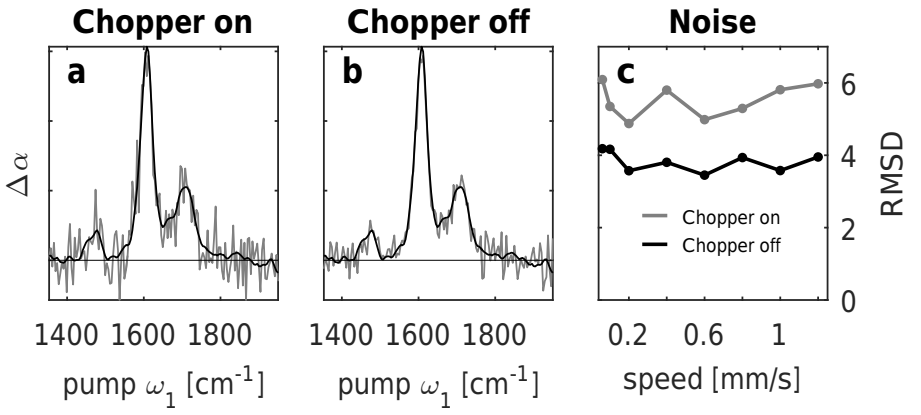

FIGURE 3.21. 2DIR acquisition with and without Chopper. Panel a) and b) show 2DIR measurements for one probe frequency which were performed under the same conditions (stage speed: 0.6 mm/s) except for the state of the chopper. To estimate the relative noise, the root mean square deviation to a high signal-to-noise measurement (black) was calculated. c) compares these values for different speeds of the interferometer translation stage.

the translation stage, and $\sim\sqrt{2}$ lower when compared to measurements with chopper. The most straightforward way to acquire the full time-domain spectrum $\Delta\alpha(\tau, t_{pp}, \omega_3)$ is to move the translation stage one time step $\Delta\tau$ at a time. But, in reality, the control mechanics of the stage make this option undesirable, since every movement to a specific target position is accompanied by considerable overhead time (∼0.1–0.5 s) and inaccuracy. We circumvent both problems, by continuously moving the stage between the two end points which define the intended range; and by reading out the counter given by the HeNe interference fringes (instead of reading the position from the stage controller).

It turns out that the speed of the translation stage has a noticeable effect on the spectrum of the noise. Figure 3.22 compares two measurements under the same conditions but at different speeds of the interferometer translation stage. Pronounced fluctuations of the signal are present in the measurement at slow speeds (0.06 mm/s) but are lacking at fast speeds (0.6 mm/s). Since at a speed of 0.6 mm/s only every 2nd to 3rd time point is sampled in one pass, multiple scans of the same range are needed to fill every grid point. This effectively scrambles the noise correlations (low frequency) between different time points and redistributes the spectral density of the noise more equally throughout the spectrum, reducing spectral features which might be interpreted as real nonlinear signals.

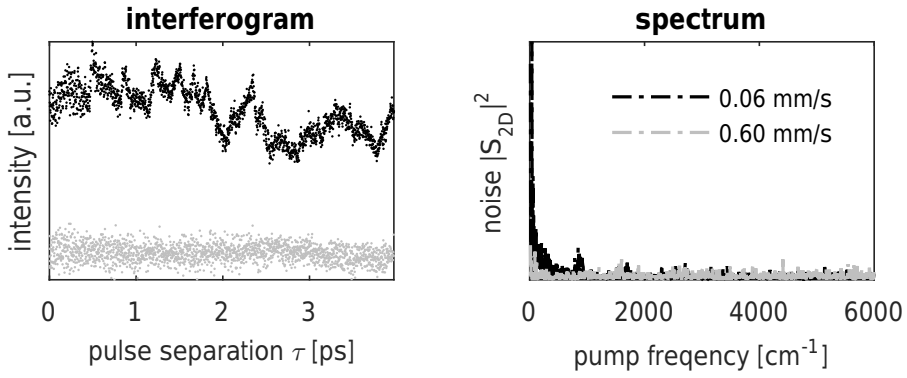

FIGURE 3.22. Dependence of the noise in 2DIR on the speed of the interferometer translation stage a) 2DIR interferogram for one probe frequency at two different interferometer scanning speeds and b) corresponding energy spectral density.

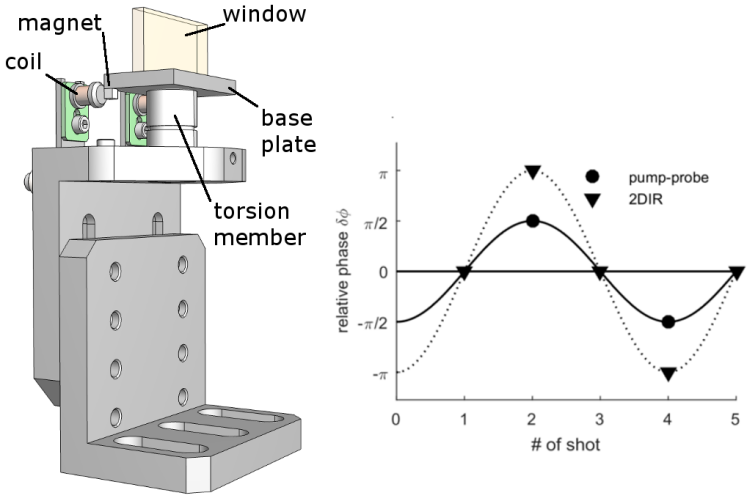

FIGURE 3.23. left: CAD model of the wobbler. right: Possible schemes for scattering suppression in pump-probe and 2DIR experiments.

3.4 SCATTERING SUPPRESSION

3.4.1 PRINCIPLE

Scattering poses a severe problem, both in pump-probe and 2DIR spectroscopy, since it can lead to strong artifacts which obscure the transient signal. It occurs when a small fraction of the pump light reaches the detector where it interferes with the probe light. There exist many possible sources for stray light, like scratches or contamination (dust, fingerprints) on the optics used, and most crucially the sample windows. Sometimes the sample itself can lead to strong stray light, examples encountered in this thesis are protein aggregates (Chapter 4) and metallic nanostructures (Chapter 5). If we assume that only a small fraction $\alpha \ll 1$ (e.g. 0.001) of a strong pump pulse $E_{pump} \approx 100 \times E_{probe}$ reaches the detector, then the measured total intensity is given by:

$$|E_{probe} + \alpha E_{pump}|^2 \tag{3.41}$$

$$= |E_{probe}|^2 + \alpha^2 |E_{pump}|^2 + 2\alpha \mathcal{R}e(E_{probe} E^*_{pump}). \tag{3.42}$$

The last term in Eq. (3.42) introduces an interference term between the pump and probe field. This interference term can have a similar or even greater amplitude than the absorption change originating from molecular vibrations, and, for convenience, we will refer to it as scattering for the rest of the chapter.
For simplicity, we are going to assume that the electric fields in the frequency domain are bandwidth limited and can be described by:

$$E(\omega) = A(\omega) e^{-i(\omega t + \phi)} \tag{3.43}$$

with the real-valued envelope $A(\omega)$, and the phase factor ϕ. Since the scattering signal is an interference between the pump and the probe field its spectral shape strongly depends on the time separation $\Delta t = t_{pp}$ between the two fields:

$$\mathcal{R}e(E_{probe} E^*_{pump}) = |A(\omega)_{pump}||A(\omega)_{probe}| \underbrace{|\cos(\omega \Delta t + \delta\phi)}_{S(\delta\phi)} \tag{3.44}$$

where $\delta\phi$ is the relative phase between pump and probe. From Eq. (3.44) we see that with increasing delay Δt the separation between adjacent interference fringes becomes smaller, but the amplitude of S does not change. Thus, the scattering signal becomes increasingly larger, compared to the pump-probe signal which decays with the vibrational lifetime. The phase term $\delta\phi$ has no influence on the periodicity or the amplitude of S, but leads to a shift along the frequency axes.
In most experiments, we perform multiple measurements for every time delay $\Delta t = t_{pp}$, e.g. in pump-probe experiments one usually acquires 1000 shots per delay. Hence, if we find a way to modify the relative phase, therefore shift the scattering along the frequency axes, on a shot-to-shot basis, it is possible to find conditions where the average scattering signal cancels out. To give one example, the average

scattering signal vanishes if two consecutive measurement have a relative phase of π:

$$\frac{1}{2}\left(S(-\frac{\pi}{2})+S(\frac{\pi}{2})\right)=\frac{1}{2}\left(\cos\left(\omega\Delta t-\frac{\pi}{2}\right)+\cos\left(\omega\Delta t+\frac{\pi}{2}\right)\right) \tag{3.45}$$

$$=\frac{1}{2}\left(\cos(\omega\Delta t)\cos\left(\frac{\pi}{2}\right)\right)=0 \tag{3.46}$$

This can be generalized for any integer valued subdivision n of one period (2π) of the phase:

$$\sum_{k=1}^{n}S(\frac{2\pi}{n}k+c)=\sum_{k=1}^{n}\cos\left(\omega\Delta t+\frac{2\pi}{n}\cdot k+c\right)=0 \quad n=2,3,4,... \quad c\in\mathbb{R} \tag{3.47}$$

Thus, there are infinitely many possibilities to adjust the phase between consecutive measurements for which the scattering signal vanishes in the average.
In practice there are two common approaches to modulate the relative phase between the pump and probe pulse: one can either directly modify the phase of either pump or probe by employing a pulse shaper, or one can introduce a small additional delay $\Delta t+\frac{\delta\phi}{\omega_0}$ which results in quasi-phase shift. We will focus on the second approach.
Although significantly simpler than the pulse shaper approach, the introduction of some additional path length has the downside of only yielding the desired phase $\delta\phi$ for one specific frequency ω_0. We can consider the implications by modifying Eq. (3.46):

$$\cos(\omega\Delta t)\cos\left(\frac{\pi}{2}\frac{\omega}{\omega_0}\right)=0 \tag{3.48}$$

The $\cos\left(\frac{\pi}{2}\frac{\omega}{\omega_0}\right)$-term shows that perfect scattering suppression can only be achieved at the frequency ω_0, and that the cancellation becomes less effective for increasing frequency deviation from ω_0.

3.4.2 HARDWARE IMPLEMENTATION: WOBBLER

During all experiments in this thesis the relative phase was adjusted with the help of a ZnSe-window which was inserted into the pump beam path. The length of the optical path was then modulated by changing the angle of incidence. The window is mounted on top of a torsion oscillator, where a flexure bearing is used as a spring, and displacement is achieved by modulating the voltage through a coil (electromagnet) which interacts with a magnet attached to the base plate. The oscillating voltage is synchronized to the laser trigger, and the relative phase can be adjusted by changing the amplitude of the voltage and by introducing a delay to the laser trigger. Figure 3.23 shows the design of the so-called wobbler.
Next, let us consider a possible implementation for pump-probe spectroscopy. Since the laser system used in our experiments operates at 1 kHz, the fastest possible modulation with two alternating relative phase values ($\delta\phi=\pi$) is 250 Hz, since every other shot is chopped and does not contribute to the scattering suppression. Figure

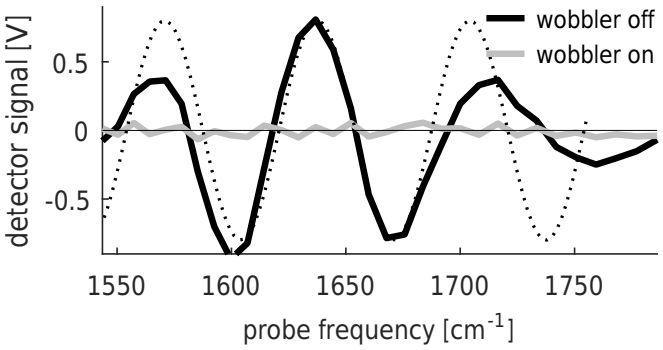

FIGURE 3.24. Example of scattering suppression with the wobbler using the pump-probe scheme. Shown are the background (probe on, pump off) subtracted probe signals at a center frequency of 1660 cm^{-1} and a pump-probe delay $\Delta t = 0.5$ ps. The black dotted line indicates the expected scattering signal according to Eq. (3.44).

3.23 shows one possible modulation scheme where consecutive shots (including not pumped ones) have the relative phase: 0, $\pi/2$, 0, $-\pi/2$. Figure 3.24 shows a pump-probe measurement in a highly scattering sample with and without employing the wobbler.

During 2DIR experiments the chopper is not used (see Sec. 3.3.5), rendering the previously introduced modulation scheme less efficient because the average scattering signal does not fully vanish. Since the frequency of the wobbler is fixed to 250 Hz, it would be convenient to have an alternative modulation scheme for 2DIR spectroscopy which still operates at the same driving frequency. Figure 3.23 shows how this can be achieved using relative phases of 0, π, 0, $-\pi$ for 4 consecutive measurements[j].

The choice of the window material will impact by how far one has to tilt the window to achieve a certain relative phase. To introduce a change in phase of $\delta\phi$, the optical beam path has to be extended by:

$$\delta\phi(\Delta l) = \frac{\Delta l\, \omega n(\omega)}{c} \tag{3.49}$$

where c is the speed of light and $n(\omega)$ the refractive index of the medium. Figure 3.25 depicts a schematic representation of the light path through the wobbler window of thickness d and refractive index n. Increasing the angle of incidence (tilting the window) from α to $\alpha + \Delta\alpha$, extends the optical path length by:

$$\Delta l(\alpha, \Delta\alpha) = \Delta s + \Delta t - \Delta u \tag{3.50}$$

where Δs is the change in optical path length inside the window, Δu the reduction of the path length after the window and Δt the additional path due to the displacement

[j] Using the two introduced schemes has the additional advantage that when switching from pump-probe to 2DIR experiments one just has to double the amplitude of the used voltage.

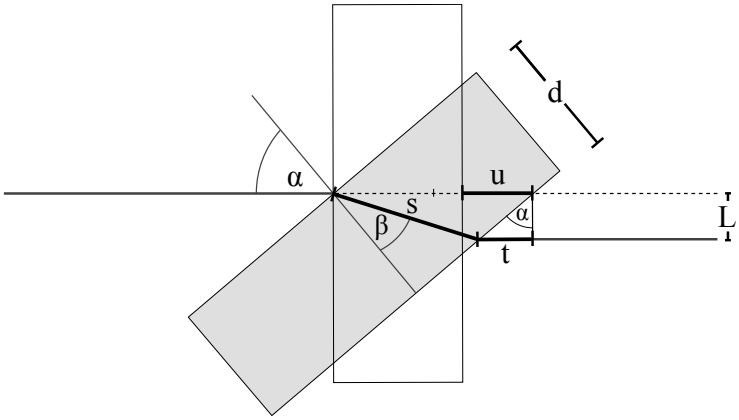

FIGURE 3.25. Schematic representation of light path through the wobbler window (top view)

of the beam after the window[k]. Employing Snell's law[l], it is straightforward to find an expression for the path lengths s, t and u:

$$s = \frac{d}{\cos(\beta(\alpha))} \tag{3.51}$$

$$u = d\left(1 - \frac{1}{\cos(\alpha)}\right) \tag{3.52}$$

$$\begin{aligned} t &= L\tan(\alpha) \\ &= d\frac{\sin^2(\alpha)}{\cos(\alpha)}\left(1 - \frac{1}{n}\frac{\cos(\alpha)}{\cos(\beta(\alpha))}\right) \end{aligned} \tag{3.53}$$

Substituting the angle differentials of the last three equations into Eq. (3.50) allows us to determine the change in path length Δl for a given angle change $\Delta\alpha$ as a function of angle of incidence α. In general, it is favorable to operate the wobbler at Brewster's angle, to minimize losses due to reflection. Figure 3.26a shows that the path-length change inside the window Δs is always positive, whereas the sign of the path length change outside of the window $\Delta t - \Delta u$ depends on the refractive index. Still, the total length change ΔL as a function of angle of incidence is monotonically increasing, independently of the window material (Fig 3.26b).

[k]This is justified since at the end of the beam path we use a parabolic mirror to focus into the sample, and parallel translation of the light source does not change the path length to the focal point of parabolic mirrors (Fermat's principle).[85]

[l]For the current discussion we are going to assume $n_{air} = 1$ resulting in $\sin(\alpha) = n\sin(\beta)$ for Snell's law.

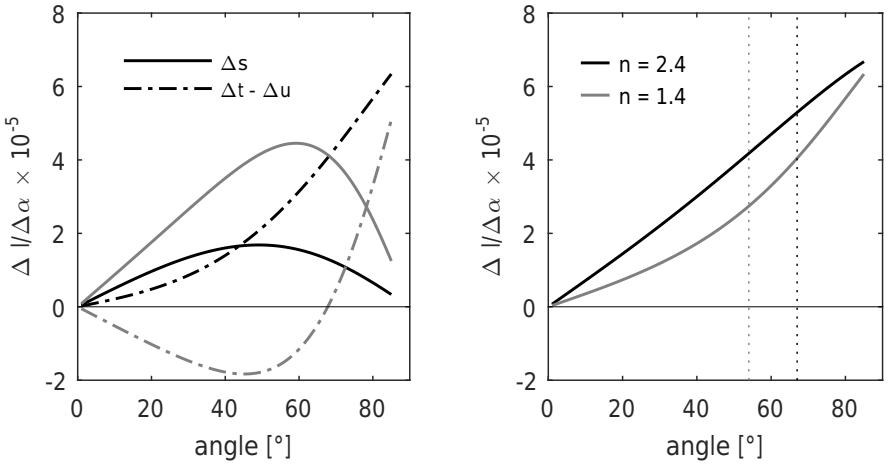

FIGURE 3.26. Change in optical path length upon changing the angle as a function of angle of incidence for a 4 mm window. a) The straight lines show the increase of optical path length inside the windows Δs, the dot-dashed lines show the increase in optical path length after the window $\Delta t - \Delta u$. b) Total optical path length difference $\Delta l/\Delta\alpha$. The dotted lines mark the Brewster's angle. The curves were calculated for ZnSe (n=2.4 at 6 μm) and CaF_2 (n=1.4 at 6 μm).

3.5 NANO FABRICATION

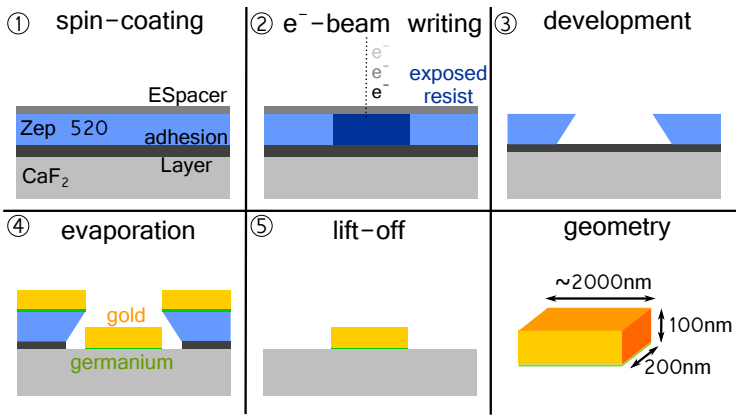

FIGURE 3.27. Electron beam lithography: fabrication process.

In Chapter 5 we will investigate how the signals in nonlinear infrared spectroscopy can be enhanced with plasmonic nanostructures. These gold nanoantennas were fabricated on CaF_2-substrates by electron beam lithography. Figure 3.27 outlines the fabrication process. In the following description we will focus on the objective of every fabrication step. Details about the specific parameters for every step are given

in the corresponding tables.

0. Before the actual fabrication process is started, the substrates are thougtoughly cleaned. To this end, the substrates are first rinsed with isopropanol and subsequently exposed to an O_2 plasma (Plasmalab 80+, strike pressure: 30 mbar) for 20 sec.

1. In the first step, the sample is prepared for the exposure with electrons. The main ingredient is the positive resist (ZEON, ZEP520A) which, when exposed to the electron beam, will change its molecular structure allowing for a selective removal later on. To improve the adhesion between the substrate and the resist an initial layer of hexamethyldisilazane (HDMS, <1 nm) is applied. In the next coating step the actual resist is added. Since an insulating substrate is used, a conductive polymer (∼20 nm, ESpacer 300Z) is needed in the last coating step to prevent charge accumulation during the writing process. All materials are applied by spincoating (Karl Suss Delta 80) which allows for precise control of the layer thickness down to several nanometers.

Material	Function	Spincoating			Baking	
		Accel. [rpm/s]	Speed [rpm]	Time [s]	Temp. [°C]	Time [min]
HDMS	Adhesion	4000	1000	50	150	1
Zep520A	Resist	2400	1000	35	180	5
ESpacer	Conduction	3000	600	50	110	5

2. The actual nano-structuring is accomplished with the help of a scanning electron microscope (Raith, eLine) where electrons are used to write an earlier designed pattern into the resist.

Parameter	Value
High tension [kV]	20
Aperture size [μm]	30
Typical current value [nA]	0.3–0.4
Writefield size [μm]	200 or 400
Nominal area does [μC cm^2]	85
Area step size [nm]	10
Calculated beam speed [mm s^{-1}]	35<v<45
Calculated dwell time [μs]	0.2 <t<0.3

3. Next, the sample is exposed to a chemical agent (n-amyl acetate) which selectively targets and dissolves the exposed resist. This creates a mask, where the resist is removed down to the substrate at the position of the future nano structures. A slight "over-exposure" leads to tilted side walls (undercut), which is desirable for the success of the following steps.

Step	Solvent	Function	Time [s]
1	H_2O	Cleaning	30
2	H_2O	Cleaning	15
3	NP	Start development	105
4	MIBK:IPA (9:1)	End development	15
5	IPA	Remove residual MIBK	15

TABLE I. NP: n-amyl acetate, MIBK: methyl isobutyl ketone, IPA: isopropanyl alcohol

4. Afterwards, the sample is transferred into a high vacuum chamber (Nanoontje, AMOLF). The final structures are formed by thermal evaporation of an initial layer of germanium (1-2 nm) or chrome (1-2 nm), to increase adhesion between the substrate and the gold, and the consecutive evaporation of gold (100 nm). The metal source is located at a large distance ($\sim$1 m) from the substrate to ensure that the (metal) particle-stream reaching the substrate propagates parallel to the surface normal.

Material	Current [A]	Nom. rate [nm s^{-1}]	thickness [nm]
Cr	310	0.01	1-3
or Ge	215	0.01	1-3
Au	210	0.5	100

5. The large distance to the evaporation source, in combination with the undercut, prevents the growth of a continuous gold film, and allows to remove the resist and the unwanted residual metal layers by chemical etching. To this end, the sample is submerged in N-Methyl-pyrrolidone, which dissolves the resist and leaves the free standing gold nanostructures.

The outline procedure allows for a simultaneous structuring of 6 substrates (limited by the eLine). A variety of fields with different antenna geometries, configurations and densities can be written on every substrate. For spectroscopic purposes it has proven convenient to have a field geometry of >400x400 μm allowing for up to 60 fields per substrate.

Chapter 4

Temperature-Induced Collapse of Elastin-Like Peptides Studied by 2DIR Spectroscopy

Elastin-like peptides (ELP) are hydrophobic biopolymers that exhibit a reversible coacervation transition when the temperature is raised above a critical point. Here we use a combination of linear infrared spectroscopy, two-dimensional infrared (2DIR) spectroscopy and molecular dynamics simulations to study the structural dynamics of two elastin-like peptides. Specifically, we investigate the effect of the solvent environment and temperature on the structural dynamics of a short (5-residue) elastin-like peptide and of a long (450-residue) elastin-like peptide. We identify two vibrational energy transfer processes that take place within the amide I′ band of both peptides. We observe that the rate constant of one of the exchange processes is strongly dependent on the solvent environment and argue that the coacervation transition is accompanied by a desolvation of the peptide backbone where up to 75% of the water molecules are displaced. We also study the spectral diffusion dynamics of a valine residue that is present in both peptides. We find that these dynamics are relatively slow and are indicative of an amide group that is shielded from the solvent. We conclude that the coacervation transition of elastin-like peptides is probably not associated with a conformational change involving this residue.

4.1 INTRODUCTION

Elastin is the protein which provides elasticity to many mammalian tissues, such as the lungs,[86–88] skin[89–91] and arteries.[89,92,93] Inside these tissues elastin is present as elastic fibers formed by the self-assembly of the precursor protein tropoelastin (mature elastin fibers result from the enzymatic cross-linking of tropoelastin molecules). The properties of (tropo)elastin are intimately linked to its special structure which consists of alternating hydrophilic and hydrophobic domains.[94] The hydrophilic domains are the regions where the cross-links occur while the hydrophobic domains turn out to play a crucial role in the self-assembly process. These hydrophobic regions consist of short stretches of amino-acid residues that are repeated many times and adopt a disordered conformation.[94] An example of such a repetitive sequence encountered in elastin is the pentapeptide repeat (Val-Pro-Gly-Val-Gly)$_n$. Interestingly, synthetic polypeptides based on this repeating sequence, also known as elastin-like peptides (ELP), can excellently mimic specific properties of elastin.[95–97] For instance, solutions of ELPs display an inverse temperature transition around 37 °C: at low temperatures ELPs are highly soluble in water while they reversibly aggregate when the temperature is increased beyond the transition temperature. This phenomenon, also referred to as coacervation, is thought to lie at the origin of the self-assembly of elastin. In addition to forming an excellent model system for studying the self-assembly of elastin, elastin-like peptides have attracted considerable research interest because of their application perspective in, for example, tissue engineering[98,99] and drug delivery.[100,101]

The molecular mechanism underlying the inverse temperature transition of elastin-like peptides is not well understood. Pioneering work by Urry et al.[95,102] suggested that the coacervation may be due to the formation of a β-turn between the two valine residues within the pentapeptide repeat unit (i.e. around the Pro-Gly fragment). These researchers hypothesized that the formation of a high density of β-turns would force the disordered peptide conformation (observed below the transition temperature) into a conformation displaying long-range order, termed a β-spiral.[103,104] However, the existence of the β-spiral remains highly speculative as molecular dynamics simulations indicate that this structure is not stable in water.[105,106] In the past a variety of spectroscopic techniques, including infrared,[107–109] Raman,[110,111] NMR[102,112,113] and circular dichroism[95,96,109,114] spectroscopy, have been used to study the coacervation transition in ELPs. However, obtaining a detailed molecular picture of the coacervation mechanism has proven extremely difficult. The main challenge lies in the fact that ELPs populate a large ensemble of disordered conformations which, moreover, interconvert on very short timescales (down to nanoseconds).[115] Ultrafast spectroscopic methods are in principle well suited to characterize the disordered conformational ensemble of ELPs because they probe molecular structures on timescales short with respect to the interconversion time. Recently Tokmakoff and coworkers used 2DIR spectroscopy in combination with computational methods to study the structure of a number of very short elastin-like peptides (i.e. consisting of a single repeat unit).[116,117] The authors found that the ELPs studied can indeed adopt a β-turn, but the β-turn turned out to be very labile, with the result that only a small fraction of the molecules adopts

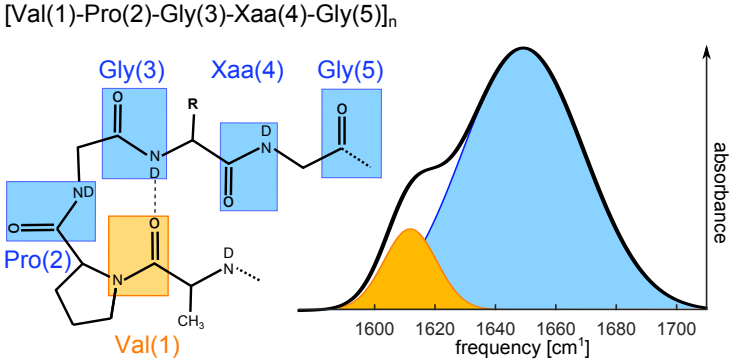

FIGURE 4.1. Chemical structure and typical infrared spectrum of elastin-like peptides in D_2O. The amide I′ groups are indicated with rectangles. The resonance at 1615 cm^{-1} (orange) originates from the amide I′ mode of the Val(1) residue, and the mode at 1650 cm^{-1} (blue) is attributed to the amide I′ mode of the other four residues.

the β-turn. It should be noted that because of their short length the ELPs in question did not exhibit a coacervation transition. As a result the exact role of the β-turn in the coacervation transition of ELPs is not resolved.

In this work we use 2DIR spectroscopy to study the coacervation transition of ELPs. This chapter is divided into two parts. The first part deals with a 450-residue ELP of the type $(Val(1)\text{-}Pro(2)\text{-}Gly(3)\text{-}Xaa(4)\text{-}Gly(5))_n$. Here Xaa represents a guest residue that can be any residue except proline. This ELP displays a sharp coacervation transition, and the transition temperature can be tuned by varying the hydrophobicity of the Xaa residue. We will specifically focus on spectroscopic observables that report on the local fluctuations experienced by the peptide, such as vibrational energy transfer rates and spectral diffusion rates. These observables provide information about the interaction of the peptide with its solvation shell, and we will study how this interaction changes as a function of temperature. In the second part of the chapter we will draw a parallel between the behavior of this long ELP and that of a very short ELP, which is composed of the single pentapeptide repeat Val-Pro-Gly-Val-Gly. This latter ELP does not display a coacervation transition. Nevertheless, it serves as a good model system for studying the conformational flexibility of longer ELPs. In this case we will modify the solvation shell of the peptide, and thereby likely also its secondary structure, by adding the amphiphilic trifluoroethanol (TFE) as a cosolvent. TFE is known to enhance secondary structural elements in peptides.[118,119] By comparing the effects of temperature and solvent composition on the ELPs studied, we gain insight into the mechanism of the coacervation transition.

4.2 MATERIALS AND METHODS

4.2.1 SAMPLE

Fig. 4.1 provides a general overview of the chemical structure of elastin-like peptides and illustrates the basic features observed in the infrared spectrum of this class of peptides. The two different elastin-like peptides investigated in this work are referred to as ELP90 and ELP1. ELP90 is a 90-repeat elastin-like peptide described by the sequence $(\text{Val-Pro-Gly-Xaa-Gly})_{90}$ where the guest position Xaa is occupied by the residues Val, Leu and Gly in a 5:2:3 ratio. ELP90 was synthesized using recombinant-DNA techniques as previously documented.[120] The peptide was purified using inverse transition cycling[121] and its purity was checked by SDS-PAGE. For the spectroscopic measurements the peptide was dissolved in D_2O (Cambridge Isotopes Laboratories, Inc.) at concentrations ranging from 10 mg/ml to 60 mg/ml.
ELP1 stands for the single-repeat pentapeptide Ac-Val-Pro-Gly-Val-Gly-NH_2. The peptide was custom-synthesized by GL Biochem (Shanghai, China). In order to remove residual trifluoroacetic acid (TFA) the peptide was dissolved in DCl and lyophilized before use.[122] The spectroscopic measurements were perfomed on solutions of ELP1 (25 mg/ml) in TFE:D_2O mixtures (trifluoroethanol-d3, Sigma-Aldrich). In these experiments the volume fraction of TFE was varied from 0% to 65%.

4.2.2 INFRARED SPECTROSCOPY

Linear infrared spectroscopy All linear absorption measurements were performed using a Bruker Vertex 80v FTIR spectrometer equipped with a liquid-nitrogen-cooled mercury-cadmium-telluride (MCT) detector. The spectra were recorded under a N_2 atmosphere at a resolution of 2 cm^{-1}. For every spectrum 50 scans were averaged. In all measurements a standard sample cell with a path length of 50 μm was used. The reported spectra were corrected for the absorption of the (TFE:D_2O) solvent background. The temperature-dependent FTIR measurements on ELP90 were performed using a peltier-cooled temperature cell (Mid-IR Falcon, Pike technologies). The temperature was ramped from 293 K to 323 K at a rate of 0.4 K/min, and the spectra were acquired at intervals of 2 K. The background measurements on neat D_2O were performed using the same ramping parameters.

Two-dimensional infrared spectroscopy The experimental setup used in the experiments is described in Chapter 3. The pump and probe pulses are centered at $\sim$1650 cm^{-1}, in resonance with the amide I′ vibration. All experiments are performed under an N_2 atmosphere and with the help of a standard sample cell with a path length of 50 μm. The temperature of the ELP90 samples is kept at 296 K and 318 K using a peltier element with an active feedback loop.

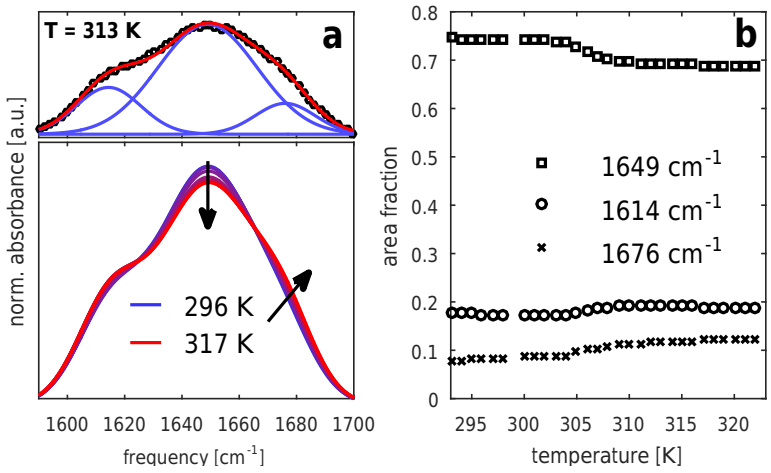

FIGURE 4.2. a) Linear infrared spectra of ELP90 in D_2O (20 mg/ml) for temperatures between 296 K and 317 K. The top panel illustrates the decomposition of the spectrum at 313 K (black squares) into three Gaussian bands (blue lines). The red solid line represents the sum of the three Gaussians. b) Relative contributions of the three bands to the amide I′ spectrum of ELP90 as a function of temperature. The relative contribution is expressed as the integrated intensity of the respective band divided by the integrated intensity of the amide I′ spectrum.

4.3 RESULTS

4.3.1 EFFECT OF TEMPERATURE ON THE STRUCTURAL DYNAMICS OF ELP90

LINEAR INFRARED SPECTRA We start by characterizing the temperature-induced collapse of ELP90 using conventional FTIR spectroscopy. Figure 4.2 displays linear infrared spectra of ELP90 recorded at a range of temperatures starting at ∼15 K below until ∼15 K above the transition temperature. The ELP90 spectrum clearly exhibits two resonances as is schematically illustrated in Fig. 4.1: the redshifted resonance at 1615 cm^{-1} is attributed to the amide group of Val(1), and the resonance at 1650 cm^{-1} is due to the other four amide groups in the pentapeptide repeat. Upon increasing the temperature the peak absorbance at 1650 cm^{-1} decreases, and an increased absorption develops around 1675 cm^{-1} . In order to quantify these spectral changes we use a fitting procedure to deconvolute the ELP90 spectra into Gaussian bands (Figure 4.2a). It turns out that three Gaussians are required to adequately describe the IR spectra at all temperatures. The Gaussian bands are centered at 1614 cm^{-1}, 1649 cm^{-1}, and 1676 cm^{-1} and have full-width-at-half-maxima (FWHM) of 24 cm^{-1}, 41 cm^{-1}, and 24 cm^{-1}, respectively. In the fitting procedure only the amplitudes of the bands are allowed to vary as a function of temperature (their center position and FWHM remain fixed). Figure 4.2 shows the integrated intensity of these bands as a function of temperature. All bands show a sigmoidal dependence on temperature with a transition point at 305 K. The sigmoidal temperature dependence

clearly indicates that the temperature-induced aggregation is a two-state transition.

TWO-DIMENSIONAL INFRARED SPECTRA In order to gain more insight into the origin of the different bands observed in the linear infrared spectrum of ELP90, we performed 2DIR experiments on the peptide. Figure 4.3 displays the (delay-dependent) 2DIR spectra of ELP90 recorded at temperatures below (296 K; left-hand side) and above (318 K; right-hand side) the transition temperature. We first consider the low-temperature 2DIR spectra. At short delays (0.3 ps) we observe a diagonally elongated lineshape, which indicates that the amide I′ spectrum is strongly inhomogeneously broadened. The 2DIR spectrum consists of a negative component on the diagonal, due to ground-state bleaching and stimulated emission of the $0\rightarrow1$ transition, and a positive component at lower probe frequencies, due to the induced absorption of the $1\rightarrow2$ transition. Contrary to the FTIR spectrum, in the 2DIR spectrum the Val(1) band shows up as a well separated resonance at 1615 cm^{-1}. The other subbands constituting the amide I′ spectrum overlap and give rise to one broad resonance around 1660 cm^{-1}. As the pump-probe delay is increased, two effects are observed. Firstly, we see that cross-peaks appear between the Val(1) band and the band at 1660 cm^{-1}. These ingrowing cross-peaks point at vibrational energy transfer between the Val(1) mode and the mode at 1660 cm^{-1}. The appearance of cross-peaks on both sides of the diagonal demonstrates that both uphill and downhill energy transfer processes occur. The second effect observed with increasing pump-probe delay is the spectral reshaping of the band around 1660 cm^{-1}: from a diagonally elongated lineshape at short delays to a round lineshape at long delays.

Next we consider the changes that occur upon increasing the temperature above the transition point. For short delays (0.3 ps) we observe the appearance of a pronounced blue shoulder at $\sim$1675 cm^{-1}. The delay-dependence of the 2DIR spectra is the same as observed at temperatures below the transition point. Cross-peaks develop between the high-frequency band and the Val(1) band; and the shape of the 1660 cm^{-1} band evolves from diagonal to round. In Figure 4.4a we compare the delay dependence of the 2DIR signals at three positions along the diagonal that correspond to the center positions of the three main bands identified in the linear spectra. Figure 4.4a shows that the relaxation of the amide I′ mode speeds up with decreasing frequency of the vibration, and that the relaxation rate does not depend on the aggregation state of the peptide.

RELAXATION AND EXCHANGE DYNAMICS In the previous section we have identified two energy transfer processes. In the first process energy is transferred to and from the Val(1) residue, and in the second process energy is exchanged between the two high frequency modes (reshaping of the $\sim$ 1650 cm^{-1} band). We can assign time constants to these two exchange processes by fitting a relaxation model to our data. The relaxation model used is summarized in Figure 4.5. The model describes the time-dependent populations of the three bands identified in the linear spectrum. These modes exchange population with each other and lose population through vibrational relaxation. The vibrational relaxation of the three modes proceeds via an intermediate state to a so-called hot ground state. The hot ground state accounts for the fact that vibrational relaxation leads to a slight increase in the sample temperature (which in turn affects the amide I′ spectrum).[123] The intermediate state serves to

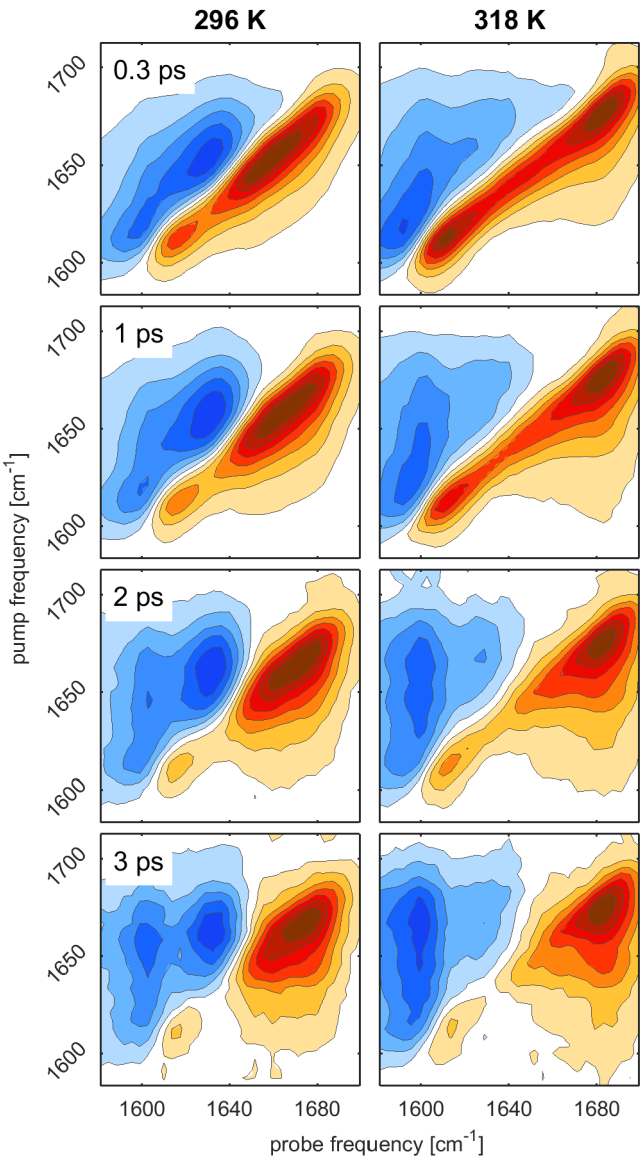

FIGURE 4.3. Isotropic 2DIR spectra of ELP90 in D_2O (20 mg/ml) at different pump-probe delays and for two different temperatures. Negative absorption changes are depicted in red, positive absorption changes in blue. The contour lines are drawn equally spaced at 12,5% increments.

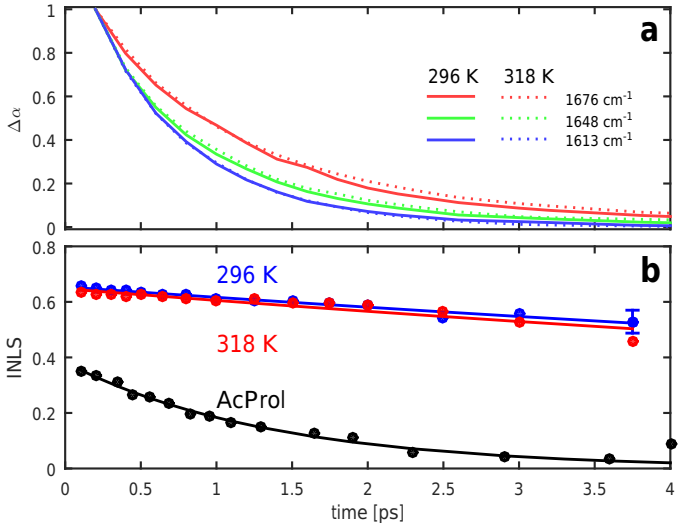

FIGURE 4.4. a) Time-dependent signal corresponding to three different frequencies on the diagonal of the 2DIR spectra of ELP90 for two different temperatures. b) Inverse nodal line slope (INLS) of the Val(1) resonance of ELP90 above (red) and below (blue) the transition temperature. For comparison, the INLS of acetylated proline in D_2O is shown in black.

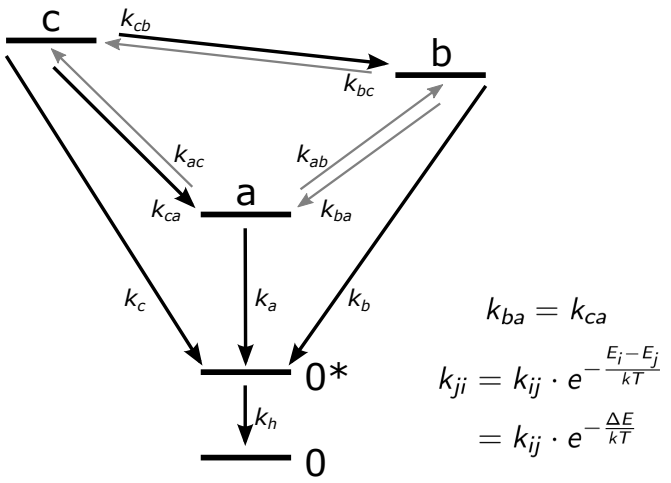

FIGURE 4.5. Schematic representation of the model used to describe the exchange dynamics of the amide I′ vibrations of ELP90 in D_2O. The three main modes identified in the linear infrared experiments are used to represent the amide I′ band: $a = 1613$ cm^{-1}, $b = 1648$ cm^{-1} and $c = 1675$ cm^{-1}. Thick arrows denote independent time constants and thin arrows denote time constants that are derived from the independent constants using the equations on the right.

describe the observation that sample heating is often slightly delayed with respect to the vibrational relaxation.[63] The time-dependent populations of the levels n_i (Figure 4.5) are governed by the following set of rate equations.

$$\frac{d}{dt}\begin{pmatrix} n_a \\ n_b \\ n_c \\ n_* \\ n_0 \end{pmatrix} = \begin{pmatrix} -k_a - k_{ab} - k_{ac} & k_{ba} & k_{ca} & 0 & 0 \\ k_{ab} & -k_b - k_{ba} - k_{bc} & k_{cb} & 0 & 0 \\ k_{ac} & k_{bc} & -k_c - k_{ca} - k_{cb} & 0 & 0 \\ k_a & k_b & k_c & -k_h & 0 \\ 0 & 0 & 0 & k_h & 0 \end{pmatrix} \cdot \begin{pmatrix} n_a \\ n_b \\ n_c \\ n_* \\ n_0 \end{pmatrix} \tag{4.1}$$

We assume that the uphill exchange rates are related to the downhill rates via the detailed-balance condition $k_{ji} = k_{ij}\exp\left(-\frac{E_i - E_j}{kT}\right) = k_{ij}\exp\left(-\frac{\Delta E}{kT}\right)$ where k is Boltzmann's constant, T is the absolute temperature and ΔE is the energy difference between the two modes. In order to further reduce the number of fitting parameters we assume that the exchange process with the Val(1) band is governed by a single time constant (that is we set $k_{ba} = k_{ca}$). We aim to describe the experimental 2DIR signal at three specific pump frequencies, specifically at the center frequencies of the three modes identified in the linear spectra. The 2DIR signal at these pump frequencies is given by

$$\Delta\alpha\left(\nu_{\mathrm{pu}}^{(\mathrm{i})}, \nu_{\mathrm{pr}}, t\right) = \sigma_{\mathrm{heat}}^{(\mathrm{i})}\left(\nu_{\mathrm{pr}}\right) \cdot n_0^{(\mathrm{i})}(t) + \sum_j R_{ij} \cdot \sigma_{\mathrm{j}}\left(\nu_{\mathrm{pr}}\right) \cdot n_j^{(\mathrm{i})}(t) \tag{4.2}$$

In this expression the indices i and j serve as mode labels, which run over the set $\{a, b, c\}$. ν_{pr} represents the probe frequency, and $\nu_{\mathrm{pu}}^{(i)}$ represents the center frequency of mode i. The transient spectrum associated with mode j is denoted as $\sigma_{\mathrm{j}}(\nu_{\mathrm{pr}})$ and can be obtained from the 2DIR spectrum at zero pump-probe delay (it is given by $\Delta\alpha(\nu_{\mathrm{pu}}^{(\mathrm{j})}, \nu_{\mathrm{pr}}, 0)$). The heating spectrum $\sigma_{\mathrm{heat}}^{(i)}(\nu_{\mathrm{pr}})$ is obtained from the 2DIR spectrum at long delays (the dependence on mode index i amounts to a scaling factor due to the variation of the sample absorbance with the pump frequency). We note that every pump frequency in the 2DIR spectrum is associated with a different set of time-dependent populations. This is because the initial conditions for the populations in Eqn. 4.1 depend on the pump frequency according to

$$n_j^{(\mathrm{i})}(0) = \delta_{ij}, \qquad n_0^{(i)}(0) = 0 \tag{4.3}$$

where δ_{ij} is the Kronecker delta. Finally we mention that the scaling factors R_{ij} are necessary to account for the different cross sections of the three modes. These 9 factors are not independent, and they can all be expressed in terms of the cross-section ratios of modes a to b and modes a to c (so that there are only two free parameters).

In summary, this model describes the time-dependence of the 2DIR spectrum (at three specific pump frequencies) in terms of 4 time-independent spectra that are directly extracted from the 2DIR spectrum (three mode spectra and one heating spectrum), and eight fitting parameters (three relaxation rates k_j, the heating rate k_{h}, two independent exchange constants k_{cb} and k_{ba}, and two independent scaling factors R_{ij}). Here we remark that, in fact, the two exchange constants, correspond directly

Temp. [K]	k_c [ps^{-1}]	k_b [ps^{-1}]	k_a [ps^{-1}]	k_{ba} [ps^{-1}]	k_{cb} [ps^{-1}]	k_{SD} [ps^{-1}]
296	0.55 ± 0.01	0.71 ± 0.02	1.04 ± 0.03	0.18 ± 0.02	0.38 ± 0.01	0.09 ± 0.02
318	0.54 ± 0.03	0.71 ± 0.05	1.04 ± 0.03	0.18 ± 0.02	0.31 ± 0.03	0.06 ± 0.02

TABLE I. Results of the fitting of the relaxation model to the ELP90 2DIR data. The rate constants reported are the result of averaging 5 independent measurement series per temperature. The errors give the standard deviation of the mean.

to the two exchange processes that were mentioned in our qualitative description of the 2DIR spectra: reshaping of the 1660 cm^{-1} band (k_{cb}) and energy transfer to and from the Val(1) band (k_{ba}).

We have fitted the relaxation model described above to a large number of ELP90 data sets, which were recorded both above and below the transition temperature. Figure 4.6 displays the fitting results for a typical data set. Note that in this figure the transient spectra have been normalized to emphasize the ingrowth of the cross peaks. We observe very good agreement between the experimental and the calculated spectra. Table I summarizes the rate constants extracted from the fits at both temperatures. We see that the relaxation constants and the exchange rate k_{ba} do not show a significant variation with the aggregation state of the peptide. Only the exchange between the two high-frequency modes (k_{cb}) shows a small but significant slowdown upon aggregation.

SPECTRAL DIFFUSION OF THE VAL(1) RESONANCE The 2DIR spectra in Figure 4.3 show that the Val(1) resonance (1615 cm^{-1}) is essentially decoupled from the rest of amide I′ band of ELP90. This resonance therefore reports on the local fluctuations experienced by the Val(1) residue. At short delays (0.3 ps) we see that the Val(1) resonance shows a pronounced diagonal elongation, which points to a strong inhomogeneous broadening of the resonance. It is interesting to consider how fast this inhomogeneity decays over time because the decay constant reflects the degree of solvent exposure of the respective residue: a fast decay corresponds to a solvent-exposed residue while a slow decay points to a residue that is shielded from the solvent.[27,76,124] We quantify the (time-dependent) inhomogeneity of the Val(1) resonance through the (inverse of the) slope of the nodal line. The time-dependence of this parameter is shown in Fig. 4.4b for temperatures above and below the transition temperature. We observe a very slow decay of the inverse nodal line slope at temperatures below the transition temperature, and, interestingly, this decay does not change upon aggregation of the peptide. As a reference experiment we have repeated these spectral diffusion measurements for a molecule which has an amide group that is fully solvent exposed. For this purpose we have chosen N-acetylated proline (AcPro) because its amide group has the same chemical environment as the amide group of the Val(1) residue in ELP90. As expected we see that for AcPro the inverse nodal line slope decays much faster compared to ELP90 (Figure 4.4b). These spectral diffusion measurements indicate that the amide group of the Val(1) residue

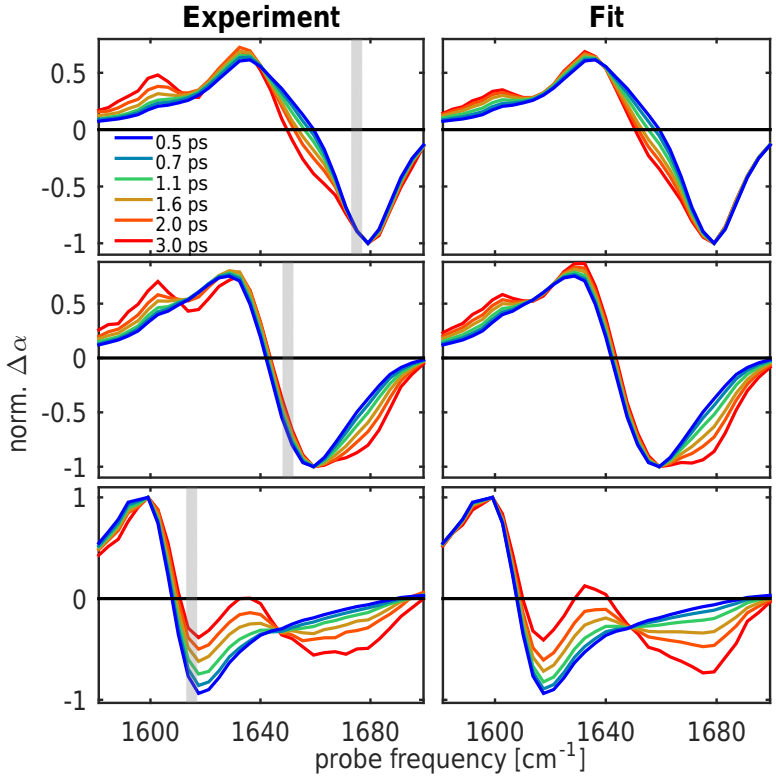

FIGURE 4.6. Comparison between the experimental (left) and calculated (right) pump slices for ELP90 (20 mg/ml) in D_2O below T_c (296 K). The pump frequencies are indicated by gray vertical bars and correspond to $\nu_{pump} = 1675$ cm^{-1}, 1648 cm^{-1} and 1615 cm^{-1}. The transient spectra are normalized to the maximum bleach (top and middle plots) or the maximum ESA (bottom plots) to emphasize the cross-peak dynamics.

is shielded from the solvent in both aggregation states of the peptide.

4.3.2 EFFECT OF THE SOLVENT COMPOSITION ON THE STRUCTURAL DYNAMICS OF ELP1

LINEAR INFRARED SPECTRA To gain more insight into the origin of the inverse temperature transition of ELP90 we performed additional experiments on the simpler ELP1 peptide, which is composed of a single pentapeptide repeat unit. Because ELP1 does not display a coacervation transition as a function of temperature, we decided to focus on possible conformational changes induced by the addition of the amphiphilic cosolvent trifluoroethanol (TFE). TFE is generally known to induce secondary structure in peptides.[125–127] In our experiments the solvent composition was varied from 0 to 65 volume percent TFE in D_2O [v/v%]. The FTIR spectra of these solutions are displayed in Figure 4.7. We have used the same global fitting

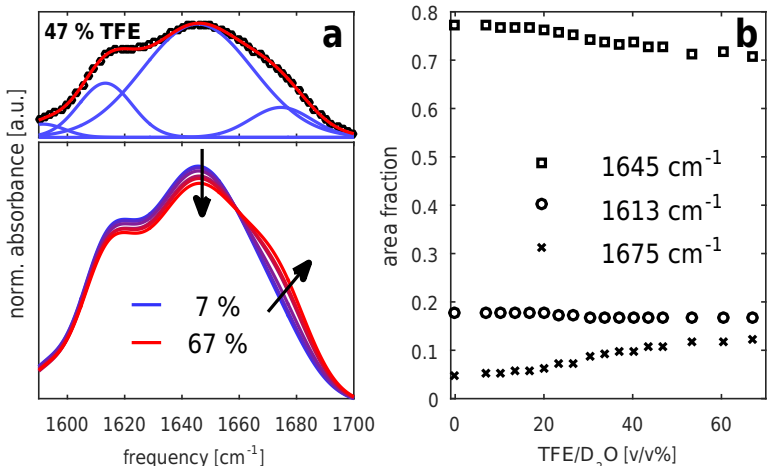

FIGURE 4.7. a) Linear infrared spectra of ELP1 (25 mg/ml) in TFE:D_2O mixtures of varying composition. The top panel illustrates the decomposition of a typical spectrum (black squares) into four Gaussian bands (blue lines). The red solid line represents the sum of the four Gaussians. b) Relative contribution of the three main bands to the amide I′ spectrum of ELP1 as a function of the solvent composition.

procedure as for ELP90 to decompose these spectra into Gaussian bands (Figure 4.7, top panel). The ELP1 amide I′ band can be excellently described using a linear combination of four Gaussians (centered around 1590 cm^{-1}, 1613 cm^{-1}, 1645 cm^{-1} and 1675 cm^{-1}). Three of the four bands have close to identical center positions as for ELP90. The fourth band at 1590 cm^{-1} is assigned to a carboxylic acid group due to incomplete amidation of the C-terminus of the pentapeptide. The intensity of this band is very small and it does not vary with solvent composition, so that we disregard the band in our analysis. Interestingly, the spectral evolution of ELP1 as a function of TFE concentration looks very similar to the spectral changes that were previously observed for ELP90 with increasing temperature.

2DIR SPECTROSCOPY Figure 4.8 shows the 2DIR spectra of ELP1 for two representative solvent compositions. We observe a number of effects in these spectra which parallel the observations made for ELP90. Firstly, the pronounced separation between the Val(1) band at 1615 cm^{-1} and the 1660 cm^{-1} band is clearly visible. Secondly, as a function of delay time we observe energy transfer between these two bands, as well as a reshaping of the 1660 cm^{-1} band. Finally, when considering the time dependence of the 2DIR signal (Fig. 4.9a) on the diagonal we observe a trend which is analogous to that of ELP90. Specifically, the relaxation speeds up with increasing redshift of the amide I′ vibration, but it is independent of the solvent composition.

RELAXATION AND EXCHANGE DYNAMICS We use the same relaxation model that we used above in our analysis of the ELP90 data, to quantitatively describe

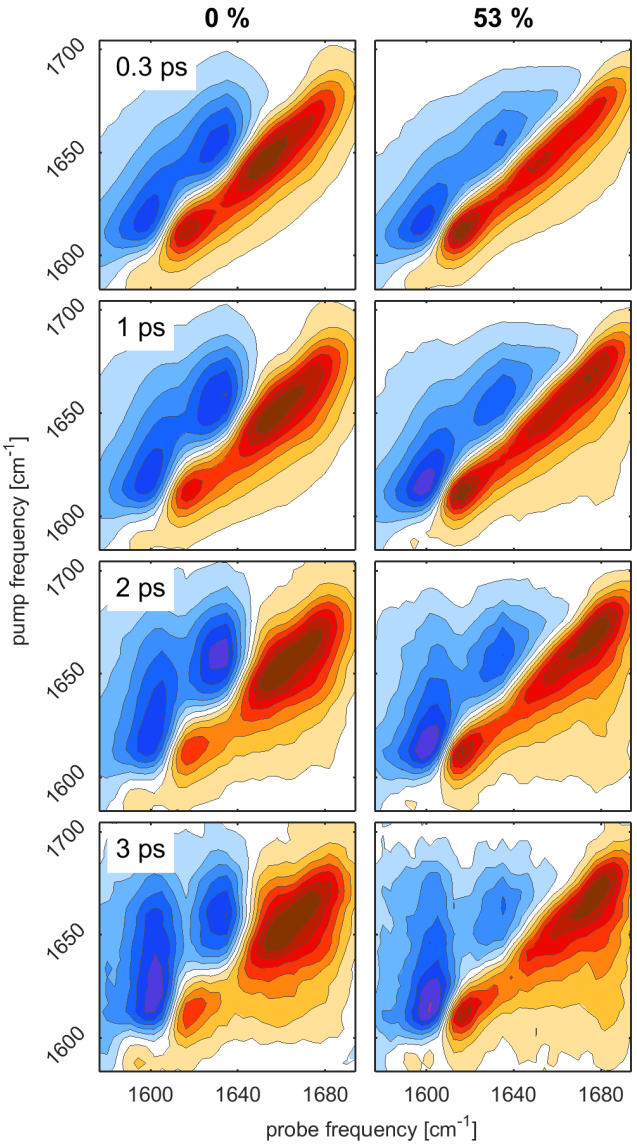

FIGURE 4.8. Isotropic 2DIR spectra of ELP1 (25 mg/ml) in TFE:D_2O mixtures at different pump-probe delays and for two solvent compositions: 0% TFE (left) and 53% TFE (right). Negative absorption changes are depicted in red, positive absorption changes in blue. The contours are drawn equally spaced at 12.5 % increments.

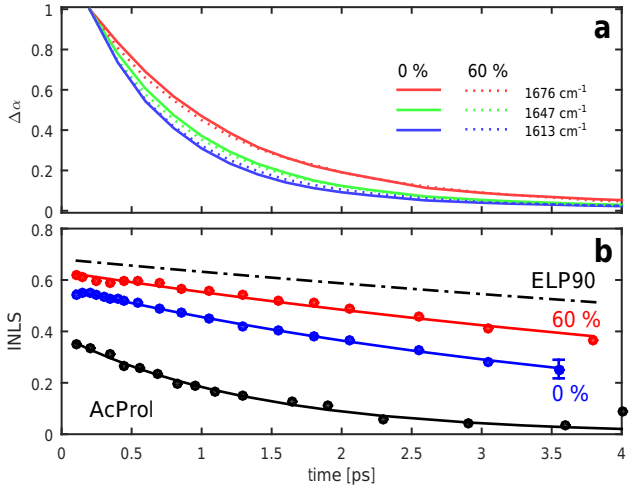

FIGURE 4.9. a) Time dependent bleaching signal extracted from the 2DIR spectra of ELP1 (25 mg/ml) in TFE:D_2O mixtures. The decay traces are shown for solvent mixtures at a low (0%, straight lines) and at a high (60%, dotted lines) volume fraction of TFE. The three colors correspond to the three modes, as indicated in the legend. b) Inverse nodal line slope (INLS) of Val(1) at a low (red) and at a high (blue) volume fraction of TFE. The INLS was extracted from the same datasets as in a). For comparison, the INLS of acetylated proline (30 mg/ml) in D_2O (black, point dashed) and the INLS of ELP90 (20 mg/ml) in D_2O (black, point dashed) is shown.

the ELP1 data sets. The fitting results are summarized in Figure 4.10. We see that the vibrational relaxation rates of the three modes that appear in the model are independent of the solvent composition (Figure 4.10a). Next we consider the exchange dynamics, and interestingly we observe that the two exchange constants show a very different solvent dependence. Apparently the exchange with the Val(1) band (characterized by the exchange constant k_{ba}) is independent of the solvent composition. The other exchange process (i.e. the reshaping of the high-frequency band characterized by the constant k_{cb}), on the other hand, slows down dramatically with increasing TFE concentration.

SPECTRAL DIFFUSION OF THE VAL(1) RESONANCE Finally we again look into the local solvation dynamics of the Val(1) residue. In Figure 4.9b we have plotted the inverse nodal line slope of the Val(1) resonance of ELP1 for the two limiting solvent compositions studied (0% and 60% TFE). As a reference the figure also summarizes the spectral diffusion dynamics of ELP90 (dashed black lined) and AcPro (solid black line). We see that for ELP1 in neat D_2O the spectral diffusion is much slower than was the case for AcPro (whose amide group is fully solvent exposed). Upon increasing the TFE concentration of the solvent these dynamics slow down slightly, and they become very similar to the spectral diffusion dynamics observed in ELP90. We have quantified these observations by fitting a monoexponential to the decay curves, and

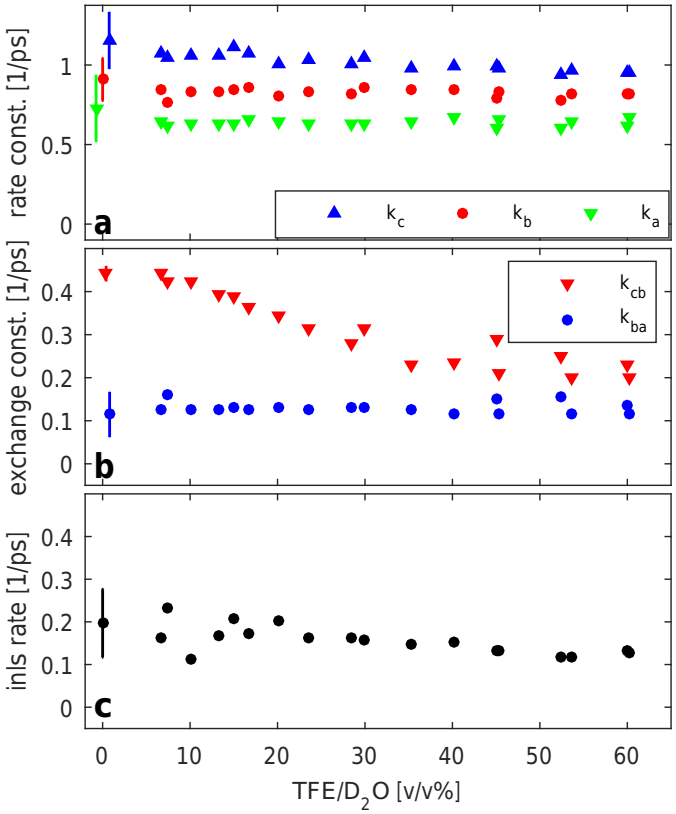

FIGURE 4.10. Fitting results of the relaxation model described in the text to the ELP1 data sets a) Relaxation rates of the three amide I′ modes as a function of the TFE volume fraction. b) Exchange constants k_{cb} and k_{ba} versus TFE volume fractions. c) Decay rate of the spectral diffusion curves of the Val(1) resonance versus TFE volume fraction. The error bars give the standard deviation of the mean of three measurements.

we have plotted the resulting decay constants in Figure 4.10c.

4.4 DISCUSSION

In this work we have performed experiments on two elastin-like peptides. A striking observation is the similar appearance of both the linear and the nonlinear spectra of these two peptides. We have seen that the spectra of ELP1 and ELP90 are accurately described as a superposition of the same three Gaussian bands. As a first point we look into the assignment of these bands. As was already explained, the band at 1615 cm^{-1} is attributed to the Val(1) residue, whose frequency is redshifted due to the adjacent proline residue. The band at 1650 cm^{-1}, on the other hand, is typical of disordered protein structures, so that the question remains what the origin is

Solvent	H-bond type	ELP1 Conformation	
		Extended	Folded
D_2O	peptide-water	12.61 ± 1.77	10.86 ± 1.57
D_2O:TFE	peptide-water	3.88 ± 1.70	3.30 ± 1.52
	peptide-TFE	5.40 ± 2.14	4.31 ± 1.71

TABLE II. Average number of hydrogen bonds per ELP1 molecule in the MD simulations. The errors give the standard deviation.

of the band at 1675 cm^{-1}. A first clue is provided by the fact that for ELP1 the intensity of this band increases upon the replacement of the aqueous solvent for a solvent environment with a lower density of hydrogen bonds (i.e. D_2O:TFE). It is well known that there is a direct correlation between the (local-mode) amide I′ frequency of a residue and the strength of its hydrogen bond.[21,128,129] Therefore a likely explanation for the high-frequency band is that it originates from amino-acid residues which are relatively weakly hydrogen-bonded, either to the solvent or to other amino-acid residues. In order to confirm this interpretation, Ana V. Cunha and Thomas L.C. Jansen performed molecular-dynamics simulations for two ELP1 solutions (in D_2O and in 60% TFE:D_2O), and they measured the number of peptide-solvent hydrogen bonds in these two systems. These simulations were performed for both an extended ELP1 conformation and for a folded ELP1 conformation (i.e. with a hydrogen bond between the two valine residues, see Fig. 4.11). Table II gives the average number of peptide-water and peptide-TFE hydrogen bonds in these simulations. As can be seen the total number of peptide-solvent hydrogen bonds decreases by approximately 30% when the TFE volume fraction is increased from 0 to 60%. This result suggests that the ingrowth of the blue shoulder in the ELP1 spectrum (with increasing TFE volume fraction) can indeed be attributed to a weakening of the average strength of the hydrogen bonds formed by the peptide groups. Another effect that could contribute to the weakening of the *average* hydrogen-bond strength (that is, apart from the presence of a large fraction of broken hydrogen bonds) is the truncation of the water hydrogen-bond network by TFE; this truncation causes the *intact* peptide-water hydrogen bonds to weaken as they are no longer part of an extended network. The spectral similarities between ELP1 and ELP90 strongly suggest that the molecular environment experienced by ELP90 in the coacervate is very similar to environment created by the mixed D_2O:TFE solvent. This means that the spectral changes observed upon the coacervation of ELP90 are very likely attributable to the desolvation of the peptide backbone during the coacervation process. Having assigned the Gaussian bands that appear in our kinetic model, we next consider how to interpret the dynamics observed in the 2DIR spectra. As was described in the previous section there are in essence two delay-dependent processes that can be observed in the 2DIR spectra of ELP1 and ELP90. The first process is the energy exchange between the Val(1) residue and the residues

of the remaining tetrapeptide. The second process is the energy exchange among the residues that form the tetrapeptide. A first point to note is that for ELP90 these two processes occur on the picosecond timescale, both in the solvated and in the aggregated state. The occurrence of picosecond vibrational energy transfer points to a well hydrated structure. The reason is that vibrational energy transfer requires the presence of fluctuations to compensate for the energy mismatch between the modes involved,[69,72,74,130] and these fluctuations are typically provided by the motions of water molecules inside the hydration shell. The fact that energy transfer remains possible in the aggregated state of ELP90 indicates that, despite the desolvation described above, the ELP90 aggregates apparently still contain a relatively large fraction of mobile water molecules. If we examine the rate constants of the exchange processes, we see that for ELP90 the exchange process involving Val(1) does not depend on temperature and the second process slightly slows down with increasing temperature. These observations are mirrored in the ELP1 data where one sees that the Val(1)-exchange is independent of the volume fraction of TFE, while the second process slows down with increasing TFE volume fraction. This slowing down of the energy transfer for ELP1 is likely due to the replacement of light and mobile water molecules in the hydration shell of ELP1 by the heavier and relatively immobile TFE molecules. An additional effect that plays a role here is the fact that TFE molecules are known to preferentially aggregate around peptides,[119,131] so that TFE is very effective at displacing water molecules. Another interesting observation is the fact that for both ELP90 and ELP1 $k_{cb} > k_{ba}$. That is, energy transfer proceeds more slowly whenever the Val(1) residue is involved. A likely explanation could be that for this exchange process the frequency mismatch is relatively large, i.e. larger than the typical magnitude of the frequency fluctuations.

Given that for ELP1 the exchange constant k_{cb} is sensitive to the degree of hydration, it would be interesting to use the ELP1 data as a reference and to estimate the degree of desolvation that occurs during the aggregation of ELP90. This can be done as follows. For ELP90 the rate constant k_{cb} decreases by about 20% upon aggregation of the peptide (Table I). In order to achieve a similar decrease for ELP1 the volume fraction of TFE needs to be ~25% (Figure 4.10). Because of the preferential aggregation of TFE, mentioned above, this actually corresponds to an even higher TFE concentration inside the solvation shell of ELP1. The MD simulations were used to calculate the preferential aggregation of TFE around the folded ELP1 peptide assuming a solvation shell of 0.6 nm, identically to ref.[119] The first solvation shell concentration of TFE was found to be 3.0 times higher than the bulk concentration, which is similar to previous findings for other proteins.[119] Using this result we find that for an ELP1 solution in 25% D_2O:TFE the TFE volume fraction inside the solvation shell is as large as 75%, which means that the concentration of water molecules is only 25% of the bulk value. From this we conclude that during the aggregation of ELP90 roughly 3 out of 4 water molecules are displaced from its solvation shell.

We end the discussion of our results by turning to the spectral diffusion dynamics of the Val(1) residue, which are displayed in Figures 4.4 and 4.9. The decay of the inverse nodal line slopes shown in these figures directly reflects the degree of solvent exposure of the Val(1) residue. As can be seen from the black curve in Figure 4.4b a

fully solvent exposed residue, such as the amide group of AcPro, exhibits a complete decay of the nodal line slope on a ∼2 ps timescale. In contrast, for ELP90 we observe a much slower decay of the nodal line slope, which indicates that in this peptide the Val(1) residue is shielded from the solvent. A likely explanation for this strong shielding from the solvent is that the C=O group of the Val(1) residue may form an intrapeptide hydrogen bond with the NH group of the Val(4) residue. The presence of such a hydrogen bond is in line with the notion that the Pro-Gly sequence is often located inside a β-turn.[132,133] The molecular dynamics simulations were used to further investigate this interpretation of our experimental results. For both simulated conformations the frequency-frequency correlation function (FFCF) of the Val(1) residue was computed. It turns out that on the timescale of the simulations (10 ns) these two conformers do not interconvert, i.e. the peptide maintains the conformation chosen at the start of the simulation. Figure 4.11 displays the FFCF for these two simulations. If we compare the simulation of the folded and extended structures (in water), we see that indeed the presence of the β—turn causes a slowing down of the decay of the FFCF, which corroborates our interpretation. We further note that for the folded structure the replacement of the aqueous solvent by a TFE:water mixture leads to an upward shift of the simulated FFCF, and this observation is again in line with our experimental observation (Fig. 4.9). Interestingly, our experiments show that the spectral diffusion dynamics and thereby the degree of solvent shielding are identical in the dissolved and aggregated state of ELP90 and show very little change in ELP1 as a function of TFE concentration. This implies that the β-turn is present in both states of the peptide, and therefore we conclude that contrary to suggestions found in the literature[134–137] the coacervation transition of elastin-like peptides may not be driven by the formation of a β-turn. Instead we speculate that the role of the β-turn may be more indirect: that is to say, the β-turn may stabilize a conformation in which a large number of hydrophobic sidechains are exposed, so that hydrophobic association can occur once the driving force (and therefore the temperature) is high enough.

4.5 CONCLUSION

We used linear infrared spectroscopy, 2DIR spectroscopy and MD simulations to study the structural dynamics of elastin-like peptides (ELP). To gain insight into the coacervation transition displayed by this class of peptides we performed experiments on two different ELPs. We studied a 90-repeat ELP (450 residues), for which coacervation can be induced by increasing the temperature above the transition point. We also performed reference measurements on a single-repeat ELP (5 residues). This ELP was too short to show a coacervation transition, and therefore in this case experiments were performed as a function of the solvent composition (i.e. different volume fractions of TFE in water).

Our results show that for both peptides the amide I′ spectrum can be well described as a superposition of three Gaussian bands located at 1615 cm^{-1}, 1645 cm^{-1} and 1675 cm^{-1}. We assign the 1615 cm^{-1} band to the localized amide I′ resonance of the Val(1) residue. The 1645 cm^{-1} and the 1675 cm^{-1} bands are associated with

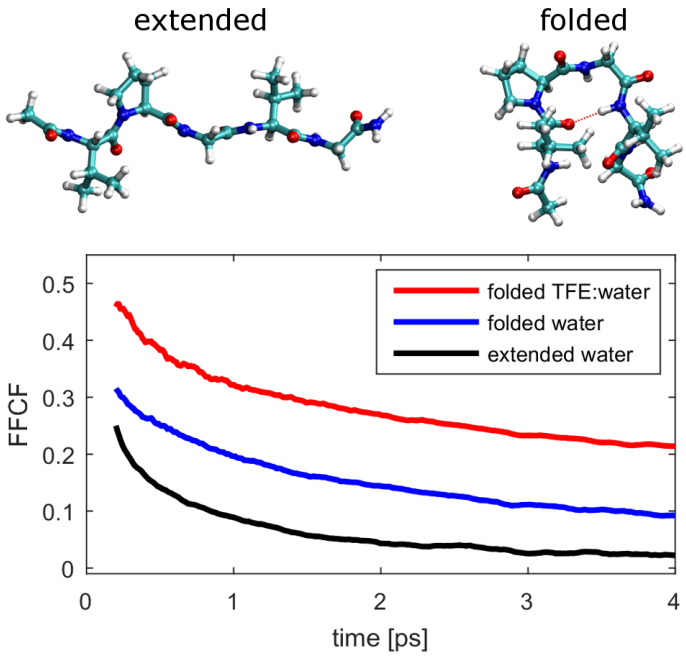

FIGURE 4.11. Frequency-frequency correlation function (FFCF) of the amide I′ vibration of Val(1) in ELP1 extracted from MD simulations. The simulations were performed for an extended and hydrogen bonded confirmation (see top) in two different solvents (water and TFE:water).

residues 2 to 5 in the pentapeptide repeat and probably have a more delocalized character. We attribute the 1645 cm^{-1} band to well-hydrated residues and the 1675 cm^{-1} band to more weakly hydrated residues. In the 2DIR experiments we have identified two vibrational energy transfer processes that take place between the three bands. One of these transfer processes is independent of the solvent environment of the peptides while the second process slows down when water molecules in the solvent are replaced by TFE for ELP1 or when the temperature is raised above the coacervation temperature for ELP90. We use the solvent-dependent process to estimate the degree of desolvation that takes place upon coacervation of 90-repeat ELP, and we find that this desolvation corresponds to a loss of roughly three out four water molecules in the hydration shell.

Finally we studied the spectral-diffusion dynamics of the Val(1) residue. We find that these dynamics are very slow and indicative of an amide group that is shielded from the solvent. Surprisingly, for the 90-repeat ELP these dynamics do not change with the aggregation state of the peptide. We conclude that the slow dynamics are likely due to the fact that the Val(1) residue forms an intrapeptide hydrogen bond with the Val(4) residue (β-turn), already below the coacervation transition.

Chapter 5

Ultrasensitive Ultrafast Vibrational Spectroscopy Employing the Near Field of Gold Nanoantennas[a]

We introduce a novel method to perform nonlinear vibrational spectroscopy on nanoscale volumes. Our technique uses the intense near field of infrared nanoantennas to amplify the nonlinear vibrational signals of molecules located in the vicinity of the antenna surface. We demonstrate the capabilities of the method by performing infrared pump-probe spectroscopy and two-dimensional infrared (2DIR) spectroscopy on 5 nm layers of polymethylmetacrylate (PMMA). In these experiments we observe enhancement factors of the nonlinear signals of more than 4 orders of magnitude. We discuss the mechanism underlying the amplification process as well as strategies for further increasing the sensitivity of the technique.

[a]Adapted from: O. Selig, R. Siffels, and Y. L. A. Rezus, "Ultrasensitive Ultrafast Vibrational Spectroscopy Employing the Near Field of Gold Nanoantennas", PRL, **114**, 233004 (2015)

5.1 INTRODUCTION

Vibrational spectroscopy is a powerful, label-free technique that provides detailed information about molecular structures. The method uses vibrational marker modes to identify the chemical groups present inside a molecule as well as to probe their chemical nanoenvironments. In recent years vibrational spectroscopy has experienced a revival with the advent of novel, *nonlinear* vibrational spectroscopies, in particular infrared pump-probe spectroscopy and two-dimensional infrared (2DIR) spectroscopy.[138–142] In these techniques the sample is interrogated by a number of time-delayed femtosecond infrared pulses, allowing one to study not only the structures of molecules but also their dynamics.[25,143–145] While these two nonlinear methods are mostly applied to macroscopic samples, they could in principle provide valuable information about nanoscale systems consisting of molecular monolayers, such as the active areas of biosensors, supported lipid bilayers, and responsive surfaces.[146,147] Unfortunately, because of the low absorption cross-section of molecular vibrations, the only molecular monolayers that are amenable to study using these techniques are those composed of extremely strong infrared absorbers: in particular, to date such measurements have only been reported for metal-carbonyl compounds.[148,149] Obviously, a method allowing for the application of these nonlinear spectroscopies to other, less absorptive, molecular vibrations at the (sub)monolayer level would be highly beneficial.

An attractive option for amplifying the interaction of molecular vibrations with infrared radiation is the use of optical nanoantennas. These metallic nanostructures have recently attracted considerable interest due to their ability to funnel light to subwavelength volumes and thereby strongly enhance the local electromagnetic field.[49,150] Particularly strong field enhancements can be achieved with the help of resonant nanostructures, such as rod-shaped nanoantennas, which exhibit a dipolar resonance that can be tuned all the way from the visible spectral region to the far infrared, simply by varying the length of the nanoantenna. In the past it has been demonstrated that infrared-resonant nanoantennas can strongly amplify the linear vibrational spectroscopic signals of molecules located in their near fields.[37,151–154] In addition nonlinear frequency-mixing processes such as second-harmonic generation,[155] third-harmonic generation[156] and four-wave mixing[157,158] have been demonstrated to occur in the near fields of nanoantennas. An application that has not been explored to date is the use of infrared nanoantennas as a means to perform highly efficient nonlinear spectroscopy. Recently it was demonstrated that nonlinear vibrational signals (2DIR) can be enhanced using colloidal gold nanoparticles,[159] but the possibilities provided by nanoantenna structures designed to be resonant with a specific vibrational mode have not yet been exploited.

Here we report on a proof-of-principle experiment in which we use the enhanced near field of nanoantenna arrays to perform femtosecond vibrational pump-probe spectroscopy on the carbonyl vibration of ultrathin layers of polymethylmetacrylate (PMMA) deposited on top of the arrays. The enhanced near field of the nanoantennas decays rapidly with distance, and, consequently, we only probe those regions of the PMMA film located directly on top of the nanoantennas. We demonstrate that with this method the nonlinear spectroscopic signals are amplified by more than 4 orders

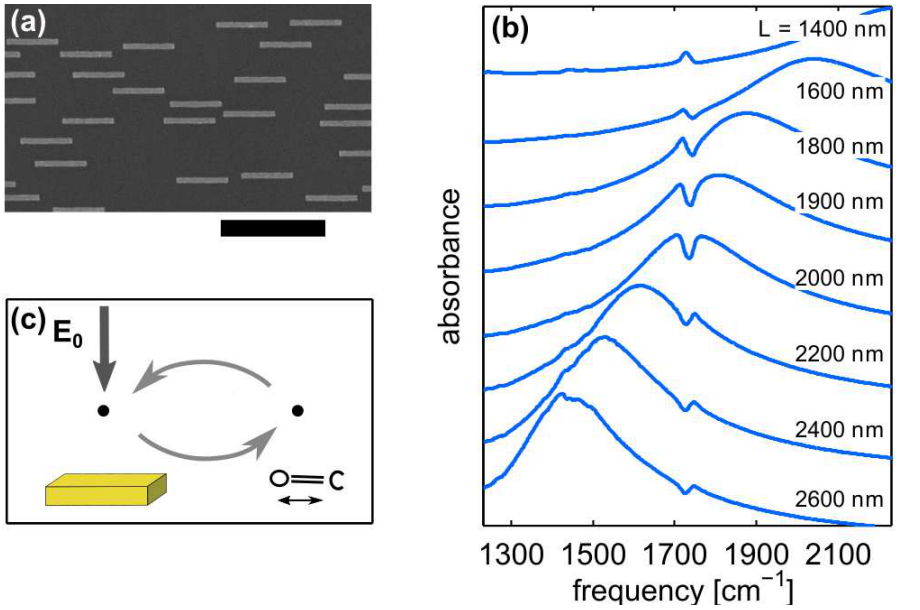

FIGURE 5.1. a) Scanning electron microscope (SEM) image of one of the antenna arrays. The scale bar corresponds to a distance of 4 μm. (b) Infrared absorbance spectra (light polarized along the long antenna axis) of randomized nanoantenna arrays coated with a 14 nm layer of PMMA. The spectra are offset vertically for clarity. (c) Schematic representation of the coupled-dipole model described in the text. Both the nanoantenna and the PMMA patch on top are represented as point dipoles.

of magnitude.

5.2 LINEAR INFREARED SPECTROSCOPY

In our experiments we use gold nanoantenna arrays that are fabricated on CaF_2 substrates using standard e-beam lithography (for a detailed description see Section 3.5). The antennas are arranged in 800 μm × 800 μm randomized arrays at a density of 0.17 μm^{-2} (Fig. 5.1(a)). The random antenna arrangement serves to average out the effects of coupling between the individual antennas.[151] The antennas are 200 nm wide, 100 nm high, and their length varies between 1400 and 2600 nm. Antennas of these lengths interact strongly with midinfrared light that is polarized along the long antenna axis. This is illustrated in Fig. 5.1(b) where we show the IR transmission spectra of a number of antenna arrays that are covered with a 14 nm layer of PMMA. These spectra were recorded with a Bruker Vertex 80v FTIR spectrometer coupled to a Hyperion 3000 IR microscope. The longitudinal plasmon resonance has a width of 300–500 cm^{-1} and the resonance shifts to the red with increasing antenna length.[152] In addition a small modulation on top of the antenna spectrum is observed around

1730 cm^{-1}, which is due to the interaction with the PMMA carbonyl vibration. The spectra in Fig. 5.1(b) illustrate that the antennas do not merely amplify the *absorption* by the PMMA: in that case one would observe positive absorptive peaks on top of the antenna spectra (i.e., an increased absorption). Instead the enhancement mechanism leads to complex vibrational line shapes that depend on the detuning between the vibrational transition and the antenna resonance.[152] In the following we use a simple, coupled-dipole model[160, 161] to explain the observed line shapes and their intensities (Fig. 5.1(c)). An extended discussion of this model will be presented in Chapter 6. In order to keep the notation simple we use a scalar description. We treat the antenna and the PMMA patch on top of it as two dipolar point scatterers with respective complex polarizabilities $\alpha_{ant}(\omega)$ and $\alpha_{vib}(\omega)$ and locations r_{ant} and r_{vib}. We note that both polarizabilities are frequency dependent: $\alpha_{vib}(\omega)$ due to the vibrational resonance of the CO vibration of PMMA, and $\alpha_{ant}(\omega)$ due to the plasmonic antenna resonance (tunable by varying the antenna length). The incident electric field $E_0(\omega)$ polarizes the antenna, which leads to an enhanced near field that induces a vibrational dipole given by

$$p_{vib}(\omega) = \alpha_{vib}(\omega) G(r_{vib}, r_{ant}) \alpha_{ant}(\omega) E_0(\omega) \tag{5.1}$$

where $G(r_{vib}, r_{ant})$ is the Green function for a radiating dipole located at position r_{ant}. In this expression we have neglected the contribution of the incident field itself to the vibrational polarization as its effect is much smaller than that of the local field. The induced vibrational dipole acts back and induces a change in the antenna polarization

$$\Delta p_{ant}(\omega) = \alpha_{ant}(\omega) G(r_{ant}, r_{vib}) p_{vib}(\omega) \tag{5.2}$$

Combining these expressions and using the fact that the extinction cross section of the antenna $\sigma_{ant}(\omega)$ is given by the ratio of the work done on the antenna by the *incident* field $\frac{1}{2}\omega \mathrm{Im}[p_{ant}(\omega) E_0^*(\omega)]$ to the incident intensity we arrive at the following expression for the modification of the antenna cross section due to the presence of the PMMA

$$\Delta\sigma_{ant}(\omega) = \frac{2\pi}{\lambda \varepsilon_0} \mathrm{Im}\left\{ [\alpha_{ant}(\omega) G]^2 \alpha_{vib}(\omega) \right\} \tag{5.3}$$

In this equation λ is the free-space wavelength and ε_0 is the permittivity of free space. We have used the reciprocity relation to equate the two appearing Green functions and simply denoted them by G. Despite the approximations made in the above treatment this equation provides an excellent description of the antenna-enhanced vibrational line shapes, as we have confirmed through finite-difference time domain simulations (see Chapter 6). Equation 5.3 shows that the nanoantenna amplifies the original vibrational spectrum by the complex-valued factor $(\alpha_{ant}(\omega) G)^2$, which represents the square of the field enhancement. Because of the complex nature of the amplification factor the (enhanced) vibrational signal $\Delta\sigma_{ant}(\omega)$ typically contains both an absorptive $\mathrm{Im}[\alpha_{vib}(\omega)]$ and a dispersive $\mathrm{Re}[\alpha_{vib}(\omega)]$ component as can be seen in Fig. 5.1(b). It is straightforward to see that there are three circumstances under which purely absorptive line shapes are observed: if the antenna is driven on resonance, far below resonance, or far above resonance. In the first case there is a

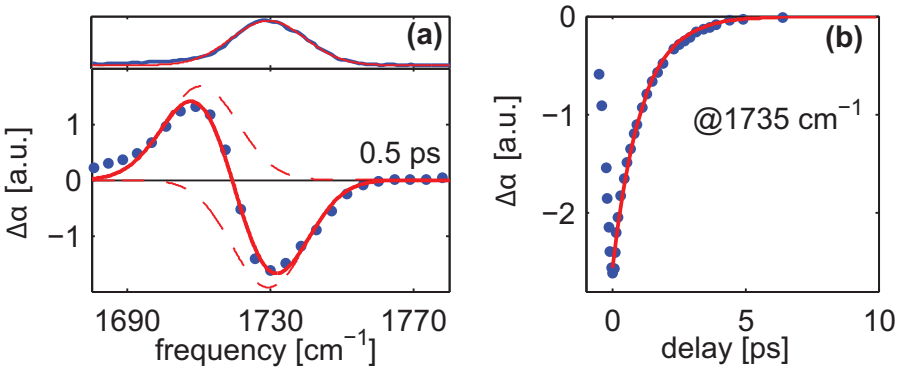

FIGURE 5.2. (a) Top: Linear infrared spectrum (blue line) of the carbonyl vibration of a 150 nm film of PMMA on a CaF_2 substrate. The red line represents a Gaussian fit. Bottom: Transient spectrum of the same sample (isotropic signal). The solid red line is a fit to a linear combination of two Gaussian bands (dashed lines) whose widths are taken from the linear spectrum. b) Delay scan of the transient signal at a frequency of 1735 cm^{-1}. The red line is a monoexponential fit.

$\pi/2$ phase lag between the incident electric field and the antenna polarization: this leads to a negative value ($(e^{i\pi/2})^2 = -1$) of the amplification factor $(\alpha_{ant}(\omega)G)^2$, so that the vibrational signal is observed as an absorption *dip* on top of the antenna resonance. Driving the antenna far below resonance or far above resonance results in phase shifts of 0 and π, respectively, so that in these two circumstances absorptive *peaks* ($(e^{i0})^2 = -1$ and $(e^{i\pi})^2 = -1$) are observed.

5.3 PUMP-PROBE SPECTROSCOPY

We investigate the nonlinear optical properties of the PMMA-covered arrays using femtosecond IR pump-probe spectroscopy (see Chapter 3 for a detailed description of the experimental setup). In these measurements we use a femtosecond (∼100 fs, 150 nJ) infrared pulse centered at 1700 cm^{-1} to excite a significant fraction of the carbonyl vibrations in the PMMA layer. The pump-induced absorption changes ($\Delta\alpha = -\ln T/T_0$) are monitored by a delayed probe pulse. In order to perform polarization-resolved measurements the probe polarization is set at an angle of 45 deg with respect to the pump polarization. Using polarizers behind the sample we then select the probe component that is polarized either parallel or perpendicular to the pump polarization. Scattered pump light is suppressed by rapidly modulating the pump-probe delay by half an optical period.[162]

As a reference measurement the pump-probe spectrum of a thick layer of PMMA (∼150 nm) deposited on a CaF_2 substrate is shown in Fig. 5.2. We observe the characteristic transient spectrum of an anharmonic vibration. At the fundamental frequency (1730 cm^{-1}) there is a decreased absorption due to the depletion of the

ground state and stimulated emission from the vibrationally excited state. At lower frequencies (∼1710 cm^{-1}) an induced absorption is observed due to absorption by the excited state. A fit of the transient spectrum to a linear combination of two Gaussian bands reveals an anharmonicity of 19 cm^{-1}. The ratio of the 0-1 and 1-2 cross sections is 1.8, which is very close to the value of 2 expected for a purely harmonic vibration. Figure 5.2(b) shows a delay scan for a frequency corresponding to the peak of the bleach (∼1735 cm^{-1}). We observe a monoexponential decay with a time constant of 1.1 ps which we attribute to the vibrational relaxation of the carbonyl vibration.

Having characterized the transient vibrational response of PMMA itself we move on to study the effect of coupling with the nanoantennas. For this purpose we work with a 5 nm film of PMMA (see Section 5.6.2 for the determination of the thickness), which gives no appreciable pump-probe signal in the absence of antennas: the smallest signal we could detect ($\Delta\alpha = 2 \times 10^{-5}$) was for a 10 nm thick film, which is shown in Fig. 5.3(a). Next we consider the situation of a 5 nm film deposited on an array of nanoantennas ($L = 2000$ nm) that are tuned to resonance with the carbonyl vibration. Figure 5.3(b) shows the pump-probe signal for a measurement in which the pump pulse is polarized parallel to the long axis of the antennas and the probe pulse is polarized along the short antenna axis. Remarkably even though the (perpendicularly polarized) probe is not resonant with the antennas, we nevertheless observe an increase in the nonlinear signal by a factor of 100. Next we polarize the probe along the long axis of the nanoantennas (Fig. 5.3(c)). We observe a further increase of the nonlinear signal to a value as high as $\Delta\alpha = 0.055$. In addition we see that the sign of the nonlinear signal is inverted compared to the reference signals in Figs. 5.2(a) and 5.3(a). This inversion can be understood from the linear spectrum of the 2000 nm antennas in Fig. 5.1(b). As was explained above, in this case the coupling to the nanoantennas is such that the presence of the carbonyl vibration leads to a decrease of the absorption. As a consequence the depletion of the ground state of this vibration by a pump pulse leads to an increased absorption while the coupling of the antennas with the newly accessible $1 \rightarrow 2$ transition leads to a decreased absorption. We note that when the antennas are probed along their short axis we also observe an enhancement of the nonlinear signal (Fig. 5.3(b)). In this case the nonlinear signal has the regular sign: a decreased absorption at the fundamental frequency and an increased absorption at the excited-state frequency. This nonlinear signal originates from the coupling of the excited vibrations (and the depleted ground state) with the transverse resonance of the nanoantennas, which lies at much higher frequencies in the visible spectral region.[163] The normal sign follows from the fact that the vibrations drive this transverse antenna mode far below its resonance frequency, which, according to Eqn. (5.3), leads to a positive (and real-valued) amplification factor in the linear spectrum and therefore also in the nonlinear spectrum.

It should be noted that the nonlinear signal in Fig. 5.3(c) originates from only a small fraction of the CO vibrations on the substrate (i.e. those vibrations located close to the antenna surface). The nonlinear signal enhancement is, therefore, much larger than the ratio of the absorption changes in Figs. 5.3(a) and (c). The question arises of how large the enhancement actually is. The nonlinear signal is described by an equation identical to Eqn. (5.3) except for the replacement of $\alpha_{\mathrm{vib}}(\omega)$ by the pump-induced change $\Delta\alpha_{\mathrm{vib}}(\omega)$, which is proportional to the number of excited

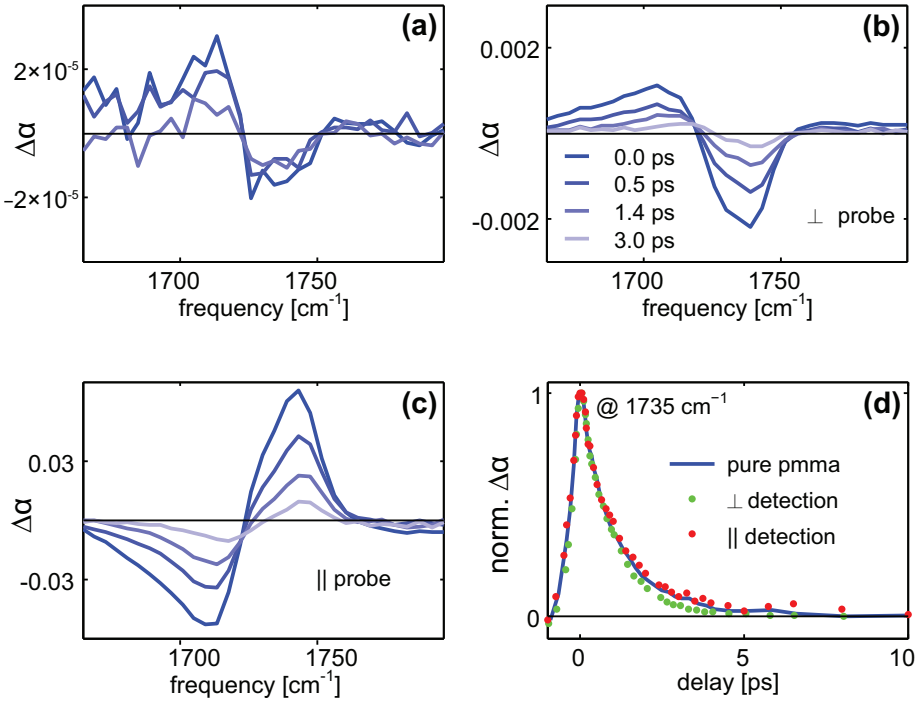

FIGURE 5.3. a) Transient spectrum of a 10 nm layer of PMMA on CaF_2 (isotropic signal). b) Transient signal for a 5 nm PMMA film deposited on top of nanoantennas. The pump polarization is along the long axis of the antenna while the probe polarization is along the short axis. c) Transient signal for the same sample as in (b) with the pump and probe polarizations set parallel to the long axis of the antennas. (d) Normalized delay traces at 1735 cm^{-1} for the reference measurement on a 150 nm layer of PMMA (blue line) and for a 5 nm layer of PMMA on a nanoantenna array ($L = 2000$ nm) with a perpendicular probe (red dots) and a parallel probe (green dots).

vibrations and therefore to the local field *intensity*. Since $\alpha_{ant}(\omega)G$ represents the field enhancement, the nonlinear signal is proportional to the fourth power of the field enhancement. Using this result in combination with finite-difference time domain simulations, we find that more than 90% of the nonlinear signal originates from CO vibrations that are within 40 nm of the antenna surface. This means that the nonlinear signal in Fig. 5.3(c) originates from 10% of the CO vibrations covering the antenna array (the nanoantennas cover 7% of the surface), from which a net enhancement factor of 6×10^4 for the nonlinear spectrum in Fig. 5.3(c) can be determined (see Section 5.6.1 for details).

Next we turn to the time dependence of the enhanced vibrational signal. An important point is whether the temporal decay of the signal tracks the excited state population of the carbonyl vibration or whether it is affected nontrivially by the coupling with the nanoantenna. To investigate this issue we compare the delay traces

of the enhanced signals (i.e. for parallel and perpendicular probing) with the delay trace of the unenhanced reference measurement (Fig. 5.3(d)). The strong resemblance of the three signals demonstrates that the enhanced signals indeed accurately reflect the intrinsic vibrational dynamics of the molecular system (and therefore provide information about the molecular system itself).

5.4 TWO-DIMENSIONAL INFRARED SPECTROSCOPY

The high signal strength and excellent signal-to-noise ratio of the antenna-enhanced pump-probe spectra (Fig. 5.3(c)) allows us to move beyond one-color pump-probe spectroscopy and explore the capabilities of antenna enhancement in 2DIR spectroscopy. We employ a pumping technique in which a Mach-Zehnder interferometer is used to generate a pair of collinear pump pulses.[78] Transient spectra are recorded as a function of the delay between the two pump pulses, and Fourier transformation of this time variable yields the pump-frequency axis in the two-dimensional spectrum (see Section 3.3 for additional details). Figure 5.4 shows examples of 2DIR spectra for two different antenna fields ($L = 1900$ nm and $L = 2200$ nm) coated with 5 nm of PMMA. The pronounced diagonal elongation in these spectra indicates that the carbonyl band of PMMA is in fact composed of an inhomogeneous distribution of CO oscillators that can be excited independently of each other: the band shows strong inhomogeneous broadening. In passing we note that a homogeneously broadened band would show a nearly vertical central line. A measure for the degree of inhomogeneous broadening is provided by the tilt of the central line, which is drawn in the 2D spectra. The two spectra in Fig. 5.4 exhibit different two-dimensional line shapes reflecting the difference in the corresponding linear line shapes. Nevertheless, the central line slope is identical for both spectra (1.2 ± 0.1) indicating that this parameter can be extracted quite robustly from the antenna-enhanced 2D spectra. In the future it will be interesting to perform these measurements as a function of the pump-probe delay, which will provide information about the time scale on which spectral fluctuations occur.

5.5 OUTLOOK

An obvious question that arises after these proof-of-principle experiments is how far we are removed from performing nonlinear vibrational spectroscopy on molecular monolayers, such as supported lipid membranes. From the density and molecular weight of PMMA we estimate that a 5 nm layer of PMMA contains ~35 CO groups/nm^2. For a lipid bilayer this number is ~6 CO groups/nm^2 as can be deduced from the typical surface area of 0.7 nm^2 per lipid molecule.[164] This comparison shows that we are already within an order of magnitude of the required sensitivity. Given that the nonlinear signal in our experiments scales with the fourth power of the field enhancement, an obvious way to increase the sensitivity would be to use nanostructures which provide higher field enhancements. Examples of structures that could provide exceptionally high field enhancements are optimally coupled arrays of nanoantennas,[163] fractal-shaped antennas[153] and perfect-absorber

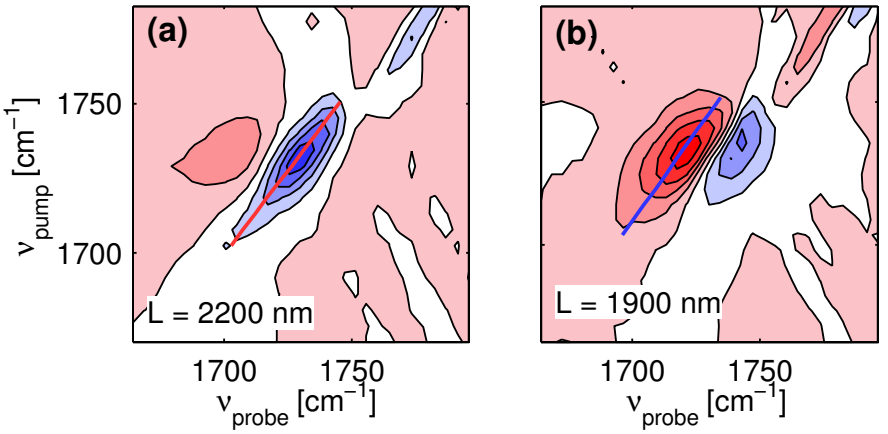

FIGURE 5.4. 2DIR spectra of 5 nm PMMA on nanoantennas of (a) 2200 nm and (b) 1900 nm. The thin solid lines represent equidistantly spaced contours. Positive absorption changes are shown in red and negative absorption changes in blue. The spectra correspond to a pump-probe delay of 0.5 ps. The thick solid lines represent the central lines and are calculated by fitting the locations of the local maxima of the 2D spectra to a straight line.

metamaterials.[165] In conclusion, we have demonstrated that metallic nanoantennas can be used to amplify nonlinear vibrational signals by more than 4 orders of magnitude. This new technique will allow the study of molecular structures and dynamics of nanoscopic volumes including molecular monolayers.

5.6 APPENDIX

5.6.1 CALCULATION OF THE ENHANCEMENT FACTOR FOR THE NONLINEAR SIGNAL

In this section we outline the procedure used to determine the amplification factor of the nonlinear spectrum in Figure 5.3(c). To compute this amplification factor we need to estimate how far the influence of a nanoantenna extends beyond its surface. This characteristic distance depends on the field enhancement profile around the nanoantenna, which was calculated using finite-difference time domain simulations (for details see Chapter 6) and is displayed in Figure 5.5(a). The figure shows the absolute value of the field enhancement in a plane 5 nm above the substrate. As was explained previously the nonlinear signal is proportional to the fourth power of the field enhancement. Using these results we can determine how close a CO vibration should be to the antenna surface in order to still make a reasonably-sized contribution to the nonlinear signal. To this end we compute the integrated nonlinear signal that would originate from a strip-like region surrounding the nanoantenna (see inset of Figure 5.5(b)). We have plotted this quantity as a function of the strip width ΔL in Figure 5.5(b). The plot shows that more than 90% of the nonlinear signal originates from CO vibrations that are within 40 nm of the antenna surface (the value of 90% is a lower limit because the contribution of the CO vibrations located on top of the nanoantenna has not been taken into account). Consequently for a single nanoantenna of 2000 nm by 200 nm the nonlinear signal originates from a patch of PMMA with a surface area that is 45% larger than the footprint of the nanoantenna. We therefore conclude that the nonlinear signal in Figure 5.3(c) originates from 10% of the CO vibrations covering the whole substrate (the nanoantennas cover 7% of the surface).

The ratio of the absorption changes in Figure 5.3(a) and (c) is 3×10^3. We take into account that the reference spectrum in Figure 5.3(a) corresponds to a 10 nm layer of PMMA while the spectrum in Figure 5.3(c) is for a 5 nm layer, and that the amplified nonlinear signal originates from 10% of the molecules on the substrate. This gives the net amplification factor of 6×10^4 quoted in the main text.

5.6.2 THICKNESS DETERMINATION OF THE PMMA LAYERS

The PMMA films used in the experiments were produced by spin coating from solution (mr-I PMMA, micro resist technology GmbH). A spinning speed of 4000 rpm was used, and the layer thickness was varied by diluting the stock solution in anisole. The layer thickness was determined through a combination of ellipsometry, profilometry and IR transmission spectroscopy. Due to the relative softness and roughness of CaF_2 profilometry could only provide accurate data for a relatively thick layer (25 nm) of PMMA on CaF_2. The thickness of the thinner layers was determined from the IR absorption of the carbonyl band. As a reference we also determined the layer thickness for other substrates (silicon and glass), using ellipsometry and profilometry. Figure 5.6 displays the full calibration series.

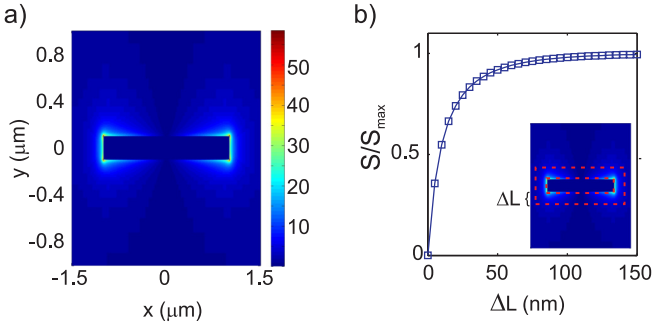

FIGURE 5.5. a) Field enhancement for a nanoantenna of 2000 nm on a CaF_2 substrate. The calculation pertains to a height of 5 nm above the substrate. b) Total nonlinear signal originating from the region between the two red dashed rectangles in the inset. This quantity was obtained by integrating the fourth power of the field enhancement over this region. The inner rectangle has the same dimensions as the nanoantenna; the outer rectangle extends beyond the nanoantenna surface by a distance ΔL. The integrated signal is normalized to its limiting value for large values of ΔL.

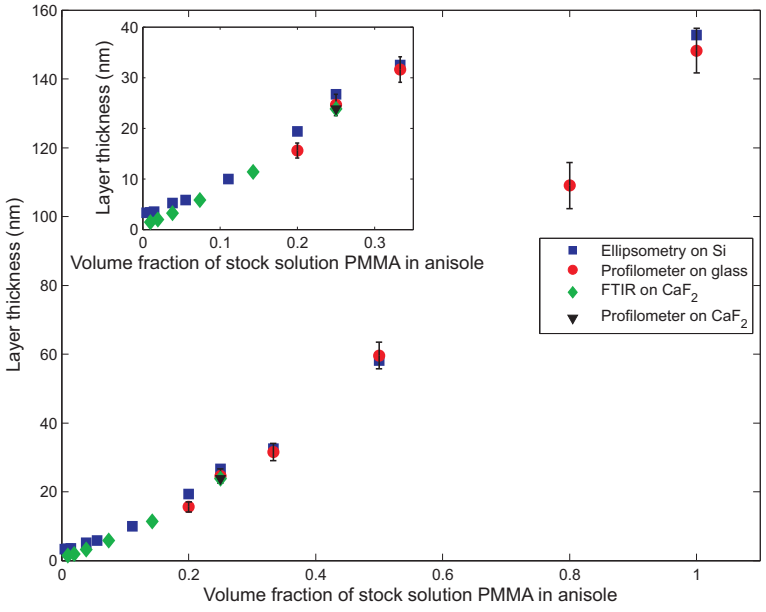

FIGURE 5.6. Thickness of the PMMA layers determined using different methods.

Chapter 6

Impact of Local-Field Effects on the Plasmonic Enhancement of Vibrational Signals by Infrared Nanoantennas[a]

We have developed an analytical model that provides a mechanistic description of the plasmonic enhancement of vibrational signals by infrared nanoantennas. Our treatment is based on a coupled-point-dipole model which considers the interaction between a point-like nanoantenna and a single vibrational dipole moment. This idealized model is refined in two consecutive steps. The first step generalizes the model to make the treatment of non-point-like nanoantennas possible. The second step deals with local-field effects originating from the mutual interaction of the molecular vibrations. We have compared the results of our model with finite-difference time-domain simulations, and we find that our model predicts both the lineshapes and the amplitudes of the vibrational signals in a quantitative manner. Our analysis shows that the local-field effects play a surprisingly dominant role in the plasmonic enhancement, and we discuss possibilities of engineering this local field in order to further boost the plasmonic amplification.

[a]Adapted from: Y. L. A. Rezus and O. Selig, "Impact of local-field effects on the plasmonic enhancement of vibrational signals by infrared nanoantennas", OPTICS EXPRESS, **24**, 12202 (2016)

6.1 INTRODUCTION

Infrared spectroscopy is a well-known analytical tool that is widely used to identify molecular species. The technique owes its chemical specificity to the fact molecules leave their 'vibrational fingerprint' in the infrared spectrum. That is, the chemical groups inside molecules possess characteristic vibrational frequencies which give rise to sharp infrared absorption bands. Unfortunately, despite its exquisite chemical specificity, infrared spectroscopy is a relatively insensitive technique requiring large quantities of material. This poor sensitivity is a consequence of the weak absorption cross sections of molecular vibrations, which are typically a thousand times smaller compared to the cross sections of electronic transitions. The sensitivity problem of infrared spectroscopy is partly overcome in a variant of the method known as surface-enhanced infrared absorption (SEIRA) spectroscopy.[166–171] In this technique chemically roughened metal films are employed onto which the molecules of interest are adsorbed. The excitation of plasmonic modes inside the metal film leads to strong near fields which couple to the molecular vibrations and enhance the spectroscopic signals. However, in conventional SEIRA spectroscopy the spectral overlap between the broad plasmonic modes and the sharp molecular vibrations is far from optimal, so that in practice the signal enhancement remains modest.

In recent years the SEIRA technique has undergone a revival with the substitution of the metal films for tailored (metallic or non-metallic) nanostructures,[37, 151–154, 172–177] fabricated using lithographic means. These nanostructures, which we will generically refer to as infrared nanoantennas, exhibit a resonance in the mid-infrared that can be tuned to a molecular vibration of interest. The resonant character of the plasmonic excitation in these structures leads to much larger field enhancements compared to metallic films and thereby to comparatively larger signal enhancements. To date a variety of IR nanoantennas have been explored for the ultrasensitive detection of molecules, among which figure coupled arrays of nanoantennas,[151] various nanoclusters, fractal-shaped antennas[153, 178] and perfect absorber structures.[165] Very recently we have shown that it is possible to use the intense near fields of infrared nanoantennas to move beyond the conventional linear spectroscopic detection of molecules and to even perform advanced nonlinear spectroscopic experiments on the detected molecules.[179] In the future this extension of the SEIRA technique will allow one to study dynamic processes, such as chemical reactions or energy transfer processes within or between the detected molecules.

An important aspect of infrared nanoantennas is the fact that the amplified vibrational signals do not necessarily give rise to the familiar absorptive lineshapes known from conventional infrared spectroscopy. Instead the nanoantenna-enhanced vibrational resonances often have a dispersive character, so that they appear distorted. These lineshape distortions are not a serious problem if one simply considers nanoantenna-SEIRA as an ultrasensitive *detection* technique. However, from the *spectroscopic* perspective these distortions are more problematic. In molecular spectroscopy one typically relies on the widths, amplitudes, spectral shifts and detailed shapes of the vibrational bands to deduce information about molecular structures and dynamics. Therefore for spectroscopic applications—both linear and nonlinear—it is important to understand how the metal nanostructures affect the

vibrational lineshape, so that one can distinguish between lineshape features that contain molecular information and lineshape features that are merely a consequence of the amplification process. In the literature finite element electromagnetic simulations are commonly used to predict the vibrational lineshapes observed in nanoantenna-SEIRA.[152] While these methods can accurately predict the lineshapes observed, they do not provide intuitive understanding of the underlying physical mechanisms. In this work we aim to develop such intuitive understanding by constructing an analytic model of the coupling between molecular vibrations and infrared nanoantennas. This model will provide insight into the factors that govern the degree of signal enhancement, as well as how these factors affect the observed lineshapes.

Our approach consists of three steps. We start out with a highly idealized model in which we consider only two point dipoles. The first point dipole represents the nanoantenna while the second point dipole represents all the molecular vibrations interacting with the nanoantenna. This model can be solved analytically, and we show that despite its simplicity the model already describes many features of the amplification process in a qualitative manner. In the second step we refine the model in such a way that it becomes applicable to realistic nanoantenna geometries (as opposed to a point-like nanoantenna). The refined model allows the quantitative computation of the response of a nanoantenna covered by a thin layer of dielectric material, as long as this material is described by either a purely resonant or by a purely non-resonant permittivity. It turns out that the model, at this stage, breaks down for materials that have both a resonant and a non-resonant permittivity. In the third step we show that this breakdown is due to the neglect of local-field effects, and we finish by incorporating these effects into the model. The resulting model allows one to accurately compute the plasmonic enhancement factor for a particular vibrational band, and, moreover, it identifies the different physical contributions to this enhancement factor. A major result of the present work is the finding that for most molecular vibrations the local molecular field, which was mostly overlooked in the past, plays a surprisingly large role in the plasmonic enhancement mechanism.

6.2 RESULTS AND DISCUSSION

Figure 6.1 illustrates the principles underlying the use of infrared nanoantennas. Typically, an array of such nanoantennas is fabricated on top of an infrared-transparent substrate, such as CaF_2, and the material to be detected is deposited as a thin layer on top of the nanoantennas (Fig. 6.1(a)). In this work we focus on rod-like nanoantennas because their resonance frequency can easily be tuned to the mid-infrared. We have computed the (extinction) cross-section spectra of three isolated gold nanoantennas of different length using finite-difference time-domain (FDTD) simulations (Fig. 6.1(b)). For light polarized along the long antenna axis the nanoantennas display a plasmon resonance in the mid-infrared, which shifts to lower frequencies with increasing nanoantenna length.[52,152] The nanoantenna spectrum is extremely sensitive to the material in its direct environment, which makes the nanoantennas ideal for sensing applications. This point is illustrated in Fig. 6.2(a),

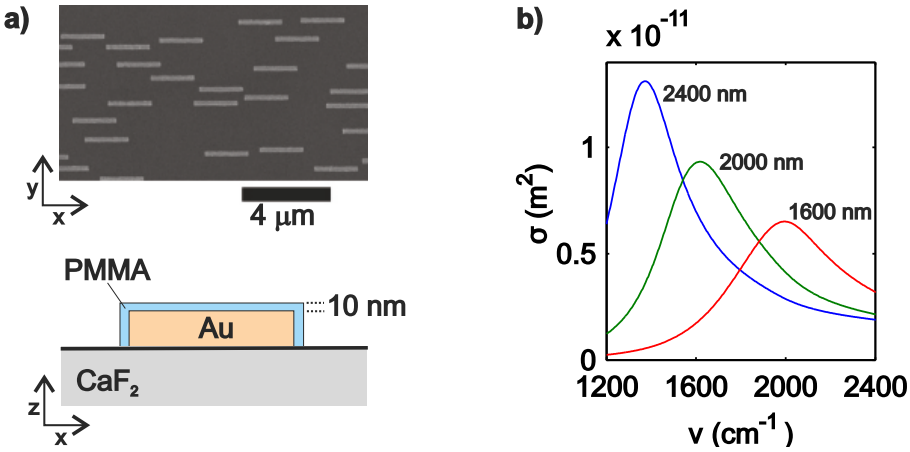

FIGURE 6.1. (a, top) Scanning electron microscope image of an array of gold nanoantennas fabricated on top of a CaF_2 substrate. (a, bottom) Geometry used in the FDTD simulations to calculate the cross section of an isolated nanoantenna and its modification due to the presence of a shell of dielectric material. (b) Simulated extinction cross sections of gold nanoantennas on top of CaF_2. The nanoantennas have a width of 200 nm, a height of 100 nm and a varying length (1600 nm, 2000 nm and 2400 nm).

which shows that covering the nanoantenna by a 10 nm layer of dielectric material with a refractive index of 1.48 leads to a significant redshift of the spectrum. Next we consider the effect of covering the nanoantenna by a material that exhibits a vibrational resonance. As a prototypical example of such a material we have chosen the molecular polymer polymethylmetacrylate (PMMA) because it is often used in experimental studies due to its ease of spincoating.[174,180] PMMA displays a sharp vibrational resonance at 1730 cm^{-1} which results from its C=O stretching vibration. It can be seen that the spectrum of the C=O vibration shows up as an absorptive dip on top of the nanoantenna spectrum (Fig. 6.2(b)). In order to highlight the amplified vibrational spectrum we subtract the bare nanoantenna spectrum from the spectrum of the coated nanoantenna as is illustrated in Fig. 6.2(c). This figure also shows the amplified vibrational spectrum for nanoantennas of different lengths. It can be seen that, depending on the detuning between the nanoantenna and the vibrational resonance, a variety of lineshapes can be observed, from absorptive to dispersive as well as any shape in between. In the following we develop an analytical model, along the lines described in the introduction, that can quantitatively explain the spectral effects illustrated in Fig. 6.2.

6.2.1 STEP 1: POINT-DIPOLE MODEL

We start by describing the interaction between a nanoantenna and the molecules that cover it using a simple coupled-dipole model. In this model we only consider two

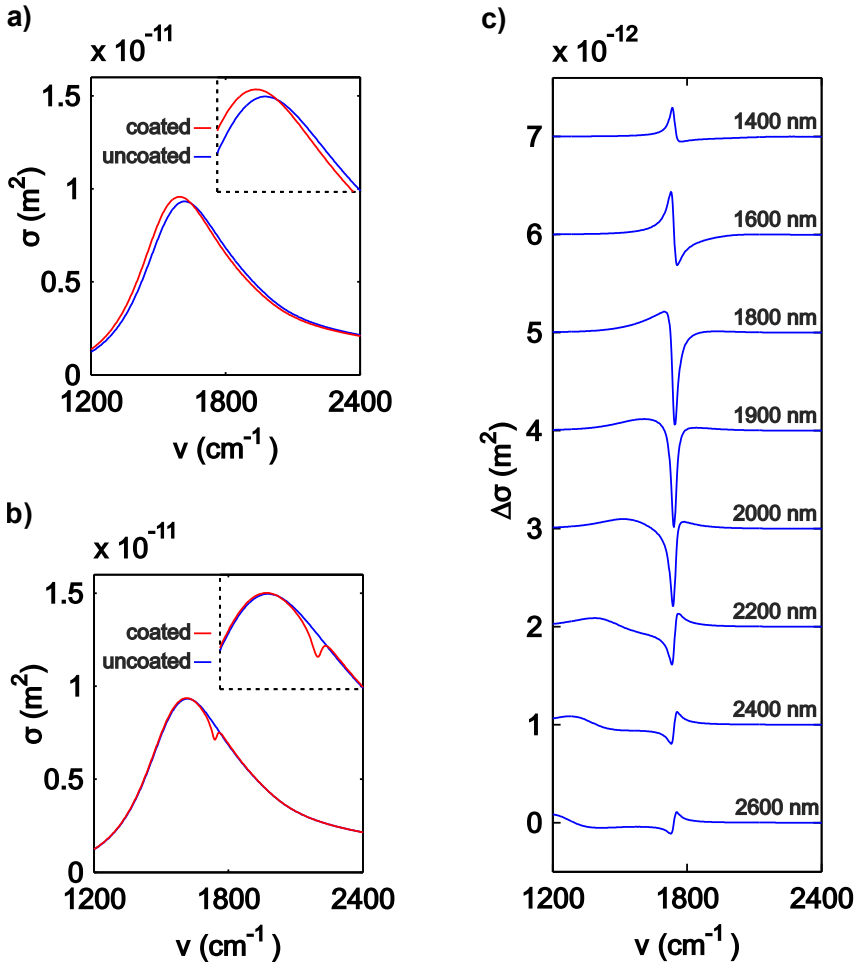

FIGURE 6.2. (a) Cross-section spectrum of a 2000 nm nanoantenna (blue line) and of the same nanoantenna coated with a 10 nm layer of dielectric material characterized by a refractive index of 1.48 (red line). The inset shows a zoom around the cross section maximum. (b) Cross-section spectrum of a 2000 nm nanoantenna (blue line) and of the same nanoantenna coated with a 10 nm layer of PMMA. The PMMA is modeled using a Lorentzian absorption at 1730 cm^{-1} and a background refractive index of 1. (c) Effect of the nanoantenna length on the amplified vibrational lineshape. The curves are calculated by subtracting the spectrum of a bare nanoantenna from the spectrum of a coated nanoantenna. For clarity the different curves are shifted vertically by 10^{-12} m^2.

point dipoles: the first point dipole (p_{ant}) represents the nanonantenna while the second point dipole (p_{vib}) represents all molecular vibrations lumped together. The nanoantenna is characterized by the frequency-dependent polarizability $\alpha_{\text{ant}}(\omega)$ and the vibrational dipole moment by the frequency-dependent polarizability $\alpha_{\text{vib}}(\omega)$. To avoid clutter we will drop the explicit frequency dependence henceforward. For the moment we treat the case of free-space coupling between the two point dipoles, and we will discuss the effect of the substrate at the end of this section.

Our experimental observable is the extinction cross section σ_{ant} of the nanoantenna and its modification $\Delta\sigma$ due to the presence of the vibrational dipole. In general the extinction cross section σ of a dipolar particle is related to the imaginary part of its polarizability[181]

$$\sigma = \frac{2\pi}{\lambda\varepsilon_0}\text{Im}[\alpha] \tag{6.1}$$

Here ε_0 is the permittivity of free space, and λ is the free-space wavelength. For the treatment to come it is useful to briefly recall the origin of this expression, which can be done by considering the definition of the extinction cross section

$$\sigma = \frac{P_{\text{inc}}}{I_{\text{inc}}} \tag{6.2}$$

where P_{inc} is the work (per unit time) done on the particle by the incident field and I_{inc} is the incident intensity. By substituting the standard expressions $I_{\text{inc}} = \frac{1}{2}\varepsilon_0 c|E_0|^2$ and

$$P_{\text{inc}} = \frac{1}{2}\omega\text{Im}[pE_0^*], \tag{6.3}$$

with p the complex amplitude of the induced dipole moment of the particle and E_0 the complex amplitude of the incoming electric field (we have assumed that all fields vary as $\sim \exp[-i\omega t]$) one directly obtains Eq. (6.1).

Let us now consider the coupling of p_{ant} and p_{vib}. Both dipoles experience two fields: the incident field and the field originating from the other particle. This leads to the coupled-dipole equations[182,183]

$$p_{\text{ant}} = \alpha_{\text{ant}}E_0 + \alpha_{\text{ant}}G(r_{\text{ant}}, r_{\text{vib}})p_{\text{vib}} \tag{6.4}$$

$$p_{\text{vib}} = \alpha_{\text{vib}}E_0 + \alpha_{\text{vib}}G(r_{\text{vib}}, r_{\text{ant}})p_{\text{ant}} \tag{6.5}$$

Here $G(r_1, r_2)$ is the Green's function for a dipole located at r_2. We should point out that for simplicity we have adopted a scalar description. By solving for the dipole moments we see that the effect of the coupling is to modify the polarizabilities of the two dipoles into new, effective polarizabilities

$$p_{\text{ant}} = \alpha_{\text{eff,ant}}E_0 = \frac{\alpha_{\text{ant}} + \alpha_{\text{ant}}\alpha_{\text{vib}}G}{1 - \alpha_{\text{ant}}\alpha_{\text{vib}}G^2}E_0 \tag{6.6}$$

$$p_{\text{vib}} = \alpha_{\text{eff,vib}}E_0 = \frac{\alpha_{\text{vib}} + \alpha_{\text{ant}}\alpha_{\text{vib}}G}{1 - \alpha_{\text{ant}}\alpha_{\text{vib}}G^2}E_0 \tag{6.7}$$

Here we have used the reciprocity theorem to equate the two Green's functions and simply denoted them as G.[184] In our experiments we typically measure the

absorption difference of the coated and the uncoated nanoantennas, so that we have the following experimental observable

$$\Delta\sigma = \frac{2\pi}{\lambda\varepsilon_0}\mathrm{Im}\left[\alpha_{\mathrm{eff,ant}} + \alpha_{\mathrm{eff,vib}} - \alpha_{\mathrm{ant}}\right] \tag{6.8}$$

While Eq. (6.8) provides an exact analytical expression for the cross-section change of the nanoantenna, it turns out to be useful to expand the solution in a geometric series

$$\Delta\sigma = \frac{2\pi}{\lambda\varepsilon_0}\mathrm{Im}\left\{\sum_{n=1}^{\infty}\alpha_{\mathrm{ant}}^{n+1}\alpha_{\mathrm{vib}}^{n}G^{2n} + \sum_{n=0}^{\infty}\alpha_{\mathrm{ant}}^{n}\alpha_{\mathrm{vib}}^{n+1}G^{2n} + 2\sum_{n=0}^{\infty}\alpha_{\mathrm{ant}}^{n+1}\alpha_{\mathrm{vib}}^{n+1}G^{2n+1}\right\} \tag{6.9}$$

The expansion above allows one to view the amplification mechanism as a multiple-scattering problem, which is a useful approach that has, for example, also been followed to describe the signals in near-field scanning optical microscopy.[185] The terms in the expansion can be interpreted as different interaction processes between the two point dipoles. We will represent these interaction processes symbolically using scattering diagrams as those illustrated in Fig. 6.3. In the following we will briefly illustrate how to read these diagrams. The diagram in Fig. 6.3(a) represents the leading term in the expansion ($n = 1$ term in the first summation symbol). In this diagram the incident arrow (1) represents the incident field E_0 which polarizes the antenna. As a result the antenna generates an enhanced near field which polarizes the vibrational dipole (2). In turn, the vibrational dipole acts back and generates a field at the location of the antenna, which modifies the antenna polarization (3). Finally we compute the work done by the incident field on this part of the antenna polarization (4). This last process is represented by the wiggly arrow. Below the diagram we have written the contribution to the cross-section change due to this interaction process. Inspection of Fig. 6.3 makes it clear that there are three types of scattering diagrams, each type corresponding to one of the three summation symbols in Eq. (6.9). The first summation symbol groups together the diagrams that start and end on the nanoantenna, an example of which is the diagram that we just discussed (Fig. 6.3(a)). The second summation symbol corresponds to diagrams that start and end on the vibrational dipole (see, for example, Fig. 6.3(b)). Finally the third summation symbol contains diagrams that start on one dipole and end on the other dipole. The diagram in Fig. 6.3(c) is an example of this third type of scattering diagram. Here the incident field polarizes the vibrational dipole (1). Next the vibrational dipole polarizes the nanoantenna (2). Finally we compute the work done on the nanoantenna (3). We note that the factor of 2 in front of the third summation symbol (Eq. (6.9)) comes from the fact that this summation symbol groups together two types of diagrams (i.e. diagrams starting on the nanoantenna and ending on the vibration and vice versa), which contribute equally to the total cross-section change.

Replacing Eq. (6.9) by the leading term in its expansion we obtain the following approximation for the cross-section change

$$\Delta\sigma = \frac{2\pi}{\lambda\varepsilon_0}\mathrm{Im}\left[(\alpha_{\mathrm{ant}}G)^2\alpha_{\mathrm{vib}}\right] \tag{6.10}$$

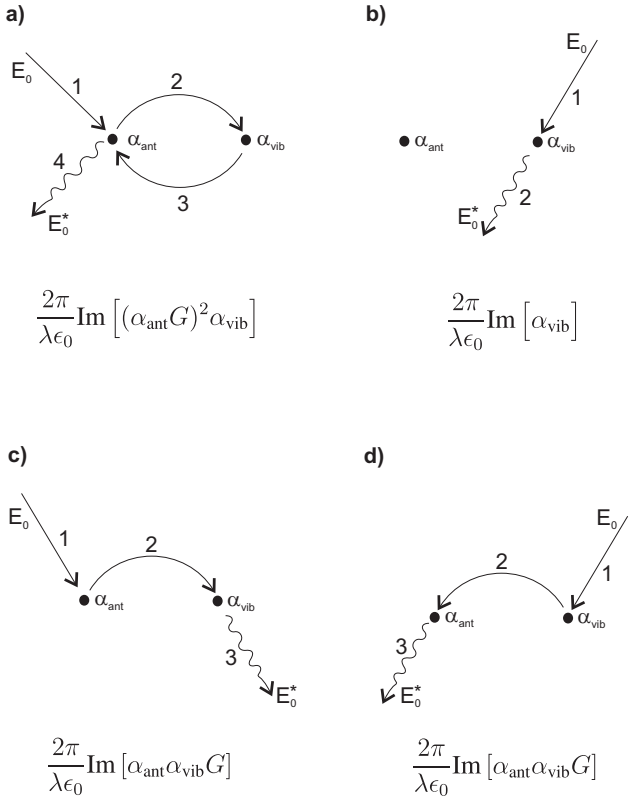

FIGURE 6.3. Scattering diagrams representing the different terms in the expansion from Eq. (6.9). (a) Diagram representing the leading term in the expansion ($n = 1$ in the first summation symbol). (b) Diagram representing the leading term ($n = 0$) of the second summation symbol. This interaction process represents the direct interaction of the light with the vibrational dipole. (c,d) Scattering diagrams that are grouped together under the third summation symbol of Eq. (6.9).

Interestingly, although Eq. (6.10) is based on a highly idealized model, this expression can already qualitatively explain many of the features observed in Fig. 6.2. Equation (6.10) shows that the nanoantenna amplifies the original vibrational spectrum by the complex-valued factor $(\alpha_{\mathrm{ant}}G)^2$, which represents the square of the field enhancement. Due to the complex nature of the amplification factor the (enhanced) vibrational signal $\Delta\sigma$ typically contains both an absorptive ($\mathrm{Im}[\alpha_{\mathrm{vib}}]$) and a dispersive component ($\mathrm{Re}[\alpha_{\mathrm{vib}}]$). It is straightforward to see that there are three circumstances under which purely absorptive lineshapes are observed: if the antenna is driven on resonance, far below resonance or far above resonance. In the first case there is a $\pi/2$ phase lag between the incident electric field and the antenna polarization: this leads to a negative value of the amplification factor $(\alpha_{\mathrm{ant}}G)^2$, so that the vibrational signal is observed as an absorption *dip* on top of the

antenna resonance. Driving the antenna far below resonance or far above resonance results in phase shifts of 0 and π, respectively, so that in these two circumstances absorptive *peaks* are observed. It is useful to point out that it is the backaction of the vibrational dipole on the nanoantenna which is responsible for the amplification of the vibrational spectrum (as also becomes apparent from the scattering diagram in Fig. 6.3(a)). Intuitively one might have expected the amplification to be a consequence of the (far-field) radiation emitted by the vibrational dipole after its excitation by the strong near field of the nanoantenna. This process does in fact contribute to the amplification process (it corresponds to the scattering diagram depicted in Fig. 6.3(c)). Its contribution is, however, relatively small because its amplitude scales only linearly with the field enhancement $\alpha_{\text{ant}}G$, which should be compared to the quadratic scaling of the backaction process (Fig. 6.3(a)). Moreover, it is interesting to note that the scattering diagram in Fig. 6.3(c) leads to dispersive lineshapes for a vibration that is in perfect resonance with a nanoantenna, in contrast to the inverted absorptive shapes which are observed in experiments and simulations.[179,186]

Before continuing, it is useful to roughly estimate the accuracy of the approximation at the origin of Eq. (6.10). We readily see that compared to the leading scattering diagram (Fig. 6.3(a)) the contributions of the scattering diagrams in Fig. 6.3(b) and Figs. 6.3(c)-(d) are smaller by a factor of $(\alpha_{\text{ant}}G)^2$ and $(\alpha_{\text{ant}}G)$, respectively. Using the fact that $\alpha_{\text{ant}}G$ represents the field enhancement of the antenna at the location of the vibrational dipole, we can get a numerical estimate of these factors from FDTD simulations of bare nanoantennas (Fig. 6.1(b)). It turns out that the average nanoantenna field enhancement experienced by the shell of PMMA is approximately 10. From this value we conclude that, compared to the leading scattering diagram, the contribution of the diagram in Fig. 6.3(b) is smaller by two orders of magnitude while those in Fig. 6.3(c)-(d) are smaller by one order of magnitude. Next we consider the scaling behavior of the consecutive scattering diagrams grouped together under the first summation symbol in Eq. (6.9). These scale by the factor $\alpha_{\text{ant}}\alpha_{\text{vib}}G^2$. In order to estimate this factor we again turn to the FDTD simulations. The cross section of a nanoantenna is approximately 10^{-11} m^2. On the other hand from the known transmission (98.9 %) of a 10 nm film of PMMA we estimate the cross section of the PMMA shell to be 10^{-14} m^2. From the ratio of these cross sections combined with the nanoantenna field enhancement ($\alpha_{\text{ant}}G \sim 10$) we find that $\alpha_{\text{ant}}\alpha_{\text{vib}}G^2 \sim 10^{-1}$. We conclude that the largest correction terms to the cross-section change (Eq. (6.10)) are approximately one order of magnitude smaller than the leading term.

We conclude this section by discussing the effect of the substrate. In principle, all expressions can remain unmodified if (whenever a substrate is present) we simply consider α_{ant} and G as functions that are renormalized to contain the effect of the interface in them. There is, however, a subtlety which has to do with the Fresnel reflection of the interface and the fact that the cross sections are defined with respect to the *incident* electric field (as opposed to the local electric field). Due to the reflection, the electric field experienced by our point dipoles is attenuated relative to the incident field by the factor $(1-r)$ where $r = (n_s-1)/(n_s+1)$ is the Fresnel reflection coefficient and n_s the refractive index of the substrate. Because the incident intensity, however, is still given by $I_{\text{inc}} = 1/2c\varepsilon_0|E_0|^2$, this results in the scaling of all expressions by the

factor $(1-r)^2$. The expression for the cross-section change of a nanoantenna on a surface becomes

$$\Delta\sigma = \frac{2\pi S_{\text{sub}}}{\lambda\varepsilon_0}\text{Im}\left[(\alpha_{\text{ant}}G)^2\alpha_{\text{vib}}\right] \tag{6.11}$$

where we defined the substrate scaling factor

$$S_{\text{sub}} = \frac{4}{(1+n_s)^2} \tag{6.12}$$

It can be seen that due to the interference between the incoming and the reflected field at the dielectric interface the refractive index of the substrate has quite an influence on the degree of vibrational amplification. For instance, even if we design two nanoantennas to have the same field enhancement ($\alpha_{\text{ant}}G$) on silicon ($n = 3.42$) and on calcium fluoride ($n = 1.42$), the amplification factor will still be 70% smaller in the case of silicon compared to calcium fluoride.

6.2.2 STEP 2: FINITE ANTENNA SIZE

Equation (6.11) has given us an intuitive picture of the mechanism underlying the vibrational amplification process. Unfortunately, one cannot use this expression to quantitatively evaluate the amplified vibrational spectrum in the case of a realistic nanoantenna (i.e. a nanoantenna that cannot be described as a point dipole). The main issue lies in the backaction process (step 3 in Fig. 6.3(a)). Here we had implicitly assumed that the dipole moment induced in the nanoantenna by the vibrational dipole is $\Delta p_{\text{ant}} = \alpha_{\text{ant}}G(r_{\text{ant}}, r_{\text{vib}})p_{\text{vib}}$. However, this expression obviously breaks down for a finite-sized nanoantenna because it is not clear at what location r_{ant} the Green's function should be evaluated. The aim of this section is to rewrite Eq. (6.11) in such a way that it provides a quantitative description of the interaction of a finite-sized nanoantenna with a collection of point-like vibrational dipoles.

Before we start, let us generalize Eq. (6.11) to take into account the tensorial nature of α_{ant} and G. For the moment we still assume point dipoles. We assume that the polarizability tensor of the nanoantenna is diagonal in the coordinate system of Fig. 6.1(a) (with diagonal elements $\alpha_{\text{ant,x}}$, $\alpha_{\text{ant,y}}$ and $\alpha_{\text{ant,z}}$). For the vibrational dipole we assume an isotropic polarizability α_{vib} to account for the isotropic distribution of the transition dipole moments of the vibrations. It is straightforward to show that, for an incident field $E_x^{(0)}$ polarized along the long antenna axis, Eq. (6.11) generalizes to the following expression.

$$\Delta\sigma = \frac{2\pi S_{\text{sub}}}{\lambda\varepsilon_0}\text{Im}\left[\alpha_{\text{ant,x}}^2(G_{xx}^2 + G_{yx}^2 + G_{zx}^2)\alpha_{\text{vib}}\right] \tag{6.13}$$

In writing Eq. (6.13) we used the general form of the reciprocity relation[184]

$$G_{\alpha\beta}(r_1, r_2) = G_{\beta\alpha}(r_2, r_1) \tag{6.14}$$

As a next step we rewrite Eq. (6.13) in a way which does not make reference to the Green's function. To this end, it is useful to recall that the scattering diagram in

Fig. 6.3(a) describes two processes. Firstly, the enhancement of the incident field E_0 by the nanoantenna, and secondly the amplification of the vibrational dipole moment p_{vib} by the nanoantenna. In order to describe these two amplification processes we introduce two tensorial quantities: the field-enhancement tensor $f_{\alpha\beta}$ and the dipole-amplification tensor $f'_{\alpha\beta}$. We define the field-enhancement tensor as

$$f_{\alpha\beta} = \frac{E_\alpha(r_{\text{vib}})}{E^{(0)}_\beta(r_{\text{vib}})} \tag{6.15}$$

where $E^{(0)}_\beta(r_{\text{vib}})$ is the field at the location of the vibrational dipole in the absence of the nanoantenna, and $E_\alpha(r_{\text{vib}})$ is the same field in the presence of the nanoantenna. This definition assumes that the incident field points in the direction of one of the cartesian axes. We further remark that the field-enhancement tensor depends on the type of illumination used, which we consider here to be plane-wave illumination at normal incidence. In terms of the field-enhancement tensor we can express the induced vibrational dipole moment $\Delta\vec{p}_{\text{vib}}$ (i.e. steps 1 and 2 in Fig. 6.3(a)) as

$$\Delta\vec{p}_{\text{vib}} = \alpha_{\text{vib}} \begin{pmatrix} f_{xx} - 1 \\ f_{yx} \\ f_{zx} \end{pmatrix} E^{(0)}_x(r_{\text{vib}}) \tag{6.16}$$

Here we point out that the different form of $\Delta p_{\text{vib,x}}$ is due to the fact that the scattering diagram in Fig. 6.3(a) does not include the direct polarization of the vibrational dipole by the incident field. Next we introduce the dipole amplification tensor $f'_{\alpha\beta}$, which describes the factor by which a vibrational dipole (that is aligned with one of the cartesian axes) is amplified by the nanoantenna.

$$f'_{\alpha\beta} = \frac{p_{\text{tot},\alpha}}{p_{\text{vib},\beta}} \tag{6.17}$$

Here we have defined $f'_{\alpha\beta}$ in such a way that it corresponds to the factor by which the dipole moment $p_{\text{tot},\alpha}$ of the whole assembly (i.e. vibrational dipole plus nanoantenna) is amplified compared to the situation in which there is only a vibrational dipole. For our analysis we will only need the following three elements

$$f'_{xx} = \frac{\Delta p_{\text{ant,x}}}{p_{\text{vib,x}}} + 1, \qquad f'_{xy} = \frac{\Delta p_{\text{ant,x}}}{p_{\text{vib,y}}}, \qquad f'_{xz} = \frac{\Delta p_{\text{ant,x}}}{p_{\text{vib,z}}} \tag{6.18}$$

where $\Delta p_{\text{ant,x}}$ is the induced dipole moment in the nanoantenna. In terms of the tensors $f_{\alpha\beta}$ and $f'_{\alpha\beta}$ Eq. (6.13) reads as follows

$$\Delta\sigma = \frac{2\pi S_{\text{sub}}}{\lambda\varepsilon_0} \text{Im}\Big[\big((f_{xx}-1)(f'_{xx}-1) + f_{yx}f'_{xy} + f_{zx}f'_{xz}\big)\alpha_{\text{vib}}\Big] \tag{6.19}$$

The obvious question arises whether it is possible to relate the dipole amplification tensor $f'_{\alpha\beta}$ to the field enhancement tensor $f_{\alpha\beta}$ (given that the field enhancement can easily be obtained from FDTD simulations). In the next section we will show that this is indeed possible using electromagnetic reciprocity.[184, 187]

RELATIONSHIP BETWEEN THE FIELD ENHANCEMENT AND THE DIPOLE AMPLIFICATION In this section we aim to express the dipole amplification tensor elements $f'_{x\beta}$ in terms of the field enhancement tensor elements $f_{\beta x}$. We will compute the elements f'_{xx}, f'_{xy} and f'_{xz} by explicitly considering the source generating the plane wave that excites the nanoantenna. This source will be a point dipole located far away from the nanoantenna (so that the nanoantenna is effectively excited by a plane wave at normal incidence). This procedure will allow us to write the tensor elements $f_{\alpha\beta}$ and $f'_{\alpha\beta}$ as a ratio of Green's functions. It turns out that this calculation needs to be performed separately for the three elements f'_{xx}, f'_{xy} and f'_{xz}. The simplest situation occurs for the element f'_{xx}, which we will treat below. The elements f'_{xy} and f'_{xz} require a slightly more complex treatment. Because the final result is the same, we leave this treatment for the appendix. The appendix also considers the effect of the substrate, which we ignore for the moment.

Our derivation is based on the characteristics of the far-field radiation pattern of a radiating dipole (dipole amplitude p). In particular we use the fact that the far-field radiation is transverse

$$\vec{E}(\vec{r}) \propto -\sin\theta\, p\, \hat{\theta} \tag{6.20}$$

where θ is the angle between $\vec{r}$ and $\vec{p}$ and $\hat{\theta}$ is the corresponding unit vector.[188] This means that the dipole amplitude can be obtained from the electric field if one assumes that the viewing direction is known

$$p \propto E/\sin\theta \tag{6.21}$$

We begin by considering Fig. 6.4(a). Here a nanoantenna is illuminated by a test dipole oscillating parallel to the x axis. We will denote this dipole $p_{\text{test,x}}$. Because the test dipole is located far away from the nanoantenna (at position r_{far}), this situation is equivalent to illuminating the nanoantenna with an x-polarized plane wave. We consider the induced field at the location r_{vib} close to the nanoantenna (this is the location where the vibrational dipole will be placed later on). This field will generally contain an x, y and z component. However, we only focus on the x component for now. In terms of the Green's function of this system we can write for this electric field

$$E_x(r_{\text{vib}}) = G_{xx}(r_{\text{vib}}, r_{\text{far}})\, p_{\text{test,x}} \tag{6.22}$$

The situation in the absence of the nanoantenna can be described with a similar diagram, which is displayed in Fig. 6.4(b). This system is described by the Green's function $G^{(0)}$ and in terms of this Green's function we can write

$$E_x^{(0)}(r_{\text{vib}}) = G_{xx}^{(0)}(r_{\text{vib}}, r_{\text{far}})\, p_{\text{test,x}} \tag{6.23}$$

This shows that we can write for the field enhancement tensor element f_{xx}

$$f_{xx} = \frac{G_{xx}(r_{\text{vib}}, r_{\text{far}})}{G_{xx}^{(0)}(r_{\text{vib}}, r_{\text{far}})} \tag{6.24}$$

Next we focus on the dipole amplification factor f'_{xx}, for which we turn to Fig. 6.4(c) where we have placed the test dipole at the location r_{vib}. This dipole induces a

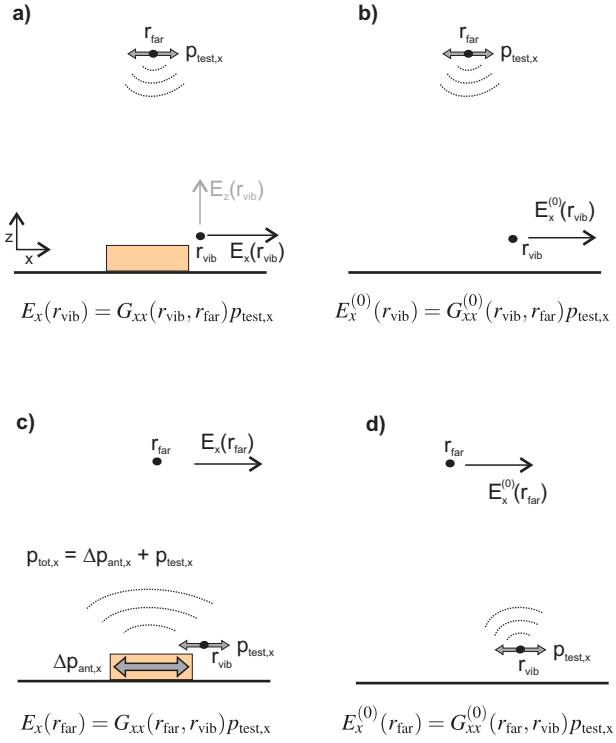

FIGURE 6.4. Diagrams for computing the elements f_{xx} and f'_{xx}. In (a) and (b) a radiating test dipole is located at position r_{far} and the radiation pattern experienced by the nanoantenna resembles an x-polarized plane wave. In (c) and (d) the radiating test dipole is placed in the near field of the nanoantenna at position r_{vib}, so that it emulates a radiating vibrational dipole. Thin black arrows indicate electric fields while thick gray arrows indicate oscillating dipoles.

dipole moment $\Delta\vec{p}_{\text{ant}}$ in the antenna (see Fig. 6.4(d)), and we are interested in its x component. Referring to Fig. 6.4(c)-(d) we write for the dipole amplification factor

$$f'_{xx} = \frac{p_{\text{tot,x}}}{p_{\text{test,x}}} \tag{6.25}$$

The aim is to obtain $p_{\text{tot,x}}$ from the far-field radiation pattern. The radiation pattern in Fig. 6.4(c) is the superposition of the radiation emitted by the nanoantenna ($\Delta p_{\text{ant,x}}$) and that of the test dipole $p_{\text{test,x}}$. However, for an observer located in the far-field this radiation pattern is equivalent to the radiation that would be emitted by a point-dipole with amplitude $p_{\text{tot,x}}$. As a consequence we can write

$$p_{\text{tot,x}} \propto E_x(r_{\text{far}}) \tag{6.26}$$

In similar manner we can obtain the amplitude of the test dipole in the absence of the

nanoantenna (see Fig. 6.4) from the far-field

$$p_{\text{test,x}} \propto E_x^{(0)}(r_{\text{far}}) \tag{6.27}$$

In both cases we have assumed that the observation point is located directly above the dipole (i.e. $\theta = 0$). It is also important to realize that $p_{\text{tot,y}}$ and $p_{\text{tot,z}}$ do not necessarily vanish. However, they do not contribute to $E_{\text{far,x}}$ because of the vectorial properties of the far-field dipole radiation. Again we rewrite these electric fields in terms of the Green's functions, which gives.

$$f'_{xx} = \frac{p_{\text{tot,x}}}{p_{\text{test,x}}} = \frac{E_x(r_{\text{far}})}{E_x^{(0)}(r_{\text{far}})} = \frac{G_{xx}(r_{\text{far}}, r_{\text{vib}})}{G_{xx}^{(0)}(r_{\text{far}}, r_{\text{vib}})} \tag{6.28}$$

Using the reciprocity relation we arrive at

$$f'_{xx} = f_{xx} \tag{6.29}$$

As is outlined in the appendix, it turns out that this equality remains valid in the presence of a substrate, and that similar equalities hold for the tensor elements f'_{yx} and f'_{zx}.

EXPRESSION FOR THE CROSS-SECTION CHANGE Incorporating the results of the previous section we arrive at the following expression for the cross-section change of the nanoantenna

$$\Delta\sigma = \frac{2\pi S_{\text{sub}}}{\lambda\varepsilon_0}\text{Im}\left[\left((f_{xx}-1)^2 + f_{yx}^2 + f_{zx}^2\right)\alpha_{\text{vib}}\right] \tag{6.30}$$

This expression holds for an antenna on a substrate. Equation (6.30) was derived for a nanoantenna interacting with a single vibrational dipole. However, because the expression is linear in α_{vib}, it can easily be generalized to the case of a nanoantenna interacting with many vibrations.

$$\Delta\sigma = \frac{2\pi N S_{\text{sub}}}{\lambda\varepsilon_0}\text{Im}\left[\overline{F_A^2}\alpha_{\text{vib}}\right] \tag{6.31}$$

where N represents the number of vibrational dipoles and

$$\overline{F_A^2} = \frac{1}{V}\int_V \left((f_{xx}-1)^2 + f_{yx}^2 + f_{zx}^2\right) dV \tag{6.32}$$

represents the average nanoantenna amplification factor over the volume V where the vibrational dipoles are present. At first sight it may seem surprising that in the expression above there is an asymmetry between the appearance of the three tensor elements. We point out that this is merely a consequence of where we have truncated the perturbation expansion in Eq. (6.9). It turns out that the more symmetric expression

$$\overline{F_A^2} = \frac{1}{V}\int_V \left(f_{xx}^2 + f_{yx}^2 + f_{zx}^2\right) dV \tag{6.33}$$

corresponds to the sum of the four scattering diagrams displayed in Fig. 6.3. However, since it is convenient for the coming treatment, we will stick to a description based on a single scattering diagram and work with Eq. (6.32).

We are now in a position to compare the predictions of our analytical model with FDTD simulations. To this end we have simulated nanoantennas of varying length that are covered by a 10 nm layer of dielectric material. The antennas are simulated on top of a CaF_2 substrate ($n = 1.42$). The dielectric material is described by the following permittivity function that contains both a resonant and a non-resonant part

$$\varepsilon = \varepsilon_{nr} + \varepsilon_{\text{res}}(\omega) \tag{6.34}$$

where a Lorentz lineshape function is used for the resonant part

$$\varepsilon_{\text{res}}(\omega) = \frac{\varepsilon_{\text{lor}}\omega_0^2}{\omega_0^2 - \omega^2 - 2i\gamma\omega} \tag{6.35}$$

As a first step we consider a material that mimics the narrow-band absorption line of the carbonyl vibration of PMMA. We model this absorption band using a background permittivity ε_{nr} of 1, a center frequency ω_0 of 1730 cm^{-1}, a FWHM (2γ) of 23 cm^{-1}, and an amplitude ε_{lor} of 0.015 (reproducing the experimentally observed absorption coefficient of the carbonyl band of PMMA). Using these permittivity parameters we performed FDTD simulations to obtain the nanoantenna-enhanced vibrational spectrum (Fig. 6.5, blue lines) for two representative nanoantennas. In order to use Eq. (6.31) we need to relate the permittivity to the vibrational polarizability, for which we employ the Clausius-Mossotti equation[188]

$$\rho\alpha_{\text{vib}} = 3\varepsilon_0\left(\frac{\varepsilon - 1}{\varepsilon + 2}\right) \tag{6.36}$$

where ρ is the volume concentration of dipoles. Here we have arbitrarily assumed one dipole per FDTD simulation mesh cell ($\rho = 1/125\ \text{nm}^{-3}$). In Fig. 6.5 we compare the antenna-enhanced vibrational spectrum as obtained from the FDTD simulations with a calculation based on Eq. (6.31). The amplification factor $\overline{F_a^2}$ needed for this calculation was obtained from the simulations of the uncoated antennas. As can be seen the agreement between the FDTD simulations and Eq. (6.31) is excellent except for a very small frequency shift of a few wavenumbers (see inset). Next it is interesting to see whether our model can explain the observed shift of the nanoantenna resonance (Fig. 6.2(a)) when the dielectric material on top of the nanoantenna is characterized by a frequency-independent index of refraction. To this end we describe the dielectric using the known index of refraction (n_{nr}) of PMMA of 1.48, i.e. $\varepsilon_{nr} = n_{nr}^2$ and $\varepsilon_{\text{lor}} = 0$.[189] Again we use the Clausius-Mossotti equation to obtain the polarizability from the permittivity. In Fig. 6.6 we compare the cross-section change from the FDTD simulation with the analytical model. Again we get a very good agreement between the analytical model and the simulations, except that the model overestimates the cross-section change by approximately 20%. For both nanoantennas we observe an increased cross-section on the low-frequency side and a decreased cross-section on the high-frequency side, which is exactly the redshift illustrated in Fig. 6.2(a). It

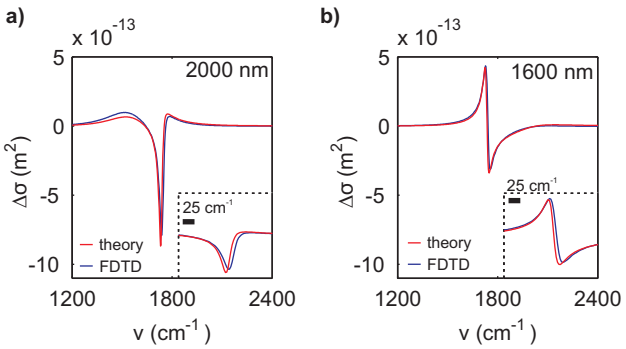

FIGURE 6.5. Comparison of the analytical model (Eq. (6.31)) with FDTD simulations. The blue curves represent FDTD simulations (coated nanoantennas minus uncoated nanoantenna) and the red curves are computed using Eq. (6.31) where the nanoantenna amplification factor $\overline{F_A^2}$ was taken from the simulations of the uncoated nanoantennas. The permittivity of the dielectric was modeled as a Lorentzian band ($\varepsilon_{\text{lor}} = 0.0149$, $\omega_0 = 1730$ cm^{-1}, $2\gamma = 23$ cm^{-1}) with a background permittivity ε_{nr} of 1.

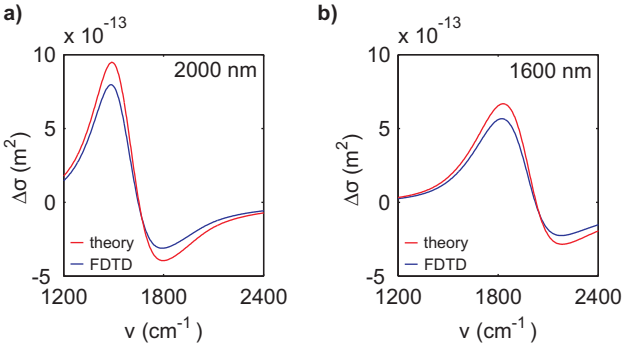

FIGURE 6.6. Comparison of the analytical model (Eq. (6.31)) with FDTD simulations in the case of a dielectric represented by a frequency-independent refractive index of 1.48. The blue curves represent FDTD simulations (coated nanoantennas minus uncoated nanoantenna) and the red curves are computed using Eq. (6.31) where the nanoantenna amplification factor $\overline{F_A^2}$ was taken from the simulations of the uncoated nanoantennas.

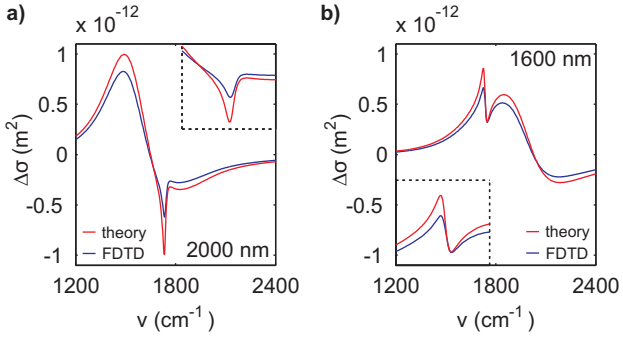

FIGURE 6.7. Simulated (blue line) and calculated (red line) cross-section changes for nanoantennas coated with a dielectric material with a realistic model for the PMMA permittivity. The permittivity parameters used are $\varepsilon_{\text{lor}} = 0.022$, $\omega_0 = 1730\ \text{cm}^{-1}$, $\gamma = 23\ \text{cm}^{-1}$ and $\varepsilon_{nr} = n_{nr}^2 = 2.19$.

is worthwhile to point out that the nanoantenna redshift is a manifestation of the backaction of the molecular dipoles on the nanoantennas, just as in the case of dipoles characterized by a vibrational resonance. In addition, it is interesting to note that the observed cross-section change is directly proportional to the imaginary part of $\overline{F_A^2}$.

As a final consistency check we simulate the effect of a material which displays both a background index of refraction (n_{nr}) and an absorptive Lorentz term. In order to accurately mimic PMMA we choose $n_{nr} = \sqrt{\varepsilon_{nr}} = 1.48$ and $\varepsilon_{\text{lor}} = 0.022$. Together these two parameters match both the real and imaginary permittivity of PMMA in the carbonyl region.[189] In a similar manner as was done above we compare the results of the simulations with the analytical model (Fig. 6.7). Curiously we observe that the very good description we achieved when simulating a material with only a resonant permittivity or only an off-resonant permittivity disappears when we simulate a realistic material which has both effects. As expected we see that the off-resonant part of the cross-section change is still overestimated by approximately 20%. However, surprisingly the resonant part of the cross-section change, which showed an almost perfect match in Fig. 6.5, is now overestimated by almost a factor of 2. This suggests that a crucial element is still missing in our analytical model. The fact that we obtain a good fit when choosing either $\varepsilon = \varepsilon_{nr}$ or $\varepsilon = \varepsilon_{\text{lor}}(\omega)$, but not when we describe ε as the sum of these contributions implies that there is an interaction effect between these different contributions to ε. Such interaction effect could arise if the interaction between different vibrational dipoles with each other is important. In the next section we will examine how this effect can be incorporated in our model.

6.2.3 STEP 3: THE LORENTZ LOCAL FIELD AND THE DEPOLARIZATION FIELD

In order to treat the interactions between the vibrational dipoles we consider the electric field inside a piece of dielectric material that is irradiated by a homogeneous

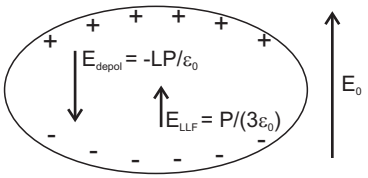

FIGURE 6.8. Schematic representation of the different electric fields that need to be considered when computing the polarizability of an ellipsoidal particle. Here we have drawn an oblate ellipsoid, for which the depolarization factor is approximately 0.5.

field E_0 (we assume the dimensions of the material are smaller than the wavelength of the light). A microscopic dipole inside the material experiences a field that differs from the externally applied field E_0. In fact, there are two additional contributions to the microscopic field. Firstly there is the Lorentz local field (LLF)

$$E_{\mathrm{LLF}} = \frac{P}{3\varepsilon_0} \tag{6.37}$$

which points in the same direction as the external field (P is the polarization of the material, i.e. dipole moment per unit volume).[188] The Lorentz local field accounts for the difference between the macroscopically averaged field applied to a sample and the microscopic field experienced inside the sample. The second field that needs to be considered is the so-called depolarization field due the accumulation of charges on the boundaries of the material. The depolarization field E_{depol} points opposite to the externally applied field E_0. In Fig. 6.8 we have schematically illustrated these fields for a dielectric particle. The reason we have chosen to illustrate these effects for an ellipsoidal particle is that for this particular shape the induced polarization is independent of the position inside the particle leading to the simple analytical expression for the depolarization field

$$E_{\mathrm{depol}} = -L\frac{P}{\varepsilon_0} \tag{6.38}$$

where L is the so-called depolarization factor (a dimensionless parameter between 0 and 1), which depends on the shape of the ellipsoid.[181] According to the reasoning above the field experienced by a microscopic dipole moment inside the material is

$$E = E_0 - L\frac{P}{\varepsilon_0} + \frac{P}{3\varepsilon_0} \tag{6.39}$$

Using $P = \rho\alpha E$ one can solve for the microscopic field

$$E = F_M E_0 \tag{6.40}$$

and it becomes clear that the microscopic field is simply related to the external field by a scaling factor, which we will call the *molecular* field-enhancement factor

$$F_M = \frac{1}{1+\rho\alpha/\varepsilon_0(L-1/3)} \tag{6.41}$$

$$= \frac{(\varepsilon+2)/3}{L(\varepsilon-1)+1} \tag{6.42}$$

In the second line we have used the Clausius-Mossotti equation to relate α and ε. We should point out that, strictly speaking, Eq. (6.40) only holds for an ellipsoidal particle that is illuminated by a homogeneous field E_0. This is quite different from our situation, in which we have a shell of PMMA that is excited by the inhomogeneous near field of the nanoantenna. Nevertheless we will make the *assumption* that Eq. (6.40) still holds in our case. This implies that the field experienced by the vibrational dipoles is scaled by the factor F_M compared to the antenna near field. Using the same reciprocity argument as in the previous section this also means that the field radiating back on the nanoantenna is scaled by the same factor compared to the field in the absence of local-field effects. This leads to the following expression for the cross-section change of the nanoantenna due to the PMMA shell

$$\Delta\sigma = \frac{2\pi N S_{\text{sub}}}{\lambda\varepsilon_0}\text{Im}\left[\overline{F_A^2}F_M^2\alpha_{\text{vib}}\right] \tag{6.43}$$

Let us now compare the prediction of this new expression, which contains one free parameter (the depolarization factor L), with the FDTD simulations. Figure 6.9 shows the simulations of the cross-section changes of two nanoantennas that are covered with a dielectric material that displays both a background permittivity and a resonant permittivity. In total we have simulated 8 nanoantennas with lengths between 1400 nm and 2600 nm, and we obtain an excellent fit of the analytic model if we choose a depolarization factor $L = 0.49$. It is important to point out that the excellent fit observed in Fig. 6.9 is not simply the result of a fortuitous scaling of α_{vib} by F_M^2 (see Eq. (6.43)). This can be seen by comparing Fig. 6.7 and Fig. 6.9, which shows that F_M^2 scales the resonant and non-resonant parts of the cross-section change by different amounts.

To gain more insight into the role of the molecular field enhancement F_M it is useful to explicitly consider its functional dependence, which we have plotted in Fig. 6.10. For comparison this figure also displays a plot of α_{vib}. We see that, similar to α_{vib}, F_M^2 contains a resonant and a non-resonant contribution, so that we can write these quantities as follows

$$\alpha_{\text{vib}}(\omega) = \alpha_{\text{res}}(\omega)+\alpha_{nr} \tag{6.44}$$

$$F_M^2(\omega) = (F_M^2)_{\text{res}}(\omega)+(F_M^2)_{nr} \tag{6.45}$$

To excellent approximation the resonant contribution of F_M^2 is Lorentzian, but contrary to the resonant contribution of α_{vib} it has a negative amplitude. It is insightful to perform a similar separation into a resonant and non-resonant

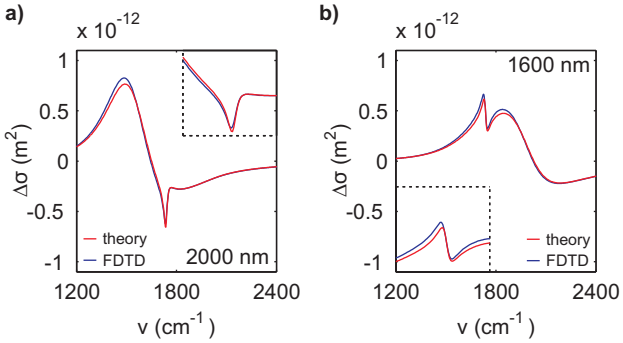

FIGURE 6.9. Simulated (blue line) and calculated (red line) cross-section changes for nanoantennas coated with a dielectric material with a realistic model for the PMMA permittivity. The calculations were done on the basis of Eq. (6.43) using a depolarization factor L of 0.49. The permittivity parameters used are $\varepsilon_{\text{lor}} = 0.022$, $\omega_0 = 1730\ \text{cm}^{-1}$, $\gamma = 23\ \text{cm}^{-1}$ and $\varepsilon_{nr} = n_{nr}^2 = 2.19$.

contribution for the amplified vibrational spectrum $\Delta\sigma$. The non-resonant contribution has the following form

$$\Delta\sigma_{\text{non-res}} = \frac{2\pi N S_{\text{sub}}}{\lambda\varepsilon_0}\text{Im}\left[\overline{F_A^2}(F_M^2)_{nr}\alpha_{nr}\right] \tag{6.46}$$

which immediately shows that the molecular field simply scales the cross-section change by the factor $(F_M^2)_{nr}$. Next we consider the resonant part of the cross-section change, which can be identified with the cross terms between the resonant and non-resonant parts of (F_M^2) and α_{vib},

$$\Delta\sigma_{\text{res}} = \frac{2\pi N S_{\text{sub}}}{\lambda\varepsilon_0}\text{Im}\left[\overline{F_A^2}\left[(F_M^2)_{nr}\alpha_{\text{res}} + \alpha_{nr}(F_M^2)_{\text{res}}\right]\right] \tag{6.47}$$

Here we neglected the contribution of the term proportional to $\alpha_{\text{res}}(F_M^2)_{\text{res}}$. It now becomes clear why neglecting the local field effects had led to such a great overestimation of the resonant cross-section change in Fig. 6.7. The point is that $\Delta\sigma_{\text{res}}$ is made up of two opposing contributions, of which one owes its resonant character to the resonance in α_{vib} while the second owes its resonant character to the resonance in F_M^2. The former contribution corresponds to the signal we had already derived in the previous section (except for the fact that it is now scaled down by the factor $(F_M^2)_{nr}$). The latter contribution, however, was missed in our previous analysis. Thus we see that the molecular field decreases the amplification of the vibrational spectrum by the nanoantenna. Let us next quantify this effect. To this end we note that α_{vib} and F_M have the same functional form, which to first order in $\varepsilon_{\text{res}}(\omega)$ can be approximated as follows.

$$\frac{a + b\varepsilon_{\text{res}}(\omega)}{c + d\varepsilon_{\text{res}}(\omega)} \approx \frac{a}{c} + \frac{a}{c}\left(\frac{b}{a} - \frac{d}{c}\right)\varepsilon_{\text{res}}(\omega) \tag{6.48}$$

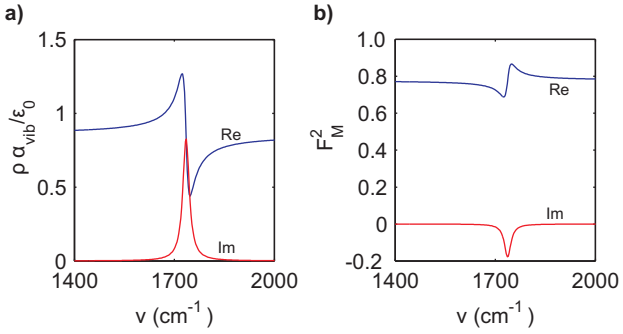

FIGURE 6.10. a) Plot of the vibrational polarizability of PMMA that follows from the experimental permittivity. b) Plot of the factor F_M^2 assuming the experimental polarizability of PMMA and a depolarization factor L of 0.49.

Using this approximation it is a simple matter to find the following expressions for $\Delta\sigma_{\text{res}}$ and $\Delta\sigma_{\text{non-res}}$

$$\Delta\sigma_{\text{non-res}}(\omega) = \frac{2\pi N S_{\text{sub}} S_{\text{nr}}}{\lambda\varepsilon_0}\text{Im}\left[\overline{F_A^2}(\omega)\right] \tag{6.49}$$

$$\Delta\sigma_{\text{res}}(\omega) = \frac{2\pi N S_{\text{sub}} S_{\text{r}}}{\lambda\varepsilon_0}\text{Im}\left[\overline{F_A^2}(\omega)\varepsilon_{\text{res}}(\omega)\right] \tag{6.50}$$

where the scaling factors for the resonant and non-resonant signals have been defined as

$$S_{\text{nr}} = \frac{(\varepsilon_{nr}+2)(\varepsilon_{nr}-1)}{3(L(\varepsilon_{nr}-1)+1)^2} \tag{6.51}$$

$$S_{\text{r}} = \frac{(2/3-L)(\varepsilon_{nr}-1)+1}{(L(\varepsilon_{nr}-1)+1)^3} \tag{6.52}$$

As expected we see that the resonant and non-resonant part of the cross-section show a different scaling behavior as a function of the background permittivity. As a final check of the validity of our treatment we compare the obtained analytical expressions for the scaling factors S_r and S_{nr} with the results of simulations. These results are shown in Fig. 6.11. The data points in this figure represent the amplitudes of the resonant and non-resonant cross-section changes of a coated 2000 nm nanoantenna, where we have used the same permittivity function $\varepsilon(\omega)$ as in Fig. 6.9 except that we have varied the background permittivity ε_{nr}. In order to separately obtain $\Delta\sigma_{\text{res}}(\omega)$ and $\Delta\sigma_{\text{non-res}}(\omega)$ from our simulations we performed two simulations for every value of ε_{nr}: one with $\varepsilon(\omega) = \varepsilon_{nr} + \varepsilon_{\text{res}}(\omega)$ and the other with $\varepsilon(\omega) = \varepsilon_{nr}$. The theoretical curves (Eq. (6.51)-(6.52)) were calculated using the previously determined value of 0.49 for the depolarization factor L. As can be seen we obtain an excellent agreement between the theory and the simulations. For reference, we have plotted two additional curves in these graphs. The first (purple line) represents the signal that

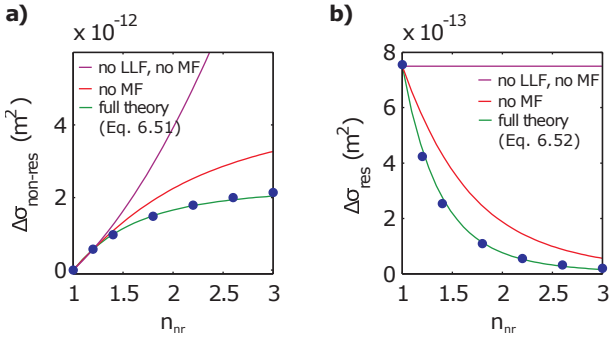

FIGURE 6.11. Amplitude of the non-resonant (a) and resonant (b) cross-section change as a function of the background refractive index $n_{nr} = \sqrt{\varepsilon_{nr}}$ of the coating material. The data points represent the maximum of the simulated cross-section change (which lies at 1420 cm^{-1} for the non-resonant signal and 1730 cm^{-1} for the resonant signal). The simulations were carried out for a 2000 nm nanoantenna coated with a 10 nm layer of dielectric material characterized by the permittivity from Eq. (6.34) with $\varepsilon_{\text{lor}} = 0.022$, $\omega_0 = 1730$ cm^{-1} and $2\gamma = 23$ cm^{-1}. The green curves represent calculations based on Eqs. (6.51) and (6.52) with $L = 0.49$. The red curves represent calculations when the molecular field (MF) enhancement is neglected (i.e. $F_M^2 = 1$). The magenta curves represent calculations where, in addition, the Lorentz local field (LLF) factor in the Clausius-Mossotti equation is ignored (i.e. $\rho\alpha_{\text{vib}} = \varepsilon_0(\varepsilon - 1)$).

one obtains if one completely ignores all local-field effects; that is, when ignoring both the factor F_M^2 and the Lorentz local field factor in the Clausius-Mossottti equation (meaning that we use $\rho\alpha_{\text{vib}} = \varepsilon_0(\varepsilon - 1)$). The second graph represents the signal one obtains upon inclusion of the Lorentz local field factor in the Clausius-Mossotti equation but without the factor F_M^2. We see that the local field effects drastically decrease the visibility of the vibrational amplification by the nanoantenna.

At this point it is instructive to briefly summarize the different screening effects that we have identified. We have seen that the *maximum* degree of amplification is determined by the square of the nanoantenna field enhancement ($\overline{F_A^2}$). This maximum amplification factor is identical for the resonant ($\Delta\sigma_{\text{res}}$) and non-resonant signals ($\Delta\sigma_{\text{non-res}}$). There are two effects that decrease this maximum amplification. Firstly, the amplification is weakened by the effect of the substrate through the parameter S_{sub} (for both the resonant and the non-resonant signals). Secondly, the amplification is further decreased due to the local-field effect (through the screening parameters S_{r} and S_{nr}). Interestingly it turns out that the local-field effect is fully mediated by the background refractive index n_{nr} of the material being sensed. This can be seen from the fact that for $n_{nr} = 1$, the amplitude of the amplified signal is independent of whether local-field effects are included or not. We also see the that the local field has a larger effect on the resonant signal compared to the non-resonant signal. For instance, up to a refractive index of approximately 1.5 the non-resonant signal is hardly affected by the local-field effects while the resonant signal already shows a marked decrease.

From a sensing perspective the result shown in Fig. 6.11 implies that vibrations which lie in a spectral region with a low refractive index can be detected most efficiently. For example, an increase in the refractive index from 1.5 to 2 leads to a decrease of the amplified vibrational signal by a factor of ~ 3. For completeness, we mention that another important factor determining the vibrational amplification is the orientation of the transition dipole moment of a vibration with respect to the local electric field (that is, vibrations with a transition dipole moment perpendicular to the local electric field are not amplified). As this effect is well documented in the literature,[167] we have not included it in our present treatment although it can be done straightforwardly.

We return to the depolarization factor and the value of 0.49, which has been found to accurately describe our data. The question arises as to how this value should be interpreted. In our treatment we have implicitly assumed that the depolarization factor is independent of the location inside the dielectric material. Strictly speaking this assumption is only correct for ellipsoidal particles. The fact that we nevertheless obtain an excellent description of our signals suggests that, although the polarization and depolarization fields are not homogeneous over the PMMA shell, the proportionality relation between these two quantities (as expressed by Eq. (6.38)) remains valid to a good approximation. To interpret the magnitude of L it is useful to consider how L depends on the shape of an ellipsoidal particle. It is well known that spherical particles are characterized by $L = 1/3$ and that L decreases to a value of 0 as the particles become prolate (for an electric field polarized parallel to the long axis). For flatter particles, i.e. oblate ellipsoids, the opposite occurs and L increases up to its limiting value of 1 (for an electric field polarized parallel to the short axis). Apparently, the flatter the particle is, the better the external electric field can be shielded by the depolarization field. The value of $L = 0.49$, which corresponds to an oblate ellipsoid with a shape similar to the one drawn in Fig. 6.8 (that is, with a short axis approximately half the length of the long axis), indicates a rather good shielding of the nanoantenna field by the PMMA. This is probably a consequence of the fact that for the entire PMMA shell the near field of the nanoantenna is perpendicular to the surface of the PMMA. With respect to the nanoantenna near field the PMMA shell therefore acts as a flat particle.

We have seen that for the nanoantenna geometry described in this work the local-field effects tend to decrease the plasmonic enhancement of a vibrational resonance ($S_r < 1$; see Fig. 6.11(b)). Now the interesting question arises as to whether it would be possible to design a nanoantenna whose plasmonic enhancement is actually boosted by the local fields rather than weakened. From Eq. (6.52) it can easily be seen that decreasing the depolarization factor L leads to an increase of S_r thereby increasing the plasmonic enhancement. It turns out that for $L < 0.1$ the resonant scaling factor S_r can even attain values that are larger than unity over the entire refractive index range displayed in Fig. 6.11. For instance, if one could achieve a vanishing depolarization factor ($L = 0$), then for a vibrational mode with a typical background refractive index n_{nr} of 1.65 one would obtain a plasmonic enhancement that is 10 times larger compared to the enhancement obtained with the present geometry ($L = 0.49$). A depolarization factor of zero corresponds to the case in which the depolarization field effectively vanishes over the volume of the sensed material. This situation occurs naturally for strongly prolate particles (with the

electric field polarized along the long axis). Alternatively one could imagine achieving this condition through a nanoantenna geometry in which the sensed material is not applied homogeneously over the entire nanoantenna, but rather as nanostructured patches, designed in such a way to cause the depolarization field to effectively vanish over the material. These considerations demonstrate that engineering of the local molecular field could potentially yield a novel strategy to significantly boost the amplification of vibrational signals by infrared nanoantennas.

6.3 CONCLUSION

We have presented a model which describes the interaction between molecular vibrations and infrared nanoantennas. The model allows one to quantitatively compute the cross-section change displayed by an infrared nanoantenna when it is covered by a thin layer of dielectric material. Our treatment is based on a perturbation expansion in which the total cross-section change of the nanoantenna is split up into a series of contributions from (virtual) interaction processes, each of which has a straightforward physical interpretation. The model demonstrates that the main contribution to the cross-section change is due to a backaction process: the nanoantenna near field excites the molecular vibrations, which in turn radiate back onto the nanoantenna. This backaction process explains both the lineshape of the amplified vibrational signal and its amplitude. The lineshape is determined by the phase lag between the incident radiation and the reradiated field. Depending on the detuning between the nanoantenna and the molecular vibrations, this phase lag can have any value between 0 and 2π, which explains the variety of observed lineshapes ranging from absorptive peaks and dips to fully dispersive shapes. The plasmonic enhancement of the vibrational signal is firstly determined by the square of the field enhancement of the nanoantenna. In addition, however, it turns out that the local molecular field plays an important role as it effectively scales the nanoantenna near field. Interestingly, depending on the exact circumstances, this local-field effect can either decrease or further boost the plasmonic enhancement by the nanoantenna. This could provide an avenue for achieving particularly strong plasmonic enhancements by rationally engineering the local field.

6.4 APPENDIX

6.4.1 SIMULATION DETAILS

The finite-difference time-domain simulation were performed using a commercially available software package (Lumerical). We used a total-field-scattered-field (TFSF) source to compute the extinction cross section of 8 nanoantennas of varying lengths (between 1400 nm and 2600 nm). The antennas were simulated on top of a CaF_2 substrate ($n = 1.42$). The optical constants of gold were taken from Palik.[190] We computed the extinction for both the bare antennas and for antennas covered with a 10 nm layer of PMMA on each face. We examined a number of different permittivity functions for the PMMA, as described in the main text. For both the antennas and the

PMMA a mesh of 5 nm was used. Because of the sharp PMMA resonance, relatively long simulation times of 2000 fs were required whenever this resonance was included in the permittivity function.

6.4.2 DERIVATIONS

In this appendix we provide the derivation proving that $f'_{xy} = f_{xy}$ and $f'_{xz} = f_{xz}$. In the second part we demonstrate that these equalities remain valid for a dipole on a surface.

THE ELEMENT f'_{xy} The element f'_{xy} can be obtained via a slightly modified approach compared to the one discussed in the main text. The diagrams required are shown in Fig. 6.12. Using the diagrams in Fig. 6.12(a)-(b) we write for the field-enhancement tensor

$$f_{yx} = \frac{G_{yx}(r_{\text{vib}}, r_{\text{far}})}{G^{(0)}_{xx}(r_{\text{vib}}, r_{\text{far}})} \tag{6.53}$$

Next from Fig. 6.12(c)-(d) we find that

$$f'_{xy} = \frac{\Delta p_{\text{ant,x}}}{p_{\text{test,y}}} = \frac{E_x(r_{\text{far}})}{E^{(0)}_y(r_{\text{far}})} \tag{6.54}$$

$$= \frac{G_{xy}(r_{\text{far}}, r_{\text{vib}})}{G^{(0)}_{yy}(r_{\text{far}}, r_{\text{vib}})} \tag{6.55}$$

In writing the first line we have used the fact that $E_x(r_{\text{far}})$ reports only on $p_{\text{ant,x}}$ even though $p_{\text{ant,y}}$ and $p_{\text{ant,z}}$ are non-vanishing. Because of symmetry

$$G^{(0)}_{yy}(r_{\text{far}}, r_{\text{vib}}) = G^{(0)}_{xx}(r_{\text{far}}, r_{\text{vib}}) \tag{6.56}$$

from which follows that

$$f'_{xy} = f_{yx} \tag{6.57}$$

THE ELEMENT f'_{xz} The element f'_{xz} is somewhat more difficult to evaluate. Here we need to consider a test dipole that is oriented along the z axis. However, the amplitude of this dipole cannot be obtained form the field at r_{far} as the radiated field vanishes in the direction parallel to the dipole moment. Because of this we will adopt a slightly different strategy in which we place the observation point r_{far} such that the dipoles are observed under a slight angle θ. We will define a second coordinate system with axes z' and x' (see Fig. 6.13(a)). We can define the following field enhancement tensor element (applying to non-normal incidence)

$$f_{zx}[\theta] = \frac{E_z(r_{\text{vib}})}{E^{(0)}_x(r_{\text{vib}})} \tag{6.58}$$

$$= \frac{G_{zx'}(r_{\text{vib}}, r_{\text{far},\theta})}{G^{(0)}_{xx'}(r_{\text{vib}}, r_{\text{far},\theta})} \tag{6.59}$$

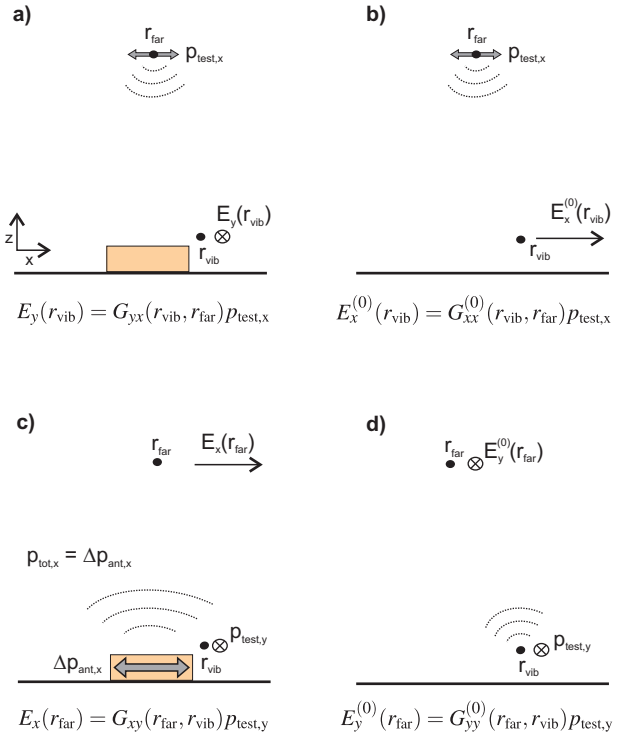

FIGURE 6.12. Diagrams for computing the element f'_{xy}. In these diagrams the far-field source is placed in such a way that the nanoantenna is illuminated under a slight angle θ. We have defined a secondary coordinate system with the z' axis parallel to the k vector of the illumination; the x' axis is perpendicular to this direction and parallel to the electric field of the source dipole.

which obviously tends to f_{zx} (which is the element that appears in Eq. (6.19)) as θ approaches zero.

Now a difficulty occurs when we attempt to obtain the dipole moment $p_{\mathrm{ant,x}}$ from the field $E_{\mathrm{far},x'}$. The point is that this field does not only depend on $p_{\mathrm{ant,x}}$ but also on $p_{\mathrm{ant,z}}$. However, if the angle θ is small then

$$p_{\mathrm{ant,x}} \propto E_{x'}(r_{\mathrm{far},\theta})/\sin(\pi/2-\theta) = E_{x'}(r_{\mathrm{far},\theta})/\cos(\theta) \tag{6.60}$$

is a good approximation, which becomes exact in the limit $\theta \to 0$. From Fig. 6.13(d) it follows that

$$p_{\mathrm{test,z}} \propto E^{(0)}_{x'}(r_{\mathrm{far},\theta})/\sin(\theta) \tag{6.61}$$

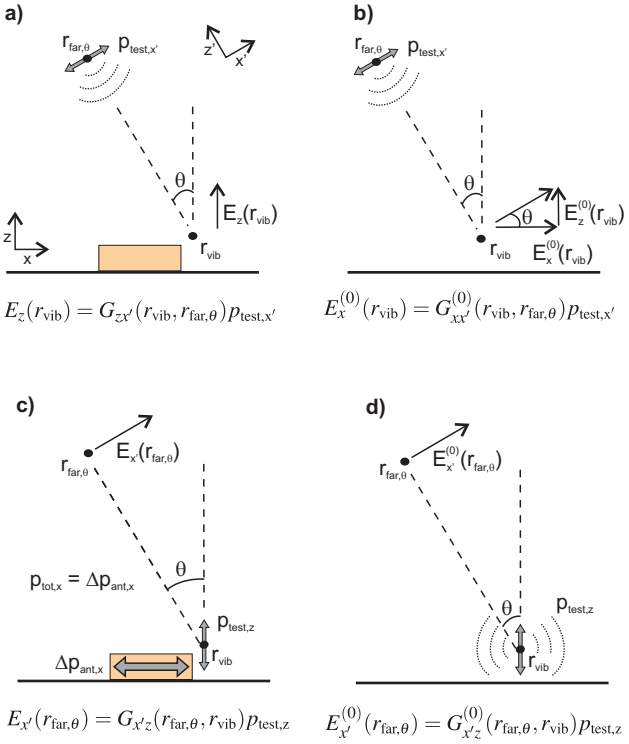

FIGURE 6.13. Diagrams for computing the element f'_{xz}. In these diagrams the far-field source is placed in such a way that the nanoantenna is illuminated under a slight angle θ. We have defined a secondary coordinate system with the z' axis parallel to the k vector of the illumination; the x' axis is perpendicular to this direction and parallel to the electric field of the source dipole.

From these two expressions we can obtain

$$f'_{xz}[\theta] = \frac{\Delta p_{\text{ant,x}}}{p_{\text{test,z}}} \tag{6.62}$$

$$= \frac{E_{x'}(r_{\text{far},\theta})}{E_{x'}^{(0)}(r_{\text{far},\theta})/\tan\theta} \tag{6.63}$$

$$= \frac{G_{x'z}(r_{\text{far},\theta}, r_{\text{vib}})}{G_{x'z}^{(0)}(r_{\text{far},\theta}, r_{\text{vib}})/\tan\theta} \tag{6.64}$$

Here the parameter θ refers to the fact that the tensor element $f'_{xz}[\theta]$ (which itself does not depend on θ) is evaluated using the observation point $r_{\text{far},\theta}$. Using the

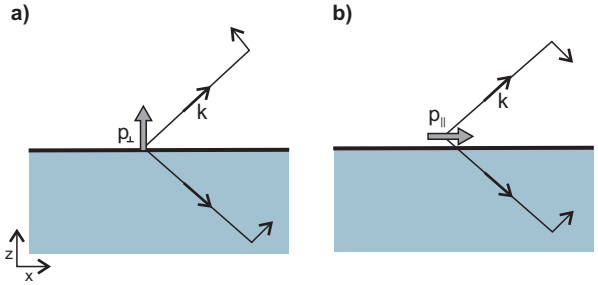

FIGURE 6.14. Diagrams for evaluating the radiation pattern of out-of-plane (a) and in-plane dipoles that are located above a substrate. We assume that the distance above the substrate is much smaller than the wavelength.

reciprocity relation we rewrite this into

$$f'_{xz}[\theta] = \frac{G_{zx'}(r_{\text{vib}}, r_{\text{far},\theta})}{G^{(0)}_{zx'}(r_{\text{vib}}, r_{\text{far},\theta})/\tan\theta} \tag{6.65}$$

$$= \frac{G_{zx'}(r_{\text{vib}}, r_{\text{far},\theta})}{G^{(0)}_{xx'}(r_{\text{vib}}, r_{\text{far},\theta})} \tag{6.66}$$

$$= f_{zx}[\theta] \tag{6.67}$$

where the second step follows from Fig. 6.13(b). In the limit $\theta \to 0$ we obtain

$$f'_{xz} = f_{zx} \tag{6.68}$$

EFFECT OF THE SUBSTRATE The derivations above have relied strongly on the properties of the dipole radiation field. The question now arises whether this derivation still holds for a dipole located above a substrate (given the fact that the substrate modifies the dipolar radiation field). Fortunately in our case the situation is relatively simple. We only need to consider the radiation pattern in the xz plane, and we need to do this for two cases: a dipole aligned along the z axis and a dipole aligned along the x axis. The radiation pattern in the upper plane is the superposition of the field emitted in the upward direction and the field reflected by the substrate. To obtain the far-field radiation patterns for the dipoles shown in Fig. 6.14(a) and (b) we simply reflect the downward travelling ray and scale it by the Fresnel reflection coefficient. The validity of this approach follows from the fact that in the far-field the radiation pattern of a dipole is given by its angular spectrum;[184] the rays in Fig. 6.14 should be interpreted as the plane-wave components that form the angular spectrum representation of the dipole radiation field. Taking into account the direction of the different electric field vectors we see that this leads to different radiation patterns for parallel and perpendicular pointing dipoles.

$$E \propto (1 + r_\theta)\sin\theta\, p_\perp \tag{6.69}$$

$$E \propto (1 - r_\theta)\cos\theta\, p_{||} \tag{6.70}$$

Here r_θ is the Fresnel reflection coefficient for a p-polarized plane wave incident at an angle θ. Now it becomes clear that in the evaluation of f'_{xx} and f'_{xy} this effect has no influence as in these cases we only compare in-plane dipoles with each other (see Figs. 6.4(c)-(d) and Figs. 6.12(c)-(d)). For the evaluation of f'_{xz} this is not the case, however. That is because there we compare an in-plane dipole with an out-of-plane dipole (Figs. 6.13(c)-(d)), and Eq. (6.65) therefore modifies into

$$f'_{xz}[\theta] = \frac{1+r_\theta}{1-r_\theta}\frac{E_{x'}(r_{\text{far},\theta})}{E^{(0)}_{x'}(r_{\text{far},\theta})/\tan\theta} \tag{6.71}$$

$$= \frac{1+r_\theta}{1-r_\theta}\frac{G_{x'z}(r_{\text{far},\theta}, r_{\text{vib}})}{G^{(0)}_{x'z}(r_{\text{far},\theta}, r_{\text{vib}})/\tan\theta} \tag{6.72}$$

At first sight it seems that this expression implies that Eq. (6.68) no longer holds. However, one should consider that in the presence of a substrate (see Fig. 6.13(b))

$$E^{(0)}_z(r_{\text{vib}}) \neq \tan\theta E^{(0)}_x(r_{\text{vib}}) \tag{6.73}$$

In fact, the Fresnel reflection of the incoming plane wave leads to

$$E^{(0)}_x(r_{\text{vib}}) = (1-r_\theta)\cos\theta E_0 \tag{6.74}$$

$$E^{(0)}_z(r_{\text{vib}}) = (1+r_\theta)\sin\theta E_0 \tag{6.75}$$

and as a consequence

$$G^{(0)}_{zx'}(r_{\text{vib}}, r_{\text{far},\theta}) = \tan\theta\frac{1+r_\theta}{1-r_\theta}G^{(0)}_{xx'}(r_{\text{vib}}, r_{\text{far},\theta}) \tag{6.76}$$

Therefore we again end up with

$$f'_{xz} = f_{zx} \tag{6.77}$$

Chapter 7

Real-Time Observation of Organic Cation Reorientation in Methylammonium Lead Iodide Perovskites[a]

The introduction of a mobile and polarised organic moiety as a cation in three-dimensional lead-iodide perovskites brings fascinating optoelectronic properties to these materials. The extent and the timescales of the orientational mobility of the organic cation and the molecular mechanism behind its motion remain unclear, with different experimental and computational approaches providing very different qualitative and quantitative description of the molecular dynamics. Here we use ultrafast two-dimensional vibrational spectroscopy of methylammonium (MA) lead iodide, to directly resolve the rotation of the organic cations within the $MAPbI_3$ lattice. Our results reveal two characteristic time constants of motion. Using ab-initio molecular dynamics simulations, we identify these as a fast (∼300 fs) 'wobbling-in-a-cone' motion around the crystal axis, and a relatively slow (∼3 ps) jump-like reorientation of the molecular dipole with respect to the iodide lattice.

[a] Adapted from: A. A. Bakulin, O. Selig, H. J. Bakker, Y. L. A. Rezus, C. Müller, T. Glaser, R. Lovrincic, Z. Sun, Z. Chen, A. Walsh, J. M. Frost, T. L. C. Jansen, "J. Phys. Chem. Lett.", **6**, 3663-3669 (2015)

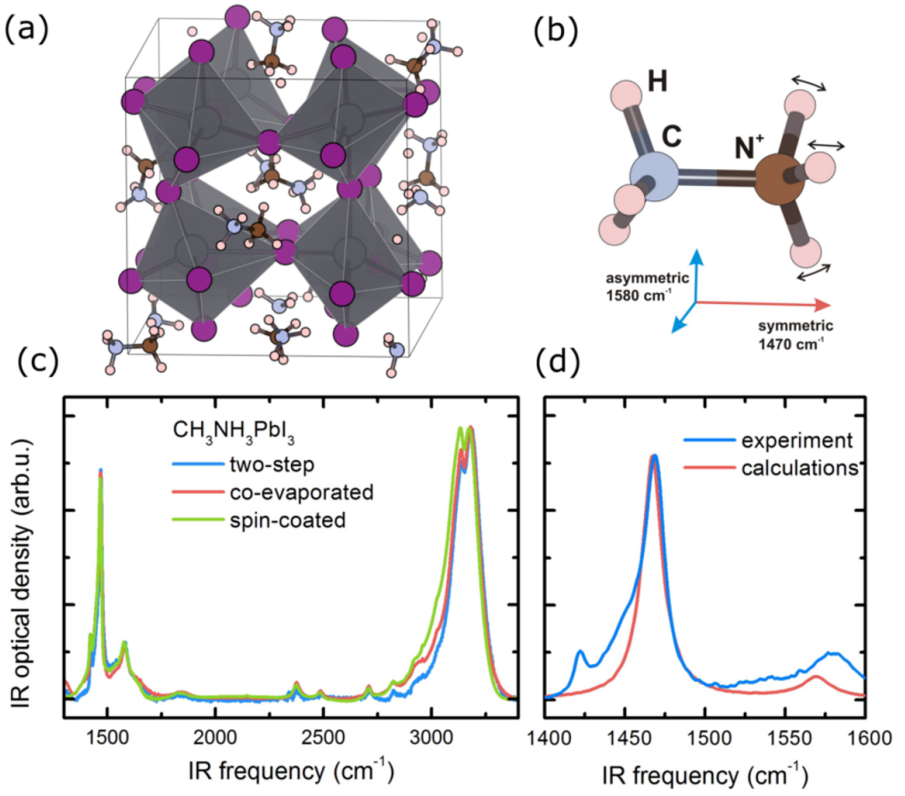

FIGURE 7.1. Perovskite material under study: (a) A snapshot from a molecular dynamics simulation showing the structure of the $MAPbI_3$ perovskite. (b) The MA molecule and the orientation of the transition dipoles of the NH_3^+ bending vibrations. (c) IR absorption spectra of $MAPbI_3$ films prepared using different methods. (d) Absorption spectra of a $MAPbI_3$ film in the NH/CH bending vibrational region. The red line shows the calculated absorption spectrum of the NH_3 bending modes (on the basis of the MD simulation).

7.1 INTRODUCTION

Hybrid organic-inorganic perovskites[191] are attracting a lot of attention for optoelectronic applications as they combine the solution processability of molecular electronic materials with the low exciton binding energy and high charge mobility of inorganic sesmiconducting crystals.[192,193] Many of these features can be related to the high dielectric constant of the material. The recent breakthroughs achieved by the application of methylammonium ($CH_3NH_3^+$ or MA) lead halides[194] in photovoltaic[195–197] and light-emitting[198] devices have triggered extensive research efforts to unravel the fundamental photophysics of these material systems. The organic cations, like MA, are not directly involved in the makeup of the valence or conduction bands. Yet they are shown to have a strong influence on the

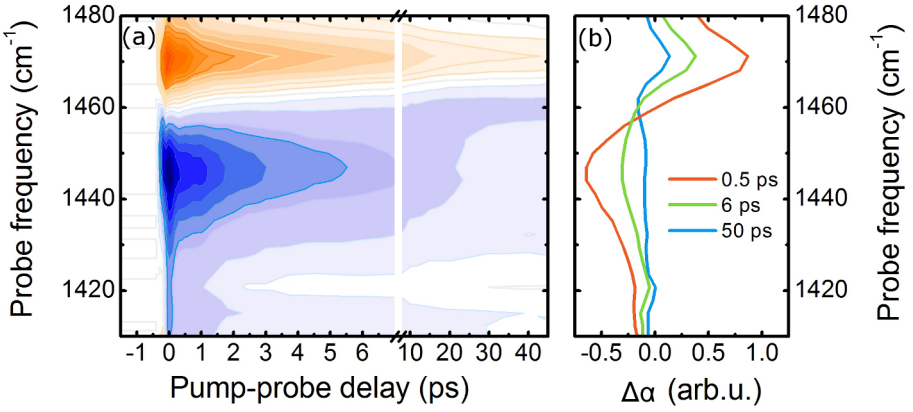

FIGURE 7.2. (a) Isotropic pump-probe transient spectra of a co-evaporated perovskite film measured using broadband excitation. (b) Isotropic pump-probe responses at different pump-probe delay times.

optoelectronic properties of the perovskites.[199,200] The size and shape of the molecular cations, as well as their embedding in the lattice, determine the macroscopic and molecular-scale perovskite crystal structure,[199,201,202] which in turn determines the band gap[200,202] of the material via the deformation potential. This offers the opportunity to tune the material properties through modification of the organic cation.[200] Furthermore, some of the unique properties of hybrid perovskites may be associated with the asymmetry and preferential alignment or to the dynamics of the embedded molecules. In contrast to spherically symmetric inorganic (atomic) cations, organic ions have a less symmetric shape and can possess a permanent dipole moment.[200,203] As a result, the positioning, orientation and rotational dynamics[204] of the organic moiety within the inorganic lattice can have a strong influence on the electronic system.[205] The reorientation of the organic cation with its associated dipole moment contributes to the dielectric response, and applies a crystal field to the material; both will affect the photovoltaic action. However, recent results suggest that though the choice of organic moieties is critical for material performance,[206,207] cations do not dominate solar cell hysteresis[208] and are not essential in obtaining high open circuit voltages.[209] A number of optoelectronic phenomena associated with molecular cation motion have been proposed based on electronic structure calculations. Cations were proposed to be responsible for the variations in dielectric constants, para- and ferroelectric behaviour,[203,210,211] current-voltage hysteresis,[199,212–214] a decrease in exciton binding energy, charge carrier segregation in the material, and dynamic disorder in valence and conduction band energies.[215,216] Most of these effects are expected to be extremely sensitive to the interplay between cation-cation and cation-anion interactions, the orientational mobility of organic molecules and the time scales of the structural dynamics. The rotational mobility of organic cations in inorganic lattices has been studied for application-relevant lead-iodide and lead-bromide perovskites using MA as

the organic cation (Figure 7.1(a)). The first estimates for MA reorientation were obtained using NMR spectroscopy, which pointed towards 0.2–0.4 ps rotational correlation functions for the C–N and N(C)–H axes,[217] comparable to the time scale of the reorientation of similarly sized molecules in free space. Dielectric relaxation and calorimetry measurements confirmed the fast rotation and orientation disorder of MA in perovskite materials at room temperature.[218,219] However, some recent theoretical[220–222] and experimental[210,213,223–225] results present arguments towards much longer reorientation timescales of 5–14 ps. Clearly, at present there is insufficient understanding of hybrid perovskite structural dynamics. This understanding requires comprehensive and direct experimental-theoretical approach that would allow one to identify the mechanistic picture behind the different timescales of the atomic and molecular motions. In this chapter, we report on an ultrafast polarization-resolved two-dimensional infrared (2DIR) vibrational spectroscopy and ab-initio molecular dynamics (MD) study of the MA cation rotation for a set of $MAPbI_3$ materials. Using the NH_3^+ symmetric bending vibration as a probe, we observe two characteristic timescales of molecular motion, which we identify as a fast ($\sim$0.3 ps) wobbling-in-a-cone around the preferential MA dipole directions parallel to the lattice axes, and relatively slow (>2 ps) jump-like reorientation of the molecular dipole (aligned with the CN axis) with respect to the crystal lattice. This result suggests that in $MAPbI_3$ at room temperature the alignment of cation dipoles, if present, is likely to be of intermediate-range order.

7.2 RESULTS AND DISCUSSION

7.2.1 INFRARED SPECTROSCOPY

To tackle the potential effect of crystal defects and grain boundaries on cation dynamics, we investigated $MAPbI_3$ films made with three different techniques:

- multilayer spin-coating,
- a solvent-free two-step formation from PbI_2 and methylammonium-iodide (MAI) precursors,[226] and
- co-evaporation from $PbCl_2$ and MAI.[227,228]

The samples were prepared and characterized by the groups of Robert Lovrincic and Zhuoying Chen (for details see Ref.[229]). All films were deposited onto infrared (IR) transparent CaF2 substrates and had a thickness of $\sim$1 μm. To observe the dynamics of molecular reorientation we used ultrafast vibrational spectroscopy, with the symmetric NH_3^+ bending vibration as a probe. Figures 7.1(b)-(d) show the structure of the MA molecule and its contribution to the perovskite IR absorption spectrum in the vibrational fingerprint region.[230] The spectrum is dominated by the NH_3^+ stretching and bending modes in the regions of $\sim$3200 cm^{-1} and $\sim$1500 cm^{-1}, respectively. We attribute the weak narrow peaks in the regions around 2800 cm^{-1} and 1420 cm^{-1} to CH_3 stretching and bending vibrations. These peaks are much less pronounced than the NH_3^+ vibrations due to the relatively small transition

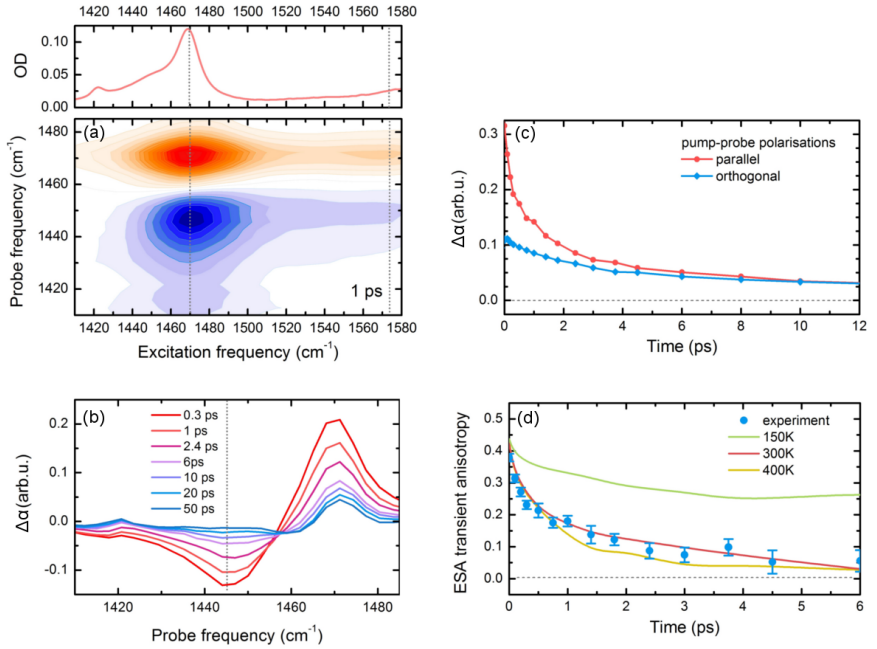

FIGURE 7.3. 2DIR response of NH bending vibrations: (a) Isotropic 2D spectra of co-evaporated perovskite film (average over three samples) 1 ps delay time. The different colours correspond to 5% steps from the maximum amplitude. Upper panel shows the corresponding absorption spectrum. (b) Cross sections through the 2D spectrum of the co-evaporated perovskite at ν_{ex}=1470 cm^{-1} for different delay times. (c) The dynamics of the excited-state absorption in the (ν_{ex} = 1470 cm^{-1}; ν_{pr} = 1445 cm^{-1}) point of 2D spectrum measured for parallel and orthogonal pump and probe pulses polarisations. (d) Anisotropy dynamics associated with the data in panel (c) with 95% confidence interval indicated. The solid lines represent the transient anisotropy dynamics calculated based on the MD simulations at different temperatures.

dipole moments of the CH vibrations as compared to the NH vibrations, and will not be adressed in this study. Due to the degeneracy of the three NH oscillators, both stretching and bending vibrations split into one symmetric and two asymmetric normal modes with orthogonal transition dipole moments. The symmetric bending mode at 1470 cm^{-1} is well separated in frequency from the asymmetric bending modes (Figure 7.1(d)) at 1580 cm^{-1} and has its transition dipole moment aligned along the C–N axis of the molecule. This makes it possible to use the transition dipole moment of the symmetric NH_3^+ bending vibration as a probe for the reorientation of the C–N bond and, thus, of the static dipole of the MA cation.

To measure the orientational dynamics of the symmetric NH_3^+ bending oscillator we performed polarization-resolved pump-probe and 2DIR experiments[77,231–233] on perovskite films in the 1400–1600 cm^{-1} frequency range (see Chapter 3 for experimental details). Using a collinear fast-scanning Mach-Zehnder scheme,[78]

molecular vibrations were first excited by an interferometric pair of strong 100 fs IR pump pulses. After a variable delay time, the excited state population was probed by weak broadband probe pulses with the polarizations parallel and orthogonal to the pump pulse. The isotropic signal and the anisotropy of the response were calculated as according to Eq 2.74 and Eq. 2.75, respectively. For non-interacting transition dipoles in an isotropic medium, the anisotropy decays from its initial value of 0.4 to 0, when the orientations of the transition dipoles are completely scrambled as a result of orientation diffusion. In the isotropic signal, the effect of the reorientation is completely removed, thereby only representing population relaxation. By scanning the delay between the two pulses of the interferometric pump we obtain a frequency resolution of $\sim$5 cm^{-1}.

We first present the pump-probe spectra for a co-evaporated $MAPbI_3$ film (Figure 7.2(a), (b)). In this measurement, only the isotropic component was extracted. At positive delay times, the bleaching/stimulated emission of the 0$\rightarrow$1 $NH_3{}^+$ symmetric bending transition is clearly observed at 1470 cm^{-1}. The excited state 1$\rightarrow$2 absorption from the first to the second excited state of the vibrational oscillator is observed at 1445 cm^{-1} and is anharmonically shifted from the 0$\rightarrow$1 transition by $\sim$25 cm^{-1}. The excited-state population decays on an timescale of 3 ps which should provide an observation window of up to 6 ps for the orientational dynamics. However, at long times we observe additional signals at 1475 cm^{-1} and 1420 cm^{-1}, which do not change significantly with time. These features coincide with the linear absorption peaks (Figure 7.1) and live for the times longer than 50 ps, which make us to assign them to a thermal response.[234] The relaxation of high-frequency bending vibrations creates multiple low-frequency excitations (a so-called hot ground state), which lead to the change in the absorption of the bending modes. The spectral overlap of the bleaching 0$\rightarrow$1 transition and the thermal response complicates the anisotropy analysis in this frequency range. Therefore, for later anisotropy analysis, we will only consider the data from the ESA probe region 1445 cm^{-1}, where the thermal signal is much smaller than population signal in the time window $<$10 ps, as can be seen from the spectra at long delay times. With this in mind, we will use the 2D-IR spectra to (i) decouple the 'clean' rotation-related anisotropy dynamics from the thermal response and (ii) to separate the responses and anisotropy dynamics coming from the symmetric and asymmetric modes. Figure 7.3(a) shows the 2D-IR spectrum of a co-evaporated $MAPbI_3$ film at a delay of 1 ps. In this chapter, we use the convention of displaying the excitation frequency, ν_{ex}, along the horizontal axis and the probe frequency, ν_{pr}, along the vertical axis. As expected from the absorption spectra and the pump-probe measurements presented above, the signal associated with the bleaching of the 0$\rightarrow$1 transition of the symmetric bending mode is located at (ν_{ex};ν_{pr})=(1470; 1470) cm^{-1} and the ESA at (1470; 1445) cm^{-1}. As can be seen from the cross sections of the response for symmetric mode excitation at ν_{ex}=1470 cm^{-1} (Fig. 7.3(b)), at delay times longer than 10 ps, the signals associated with the excitation of the ν=1 state are substantially influenced and then overtaken by the thermal response. In addition to the symmetric bending responses, the 2D-IR spectra reveal cross peaks corresponding to the population of the symmetric mode ν_{pr}=1470 cm^{-1}, following excitation of asymmetric vibrations ν_{ex}=1560 cm^{-1}. Due

to the orthogonal orientation of the transition dipoles the response at the cross peaks is strongly depolarised. To extract the anisotropy decay originating from the symmetric mode reorientation, we focus on the responses in the center of the ESA feature at (1470;1445) cm^{-1}. Figure 7.3(c) presents the population dynamics measured with different pump and probe polarization and the blue dots Figure 7.3(d) show the extracted transient anisotropy decay for the co-evaporated $MAPbI_3$ film. After photoexcitation, the initial anisotropy is close to 0.4, which is the expected value for a random distribution of uncoupled dipoles.[235] The anisotropy decays on two clearly different timescales. The faster decay occurs on a timescale of <300 fs and decreases the anisotropy approximately by half. The longer 3 ps decay brings the anisotropy close to zero within the 6 ps observation window. We did not analyze the dynamics at longer times because at longer delays the signal becomes dominated by the thermal response. We also note that, as the anisotropy is analyzed in the center of the ESA peak, it reflects the reorientation for the majority of the molecules. However, some minor sub-ensemble of MA ions may have a shifted IR absorption line or/and faster spectral diffusion with a more pronounced orientational dynamics. Around 500 fs, the residual anisotropy still has a relatively high value of ∼0.2 for all samples. While the fast time-scale observed here agrees with the 400 fs timescale reported in previous NMR experiments,[217] the slow timescale of 3 ps has not been observed before. Longer (∼5 ps) timescales were predicted based on selective dynamics (artificially constrained frozen lead positions) MD simulations[202] and measured (5–14 ps) with quasi elastic neutron scattering on bulk material.[219,236] Independent of the preparation protocol and film morphology, all our thin-film samples demonstrate similar anisotropy dynamics (Figure 7.4(a)). We can hence exclude an influence of solvent residuals on the observed time scales, as two of the samples were fabricated with solvent free methods. We speculate that this explains part of the discrepancy between the reorientation times presented here and those recently derived from neutron scattering.[225]

7.2.2 MOLECULAR DYNAMICS SIMULATIONS

To obtain molecular-scale mechanistic insight into the origin and details of the organic cation dynamics, A. Walsh, J. M. Frost and T. L. C. Jansen undertook ab-initio molecular dynamic (MD) simulations starting in a pseudo-cubic geometry and at temperatures of 150, 300 and 450 K. To validate the simulations and to allow for a direct comparison to experimental results, the MD trajectories are used directly to calculate the absorption and the full 2D-IR response of the methylammonium NH_3^+ bending vibrations.[237,238] Figure 7.1(d) shows that the NH_3^+ bending absorption spectrum calculated with the procedure described above reproduces the experimental results well. The additional small peaks observed in the experimental data are probably associated with the CH_3 bending modes; the slightly different absorption cross section ratio for the symmetric and asymmetric modes is likely to originate from their assumption that the transition dipole direction of the local NH bending modes are perpendicular to the NH bonds. Figure 7.4(b) shows the calculated 2D-IR spectrum (perpendicular polarizations), which also reproduces the experimental results (Figure 7.3(a)). This proves the adequacy of the applied

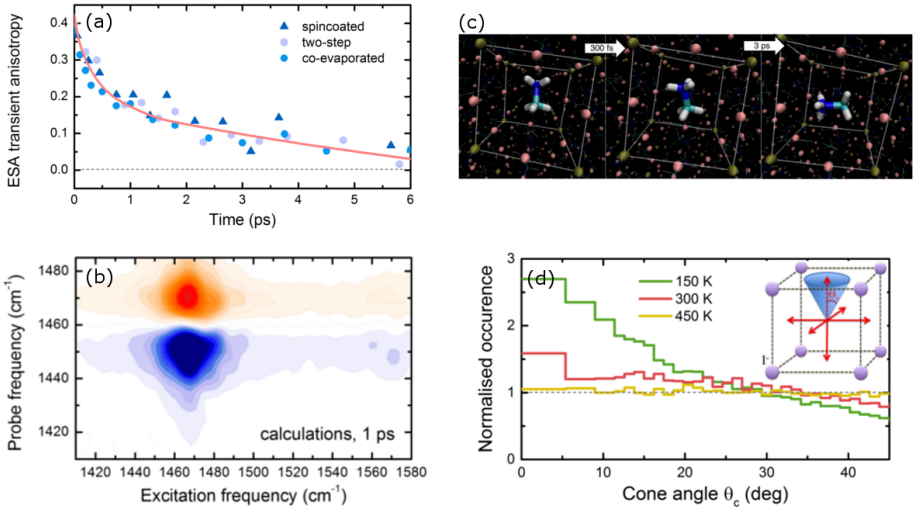

FIGURE 7.4. (a) Transient anisotropy in the peak of ESA response (ν_{ex} = 1470 cm^{-1}; ν_{pr} = 1445 cm^{-1}) for samples prepared using different techniques. The red line is a guide to the eye showing the transient anisotropy dynamics calculated based on MD simulations at 300 K. The time resolution was ∼100 fs for co-evaporated film and 300 fs for spincoated and two-step fabricated films. (b) The example of 2D-IR spectrum calculated with MD simulations. (c) An artist impression illustrating the motion of organic cation within the perovskite material. (d) Histogram of the simulated angular distribution of the MA dipoles at different temperatures normalized to the isotropic distribution. The inset illustrates the definition of the cone angle.

method for calculating the spectroscopic observables and, in turn, allows the further analysis of the anisotropy and orientation dynamics as taken explicitly from the MD simulations. The red line in Figure 7.3(d) shows the anisotropy decay in the (1470; 1445) cm^{-1} region of the calculated 2D-IR spectra, i.e. in the same area used to extract the experimental anisotropies. The simulated curve matches the experimental dynamics very well. Only the short-time component of the decay is slightly faster, which is likely to be the effect of experimental time resolution. First of all, this confirms the validity of the MD simulations and calculated orientation dynamics. Secondly, the theory-experiment match indicates the absence of intermolecular hopping of vibrational excitations. Intermolecular energy transfer is not included in the theoretical calculations and, in case it would play a role, the experimental anisotropy should decay faster as seen in other materials with fast vibrational excitation transfer.[65,234] Finally, the validated MD calculations can be used to identify the molecular picture behind the two observed timescales in anisotropy dynamics.
It is first verified that the anisotropy decay is due to rotation and not intramolecular vibrational population transfer. Simulating the 2D-IR spectra and extracting the anisotropy decay with fixed molecular orientations gives an anisotropy of 0.4 for all waiting times demonstrating that the origin of the observed decay is solely due to reorientation of the MA ions. This is not the case for the asymmetric peak at

1570 cm^{-1}, where two degenerate modes rapidly mix. The 2D-IR spectra at 150 K and 450 K were calculated and the extracted transient anisotropies are shown in Figure 7.3(d). It is apparent that at 150 K the anisotropy does not decay below 0.3, and that the anisotropy dynamics at 450 K are faster and lead to a nearly complete decay at 6 ps. Previous studies indicated a preferential orientation of the MD dipole parallel to the lattice axes[221] suggesting that at low temperatures the molecular dipole axis may be pinned to the lattice axes (Fig. 7.4(c), left). In Figure 7.4(d) histograms of the distribution of the angle between the molecular axis and the nearest of the lattice axis, which are equivalent in the simulated pseudo-cubic symmetry, are illustrated for the three simulated temperatures normalized to a random isotropic distribution of dipole directions. For 150 and 300 K there is a larger probability of finding an angle below 30 degree and lower probability of finding a larger angle. The 450 K data hardly deviate from the isotropic distribution. This suggests that the MA dipole preferentially points along one of the three lattice axes and is at 300 K confined within a semi-cone angle of about 30 degrees from each of these axes. We can consider a wobbling-in-a-cone/angular jump model,[239] where the rotational anisotropy is given by the equation:

$$r(t) = \frac{2}{5}\left(S^2 \exp\left\{ -\frac{t}{\tau_{jump}} \right\} + \left(1 - S^2\right) \exp\left\{ -\frac{1}{\tau_{jump}} + \frac{1}{\tau_{wob}} t \right\} \right) \qquad (7.1)$$

and where r(t) is the anisotropy, τ_{jump} is the effective jump time scale for 90 degree jumps, τ_{wob} is the time scale of the wobbling motion, and S is a constant depending on the semi-cone angle, Θ, of the wobbling motion given by the equation

$$S = \cos(\Theta)(1 + \cos(\Theta)/2 \qquad (7.2)$$

A biexponential fit to the simulated data results in a semi-cone angle of 31 degrees (S=0.625) from both the 150 K and 300 K data. The wobbling-in-a-cone timescale slows down from 130 fs to 1.1 ps, when cooling from 300 K to 150 K. We note that at 300 K the wobbling time fits well the 150 cm^{-1} vibration previously observed using Raman spectroscopy and assigned to librational motion,[240] which is the same as wobbling-in-a-cone motion. The time scale for the jump type motion is too long to fit for 150 K and 2.7 ps at 300 K. The 450 K data can be fitted with a single time scale of 570 fs and a small offset of 0.07 suggesting that the jump motion at this temperature is accelerated and no longer confined by the barriers. The small offset hints at the presence of an optimal orientation of the cation along one of the crystal axes, but may also be due to the error bars in the simulation data as at 450 K the cubic crystal structure prevails. It should be noted that all simulations were done for the pseudo-cubic phase and that experimentally at low temperature the structure is orthorhombic. This phase transition is thus not accounted for in the present simulations.

The combined experimental and theoretical results demonstrate that in the studied samples at 300 K the MA dipoles reorient on two distinct time scales. These are interpreted as a fast local wobbling-in-a-cone motion and slow 90 degrees jumps, respectively. We cannot fully exclude the presence of an additional slower decay

component, but the upper limit for the contribution of such a component is in the order of 0.07, corresponding to $< 20\%$ of all MA molecules moving on a slower time scale. These measurements thus dismisses the existence of large, slowly interconverting ferroelectric domains. However, we cannot rule out that the jump motion involves concerted motion of correlated MA domains.

7.3 CONCLUSION

To conclude, ultrafast 2D-IR vibrational anisotropy spectroscopy on the NH_3^+ symmetric bending vibration of MA and ab-initio MD were used to resolve in time the methylammonium cation rotation in different $MAPbI_3$ perovskites films. Excellent agreement was found between the experiment and the simulations. For all materials we observed similar dynamics with two characteristic timescales of molecular motion, which we identified as a fast wobbling-in-a-cone motion around the lattice axes and a relatively slow ($\sim$3 ps) jump-like reorientation of the molecular dipole (aligned with C–N-axis) between the different lattice axes. These timescales are directly relatable to the contribution to the dielectric response that comes from the molecular motion. Such a contribution is of extreme importance for the device physics of these materials, as the stability of excitons, polarons, and other quasi-particle states will depend on the response time of the dielectric constant. These findings represent the first real-time measurement of organic cation motion in organic-inorganic perovskite materials and provide access to the molecular mechanisms behind the optoelectronic properties of these materials.

Chapter 8

Organic Cation Rotation and Immobilisation in Pure and Mixed Methylammonium Lead-Halide Perovskites

Three-dimensional lead-halide perovskites have attracted a lot of attention due to their ability to combine solution processing with outstanding optoelectronic properties. Despite their soft ionic nature these materials demonstrate a surprisingly low level of electronic disorder resulting in sharp band edges and narrow distributions of the electronic energies. Understanding how structural and dynamic disorder impacts the optoelectronic properties of these perovskites is important for many applications. Here we combine ultrafast two-dimensional vibrational spectroscopy and molecular dynamics simulations to study the dynamics of the organic methylammonium (MA) cation orientation in a range of pure and mixed tri-halide perovskite materials. For pure $MAPbX_3$ (X=I, Br, Cl) perovskite films, we observe that the cation dynamics accelerate with decreasing size of the halide atom. This acceleration is surprising given the expected strengthening of the hydrogen bonds between the MA and the smaller halide anions, but can be explained from the increase in the polarizability with the size of halide. Much slower dynamics, up to partial immobilisation of the organic cation, are observed in the mixed $MAPb(Cl_xBr_{1-x})_3$ and $MAPb(Br_xI_{1-x})_3$ alloys, which we associate with symmetry breaking within the perovskite unit cell. The observed dynamics are essential for understanding the effects of structural and dynamical disorder in perovskite-based optoelectronic systems.

8.1 INTRODUCTION

Hybrid organic-inorganic perovskite materials have recently attracted significant attention because devices made from these materials show outstanding optoelectronic properties while the fabrication procedures are themselves very simple, for example, spin coating followed by low-temperature annealing.[196,241,242] Films of methylammonium lead iodide ($MAPbI_3$) are among the most investigated materials in the family of the 3D perovskites because they demonstrate a particularly high potential for use in thin-film solar cells with certified power conversion efficiencies exceeding 21%.[196,243] At the same time, the ease with which the bandgap of this compound can be tuned by merely changing the ionic composition opens up a whole new dimension for possible optoelectronic applications.[197,244] The bandgap can be tuned across the entire visible spectrum by varying the nature of the halide ions from I^- to Br^- and Cl^-, which makes this material particularly promising for tandem solar cell, light emitting diode (LEDs) and laser applications.[197,198,244–247] A precise and gradual control of the band structure is achieved in the mixed halide $MAPb(Cl_xBr_{1-x})_3$ and $MAPb(Br_xI_{1-x})_3$ systems. It has been recently shown that specific combinations of ions lead to the formation of alloys with well-defined intermediate-size bandgaps, surprisingly sharp band edges, and narrow distributions of emissive states.[244,248]

The structural properties of such 'soft' hybrid perovskite materials are expected to lie at the core of their optoelectronic performance. Interionic interaction opens many degrees of freedom and allows molecular motions on multiple time and length scales.[249] There are various ways in which the structural dynamics of hybrid perovskites could affect their optoelectronic properties, and to date a number of such potentially important effects have been predicted and/or observed,[250–257] including bandgap and exciton binding energy modulation,[258] ferroelectric alignment,[259,260] polaronic localisation of excited states,[251,261] charge transport[262] and assistance in water percolation.[263]

Relatively limited information is available about the molecular-scale dynamics in these systems despite their clear importance. The motions are expected to occur on multiple timescales, and these include both ultrafast cation rotations and vibrational motions of the inorganic lattice. It is worth pointing out that these structural dynamics may be heterogeneous and may vary throughout the material depending on the microscopic composition and local structure of the perovskite. All this calls for advanced spectroscopic methods and theoretical approaches able to identify and interpret the complex variety of molecular-level processes. Substantial progress towards understanding the dynamics of $MAPbI_3$ materials was achieved using a range of techniques[264] including simulations,[265,266] quasi-elastic neutron scattering,[225,267,268] NMR[217] as well as electronic[269] and vibrational[270–272] spectroscopy. At the same time, less is known about the structural dynamics of the Br^- and Cl^- systems.[273] Even fewer studies have focused on the mixed perovskites and the question as to how the structure of these materials changes as a function of their composition.[274–276]

In the previous chapter, we developed a method to directly track the orientational dynamics of the MA cations within the lead-halide lattice. We applied this method

to $MAPbI_3$ films and observed two characteristic time constants of motion. Using ab-initio molecular dynamics simulations, we identified the observed dynamics as (i) fast (∼300 fs) 'wobbling-in-a-cone' motions of the MA ions around the crystal axes and (ii) relatively slow (∼3 ps) jump-like reorientations of the organic ions with respect to the lead-iodide lattice. Within our ∼10 ps experimental window we did not witness any long-term orientation memory nor pronounced immobilisation of the MA cations. We found no evidence for the suggestion in the literature that the rearrangement of the MA would be responsible for the hysteretic behaviour observed in perovskite photovoltaic devices.[221,224]

Here we extend our previous approach to the chloride- and bromide- perovskites, as well as to mixed-halide systems. We observe that for pure $MAPbI_3$, $MAPbBr_3$ and $MAPbCl_3$ films the cation dynamics accelerate with decreasing size of the halide atom and consequent shrinking unit cell of the crystal. We observe a stronger slowing, down to a partial immobilisation of the cation, in the mixed $MAPb(Cl_xBr_{1-x})_3$ and $MAPb(Br_xI_{1-x})_3$ alloys. We associate these slower dynamics with a symmetry breaking in the unit cell. We speculate that cation immobilisation can affect the local dielectric environment and contribute to the increased static but decreased dynamic disorder in mixed-halide perovskite materials.

8.2 RESULTS AND DISCUSSION

8.2.1 LINEAR INFRARED SPECTROSCOPY

All samples used in this study were prepared by A. Sadhanala, C. Müller, R. Lovrincic and Z. Chen. Figure 8.1 shows the IR absorption spectra of the pure and mixed perovskite films under study. Here we focus on the region 1350–1700 cm^{-1} where the strongest mode (∼1475 cm^{-1}) corresponds to the NH_3^+ bending vibrations.[230] The bimodal structure of the absorption bands originates from the splitting of three degenerate vibrations into one symmetric (∼1475 cm^{-1}) and two antisymmetric (∼1580 cm^{-1}) normal modes. The low-frequency peak corresponds to the symmetric mode whose transition dipole moment is aligned with the C–N axis of the MA molecule. Following the work in the previous chapter, we use the transient anisotropy of this vibration to monitor the rotational dynamics of the organic cation. We see that the frequency of the symmetric NH_3^+ bending vibration of the MA cation decreases with increasing size of the halide anion. There are two effects that probably contribute to this redshift. The first effect is the decreasing strength of the $NH\cdots X^-$-hydrogen bond with increasing size of the X^- anion, because bending vibrations typically show a positive correlation between hydrogen-bond strength and frequency.[277] The second effect that contributes to the observed redshift is a particular local-field effect described in ref.[230] Specifically, the MA vibrations redshift due to the fact that they are embedded inside and interact with a polarizable medium—the lead-halide lattice, whose polarizability increases with increasing anion size.[230] The vibrational absorption spectrum of $MAPb(Cl_xI_{1-x})_3$ can be represented as a linear superposition of the absorption spectra of $MAPbI_3$ and $MAPbCl_3$. This is in agreement with previous reports,

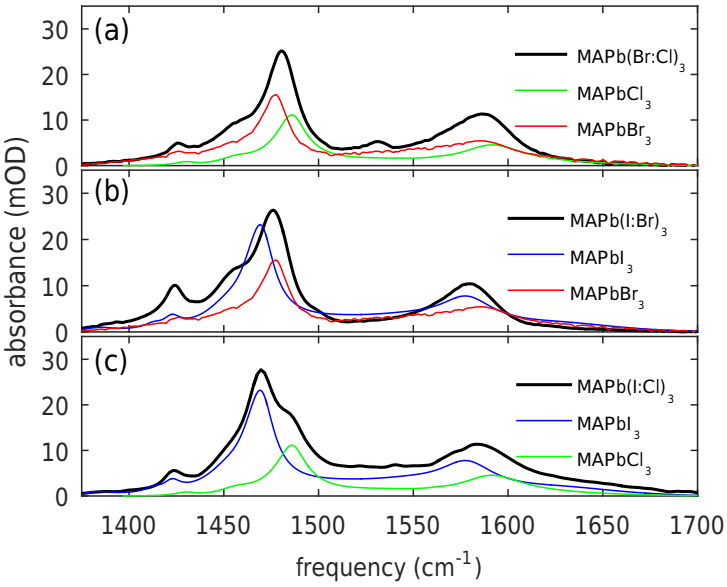

FIGURE 8.1. Linear infrared spectra of the studied materials. Every panel shows the spectrum of one hybrid sample and the corresponding pure halide spectra (a) $MAPb(Cl_{0.35}I_{0.65})_3$, (b) $MAPb(Br_{0.6}I_{0.4})_3$ and (c) $MAPb(Cl_{0.6}Br_{0.4})_3$.

showing that $MAPb(Cl_xI_{1-x})_3$ does not form a homogeneous mixture but phase segregates into pure iodide and chloride phases.[278,279] In contrast, the vibrational spectra of $MAPb(Br_xI_{1-x})_3$ and $MAPb(Cl_xBr_{1-x})_3$ contain a single narrow peak for each mode, positioned between the vibrational frequencies observed for the pure halide systems. This corroborates the previous observation that these halides are well mixed at the level of the perovskite unit cell; the MA ions experience a homogenous and relatively narrow distribution of local environments[244,248]

8.2.2 2DIR SPECTROSCOPY OF PURE-HALIDE PEROVSKITES

To study the orientational dynamics of the organic cations, we performed 2DIR anisotropy experiments on the symmetric NH_3^+ bending vibration of the MA ions. Detailed information about the experimental configuration can be found in Chapter 3. Briefly, 2DIR spectroscopy can be viewed as a version of infrared pump-probe spectroscopy, in which the transient signals are recorded as a function of both the probe and the pump frequency. This allows one to study phenomena such as mode coupling and vibrational energy transfer[77,238] In addition, the fact that the signal is spread along two frequency dimensions allows for a better separation of multiple, overlapping, resonances compared to pump-probe spectroscopy. Polarization-resolved detection of the probe pulse allows for disentanglement of the 2DIR signal into an isotropic and anisotropic contribution. The former gives direct access to the relaxation dynamics, and the latter allows one to track the reorientation of the

transition dipoles (and thereby the orientational motions of chemical groups). For example, the transition dipole of the symmetric NH_3^+ bending vibration is aligned with the C–N axis of the MA cation, so that the transient anisotropy decay of this transition follows the orientation of the cation.

Figure 8.2 shows the isotropic 2DIR spectra of the studied materials. Two dominant features can be seen in every spectrum: a negative (orange) peak originating from the depletion of the vibrational ground state and stimulated emission from the first excited state; and a positive (blue) peak at a lower frequency due to excited state absorption (ESA). Interestingly, in all samples except $MAPb(Cl_xI_{1-x})_3$, the 2D lineshapes are symmetric and show no elongation along the diagonal, which points to weak inhomogeneous broadening of this vibrational mode. This lack of diagonal elongation (i.e. inhomogeneous broadening) suggests that the MA ions experience a narrow distribution of local environments in both $MAPb(Br_xI_{1-x})_3$ and $MAPb(Cl_xBr_{1-x})_3$. In contrast, $MAPb(Cl_xI_{1-x})_3$ shows a pronounced elliptical line shape which can be interpreted as a superposition of the 2DIR spectra of the chloride and iodide perovskites. We observe no sign of cross peaks between the chloride and iodide components, which confirms the presence of strong phase segregation[279] as well as a lack of interaction (or interconversion) between the MA cations in the different phases. In the previous chapter, we showed that the region around the ground-state bleach might be affected by a thermal response which makes it difficult to extract the molecular reorientation from this signal. Consequently, we focus on the anisotropy dynamics of the ESA region, which is not affected by the thermal signal. Figure 8.3(a) shows the transient anisotropy dynamics averaged over the central region of the excited state absorption (ESA) peaks for the pure-halide perovskites. In general, the dynamics involve two components similar to those which we have previously attributed to a confined wobbling (~300 fs) of the MA molecules and to jump-like reorientations between the halide unit cell facets. In order to extract the time constants associated with these motions we have fitted the previously used wobbling-in-a-cone relaxation model to the anisotropy decays. The resulting jump rates, cone semi-angles, and wobbling time constants are summarized in Table 1. Perhaps surprisingly, the general trend observed is that as we move to smaller halide atoms and smaller unit cell sizes (from I^- to Br^- and then to Cl^-) the reorientation of the MA ions accelerates. This acceleration is primarily due to the increased probability for the occurrence of large-angle jumps; the fast process associated with the wobbling motion seems unaffected and can be well described by the same time constant for all five samples. This can be understood in terms of the large-angle jumps being driven by the tilting modes of the inorganic perovskite cage, whereas the wobbling-motion is a characteristic of the molecule rattling within the inorganic cage.[280,281] The variation of the time constant for the large scale jumps qualitatively agrees with the shift in frequency for the coupled cage-organic modes.[282]

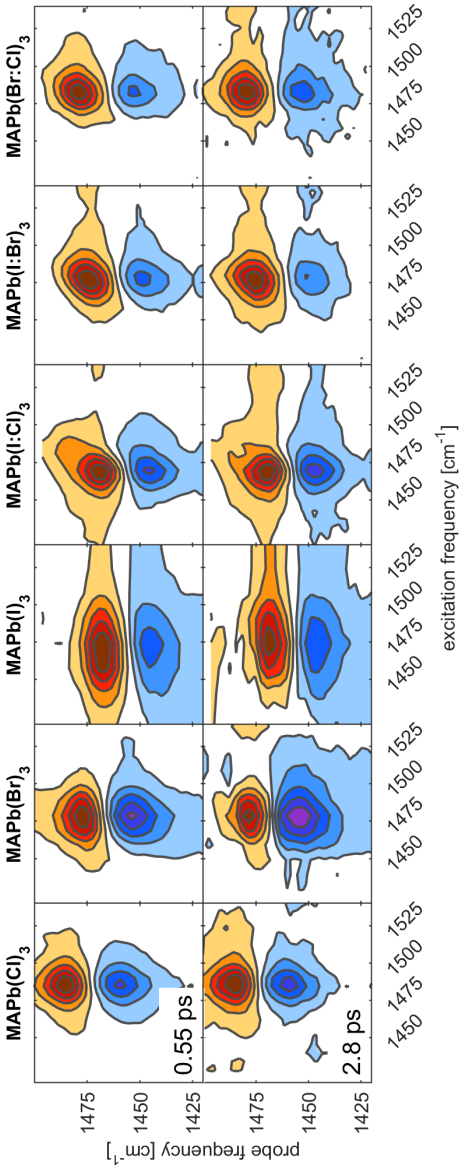

FIGURE 8.2. Isotropic 2D spectra for the studied materials at two different evolution times. The contour lines are placed at steps of 20% of the maximum amplitude. Red colors indicate negative absorption changes while blue colors indicate positive absorption changes.

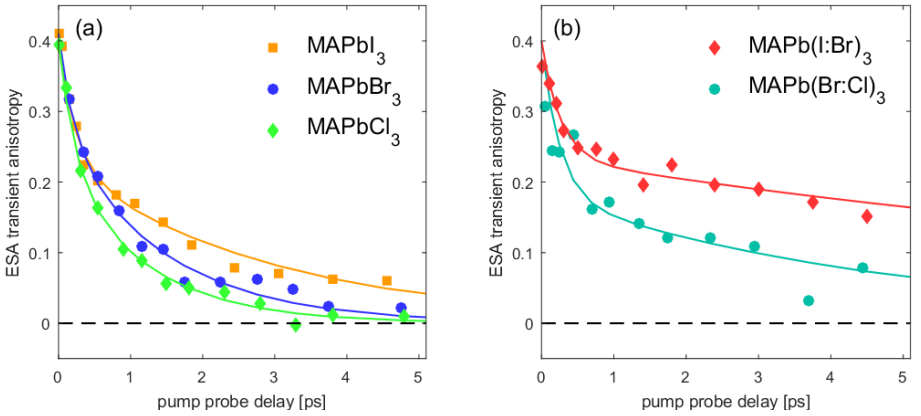

FIGURE 8.3. Transient anisotropy dynamics of the MA^+ ion as measured in the centre of the ESA for the $NH_3{}^+$ bending mode. The solid symbols show the experimentally determined anisotropy for the pure-halide perovskites in a) and for the mixed-halide perovskites in b). The lines show the fit with the wobbling-in-a-cone relaxation model.

Perovskite	Θ (°)	$\tau_{wob}(ps)$	τ_{jump} (ps)
$MAPbI_3$	34	0.3	3.0
$MAPbBr_3$	29	0.3	1.5
$MAPbCl_3$	34	0.3	1.2
$MAPb(I:Br)_3$	34	0.3	14.3
$MAPb(Br:Cl)_3$	40	0.3	5.0

TABLE I. Results of fitting the transient anisotropy data of all measured perovskite samples withe the jump/wobbling-in-a-cone relaxation model: $R(t) = 2/5e^{-t/\tau_{jump}}(S^2 + (1-S^2)e^{-t/\tau_{wob}})$ with $S = \cos(\Theta)(1+\cos(\Theta))/2$, , where Θ is the semi-cone angle, τ_{wob} and τ_{jump} are the wobbling and angle jump times scales, respectively.

8.2.3 MOLECULAR DYNAMICS SIMULATIONS OF PURE-HALIDE PEROVSKITES

In order to support our experimental findings T. C. Jansen and J. M. Frost have performed classical polarizable MD simulations with a $6 \times 6 \times 6$ unit cubic super cell. They have used these simulations to compute the second-order correlation function of the MA orientations. This correlation function is proportional to the experimentally determined transient anisotropy and is expressed as

$$R(t) = \frac{2}{5}\langle(\hat{\mu}(t)\cdot\hat{\mu}(0))\rangle \tag{8.1}$$

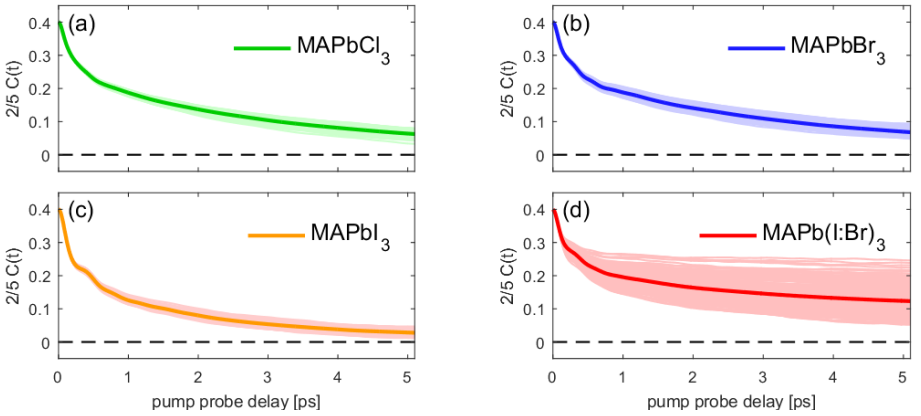

FIGURE 8.4. Rotational correlation functions of the MA ions as calculated based on classical molecular dynamics simulations for the pure-halide perovskites $MAPbCl_3$ (a), $MAPbBr_3$ (b) $MAPbI_3$ (c) and for the mixed-halide perovskite $MAPb(I:Br)_3$ (d). The faint lines represent the individual correlation functions for the different MA ions in the simulation while the thick lines represent the average over the complete calculated ensemble.

where $P_2(x)$ is the 2nd Legendre polynomial, $\hat{\mu}(t)$ is a unit vector pointing along the C–N-axis of the MA ion, and $\langle \ldots \rangle$ denotes an ensemble average. Clearly the anisotropy curves extracted from the MD trajectories show the same two-component dynamics as the experimental anisotropies (Figure 8.4(a)-(c)), however, the change of time scale for the slow component with respect to the change of the size of the halide ions is not reproduced.

At first sight it may seem surprising that the reorientation of the MA ions speeds up along the series $MAPbI_3 \rightarrow MAPbBr_3 \rightarrow MAPbCl_3$ because, as was already mentioned above, the NH···X^- hydrogen bond should strengthen when one moves in this direction. However, it should be realized that it is not the absolute strength of the hydrogen-bond, which determines the reorientation rate, but rather the activation barrier for moving between two equivalent hydrogen bonded orientations of the MA cation. This activation barrier is due to the fact that in the transition state the hydrogen bond is slightly elongated compared to the stable positions. Apparently the energy penalty for lengthening the hydrogen-bond in the transition state decreases in the direction $MAPbI_3 \rightarrow MAPbBr_3 \rightarrow MAPbCl_3$. This is probably due to the fact that the unit cell size decreases for this series, which in turn causes the potential confining the MA ions to become more spherically symmetric. A similar situation is encountered in the reorientation of water where molecules engaging in so-called bifurcated hydrogen bonds represent a low-energy transition state which speeds up reorientation.[283–285] The activation energy is apparently not well reproduced by the molecular dynamics simulations. This may not be surprising as the force field was not optimized for reproducing this. With a difference in rate in the order of a factor 2 this corresponds to a difference in the 2.5 kJ/mol range for the activation energy.

In the picture sketched above, we have described the reorientation of the MA ion

as an activated process, and we have attributed the change in reorientation rate to a change in activation barrier. However, the rate of an activated process is not only determined by the height of activation barrier but also by the dynamic changes in this barrier. Recent X-ray scattering experiments and DFT calculations suggested a moderate to strong coupling between the deformation or the inorganic lattice and the rotational motion of the organic cation.[225,281] Therefore, one could imagine that the reorientation of the MA ion is facilitated by the low-frequency vibrations of the lead-halide lattice. In this scenario, the modulation of the barrier (attempt frequency) for rotational motions is directly given by the frequency of these lattice vibrations. Recent infrared and Raman experiments have shown that the frequency of these lattice modes typically increases along the series $MAPbI_3 \rightarrow MAPbBr_3 \rightarrow MAPbCl_3$,[262,274,282] and this trend would be in line with the observed increased in the MA reorientation rate. Summarizing, according to this interpretation the speeding up of the MA reorientation with decreasing size of the halide anion is attributed to two effects that work in the same direction: an increasing influence of lead-halide lattice vibrations and a decreasing activation barrier. Next we turn to the mixed-halide perovskites.

8.2.4 2DIR SPECTROSCOPY OF MIXED-HALIDE PEROVSKITES

Figure 8.3(b) presents the transient anisotropy recorded at the centre of the ESA peaks for the $MAPb(Br_xI_{1-x})_3$ and $MAPb(Cl_xBr_{1-x})_3$ alloys. We do not discuss the anisotropy of the $MAPb(Cl_xI_{1-x})_3$ system as the linear and 2DIR spectra of this compound system show a trivial superposition of the chloride and iodide components (see Appendix Sec. 8.4, and Fig 8.2). The short-time dynamics in $MAPb(Br_xI_{1-x})_3$ and $MAPb(Cl_xBr_{1-x})_3$ are similar to those in the other pure- and mixed-halide systems, which indicates that the wobbling motions are well activated in all these materials. However, at longer time delays significantly slower anisotropy decays are observed for the mixed-halide perovskites, compared to the pure-halide perovskites. This slowing down indicates that the molecular jumps between different unit cell facets are strongly suppressed in the mixed-halide materials and that each individual MA cation remains predominantly oriented in a particular direction. This immobilisation can be understood by considering the activation energy for the rotational motion (similarly to the pure-halide systems). For the mixed-halide systems the halide lattice site is occupied by a statistical mixture of two halide ions. As a consequence the different MA orientations will no longer be characterized by identical hydrogen-bond strengths (as was the case for the pure-halide systems). Instead the statistical, usually asymmetric, distribution of the halide ions will lead to the presence of specific MA orientations which have an energetic minimum in their rotational potential. For these MA orientations the activation energy for a 90-degree jump will obviously be much larger compared to the case of the pure-halide perovskites, for which reorientation between stable positions is not associated with a change in hydrogen-bonding energy. This means that the random substitution of halogen sites within the inorganic cage effectively generates an asymmetric pocket which pins down the orientation of the MA ions.

8.2.5 MOLECULAR DYNAMICS SIMULATIONS OF MIXED-HALIDE PEROVSKITES

The mixed perovskites were modelled by T. C. Jansen using classical polarizable molecular dynamics simulations. This allowed using 6x6x6 super cells with 216 organic cations to obtain sufficient sampling of the different halogen environments. The halogen atoms were inserted in a statistical manner resulting in a heterogeneous distribution of unit cells with $x = 0.6$. Organic cations with anywhere from 3 to 11 Br^- ions in the first coordination sphere were found. Figure 8.4(d) presents the rotational correlation function for a set of individual MA cations (in the mixed $MAPb(Br_xI_{1-x})_3$ perovskite) as well as the overall ensemble average. As clearly seen from the individual pink transients the distribution of correlation functions is very broad for the mixed-halide systems, in contrast to the narrow distribution for individual cations in the pure-halide perovskites (Figure 8.4 (a)-(c)). As a general trend the jump time was found to be slower for cations surrounded by an equal number of Br^- and I^- ions than for cations in a more homogeneous environment. Considering the number of possible ways to construct these unit cells and the fact that every cation can form three hydrogen bonds, a complete analysis of the factors determining the slowdown was not possible. However, we can generally state that altering the symmetry of the unit cell should provide anisotropy and the preferred direction for the cation orientation. Changing the orientation in such way that the number of hydrogen bonds to a particular type of halogen is preserved should be more favourable as compared to when the type of halogen is changing. Interestingly, the observed immobilisation of the organic cation in mixed-halide perovskites correlates with a number of trends previously observed in material properties. For example, previous studies indicated that both the emissive bandwidth and the Urbach energy are persistently smaller in pure-halide systems compared to their respective mixtures.[244,248] Similar trends are observed in the structural measurements like XRD and in the charge transporting properties.[276] All these observations point to an increased level of disorder in mixed-halide systems compared to pure-halide systems. Our new results indicate that, at least as far as the organic cation is concerned, the static and dynamic disorders change differently upon mixing different halide ions in the material. The static disorder is clearly increased in mixed halide systems as observed in the elongation of 2D peaks in Figure 2.[286] At the same time, the dynamic motions are clearly suppressed by breaking the symmetry of the unit cell. With suppressed dynamics, the static dielectric constant will decrease (the molecules can no longer respond) potentially explaining the higher exciton binding energy reported for mixed $MAPb(Br_xI_{1-x})_3$ perovskites.[287] While we do not have direct evidence to associate the change in electronic properties with the variations in the cation dynamics, we believe that the observed correlation manifests a clear link between electronic and structural dynamics in perovskite materials.

8.3 CONCLUSION

We presented a 2D IR and MD simulation study of the orientational dynamics of the organic cation in a range of pure- and mixed-halide perovskite materials. In the pure halide materials $MAPbCl_3$, $MAPbBr_3$ and $MAPbI_3$ we observe that the reorientation of the organic cation slows down with increasing halide size. We ascribe this trend to a decreasing probability of the MA to perform large-angle jumps. In the mixed $MAPb(Cl_xBr_{1-x})_3$ and $MAPb(Br_xI_{1-x})_3$ alloys we observed a higher degree of static disorder and much slower structural dynamics down to partial immobilisation of the organic cations. We associate these effects with the symmetry breaking within the halide unit cell. The observed effects of the halide composition on the structural and dynamical properties of perovskite materials may be partly responsible for the previously observed variations in their optical and electronic properties.

8.4 APPENDIX

LINEAR COMBINATION OF FTIR SPECTRA

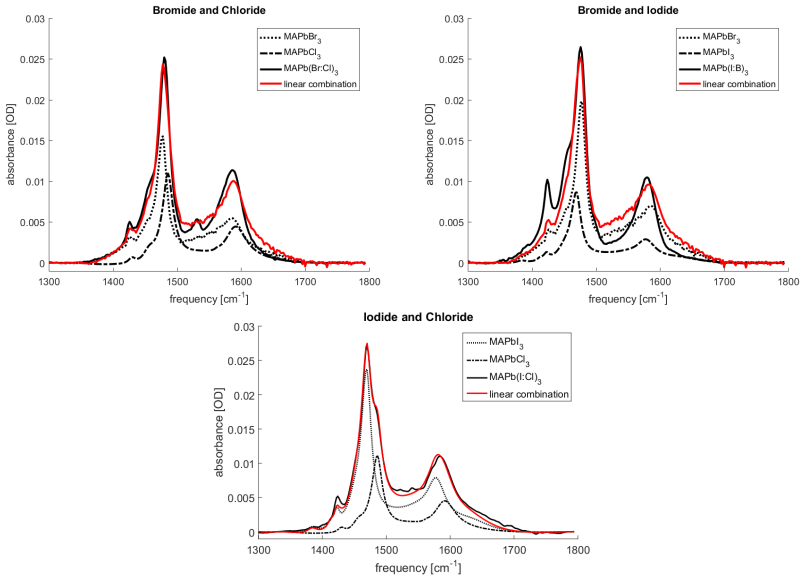

FIGURE 8.5. Comparison between the FTIR spectra of the mixed-halide perovskites and the best matching linear combination of the corresponding pure-halide perovskites spectra.

REPRESENTATIVE 2DIR DATA

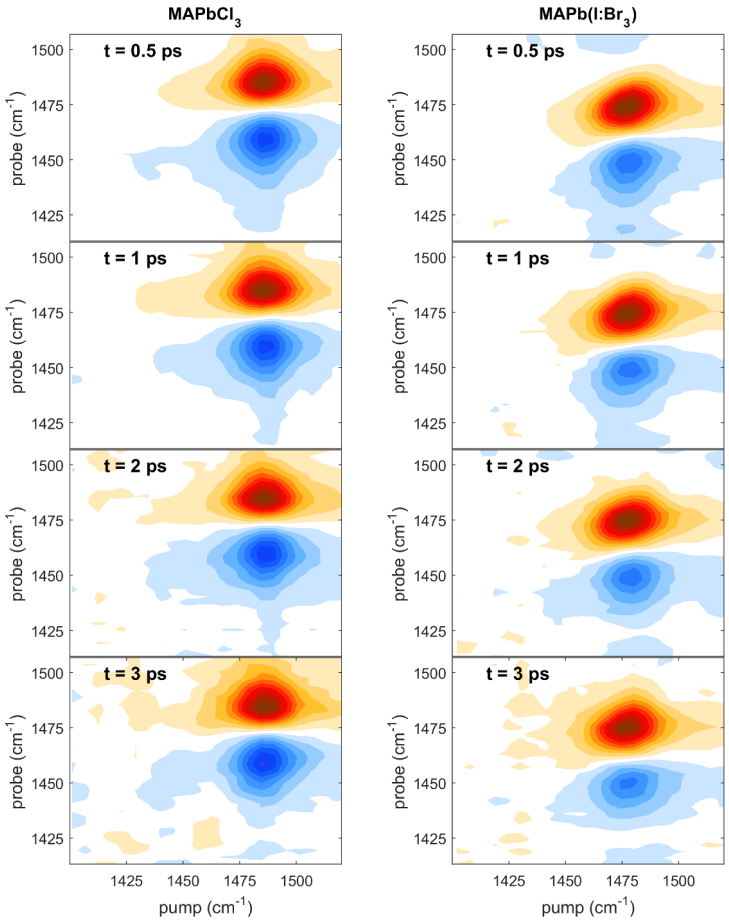

FIGURE 8.6. Typical 2DIR maps at different evolution times (isotropic component). The contour lines are positioned at steps of 10% of the maximum amplitude.

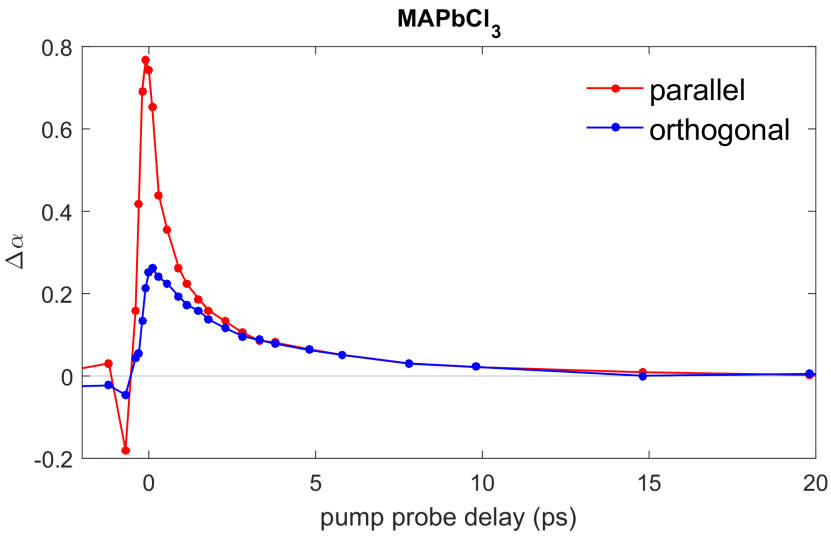

FIGURE 8.7. Typical absorption change in the ESA peak measured with parallel and orthogonal polarization of the probe pulse relative to the pump pulse. Lines are guides to the eye.

Bibliography

[1] H.E. Roscoe. *Spectrum Analysis: Six Lectures, Delivered in 1868, Before the Society of Apothecaries of London*. Macmillan and Company, 1873.

[2] H. Kayser and H.M. Konen. *Handbuch der Spectroscopie*. Number v. 5 in Handbuch der Spectroscopie. S. Hirzel, 1910.

[3] I. Newton. *Opticks: Or, A Treatise Of The Reflexions, Refractions, Inflexions and Colours Of Light: Also Two Treatises Of The Species and Magnitude Of Curvilinear Figures*. Smith and Walford, 1704.

[4] William Hyde Wollaston. A method of examining refractive and dispersive powers, by prismatic reflection. *Philosophical Transactions of the Royal Society of London*, 92:365–380, 1802.

[5] S.J. Lewis. *Spectroscopy in Science and Industry*. Blackie and Son, 1933.

[6] G. Kirchhoff and R. Bunsen. Chemische analyse durch spectralbeobachtungen. *Annalen der Physik*, 186(6):161–189, 1860.

[7] G. Kirchhoff and R. Bunsen. Xlii. chemical analysis by spectrum-observations. *Philosophical Magazine Series 4*, 22(148):329–349, 1861.

[8] W.M. Sears. *Helium: The Disappearing Element*. SpringerBriefs in Earth Sciences. Springer International Publishing, 2015.

[9] Samuel Krimm and Jagdeesh Bandekar. Vibrational spectroscopy and conformation of peptides, polypeptides, and proteins. *Advances in protein chemistry*, 38:181–364, 1986.

[10] William Herschel. Experiments on the refrangibility of the invisible rays of the sun. by william herschel, ll. d. f. r. s. *Philosophical Transactions of the Royal Society of London*, 90:284–292, 1800.

[11] Captain Abney and Lieut-Colonel Festing. On the influence of the atomic grouping in the molecules of organic bodies on their absorption in the infra-red region of the spectrum. *Philosophical Transactions of the Royal Society of London*, 172:887–918, 1881.

[12] W.W. Coblentz. *Investigations of Infra-red Spectra*. Carnegie Institution of Washington publication. Carnegie institution of Washington, 1905.

[13] F.W. Rose Jr. Infrared absorption of nineteen hydrocarbons including ten of high molecular weight. *Journal of Research, National Bureau of Standards*, 19:143–161, 1937.

[14] F.W. Rose. Quantitative analysis, with respect to the component structural groups, of the infrared (1 to 2 mu) molal absorptive indices of 55 hydrocarbons. *J Res Natl Bur Stand*, 20:129, 1938.

[15] G.M. Cooper and R.E. Hausman. *The Cell: A Molecular Approach*. ASM Press, 2007.

[16] Timo Partonen. Circadian clock proteins in mood regulation. *Frontiers in psychiatry*, 5, 2014.

[17] Miyuki Kabayama, Kazuto Sakoori, Kazuyuki Yamada, Veravej G. Ornthanalai, Maya Ota, Naoko Morimura, Kei-ichi Katayama, Niall P. Murphy, and Jun Aruga. Rines e3 ubiquitin ligase regulates mao-a levels and emotional responses. *The Journal of Neuroscience*, 33(32):12940–12953, 2013.

[18] Jeremy M. Berg, John L. Tymoczko, and Lubert Stryer. Protein structure and function. 2002.

[19] Julie S. Valastyan and Susan Lindquist. Mechanisms of protein-folding diseases at a glance. *Disease Models and Mechanisms*, 7(1):9–14, 2014.

[20] Sandra Vidak and Roland Foisner. Molecular insights into the premature aging disease progeria. *Histochemistry and cell biology*, 145(4):401–417, 2016.

[21] Andreas Barth. Infrared spectroscopy of proteins. *Biochimica et Biophysica Acta (BBA)-Bioenergetics*, 1767(9):1073–1101, 2007.

[22] Joachim A. Hering, Peter R. Innocent, and Parvez I. Haris. Automatic amide I frequency selection for rapid quantification of protein secondary structure from fourier transform infrared spectra of proteins. *Proteomics*, 2(7):839–849, 2002.

[23] Erik Goormaghtigh, Jean-Marie Ruysschaert, and Vincent Raussens. Evaluation of the information content in infrared spectra for protein secondary structure determination. *Biophysical journal*, 90(8):2946–2957, 2006.

[24] Lauren P DeFlores, Ziad Ganim, Rebecca A. Nicodemus, and Andrei Tokmakoff. Amide I'- II' 2D IR spectroscopy provides enhanced protein secondary structural sensitivity. *Journal of the American Chemical Society*, 131(9):3385–3391, 2009.

[25] Sander Woutersen and Peter Hamm. Structure determination of trialanine in water using polarization sensitive two-dimensional vibrational spectroscopy. *The Journal of Physical Chemistry B*, 104(47):11316–11320, November 2000.

[26] Igor V. Rubtsov. Relaxation-assisted two-dimensional infrared (RA 2DIR) method: Accessing distances over 10 å and measuring bond connectivity patterns. *Accounts of chemical research*, 42(9):1385–1394, 2009.

[27] Yung Sam Kim, Liu Liu, Paul H. Axelsen, and Robin M. Hochstrasser. 2D IR provides evidence for mobile water molecules in β-amyloid fibrils. *Proceedings of the National Academy of Sciences*, 106(42):17751–17756, 2009.

[28] Satoshi Fukuchi, Kazuo Hosoda, Keiichi Homma, Takashi Gojobori, and Ken Nishikawa. Binary classification of protein molecules into intrinsically disordered and ordered segments. *BMC structural biology*, 11(1):29, 2011.

[29] Zhirong Liu and Yongqi Huang. Advantages of proteins being disordered. *Protein Science*, 23(5):539–550, 2014.

[30] Vladimir N. Uversky, Vrushank Dave, Lilia M. Iakoucheva, Prerna Malaney, Steven J. Metallo, Ravi Ramesh Pathak, and Andreas C. Joerger. Pathological unfoldomics of uncontrolled chaos: Intrinsically disordered proteins and human diseases. *Chemical Reviews*, 114(13):6844–6879, 2014. PMID: 24830552.

[31] Vladimir N. Uversky. Targeting intrinsically disordered proteins in neurodegenerative and protein dysfunction diseases: another illustration of the d2 concept. *Expert review of proteomics*, 7(4):543–564, 2010.

[32] Tod D. Romo and Alan Grossfield. How fast is your camera? timescales for molecular motion and their role in restraining molecular dynamics. *Biophysical journal*, 106(12):2549–2551, 2014.

[33] Stefan Roberts, Michael Dzuricky, and Ashutosh Chilkoti. Elastin-like polypeptides as models of intrinsically disordered proteins. *FEBS letters*, 589(19PartA):2477–2486, 2015.

[34] Thomas Buergi and Alfons Baiker. Attenuated total reflection infrared spectroscopy of solid catalysts functioning in the presence of liquid-phase reactants. *Advances in Catalysis*, 50:227–283, 2006.

[35] Martin Fleischmann, Patrick J. Hendra, and A.J. McQuillan. Raman spectra of pyridine adsorbed at a silver electrode. *Chemical Physics Letters*, 26(2):163–166, 1974.

[36] A. Hartstein, J.R. Kirtley, and J.C. Tsang. Enhancement of the infrared absorption from molecular monolayers with thin metal overlayers. *Physical Review Letters*, 45(3):201, 1980.

[37] Lisa V. Brown, Ke Zhao, Nicholas King, Heidar Sobhani, Peter Nordlander, and Naomi J. Halas. Surface-enhanced infrared absorption using individual cross antennas tailored to chemical moieties. *Journal of the American Chemical Society*, 135(9):3688–3695, March 2013.

[38] Lisa V. Brown, Ke Zhao, Nancy J. Halas, and Peter J. Nordlander. Cross antennas for surface-enhanced infrared absorption (seira) spectroscopy of chemical moieties, March 13 2014. US Patent App. 14/209,310.

[39] Ronen Adato and Hatice Altug. In-situ ultra-sensitive infrared absorption spectroscopy of biomolecule interactions in real time with plasmonic nanoantennas. *Nature communications*, 4, 2013.

[40] J.D. Jackson. *Classical electrodynamics*. Wiley, 1975.

[41] E. Hecht. *Optics*. Pearson education. Addison-Wesley, 2002.

[42] D.J. Griffiths. *Introduction to Electrodynamics*. Prentice Hall, 1999.

[43] Craig F. Bohren and Donald R. Huffman. *Classical Theories of Optical Constants*, pages 226–267. Wiley-VCH Verlag GmbH, 2007.

[44] H. A. Lorentz. *The Theory of Electrons: And Its Applications to the Phenomena of Light and Radiant Heat*. CreateSpace Independent Publishing Platform, 2 2014.

[45] Neil W. Ashcroft. *Solid State Physics*. Thomson Press (India) Ltd, 1 edition, 12 2003.

[46] Ellen J. Zeman and George C. Schatz. An accurate electromagnetic theory study of surface enhancement factors for silver, gold, copper, lithium, sodium, aluminum, gallium, indium, zinc, and cadmium. *The Journal of Physical Chemistry*, 91(3):634–643, 1987.

[47] P. G. Etchegoin, E. C. Le Ru, and M. Meyer. An analytic model for the optical properties of gold. *The Journal of Chemical Physics*, 125(16), 2006.

[48] Stefan Alexander Maier. *Plasmonics: Fundamentals and Applications*. Springer, softcover reprint of hardcover 1st ed. 2007 edition, 12 2010.

[49] Paolo Biagioni, Jer-Shing Huang, and Bert Hecht. Nanoantennas for visible and infrared radiation. *Reports On Progress In Physics*, 75(2):024402, February 2012.

[50] Harald Ditlbacher, Andreas Hohenau, Dieter Wagner, Uwe Kreibig, Michael Rogers, Ferdinand Hofer, Franz R. Aussenegg, and Joachim R. Krenn. Silver nanowires as surface plasmon resonators. *Physical Review Letters*, 95:257403, Dec 2005.

[51] Jens Dorfmüller, Ralf Vogelgesang, R Thomas Weitz, Carsten Rockstuhl, Christoph Etrich, Thomas Pertsch, Falk Lederer, and Klaus Kern. Fabry-pérot resonances in one-dimensional plasmonic nanostructures. *Nano letters*, 9(6):2372–2377, 2009.

[52] Lukas Novotny. Effective wavelength scaling for optical antennas. *Physical Review Letters*, 98(26):266802–, June 2007.

[53] Ying Fang, Wei-Shun Chang, Britain Willingham, Pattanawit Swanglap, Sergio Dominguez-Medina, and Stephan Link. Plasmon emission quantum yield of single gold nanorods as a function of aspect ratio. *ACS Nano*, 6(8):7177–7184, 2012. PMID: 22830934.

[54] Colleen L. Nehl and Jason H. Hafner. Shape-dependent plasmon resonances of gold nanoparticles. *Journal of Materials Chemistry*, 18:2415–2419, 2008.

[55] P.E. Powers. *Fundamentals of Nonlinear Optics*. CRC Press, 2011.

[56] Robert W Boyd. *Nonlinear optics*. Academic press, 2003.

[57] W.S. Struve. *Fundamentals of Molecular Spectroscopy*. Wiley, 1989.

[58] M.C. Gupta. *Atomic And Molecular Spectroscopy*. New Age International (P), 2007.

[59] S. Svanberg. *Atomic and Molecular Spectroscopy: Basic Aspects and Practical Applications*. Advanced Texts in Physics. Springer Berlin Heidelberg, 2003.

[60] J.J. Sakurai and S.F. Tuan. *Modern Quantum Mechanics*. Advanced book program. Benjamin/Cummings Pub., 1985.

[61] C. Cohen-Tannoudji, B. Diu, and F. Laloe. *Quantum Mechanics, 2 Volume Set*. Wiley, 1992.

[62] Giovanni Lipari and Attila Szabo. Effect of librational motion on fluorescence depolarization and nuclear magnetic resonance relaxation in macromolecules and membranes. *Biophysical journal*, 30(3):489, 1980.

[63] Y.L.A. Rezus and H.J. Bakker. On the orientational relaxation of HDO in liquid water. *Journal of Chemical Physics*, 123(11):114502–114502, 2005.

[64] H. J. Bakker and J. L. Skinner. Vibrational spectroscopy as a probe of structure and dynamics in liquid water. *Chemical Reviews*, 110(3):1498–1517, 2010. PMID: 19916491.

[65] Sander Woutersen and Huib J. Bakker. Resonant intermolecular transfer of vibrational energy in liquid water. *Nature*, 402(6761):507–509, 1999.

[66] L. Piatkowski, K.B. Eisenthal, and H.J. Bakker. Ultrafast intermolecular energy transfer in heavy water. *Physical Chemistry Chemical Physics*, 11(40):9033–9038, 2009.

[67] P. Hamm and M. Zanni. *Concepts and Methods of 2D Infrared Spectroscopy*. Cambridge University Press, 2011.

[68] Olaf F.A. Larsen, Pavol Bodis, Wybren Jan Buma, Jeffrey S. Hannam, David A Leigh, and Sander Woutersen. Probing the structure of a rotaxane with two-dimensional infrared spectroscopy. *Proceedings of the National Academy of Sciences of the United States of America*, 102(38):13378–13382, 2005.

[69] Michael D Fayer. *Ultrafast infrared and Raman spectroscopy*, volume 26. CRC Press, 2001.

[70] Adriana Huerta-Viga, Sérgio R. Domingos, Saeed Amirjalayer, and Sander Woutersen. A salt-bridge structure in solution revealed by 2D-IR spectroscopy. *Physical Chemistry Chemical Physics*, 16(30):15784–15786, 2014.

[71] Robin M. Hochstrasser. Two-dimensional ir-spectroscopy: polarization anisotropy effects. *Chemical Physics*, 266:273 – 284, 2001.

[72] Sander Woutersen, Yuguang Mu, Gerhard Stock, and Peter Hamm. Subpicosecond conformational dynamics of small peptides probed by two-dimensional vibrational spectroscopy. *Proceedings of the National Academy of Sciences*, 98(20):11254–11258, 2001.

[73] K.E. Shuler. *Advances in Chemical Physics, Volume 15: Stochastic Processes in Chemical Physics*. Advances in Chemical Physics. Wiley, 2009.

[74] V.M. Kenkre, A. Tokmakoff, and M.D. Fayer. Theory of vibrational relaxation of polyatomic molecules in liquids. *The Journal of chemical physics*, 101(12):10618–10629, 1994.

[75] Sean T. Roberts, Joseph J. Loparo, and Andrei Tokmakoff. Characterization of spectral diffusion from two-dimensional line shapes. *The Journal of chemical physics*, 125(8):084502, 2006.

[76] Qi Guo, Philip Pagano, Yun-Liang Li, Amnon Kohen, and Christopher M. Cheatum. Line shape analysis of two-dimensional infrared spectra. *The Journal of Chemical Physics*, 142(21):212427, 2015.

[77] Peter Hamm, Manho Lim, and Robin M. Hochstrasser. Structure of the amide I band of peptides measured by femtosecond nonlinear-infrared spectroscopy. *The Journal of Physical Chemistry B*, 102(31):6123–6138, 1998.

[78] Jan Helbing and Peter Hamm. Compact implementation of Fourier transform two-dimensional IR spectroscopy without phase ambiguity. *Journal of the Optical Society of America B: Optical Physics*, 28(1):171–178, January 2011.

[79] P.R. Griffiths, J.A. De Haseth, and J.D. Winefordner. *Fourier Transform Infrared Spectrometry*. Chemical Analysis: A Series of Monographs on Analytical Chemistry and Its Applications. Wiley, 2007.

[80] B.E.A. Saleh and M.C. Teich. *Fundamentals of Photonics*. Wiley Series in Pure and Applied Optics. Wiley, 2007.

[81] R.N. Bracewell. *The Fourier Transform and Its Applications*. Electrical engineering series. McGraw Hill, 2000.

[82] T. Butz. *Fourier Transformation for Pedestrians*. Undergraduate Lecture Notes in Physics. Springer International Publishing, 2015.

[83] Robert H. Norton and Reinhard Beer. New apodizing functions for fourier spectrometry. *Journal of the Optical Society of America*, 66(3):259–264, Mar 1976.

[84] E. Bartholdi and R.R. Ernst. Fourier spectroscopy and the causality principle. *Journal of Magnetic Resonance (1969)*, 11(1):9–19, 1973.

[85] R.P. Feynman, R.B. Leighton, and M.L. Sands. *The Feynman Lectures on Physics*. Number v. 1 in The Feynman Lectures on Physics. Addison-Wesley, 1963.

[86] B.C. Starcher. Elastin and the lung. *Thorax*, 41(8):577–585, 1986.

[87] Sandra W. Foster, J.A .and Curtiss. The regulation of lung elastin synthesis. *American Journal of Physiology-Lung Cellular and Molecular Physiology*, 259(2):L13–L23, 1990.

[88] Barry C. Starcher. Lung elastin and matrix. *CHEST Journal*, 117(5_suppl_1):229S–234S, 2000.

[89] L. Robert, M.P. Jacob, C. Frances, G. Godeau, and W. Hornebeck. Interaction between elastin and elastases and its role in the aging of the arterial wall, skin and other connective tissues. a review. *Mechanisms of ageing and development*, 28(2):155–166, 1984.

[90] Hans Oxlund, Jan Manschot, and A Viidik. The role of elastin in the mechanical properties of skin. *Journal of biomechanics*, 21(3):213–218, 1988.

[91] C. Frances and L. Robert. Elastin and elastic fibers in normal and pathologic skin. *International journal of dermatology*, 23(3):166–179, 1984.

[92] Alkiviadis Tsamis, Jeffrey T Krawiec, and David A. Vorp. Elastin and collagen fibre microstructure of the human aorta in ageing and disease: a review. *Journal of the Royal Society Interface*, 10(83):20121004, 2013.

[93] Alpesh Patel, Benjamin Fine, Martin Sandig, and Kibret Mequanint. Elastin biosynthesis: the missing link in tissue-engineered blood vessels. *Cardiovascular research*, 71(1):40–49, 2006.

[94] L. Debelle and A.M. Tamburro. Elastin: molecular description and function. *The International Journal of Biochemistry & Cell Biology*, 31(2):261–272, 1999.

[95] D.W. Urry, M.M. Long, B.A. Cox, T. Ohnishi, L.W. Mitchell, and M. Jacobs. The synthetic polypentapeptide of elastin coacervates and forms filamentous aggregates. *Biochimica et Biophysica Acta (BBA) - Protein Structure*, 371(2):597–602, 1974.

[96] Herald Reiersen, Anthony R. Clarke, and Anthony R. Rees. Short elastin-like peptides exhibit the same temperature-induced structural transitions as elastin polymers: implications for protein engineering1. *Journal of Molecular Biology*, 283(1):255–264, 1998.

[97] Catherine M. Bellingham, Margo A. Lillie, John M. Gosline, Glenda M. Wright, Barry C. Starcher, Allen J. Bailey, Kimberly A Woodhouse, and Fred W. Keeley. Recombinant human elastin polypeptides self-assemble into biomaterials with elastin-like properties. *Biopolymers*, 70(4):445–455, 2003.

[98] Dana L. Nettles, Ashutosh Chilkoti, and Lori A. Setton. Applications of elastin-like polypeptides in tissue engineering. *Advanced Drug Delivery Reviews*, 62(15):1479–1485, 2010. Advances in Recombinant Polymers for Delivery of Bioactive Agents.

[99] W.F. Daamen, J.H. Veerkamp, J.C.M. van Hest, and T.H. van Kuppevelt. Elastin as a biomaterial for tissue engineering. *Biomaterials*, 28(30):4378–4398, 2007.

[100] Iqbal Massodi, Gene L. Bidwell III, and Drazen Raucher. Evaluation of cell penetrating peptides fused to elastin-like polypeptide for drug delivery. *Journal of Controlled Release*, 108:396–408, 2005.

[101] Dirk Schmaljohann. Thermo- and ph-responsive polymers in drug delivery. *Advanced Drug Delivery Reviews*, 58(15):1655–1670, 2006. 2006 Supplementary Non-Thematic Collection.

[102] Md Abu Khaled and Dan W. Urry. Nuclear overhauser enhancement demonstration of the type ii β-turn in repeat peptides of tropoelastin. *Biochemical and biophysical research communications*, 70(2):485–491, 1976.

[103] C.M. Venkatachalam and D.W. Urry. Development of a linear helical conformation from its cyclic correlate.β-spiral model of the elastin poly (pentapeptide)(vpgvg) n. *Macromolecules*, 14(5):1225–1229, 1981.

[104] Dan W. Urry. Entropic elastic processes in protein mechanisms. i. elastic structure due to an inverse temperature transition and elasticity due to internal chain dynamics. *Journal of protein chemistry*, 7(1):1–34, 1988.

[105] Bin Li, Darwin O.V Alonso, and Valerie Daggett. The molecular basis for the inverse temperature transition of elastin1. *Journal of Molecular Biology*, 305(3):581–592, 2001.

[106] Aliaksei Krukau, Ivan Brovchenko, and Alfons Geiger. Temperature-induced conformational transition of a model elastin-like peptide GVG $(VPGVG)_3$ in water. *Biomacromolecules*, 8(7):2196–2202, 2007.

[107] C. Nicolini, R. Ravindra, B. Ludolph, and R. Winter. Characterization of the temperature- and pressure-induced inverse and reentrant transition of the minimum elastin-like polypeptide GVG(VPGVG) by DSC, PPC, CD, and FT-IR spectroscopy. *Biophysical Journal*, 86(3):1385–1392, March 2004.

[108] Vesna Serrano, Wenge Liu, and Stefan Franzen. An infrared spectroscopic study of the conformational transition of elastin-like polypeptides. *Biophysical journal*, 93(7):2429–2435, 2007.

[109] Younhee Cho, Laura B. Sagle, Satoshi Iimura, Yanjie Zhang, Jaibir Kherb, Ashutosh Chilkoti, J. Martin Scholtz, and Paul S. Cremer. Hydrogen bonding of β-turn structure is stabilized in D_2O. *Journal of the American Chemical Society*, 131(42):15188–15193, 2009.

[110] Zeeshan Ahmed, Jonathan P. Scaffidi, and Sanford A. Asher. Circular dichroism and UV-resonance raman investigation of the temperature dependence of the conformations of linear and cyclic elastin. *Biopolymers*, 91(1):52–60, 2009.

[111] George J. Thomas, Betty Prescott, and Dan W. Urry. Raman amide bands of type-II β-turns in cyclo-$(VPGVG)_3$ and poly-(VPGVG), and implications for protein secondary-structure analysis. *Biopolymers*, 26(6):921–934, 1987.

[112] Dana Kurková, Jaroslav Kríz, Pavel Schmidt, Jirí Dybal, José Carlos Rodríguez-Cabello, and Matilde Alonso. Structure and dynamics of two elastin-like polypentapeptides studied by NMR spectroscopy. *Biomacromolecules*, 4(3):589–601, 2003.

[113] Rachel Glaves, Marcel Baer, Eduard Schreiner, Raphael Stoll, and Dominik Marx. Conformational dynamics of minimal elastin-like polypeptides: The role of proline revealed by molecular dynamics and nuclear magnetic resonance. *ChemPhysChem*, 9(18):2759–2765, 2008.

[114] Harald Nuhn and Harm-Anton Klok. Secondary structure formation and LCst behavior of short elastin-like peptides. *Biomacromolecules*, 9(10):2755–2763, 2008.

[115] Roger Rousseau, Eduard Schreiner, Axel Kohlmeyer, and Dominik Marx. Temperature-dependent conformational transitions and hydrogen-bond dynamics of the elastin-like octapeptide gvg (vpgvg): a molecular-dynamics study. *Biophysical journal*, 86(3):1393–1407, 2004.

[116] Joshua Lessing, Santanu Roy, Mike Reppert, Marcel Baer, Dominik Marx, Thomas La Cour Jansen, Jasper Knoester, and Andrei Tokmakoff. Identifying residual structure in intrinsically disordered systems: a 2D IR spectroscopic study of the GVGXPGVG peptide. *Journal of the American Chemical Society*, 134(11):5032–5035, 2012.

[117] Mike Reppert, Anish R. Roy, Jeremy O.B. Tempkin, Aaron R. Dinner, and Andrei Tokmakoff. Refining disordered peptide ensembles with computational amide I spectroscopy: Application to elastin-like peptides. *The Journal of Physical Chemistry B*, 2016.

[118] Matthias Buck. Trifluoroethanol and colleagues: cosolvents come of age. recent studies with peptides and proteins. *Quarterly reviews of biophysics*, 31(03):297–355, 1998.

[119] Danilo Roccatano, Giorgio Colombo, Marco Fioroni, and Alan E. Mark. Mechanism by which 2,2,2-trifluoroethanol/water mixtures stabilize secondary-structure formation in peptides: A molecular dynamics study. *Proceedings of the National Academy of Sciences*, 99(19):12179–12184, 2002.

[120] Rosalie L. M. Teeuwen, Han Zuilhof, Frits A. de Wolf, and Jan C. M. van Hest. Temperature-controlled positioning of fusion proteins in microreactors. *Soft Matter*, 5:2261–2268, 2009.

[121] Dan E. Meyer and Ashutosh Chilkoti. Purification of recombinant proteins by fusion with thermally-responsive polypeptides. *nature biotechnology*, 17:1112–1115, 1999.

[122] Valery V. Andrushchenko, Hans J. Vogel, and Elmar J. Prenner. Optimization of the hydrochloric acid concentration used for trifluoroacetate removal from synthetic peptides. *Journal of Peptide Science*, 13(1):37–43, 2007.

[123] S. Lotze, L.L.C. Olijve, and H.J. Voets, I.K.and Bakker. Observation of vibrational energy exchange in a type-iii antifreeze protein. *The Journal of Physical Chemistry B*, 118(30):8962–8971, 2014.

[124] Santanu Roy, Thomas L. C. Jansen, and Jasper Knoester. Structural classification of the amide I sites of a [small beta]-hairpin with isotope label 2DIR spectroscopy. *Physical Chemistry Chemical Physics*, 12:9347–9357, 2010.

[125] E. Vass, M. Kurz, R.K. Konat, and M. Hollósi. {FTIR} and {CD} spectroscopic studies on cyclic penta- and hexa-peptides. detailed examination of hydrogen bonding in β- and γ-turns determined by {NMR}. *Spectrochimica Acta Part A: Molecular and Biomolecular Spectroscopy*, 54(5):773–786, 1998.

[126] Satoshi Ohnishi, Akiko Koide, and Shohei Koide. Solution conformation and amyloid-like fibril formation of a polar peptide derived from a β-hairpin in the ospa single-layer β-sheet1. *Journal of Molecular Biology*, 301(2):477–489, 2000.

[127] Marina Ramirez-Alvarado, Luis Serrano, and Francisco J. Blanco. Conformational analysis of peptides corresponding to all the secondary structure elements of protein l b1 domain: Secondary structure propensities are not conserved in proteins with the same fold. *Protein science*, 6(1):162–174, 1997.

[128] Michael Jackson and Henry H. Mantsch. The use and misuse of FTIR spectroscopy in the determination of protein structure. *Critical reviews in biochemistry and molecular biology*, 30(2):95–120, 1995.

[129] F. Demmel, W. Doster, W. Petry, and A. Schulte. Vibrational frequency shifts as a probe of hydrogen bonds: thermal expansion and glass transition of myoglobin in mixed solvents. *European biophysics journal*, 26(4):327–335, 1997.

[130] H.J. Bakker, P.C.M. Planken, and A. Lagendijk. Role of solvent on vibrational energy transfer in solution. *Nature*, 347(6295):745–747, 1990.

[131] M. Fioroni, M.D. Diaz, K. Burger, and S. Berger. Solvation phenomena of a tetrapeptide in water/trifluoroethanol and water/ethanol mixtures: a diffusion NMR, intermolecular NOE, and molecular dynamics study. *Journal of the American Chemical Society*, 124(26):7737–7744, 2002.

[132] An-Suei Yang, Benjamin Hitz, and Barry Honig. Free energy determinants of secondary structure formation: III β-turns and their role in protein folding. *Journal of molecular biology*, 259(4):873–882, 1996.

[133] E. Gail Hutchinson and Janet M. Thornton. A revised set of potentials for β-turn formation in proteins. *Protein Science*, 3(12):2207–2216, 1994.

[134] Bin Li, Darwin O.V. Alonso, Brian J. Bennion, and Valerie Daggett. Hydrophobic hydration is an important source of elasticity in elastin-based biopolymers. *Journal of the American Chemical Society*, 123(48):11991–11998, 2001.

[135] William J. Cook, Howard Einspahr, Tina L. Trapane, Dan W. Urry, and Charles E. Bugg. Crystal structure and conformation of the cyclic trimer of a repeat pentapeptide of elastin, cyclo-(l-valyl-l-prolylglycyl-l-valylglycyl) 3. *Journal of the American Chemical Society*, 102(17):5502–5505, 1980.

[136] Tetsuji Yamaoka, Takumi Tamura, Yuuki Seto, Tomoko Tada, Shigeru Kunugi, and David A. Tirrell. Mechanism for the phase transition of a genetically engineered elastin model peptide (vpgig) 40 in aqueous solution. *Biomacromolecules*, 4(6):1680–1685, 2003.

[137] D.W. Urry, R.G. Shaw, and K.U. Prasad. Polypentapeptide of elastin: temperature dependence of ellipticity and correlation with elastomeric force. *Biochemical and biophysical research communications*, 130(1):50–57, 1985.

[138] Lukasz Szyc, Ming Yang, Erik T. J. Nibbering, and Thomas Elsaesser. Ultrafast vibrational dynamics and local interactions of hydrated dna. *Angewandte Chemie-international Edition*, 49(21):3598–3610, 2010.

[139] K. J. Tielrooij, N. Garcia-Araez, M. Bonn, and H. J. Bakker. Cooperativity in ion hydration. *Science*, 328(5981):1006–1009, May 2010.

[140] Joshua Manor, Prabuddha Mukherjee, Yu-Shan Lin, Hadas Leonov, James L. Skinner, Martin T. Zanni, and Isaiah T. Arkin. Gating mechanism of the influenza a m2 channel revealed by 1d and 2D IR spectroscopies. *Structure*, 17(2):247–254, February 2009.

[141] Peter Hamm, Jan Helbing, and Jens Bredenbeck. Two-dimensional infrared spectroscopy of photoswitchable peptides. *Annual Review of Physical Chemistry*, 59(1):291–317, May 2008.

[142] A. W. Smith, J. Lessing, Z. Ganim, C. S. Peng, A. Tokmakoff, S. Roy, T. L. C. Jansen, and J. Knoester. Melting of a beta-hairpin peptide using isotope-edited 2D IR spectroscopy and simulations. *Journal of Physical Chemistry B*, 114(34):10913–10924, September 2010.

[143] J. R. Zheng, K. Kwak, J. Asbury, X. Chen, I. R. Piletic, and M. D. Fayer. Ultrafast dynamics of solute-solvent complexation observed at thermal equilibrium in real time. *Science*, 309(5739):1338–1343, August 2005.

[144] Amanda Remorino, Ivan V. Korendovych, Yibing Wu, William F. DeGrado, and Robin M. Hochstrasser. Residue-specific vibrational echoes yield 3d structures of a transmembrane helix dimer. *Science*, 332(6034):1206–1209, 2011.

[145] Y. L. A. Rezus and H. J. Bakker. Observation of immobilized water molecules around hydrophobic groups. *Physical Review Letters*, 99(14):148301, October 2007.

[146] J. Christopher Love, Lara A. Estroff, Jennah K. Kriebel, Ralph G. Nuzzo, and George M. Whitesides. Self-assembled monolayers of thiolates on metals as a form of nanotechnology. *Chemical Reviews*, 105(4):1103–1170, March 2005.

[147] Martien A. Cohen Stuart, Wilhelm T. S. Huck, Jan Genzer, Marcus Mueller, Christopher Ober, Manfred Stamm, Gleb B. Sukhorukov, Igal Szleifer, Vladimir V. Tsukruk, Marek Urban, Francoise Winnik, Stefan Zauscher, Igor Luzinov, and Sergiy Minko. Emerging applications of stimuli-responsive polymer materials. *Nature Materials*, 9(2):101–113, February 2010.

[148] Daniel E. Rosenfeld, Zsolt Gengeliczki, Brian J. Smith, T. D. P. Stack, and M. D. Fayer. Structural dynamics of a catalytic monolayer probed by ultrafast 2D IR vibrational echoes. *Science*, 334(6056):634–639, 2011.

[149] Jan Philip Kraack, Davide Lotti, and Peter Hamm. Ultrafast, multidimensional attenuated total reflectance spectroscopy of adsorbates at metal surfaces. *Journal of Physical Chemistry Letters*, pages 2325–2329, June 2014.

[150] Palash Bharadwaj, Bradley Deutsch, and Lukas Novotny. Optical antennas. *Advances In Optics and Photonics*, 1(3):438–483, November 2009.

[151] R. Adato, A. A. Yanik, J. J. Amsden, D. L. Kaplan, F. G. Omenetto, M. K. Hong, S. Erramilli, and H. Altug. Ultra-sensitive vibrational spectroscopy of protein monolayers with plasmonic nanoantenna arrays. *Proc. Natl. Acad. Sci. USA*, 106(46):19227–19232, November 2009.

[152] Frank Neubrech, Annemarie Pucci, Thomas Walter Cornelius, Shafqat Karim, Aitzol García-Etxarri, and Javier Aizpurua. Resonant plasmonic and vibrational coupling in a tailored nanoantenna for infrared detection. *Physical Review Letters*, 101(15):157403–, October 2008.

[153] Heykel Aouani, Hana Sipova, Mohsen Rahmani, Miguel Navarro-Cia, Katerina Hegnerova, Jiri Homola, Minghui Hong, and Stefan A. Maier. Ultrasensitive broadband probing of molecular vibrational modes with multifrequency optical antennas. *ACS Nano*, 7(1):669–675, January 2013.

[154] Daniel Dregely, Frank Neubrech, Huigao Duan, Ralf Vogelgesang, and Harald Giessen. Vibrational near-field mapping of planar and buried three-dimensional plasmonic nanostructures. *Nature Communications*, 4:2237, July 2013.

[155] A. Bouhelier, M. Beversluis, A. Hartschuh, and L. Novotny. Near-field second-harmonic generation induced by local field enhancement. *Physical Review Letters*, 90(1):013903, January 2003.

[156] M. Lippitz, M. A. van Dijk, and M. Orrit. Third-harmonic generation from single gold nanoparticles. *Nano Letters*, 5(4):799–802, April 2005.

[157] M. Danckwerts and L. Novotny. Optical frequency mixing at coupled gold nanoparticles. *Physical Review Letters*, 98(2):026104, January 2007.

[158] Yu Zhang, Fangfang Wen, Yu-Rong Zhen, Peter Nordlander, and Naomi J. Halas. Coherent fano resonances in a plasmonic nanocluster enhance optical four-wave mixing. *Proceedings of the National Academy of Sciences of the United States of America*, 110(23):9215–9219, June 2013.

[159] P. M. Donaldson and P. Hamm. Gold nanoparticle capping layers: Structure, dynamics, and surface enhancement measured using 2D-IR spectroscopy. *Angewandte Chemie-international Edition*, 52(2):634–638, 2013.

[160] P. Alonso-Gonzalez, P. Albella, M. Schnell, J. Chen, F. Huth, A. Garcia-Etxarri, F. Casanova, F. Golmar, L. Arzubiaga, L. E. Hueso, J. Aizpurua, and R. Hillenbrand. Resolving the electromagnetic mechanism of surface-enhanced light scattering at single hot spots. *Nature Communications*, 3:684, February 2012.

[161] Nche T. Fofang, Nathaniel K. Grady, Zhiyuan Fan, Alexander O. Govorov, and Naomi J. Halas. Plexciton dynamics: Exciton-plasmon coupling in a j-aggregates au nanoshell complex provides a mechanism for nonlinearity. *Nano Letters*, 11(4):1556–1560, March 2011.

[162] Robbert Bloem, Sean Garrett-Roe, Halina Strzalka, Peter Hamm, and Paul Donaldson. Enhancing signal detection and completely eliminating scattering using quasi-phase-cycling in 2D IR experiments. *Optics Express*, 18(26):27067–27078, December 2010.

[163] Cristiano D'Andrea, Joerg Bochterle, Andrea Toma, Christian Huck, Frank Neubrech, Elena Messina, Barbara Fazio, Onofrio M. Marago, Enzo Di Fabrizio, Marc Lamy de la Chapelle, Pietro G. Gucciardi, and Annemarie Pucci. Optical nanoantennas for multiband surface-enhanced infrared and raman spectroscopy. *ACS Nano*, 7(4):3522–3531, April 2013.

[164] Norbert Kucerka, Mu-Ping Nieh, and John Katsaras. Fluid phase lipid areas and bilayer thicknesses of commonly used phosphatidylcholines as a function of temperature. *Biochimica Et Biophysica Acta-biomembranes*, 1808(11):2761–2771, November 2011.

[165] Kai Chen, Ronen Adato, and Hatice Altug. Dual-band perfect absorber for multispectral plasmon-enhanced infrared spectroscopy. *ACS Nano*, 6(9):7998–8006, August 2012.

[166] A. Hartstein, J. R. Kirtley, and J. C. Tsang. Enhancement of the infrared absorption from molecular monolayers with thin metal overlayers. *Physical Review Letters*, 45(3):201–204, July 1980.

[167] M. Osawa. Dynamic processes in electrochemical reactions studied by surface-enhanced infrared absorption spectroscopy (SEIRAS). *Bulletin of the Chemical Society of Japan*, 70(12):2861–2880, December 1997.

[168] A. E. Bjerke, P. R. Griffiths, and W. Theiss. Surface-enhanced infrared absorption of co on platinized platinum. *Analytical Chemistry*, 71(10):1967–1974, May 1999.

[169] E. Johnson and R. Aroca. Surface-enhanced infrared-spectroscopy of monolayers. *Journal of Physical Chemistry*, 99(23):9325–9330, June 1995.

[170] M. Osawa and M. Ikeda. Surface-enhanced infrared-absorption of para-nitrobenzoic acid deposited on silver island films - contributions of electromagnetic and chemical mechanisms. *Journal of Physical Chemistry*, 95(24):9914–9919, November 1991.

[171] D. Enders and A. Pucci. Surface enhanced infrared absorption of octadecanethiol on wet-chemically prepared au nanoparticle films. *Applied Physics Letters*, 88(18):184104–3, May 2006.

[172] Shahin Bagheri, Ksenia Weber, Timo Gissibl, Thomas Weiss, Frank Neubrech, and Harald Giessen. Fabrication of square-centimeter plasnnonic nanoantenna arrays by femtosecond direct laser writing lithography: Effects of collective excitations on SEIRA enhancement. *ACS Photonics*, 2(6):779–786, June 2015.

[173] Lisa V. Brown, Xiao Yang, Ke Zhao, Bob Y. Zheng, Peter Nordlander, and Naomi J. Halas. Fan-shaped gold nanoantennas above reflective substrates for surface-enhanced infrared absorption (SEIRA). *Nano Letters*, 15(2):1272–1280, February 2015.

[174] J. M. Hoffmann, X. H. Yin, J. Richter, A. Hartung, T. W. W. Mass, and T. Taubner. Low-cost infrared resonant structures for surface-enhanced infrared absorption spectroscopy in the fingerprint region from 3 to 13 mu m. *Journal of Physical Chemistry C*, 117(21):11311–11316, May 2013.

[175] Daniel Rodrigo, Odeta Limaj, Davide Janner, Dordaneh Etezadi, F. Javier Garcia de Abajo, Valerio Pruneri, and Hatice Altug. Mid-infrared plasmonic biosensing with graphene. *Science*, 349(6244):165–168, July 2015.

[176] M. Abb, Y. D. Wang, N. Papasimakis, C. H. de Groot, and O. L. Muskens. Surface-enhanced infrared spectroscopy using metal oxide plasmonic antenna arrays. *Nano Letters*, 14(1):346–352, January 2014.

[177] F. Neubrech, S. Beck, T. Glaser, M. Hentschel, H. Giessen, and A. Pucci. Spatial extent of plasmonic enhancement of vibrational signals in the infrared. *ACS Nano*, 8(6):6250–6258, June 2014.

[178] Samuel Gottheim, Hui Zhang, Alexander O. Govorov, and Naomi J. Halas. Fractal nanoparticle plasmonics: The cayley tree. *ACS Nano*, 9(3):3284–3292, March 2015.

[179] O. Selig, R. Siffels, and Y. L. A. Rezus. Ultrasensitive ultrafast vibrational spectroscopy employing the near field of gold nanoantennas. *Physical Review Letters*, 114(23):233004, June 2015.

[180] H. J. Chen, L. Shao, K. C. Woo, J. F. Wang, and H. Q. Lin. Plasmonic-molecular resonance coupling: Plasmonic splitting versus energy transfer. *Journal of Physical Chemistry C*, 116(26):14088–14095, July 2012.

[181] C.F. Bohren and D.R. Huffman. *Absorption and Scattering of Light by Small Particles*. Wiley-VCH Verlag GmbH & Co. KGaA, 2004.

[182] E. M. Purcell and C. R. Pennypacker. Scattering and absorption of light by nonspherical dielectric grains. *Astrophysical Journal*, 186:705–714, 1973.

[183] B. T. Draine and P. J. Flatau. Discrete-dipole approximation for scattering calculations. *Journal of the Optical Society of America A-optics Image Science and Vision*, 11(4):1491–1499, April 1994.

[184] L. Novotny and B. Hecht. *Principles of Nano-Optics*. Cambridge University Press, 2006.

[185] Toma Neuman, Pablo Alonso-Gonzalez, Aitzol Garcia-Etxarri, Martin Schnell, Rainer Hillenbrand, and Javier Aizpurua. Mapping the near fields of plasmonic nanoantennas by scattering-type scanning near-field optical microscopy. *Laser & Photonics Reviews*, 9(6):637–649, 2015.

[186] P. Alonso-Gonzalez, P. Albella, F. Neubrech, C. Huck, J. Chen, F. Golmar, F. Casanova, L. E. Hueso, A. Pucci, J. Aizpurua, and R. Hillenbrand. Experimental verification of the spectral shift between near- and far-field peak intensities of plasmonic infrared nanoantennas. *Physical Review Letters*, 110(20):203902–, May 2013.

[187] Andreas M. Kern and Olivier J. F. Martin. Excitation and reemission of molecules near realistic plasmonic nanostructures. *Nano Letters*, 11(2):482–487, February 2011.

[188] J. D. Jackson. *Classical Electrodynamics*. John Wiley & Sons, Inc., 1999.

[189] A. Soldera and E. Monterrat. Mid-infrared optical properties of a polymer film: comparison between classical molecular simulations: spectrometry, and ellipsometry techniques. *Polymer*, 43(22):6027–6035, October 2002.

[190] E. D. Palik. *Handbook of Optical Constants of Solids*. Academic Press, 1985.

[191] David B. Mitzi. *Synthesis, Structure, and Properties of Organic-Inorganic Perovskites and Related Materials*, pages 1–121. John Wiley & Sons, Inc., 2007.

[192] Henry J. Snaith. Perovskites: the emergence of a new era for low-cost, high-efficiency solar cells. *The Journal of Physical Chemistry Letters*, 4(21):3623–3630, 2013.

[193] Martin A. Green, Anita Ho-Baillie, and Henry J. Snaith. The emergence of perovskite solar cells. *Nature Photonics*, 8(7):506–514, 2014.

[194] Dieter Weber. $CH_3NH_3PbX_3$, ein pb (ii)-system mit kubischer perowskitstruktur/ $CH_3NH_3PbX_3$, a pb (ii)-system with cubic perovskite structure. *Zeitschrift für Naturforschung B*, 33(12):1443–1445, 1978.

[195] Jin Hyuck Heo, Sang Hyuk Im, Jun Hong Noh, Tarak N. Mandal, Choong-Sun Lim, Jeong Ah Chang, Yong Hui Lee, Hi-jung Kim, Arpita Sarkar, Md K Nazeeruddin, et al. Efficient inorganic-organic hybrid heterojunction solar cells containing perovskite compound and polymeric hole conductors. *Nature Photonics*, 7(6):486–491, 2013.

[196] Michael M Lee, Joël Teuscher, Tsutomu Miyasaka, Takurou N. Murakami, and Henry J. Snaith. Efficient hybrid solar cells based on meso-superstructured organometal halide perovskites. *Science*, 338(6107):643–647, 2012.

[197] Jun Hong Noh, Sang Hyuk Im, Jin Hyuck Heo, Tarak N. Mandal, and Sang Il Seok. Chemical management for colorful, efficient, and stable inorganic–organic hybrid nanostructured solar cells. *Nano letters*, 13(4):1764–1769, 2013.

[198] Zhi-Kuang Tan, Reza Saberi Moghaddam, May Ling Lai, Pablo Docampo, Ruben Higler, Felix Deschler, Michael Price, Aditya Sadhanala, Luis M Pazos, Dan Credgington, et al. Bright light-emitting diodes based on organometal halide perovskite. *Nature nanotechnology*, 9(9):687–692, 2014.

[199] Constantinos C. Stoumpos, Christos D. Malliakas, and Mercouri G. Kanatzidis. Semiconducting tin and lead iodide perovskites with organic cations: phase transitions, high mobilities, and near-infrared photoluminescent properties. *Inorganic chemistry*, 52(15):9019–9038, 2013.

[200] Anna Amat, Edoardo Mosconi, Enrico Ronca, Claudio Quarti, Paolo Umari, Md K. Nazeeruddin, Michael Graltzel, and Filippo De Angelis. Cation-induced band-gap tuning in organohalide perovskites: interplay of spin–orbit coupling and octahedra tilting. *Nano letters*, 14(6):3608–3616, 2014.

[201] Tom Baikie, Yanan Fang, Jeannette M Kadro, Martin Schreyer, Fengxia Wei, Subodh G Mhaisalkar, Michael Graetzel, and Tim J White. Synthesis and crystal chemistry of the hybrid perovskite (ch 3 nh 3) pbi 3 for solid-state sensitised solar cell applications. *Journal of Materials Chemistry A*, 1(18):5628–5641, 2013.

[202] Edoardo Mosconi, Claudio Quarti, Tanja Ivanovska, Giampiero Ruani, and Filippo De Angelis. Structural and electronic properties of organo-halide lead perovskites: a combined ir-spectroscopy and ab initio molecular dynamics investigation. *Physical Chemistry Chemical Physics*, 16(30):16137–16144, 2014.

[203] Ilya Grinberg, D. Vincent West, Maria Torres, Gaoyang Gou, David M. Stein, Liyan Wu, Guannan Chen, Eric M. Gallo, Andrew R. Akbashev, Peter K. Davies, et al. Perovskite oxides for visible-light-absorbing ferroelectric and photovoltaic materials. *Nature*, 503(7477):509–512, 2013.

[204] Tom Baikie, Nathan S. Barrow, Yanan Fang, Philip J. Keenan, Peter R. Slater, Ross O. Piltz, Matthias Gutmann, Subodh G. Mhaisalkar, and Tim J. White. A combined single crystal neutron/x-ray diffraction and solid-state nuclear magnetic resonance study of the hybrid perovskites $CH_3NH_3PbX_3$ (X= Cl, Br, I). *Journal of Materials Chemistry A*, 3(17):9298–9307, 2015.

[205] Jie Ma and Lin-Wang Wang. Nanoscale charge localization induced by random orientations of organic molecules in hybrid perovskite $CH_3NH_3PbI_3$. *Nano letters*, 15(1):248–253, 2014.

[206] Jin-Wook Lee, Dong-Jin Seol, An-Na Cho, and Nam-Gyu Park. High-efficiency perovskite solar cells based on the black polymorph of HC $(NH_2)_2PbI_3$. *Advanced Materials*, 26(29):4991–4998, 2014.

[207] Nam Joong Jeon, Jun Hong Noh, Woon Seok Yang, Young Chan Kim, Seungchan Ryu, Jangwon Seo, and Sang Il Seok. Compositional engineering of perovskite materials for high-performance solar cells. *Nature*, 517(7535):476–480, 2015.

[208] J. Beilsten-Edmands, G.E. Eperon, R.D. Johnson, H.J. Snaith, and P.G. Radaelli. Non-ferroelectric nature of the conductance hysteresis in $CH_3NH_3PbI_3$ perovskite-based photovoltaic devices. *Applied Physics Letters*, 106(17):173502, 2015.

[209] Michael Kulbak, David Cahen, and Gary Hodes. How important is the organic part of lead halide perovskite photovoltaic cells? efficient $CsPbBr_3$ cells. *The journal of physical chemistry letters*, 6(13):2452–2456, 2015.

[210] Yasemin Kutes, Linghan Ye, Yuanyuan Zhou, Shuping Pang, Bryan D. Huey, and Nitin P. Padture. Direct observation of ferroelectric domains in solution-processed $CH_3NH_3PbI_3$ perovskite thin films. *The journal of physical chemistry letters*, 5(19):3335–3339, 2014.

[211] Fan Zheng, Hiroyuki Takenaka, Fenggong Wang, Nathan Z Koocher, and Andrew M. Rappe. First-principles calculation of the bulk photovoltaic effect in $CH_3NH_3PbI_3$ and $CH_3NH_3PbI_{3-x}Cl_x$. *The journal of physical chemistry letters*, 6(1):31–37, 2014.

[212] A. Baumann, K. Tvingstedt, MC Heiber, S. Väth, C. Momblona, H.J. Bolink, and V. Dyakonov. Persistent photovoltage in methylammonium lead iodide perovskite solar cells. *Apl Materials*, 2(8):081501, 2014.

[213] Henry J. Snaith, Antonio Abate, James M. Ball, Giles E. Eperon, Tomas Leijtens, Nakita K. Noel, Samuel D. Stranks, Jacob Tse-Wei Wang, Konrad Wojciechowski, and Wei Zhang. Anomalous hysteresis in perovskite solar cells. *The journal of physical chemistry letters*, 5(9):1511–1515, 2014.

[214] Jing Wei, Yicheng Zhao, Heng Li, Guobao Li, Jinlong Pan, Dongsheng Xu, Qing Zhao, and Dapeng Yu. Hysteresis analysis based on the ferroelectric effect in hybrid perovskite solar cells. *The journal of physical chemistry letters*, 5(21):3937–3945, 2014.

[215] Claudio Quarti, Edoardo Mosconi, and Filippo De Angelis. Interplay of orientational order and electronic structure in methylammonium lead iodide: Implications for solar cell operation. *Chemistry of Materials*, 26(22):6557–6569, 2014.

[216] Wan-Jian Yin, Ji-Hui Yang, Joongoo Kang, Yanfa Yan, and Su-Huai Wei. Halide perovskite materials for solar cells: a theoretical review. *Journal of Materials Chemistry A*, 3(17):8926–8942, 2015.

[217] Roderick E Wasylishen, Osvald Knop, and J. Bruce Macdonald. Cation rotation in methylammonium lead halides. *Solid state communications*, 56(7):581–582, 1985.

[218] Noriko Onoda-Yamamuro, Takasuke Matsuo, and Hiroshi Suga. Calorimetric and ir spectroscopic studies of phase transitions in methylammonium trihalogenoplumbates (ii). *Journal of Physics and Chemistry of Solids*, 51(12):1383–1395, 1990.

[219] Noriko Onoda-Yamamuro, Takasuke Matsuo, and Hiroshi Suga. Dielectric study of $CH_3NH_3PbX_3$ (X= Cl, Br, I). *Journal of Physics and Chemistry of Solids*, 53(7):935–939, 1992.

[220] Jarvist M. Frost, Keith T. Butler, Federico Brivio, Christopher H. Hendon, Mark Van Schilfgaarde, and Aron Walsh. Atomistic origins of high-performance in hybrid halide perovskite solar cells. *Nano letters*, 14(5):2584–2590, 2014.

[221] Jarvist M. Frost, Keith T. Butler, and Aron Walsh. Molecular ferroelectric contributions to anomalous hysteresis in hybrid perovskite solar cells. *Apl Materials*, 2(8):081506, 2014.

[222] Marcelo A. Carignano, Ali Kachmar, and Julrg Hutter. Thermal effects on $CH_3NH_3PbI_3$ perovskite from ab initio molecular dynamics simulations. *The Journal of Physical Chemistry C*, 119(17):8991–8997, 2015.

[223] Lisheng Chi, Ian Swainson, Lachlan Cranswick, Jae-Hyuk Her, Peter Stephens, and Osvald Knop. The ordered phase of methylammonium lead chloride $CH_3ND_3PbCl_3$. *Journal of Solid State Chemistry*, 178(5):1376–1385, 2005.

[224] Zhen Fan, Juanxiu Xiao, Kuan Sun, Lei Chen, Yating Hu, Jianyong Ouyang, Khuong P Ong, Kaiyang Zeng, and John Wang. Ferroelectricity of $CH_3NH_3PbI_3$ perovskite. *The journal of physical chemistry letters*, 6(7):1155–1161, 2015.

[225] Jarvist Moore Leguy, Aurelien M.A .and Frost, Andrew P McMahon, Victoria Garcia Sakai, W. Kockelmann, ChunHung Law, Xiaoe Li, Fabrizia Foglia, Aron Walsh, Brian C. O'Regan, et al. The dynamics of methylammonium ions in hybrid organic-inorganic perovskite solar cells. *Nature communications*, 6, 2015.

[226] Feng Hao, Constantinos C. Stoumpos, Zhao Liu, Robert PH Chang, and Mercouri G. Kanatzidis. Controllable perovskite crystallization at a gas–solid interface for hole conductor-free solar cells with steady power conversion efficiency over 10%. *Journal of the American Chemical Society*, 136(46):16411–16419, 2014.

[227] Lauren E. Polander, Paul Pahner, Martin Schwarze, Matthias Saalfrank, Christian Koerner, and Karl Leo. Hole-transport material variation in fully vacuum deposited perovskite solar cells. *APL Materials*, 2(8):081503, 2014.

[228] Mingzhen Liu, Michael B Johnston, and Henry J. Snaith. Efficient planar heterojunction perovskite solar cells by vapour deposition. *Nature*, 501(7467):395–398, 2013.

[229] Artem A. Bakulin, Oleg Selig, Huib J. Bakker, Yves L.A. Rezus, Christian Müller, Tobias Glaser, Robert Lovrincic, Zhenhua Sun, Zhuoying Chen, Aron Walsh, et al. Real-time observation of organic cation reorientation in methylammonium lead iodide perovskites. *The journal of physical chemistry letters*, 6(18):3663–3669, 2015.

[230] Tobias Glaser, Christian Müller, Michael Sendner, Christian Krekeler, Octavi E Semonin, Trevor D. Hull, Omer Yaffe, Jonathan S Owen, Wolfgang Kowalsky, Annemarie Pucci, et al. Infrared spectroscopic study of vibrational modes in methylammonium lead halide perovskites. *The journal of physical chemistry letters*, 6(15):2913–2918, 2015.

[231] Junrong Zheng, Kyungwon Kwak, and M.D. Fayer. Ultrafast 2D IR vibrational echo spectroscopy. *Accounts of Chemical Research*, 40(1):75–83, 2007.

[232] David R. Skoff, Jennifer E. Laaser, Sudipta S. Mukherjee, Chris T. Middleton, and Martin T. Zanni. Simplified and economical 2D IR spectrometer design using a dual acousto-optic modulator. *Chemical physics*, 422:8–15, 2013.

[233] Krupa Ramasesha, Sean T Roberts, Rebecca A Nicodemus, Aritra Mandal, and Andrei Tokmakoff. Ultrafast 2D IR anisotropy of water reveals reorientation during hydrogen-bond switching. *The Journal of chemical physics*, 135(5):054509, 2011.

[234] Dan Cringus, Artem Bakulin, Jörg Lindner, Peter Vöhringer, Maxim S Pshenichnikov, and Douwe A. Wiersma. Ultrafast energy transfer in water-aot reverse micelles. *The Journal of Physical Chemistry B*, 111(51):14193–14207, 2007.

[235] R.G. Gordon. Molecular collisions and the depolarization of fluorescence in gases. *The Journal of Chemical Physics*, 45(5):1643–1648, 1966.

[236] T. Chen, B. Foley, B. Ipek, M. Tyagi, J. Copley, C. Brown, J. Choi, and S.H. Lee. Rotational dynamics and its relation to the photovoltaic effect of ch 3 nh 3 pbi 3 perovskite. *Preprint at http://arXiv*, 150602205, 2015.

[237] Dan Cringus, Maxim S. Pshenichnikov, Douwe A. Wiersma, et al. Ultrafast anisotropy dynamics of water molecules dissolved in acetonitrile. *The Journal of chemical physics*, 127(8):084507, 2007.

[238] Artem A. Bakulin, Dan Cringus, Piotr A. Pieniazek, James L. Skinner, Thomas L.C. Jansen, and Maxim S. Pshenichnikov. Dynamics of water confined in reversed micelles: multidimensional vibrational spectroscopy study. *The Journal of Physical Chemistry B*, 117(49):15545–15558, 2013.

[239] Minbiao Ji and Kelly J. Gaffney. Orientational relaxation dynamics in aqueous ionic solution: Polarization-selective two-dimensional infrared study of angular jump-exchange dynamics in aqueous 6m naclo4. *The Journal of chemical physics*, 134(4):044516, 2011.

[240] Claudio Quarti, Giulia Grancini, Edoardo Mosconi, Paola Bruno, James M Ball, Michael M Lee, Henry J Snaith, Annamaria Petrozza, and Filippo De Angelis. The raman spectrum of the $CH_3NH_3PbI_3$ hybrid perovskite: interplay of theory and experiment. *The journal of physical chemistry letters*, 5(2):279–284, 2013.

[241] Thomas M. Brenner, David A. Egger, Leeor Kronik, Gary Hodes, and David Cahen. Hybrid organic-inorganic perovskites: low-cost semiconductors with intriguing charge-transport properties. *Nature Reviews Materials*, 1:15007, 2016.

[242] Joseph S. Manser, Jeffrey A Christians, and Prashant V Kamat. Intriguing optoelectronic properties of metal halide perovskites. *Chemical Reviews*, 2016.

[243] Michael Saliba, Taisuke Matsui, Ji-Youn Seo, Konrad Domanski, Juan-Pablo Correa-Baena, Mohammad Khaja Nazeeruddin, Shaik M. Zakeeruddin, Wolfgang Tress, Antonio Abate, Anders Hagfeldt, et al. Cesium-containing triple cation perovskite solar cells: improved stability, reproducibility and high efficiency. *Energy & Environmental Science*, 9(6):1989–1997, 2016.

[244] Aditya Sadhanala, Shahab Ahmad, Baodan Zhao, Nadja Giesbrecht, Phoebe M. Pearce, Felix Deschler, Robert L.Z. Hoye, Karl C. Gödel, Thomas Bein, Pablo Docampo, et al. Blue-green color tunable solution processable organolead chloride–bromide mixed halide perovskites for optoelectronic applications. *Nano letters*, 15(9):6095–6101, 2015.

[245] Guichuan Xing, Nripan Mathews, Swee Sien Lim, Natalia Yantara, Xinfeng Liu, Dharani Sabba, Michael Grätzel, Subodh Mhaisalkar, and Tze Chien Sum. Low-temperature solution-processed wavelength-tunable perovskites for lasing. *Nat. Mater*, 13(5):476–480, 2014.

[246] Felix Deschler, Michael Price, Sandeep Pathak, Lina E Klintberg, David-Dominik Jarausch, Ruben Higler, Sven Hüttner, Tomas Leijtens, Samuel D Stranks, Henry J Snaith, et al. High photoluminescence efficiency and optically pumped lasing in solution-processed mixed halide perovskite semiconductors. *The journal of physical chemistry letters*, 5(8):1421–1426, 2014.

[247] David P. McMeekin, Golnaz Sadoughi, Waqaas Rehman, Giles E Eperon, Michael Saliba, Maximilian T. Hörantner, Amir Haghighirad, Nobuya Sakai, Lars Korte, Bernd Rech, et al. A mixed-cation lead mixed-halide perovskite absorber for tandem solar cells. *Science*, 351(6269):151–155, 2016.

[248] Aditya Sadhanala, Felix Deschler, Tudor H. Thomas, Siân E Dutton, Karl C. Goedel, Fabian C. Hanusch, May L Lai, Ullrich Steiner, Thomas Bein, Pablo Docampo, et al. Preparation of single-phase films of $CH_3NH_3Pb\ (I_{1-x}\ Br_x)_3$ with sharp optical band edges. *The journal of physical chemistry letters*, 5(15):2501–2505, 2014.

[249] David A. Egger, Andrew M. Rappe, and Leeor Kronik. Hybrid organic–inorganic perovskites on the move. *Accounts of chemical research*, 49(3):573–581, 2016.

[250] Edoardo Mosconi and Filippo De Angelis. Mobile ions in organohalide perovskites: Interplay of electronic structure and dynamics. *ACS Energy Letters*, 2016.

[251] Run Long, Weihai Fang, and Oleg V. Prezhdo. Moderate humidity delays electron–hole recombination in hybrid organic–inorganic perovskites: Time-domain ab initio simulations rationalize experiments. *The Journal of Physical Chemistry Letters*, 7(16):3215–3222, 2016.

[252] Angela Y. Chang, Yi-Ju Cho, Kuan-Chen Chen, Chang-Wen Chen, Alper Kinaci, Benjamin T. Diroll, Michael J. Wagner, Maria K.Y. Chan, Hao-Wu Lin, and Richard D. Schaller. Slow organic-to-inorganic sub-lattice thermalization in methylammonium lead halide perovskites observed by ultrafast photoluminescence. *Advanced Energy Materials*, 2016.

[253] María C. Gélvez-Rueda, Duyen H Cao, Sameer Patwardhan, Nicolas Renaud, Constantinos C. Stoumpos, George C. Schatz, Joseph T. Hupp, Omar K. Farha, Tom J. Savenije, Mercouri G. Kanatzidis, et al. Effect of cation rotation on charge dynamics in hybrid lead halide perovskites. *The Journal of Physical Chemistry C*, 120(30):16577–16585, 2016.

[254] Yang Zhou, Lu You, Shiwei Wang, Zhiliang Ku, Hongjin Fan, Daniel Schmidt, Andrivo Rusydi, Lei Chang, Le Wang, Peng Ren, et al. Giant photostriction in organic-inorganic lead halide perovskites. *Nature communications*, 7, 2016.

[255] Adam D. Wright, Carla Verdi, Rebecca L. Milot, Giles E. Eperon, Miguel A Pérez-Osorio, Henry J. Snaith, Feliciano Giustino, Michael B. Johnston, and Laura M. Herz. Electron-phonon coupling in hybrid lead halide perovskites. *Nature Communications*, 7, 2016.

[256] Golibjon R. Berdiyorov, Ali Kachmar, Fedwa El-mellouhi, Marcelo Andrés Carignano, and Mohamed El-Amine Madjet. Role of cations on the electronic transport and optical properties of the lead-iodide perovskite. *The Journal of Physical Chemistry C*, 2016.

[257] Haiming Zhu, Kiyoshi Miyata, Yongping Fu, Jue Wang, Prakriti P. Joshi, Daniel Niesner, Kristopher W. Williams, Song Jin, and X.-Y. Zhu. Screening in crystalline liquids protects energetic carriers in hybrid perovskites. *Science*, 353(6306):1409–1413, 2016.

[258] Carlo Motta, Pankaj Mandal, and Stefano Sanvito. Effects of molecular dipole orientation on the exciton binding energy of $CH_3NH_3PbI_3$. *Physical Review B*, 94(4):045202, 2016.

[259] Alessandro Pecchia, Desirée Gentilini, Daniele Rossi, Matthias Auf der Maur, and Aldo Di Carlo. Role of ferroelectric nanodomains in the transport properties of perovskite solar cells. *Nano letters*, 16(2):988–992, 2016.

[260] Ioannis Deretzis, Bruno N. Di Mauro, Alessandra Alberti, Giovanna Pellegrino, Emanuele Smecca, and Antonino La Magna. Spontaneous bidirectional ordering of $CH_3NH_3^+$ in lead iodide perovskites at room temperature: The origins of the tetragonal phase. *Scientific reports*, 6, 2016.

[261] X.-Y. Zhu and V. Podzorov. Charge carriers in hybrid organic–inorganic lead halide perovskites might be protected as large polarons. *The journal of physical chemistry letters*, 6(23):4758–4761, 2015.

[262] Michael Sendner, Pabitra K Nayak, David A Egger, Sebastian Beck, Christian Müller, Bernd Epding, Wolfgang Kowalsky, Leeor Kronik, Henry J Snaith, Annemarie Pucci, et al. Optical phonons in methylammonium lead halide perovskites and implications for charge transport. *Materials Horizons*, 3(6):613–620, 2016.

[263] Christian MüĬLler, Tobias Glaser, Marcel Plogmeyer, Michael Sendner, Sebastian Döring, Artem A Bakulin, Carlo Brzuska, Roland Scheer, Maxim S Pshenichnikov, Wolfgang Kowalsky, et al. Water infiltration in methylammonium lead iodide perovskite: Fast and inconspicuous. *Chemistry of Materials*, 27(22):7835–7841, 2015.

[264] Laura M. Herz. Charge-carrier dynamics in organic-inorganic metal halide perovskites. *Annual review of physical chemistry*, 67:65–89, 2016.

[265] M.A. Carignano, Y. Saeed, S. Assa Aravindh, I.S. Roqan, Jacky Even, and Claudine Katan. A close examination of the structure and dynamics of hc (nh 2) 2 pbi 3 by md simulations and group theory. *Physical Chemistry Chemical Physics*, 18(39):27109–27118, 2016.

[266] Jonathon S. Bechtel, Ram Seshadri, and Anton Van der Ven. Energy landscape of molecular motion in cubic methylammonium lead iodide from first principles. *The Journal of Physical Chemistry C*, 2016.

[267] Tianran Chen, Benjamin J. Foley, Bahar Ipek, Madhusudan Tyagi, John R.D. Copley, Craig M Brown, Joshua J. Choi, and Seung-Hun Lee. Rotational dynamics of organic cations in the $CH_3NH_3PbI_3$ perovskite. *Physical Chemistry Chemical Physics*, 17(46):31278–31286, 2015.

[268] Katharine Page, Joan E. Siewenie, Paolo Quadrelli, and Lorenzo Malavasi. Short-range order of methylammonium and persistence of distortion at the local scale in mapbbr3 hybrid perovskite. *Angewandte Chemie*, 128(46):14532–14536, 2016.

[269] Douglas H. Fabini, Tom Hogan, Hayden A. Evans, Constantinos C. Stoumpos, Mercouri G. Kanatzidis, and Ram Seshadri. Dielectric and thermodynamic signatures of low-temperature glassy dynamics in the hybrid perovskites $CH_3NH_3PbI_3$ and HC $(NH_2)_2PbI_3$. *The journal of physical chemistry letters*, 7(3):376–381, 2016.

[270] Li-Qiang Xie, Taiyang Zhang, Liang Chen, Nanjie Guo, Yu Wang, GK Liu, Jia-Rui Wang, Jian-Zhang Zhou, Jia-Wei Yan, Yixin Zhao, et al. Organic-inorganic interactions of single crystalline organolead halide perovskites studied by raman spectroscopy. *Physical Chemistry Chemical Physics*, 2016.

[271] J. Idígoras, A. Todinova, J.R. Sánchez-Valencia, A. Barranco, A. Borrás, and J.A. Anta. The interaction between hybrid organic–inorganic halide perovskite and selective contacts in perovskite solar cells: an infrared spectroscopy study. *Physical Chemistry Chemical Physics*, 18(19):13583–13590, 2016.

[272] Martin Ledinskyy, Philipp Loper, Bjoern Niesen, Jakub Holovskyy, Soo-Jin Moon, Jun-Ho Yum, Stefaan De Wolf, Antonín Fejfar, and Christophe Ballif. Raman spectroscopy of organic–inorganic halide perovskites. *The journal of physical chemistry letters*, 6(3):401–406, 2015.

[273] Carlo Motta, Fedwa El-Mellouhi, and Stefano Sanvito. Exploring the cation dynamics in lead-bromide hybrid perovskites. *Physical Review B*, 93(23):235412, 2016.

[274] Ralf G. Niemann, Athanassios G. Kontos, Dimitrios Palles, Efstratios I. Kamitsos, Andreas Kaltzoglou, Federico Brivio, Polycarpos Falaras, and Petra J. Cameron. Halogen effects on ordering and bonding of $CH_3NH_3^+$ in $CH_3NH_3PbX_3$ (X= Cl, Br, I) hybrid perovskites: A vibrational spectroscopic study. *The Journal of Physical Chemistry C*, 120(5):2509–2519, 2016.

[275] Federico Brivio, Clovis Caetano, and Aron Walsh. Thermodynamic origin of photoinstability in the ch3nh3pb (i1–x br x) 3 hybrid halide perovskite alloy. *The journal of physical chemistry letters*, 7(6):1083–1087, 2016.

[276] Waqaas Rehman, Rebecca L. Milot, Giles E. Eperon, Christian Wehrenfennig, Jessica L. Boland, Henry J. Snaith, Michael B. Johnston, and Laura M. Herz. Charge-carrier dynamics and mobilities in formamidinium lead mixed-halide perovskites. *Advanced Materials*, 27(48):7938–7944, 2015.

[277] Mathias Van Thiel, Edwin D Becker, and George C. Pimentel. Infrared studies of hydrogen bonding of water by the matrix isolation technique. *The Journal of Chemical Physics*, 27(2):486–490, 1957.

[278] Wanyi Nie, Hsinhan Tsai, Reza Asadpour, Jean-Christophe Blancon, Amanda J Neukirch, Gautam Gupta, Jared J Crochet, Manish Chhowalla, Sergei Tretiak, Muhammad A Alam, et al. High-efficiency solution-processed perovskite solar cells with millimeter-scale grains. *Science*, 347(6221):522–525, 2015.

[279] Paul Pistor, Juliane Borchert, Wolfgang Franzel, Rene Csuk, and Roland Scheer. Monitoring the phase formation of coevaporated lead halide perovskite thin films by in situ x-ray diffraction. *The journal of physical chemistry letters*, 5(19):3308–3312, 2014.

[280] Riccardo Comin, Michael K Crawford, Ayman H. Said, Norman Herron, William E Guise, Xiaoping Wang, Pamela S. Whitfield, Ankit Jain, Xiwen Gong, Alan J.H. McGaughey, et al. Lattice dynamics and the nature of structural transitions in organolead halide perovskites. *Physical Review B*, 94(9):094301, 2016.

[281] Alexander N Beecher, Octavi E. Semonin, Jonathan M. Skelton, Jarvist M. Frost, Maxwell W. Terban, Haowei Zhai, Ahmet Alatas, Jonathan S. Owen, Aron Walsh, and Simon J.L. Billinge. Direct observation of dynamic symmetry breaking above room temperature in methylammonium lead iodide perovskite. *ACS Energy Letters*, 1(4):880–887, 2016.

[282] Aurélien Leguy, Alejandro R Goñi, Jarvist M Frost, Jonathan Skelton, Federico Brivio, Xabier Rodríguez-Martínez, Oliver J Weber, Anuradha Pallipurath, M. Isabel Alonso, Mariano Campoy-Quiles, et al. Dynamic disorder, phonon lifetimes, and the assignment of modes to the vibrational spectra of methylammonium lead halide perovskites. *arXiv preprint arXiv:1606.01841*, 2016.

[283] Damien Laage and James T. Hynes. A molecular jump mechanism of water reorientation. *Science*, 311(5762):832–835, 2006.

[284] Christopher J. Fecko, Joseph J. Loparo, Sean T. Roberts, and Andrei Tokmakoff. Local hydrogen bonding dynamics and collective reorganization in water: Ultrafast infrared spectroscopy of HOD/D_2Od2o. *The Journal of chemical physics*, 122(5):054506, 2005.

[285] Keisuke Shinokita, Ana V. Cunha, Thomas LC Jansen, and Maxim S. Pshenichnikov. Hydrogen bond dynamics in bulk alcohols. *The Journal of chemical physics*, 142(21):212450, 2015.

[286] Kees Lazonder, Maxim S. Pshenichnikov, and Douwe A. Wiersma. Easy interpretation of optical two-dimensional correlation spectra. *Optics letters*, 31(22):3354–3356, 2006.

[287] ChuanXiang Sheng, Chuang Zhang, Yaxin Zhai, Kamil Mielczarek, Weiwei Wang, Wanli Ma, Anvar Zakhidov, and Z Valy Vardeny. Exciton versus free carrier photogeneration in organometal trihalide perovskites probed by broadband ultrafast polarization memory dynamics. *Physical review letters*, 114(11):116601, 2015.

SUMMARY

In this thesis we have used nonlinear infrared spectroscopy to study the ultrafast molecular dynamics of organic molecules in liquids and solids. Since all investigated phenomena occur on an ultrafast time scale (fs–ps), a special experimental method is needed to follow these phenomena in real time. Here, we employ an all-optical approach in which we use infrared pump-probe and two-dimensional infrared spectroscopy (2DIR). In both methods an intense infrared laser pulse (pump) is used to resonantly excite a molecular vibration. After a short period of time, in which the system can evolve freely, the system is interrogated with a weak test pulse (probe). To follow the relaxation and orientational dynamics of the excited vibrations, the experiment is repeated for different time delays between the pump and the probe pulses.

TEMPERATURE-INDUCED COLLAPSE OF ELASTIN-LIKE PEPTIDES STUDIED BY 2DIR SPECTROSCOPY Elastin-like peptides (ELP) are artificial biopolymeres consisting of a repeating sequence of five amino acids. These peptides are of great interest for biomedical applications due to their biochemical properties and their ability to undergo a temperature-induced, reversible aggregation (coacervation). In Chapter 4 we use linear and 2DIR spectroscopy to study the amide I′ band of a 450-residue ELP as a function of temperature. The amide I′ absorption band can be well described by three Gaussian bands and shows a blueshift with increasing temperature. One of the bands can be assigned to the amide I′ absorption band of the valine residue that is present in every pentamer. We observe two distinct energy transfer processes between these three bands. With increasing temperature, one of these processes significantly decelerates, while the rate of the other exchange process remains constant. The spectral diffusion dynamics of the amide I′ mode of the valine residue also does not change when the temperature is varied. We perform an extensive comparison of the 450 residue long peptide with a one-pentamer elastin-like peptide. Due to its short length this ELP does not undergo temperature-induced coacervation. However, a similar structural change can be induced by using trifluoroethanol (TFE) as a cosolvent. Increasing the concentration of TFE leads to changes of the linear and the nonlinear infrared spectra that are remarkably similar to the changes that are induced by increasing the temperature for the long ELP. This similarity suggests a similar molecular origin of the conformational transition in both cases. We supplement our infrared measurements by molecular dynamics simulations of the short ELP in different conformations and solvent environments. The results suggest that the conformational transition of ELPs is driven by the desolvation of the peptide backbone in which process up to 75% of the water in the solvation shell is displaced. Furthermore, the consistently slow spectral diffusion dynamics of the valine residue suggests that this residue is strongly shielded from the solvent. We propose that the

slow spectral diffusion dynamics of the valine residue can be explained from the presence of a β-turn involving the valine and the fourth residue of every pentamer at all temperatures.

ULTRASENSITIVE ULTRAFAST VIBRATIONAL SPECTROSCOPY EMPLOYING THE NEAR FIELD OF GOLD NANOANTENNAS In Chapter 5 we introduce a novel technique to enhance the signals in nonlinear vibrational spectroscopy of nanoscale volumes. To this end, we employ gold nanoantennas that show their antenna resonance in the infrared. The power of this method is demonstrated by performing polarization-resolved linear and pump-probe measurements on a 5 nm polymethylmethacrylate (PMMA) film deposited on top of the gold nanoantennas. Exciting and probing this system with pulses polarized along the long antenna axis results in an enhancement of the nonlinear vibrational signal by 4 orders of magnitude. The comparison of the measurement results with measurement of a plain thick PMMA film shows that the temporal dynamics are the same in the two systems. The observed lineshapes and the enhancement mechanism are explained by a coupled point-dipole model. Furthermore, we demonstrate that the method of nanoantenna enhanced nonlinear vibrational spectroscopy can also be used to boost the signals in 2DIR.

LOCAL FIELD EFFECT IN NANOANTENNA ENHANCED INFRARED SPECTROSCOPY In Chapter 6 we present an analytic model to describe the interaction between molecular vibrations and metal nanoantennas in plasmon enhanced infrared spectroscopy. In a first approach, we describe the molecular vibrations and the nanoantennas as coupled point dipoles, and use a perturbative approach to describe their interaction. The origin of the signal enhancement is identified as the back-action of the excited vibration onto the dipole moment of the antenna. Next, the dipole model is expanded to include the presence of a substrate and the antenna geometry. Finally, we demonstrate that local-field effects, which are determined by the geometry and the dielectric function of the sensed films, have a surprisingly strong influence on the shape of the observed spectroscopic signals, and thus need to be included in the description. The results calculated with the model are in excellent agreement with numerical finite-difference time-domain simulations.

REORIENTATION DYNAMICS OF THE ORGANIC CATION IN METHYLAMMONIUM LEAD IODIDE PEROVSKITE Organic-metal halide perovskites are a new class of solar-cell materials that can reach photon-conversion rates of above 20%. In Chapter 8 we study the reorientation dynamics of the methylammonium (MA) cation in lead iodide perovskites. We use 2DIR spectroscopy to follow the orientational dynamics of the symmetric NH_3^+ bending vibration, of which the transition dipole moment is oriented along the molecular axis of the methylammonium cation. The lifetime of the vibration is found to be 3 ps and the anisotropy shows a biexponential decay with a fast 300 fs and a slow 3 ps component. Ab initio molecular dynamics simulations are used to assign the two timescales to molecular motions. We find that the organic cation is preferentially aligned along one of the iodide lattice axes, and we associate the fast time scale with a 'wobbling-in-a-cone' motion with a semi-cone angle of 31° around a lattice axis. The slow

timescale corresponds to 90° angle jumps between different iodide lattice axes. The measurement results provide further insight into the contribution of the organic cation to the dielectric function, and falsify the previously proposed presence of long-range, slowly interconverting ferro-electric domains in organic-metal halide perovskites.

HALIDE-DEPENDENT CATION REORIENTATION IN METHYLAMMONIUM LEAD-HALIDE PEROVSKITES One of the most remarkable properties of lead-halide perovskites is their straightforward band-gap tunability by adjusting the halide composition. In Chapter 8 we extend the study from the previous chapter and investigate the influence of the halide ion on the reorientation dynamics of the organic cation in lead-halide perovskites. To this end, 2DIR measurements were performed on the three most widely studied pure-halide perovskites $MAPbX_3$ (X=I, Br, Cl) and on the mixed-halide alloys $MAPb(Cl_xBr_{1-x})_3$, $MAPb(Br_xI_{1-x})_3$. We observe an anisotropy decay on two distinct time-scales for all perovskites. The fast dynamics, associated with a 'wobbling-in-a-cone' motion, occur on a similar timescale for all samples, whereas the time constant of the slow dynamics, assigned to large angle jumps, shows a distinct variation. In the pure-halide series, the anisotropy dynamics slow down as the halide size increases. We explain this slowdown from an increase in the activation energy for reorientation of the organic cation between two energetically equal faces of the unit cell. The mixed-halide alloys show significantly slower reorientation dynamics and even partial immobilization. With the help of large-scale, classical polarizable molecular dynamics simulations, we assign these slow reorientation dynamics to symmetry breaking of the unit cell. Since the hydrogen-bond strength between the cation and the inorganic cage is halide dependent, the asymmetry leads to minima in the rotational potential of the organic cation, resulting in relatively stable orientations and a slowing down of the jumping between different lattice axes.

SAMENVATTING

In dit proefschrift hebben we niet-lineaire infraroodspectroscopie gebruikt om de ultrasnelle dynamica van organische moleculen in vloeistoffen en vaste stoffen te bestuderen. De verschijnselen die we onderzoeken spelen zich allemaal af op een ultrasnelle tijdschaal (fs-ps) en daarom hebben we een speciale experimentele methode nodig om ze te kunnen volgen. De technieken die we hiervoor gebruiken staan bekend als infrarood pomp-probe spectroscopie en tweedimensionale infraroodspectroscopie (2DIR). Bij beide technieken wordt allereerst m.b.v. een intense infrarood laserpuls (pomp) een moleculaire vibratie aangeslagen. Een korte tijd later wordt de toestand van het systeem uitgelezen d.m.v. een zwakke testpuls (probe). De relaxatie- en oriëntatiedynamica van de aangeslagen vibraties volgen we door het experiment te herhalen waarbij we de tijdsvertraging tussen de pomp- en probepuls variëren.

AGGREGATIE VAN ELASTINE-ACHTIGE PEPTIDEN Elastine-achtige polypeptiden (ELPs) zijn kunstmatige biopolymeren bestaande uit een herhalende reeks van vijf aminozuren. Deze peptides zijn vanuit biomedische oogpunt interessant omdat ze bij een temperatuursvergoging op reversibele wijze aggregeren (coacervatie). In hoofdstuk 4 bestuderen we met lineaire infrarood en 2DIR spectroscopie de amide I′ vibratie van een ELP met een lengte van 450 residuen. De amide I′ absorptieband blijkt te zijn opgebouwd uit drie Gaussische subbanden en verder vertoont de band een blauwverschuiving met toenemende temperatuur. Eén van de subbanden is het gevolg van de specifieke absorptie van een valine residu dat aanwezig is in elk pentameer. Wij nemen twee verschillende energie-overdrachtsprocessen waar tussen de drie subbanden. Met toenemende temperatuur vertraagt één van deze processen significant, terwijl de snelheid van het andere energie-uitwisselingsproces constant blijft. De spectrale diffusie dynamica van de amide I′ vibratie van het valine residu verandert ook niet als functie van de temperatuur. Wij hebben het gedrag van dit peptide vergeleken met dat van een kort ELP bestaande uit slechts 5 residuen. T.g.v. zijn korte lengte aggregeert dit peptide niet. Echter, een verglijkbare verandering in structuur kan worden geïnduceerd door het gebruik van trifluorethanol (TFE) als co-oplosmiddel. Het verhogen van de TFE concentratie leidt tot veranderingen in de lineaire en niet-lineaire infrarood spectra, die een opmerkelijke gelijkenis vertonen met de veranderingen die geïnduceerd worden door het verhogen van de temperatuur voor het lange ELP. Deze overeenkomst suggereert een gelijke oorsprong van de confomationele transitie in beide gevallen. Wij vullen onze infraroodmetingen aan met moleculaire dynamica simulaties van het korte ELP in verschillende conformaties en oplosmiddelen. De resultaten suggereren dat de conformationele overgang van ELPs gedreven wordt door de desolvatatie van het peptide, waarbij tot 75% van het water in de solvatatieschil wordt verdreven. Bovendien suggereert de langzame

spectrale diffusie van het valine residu dat dit residu sterk afgeschermd is van het oplosmiddel. Onze verklaring is dat de langzame spectrale diffusie van het valine residu het gevolg is van de aanwezigheid van een β-turn tussen het valine residu en het vierde residu binnen elk pentameer.

ULTRAGEVOELIGE ULTRASNELLE VIBRATIESPECTROSCOPIE MET BEHULP VAN HET NABIJE VELD VAN GOUDEN NANOANTENNES In hoofdstuk 5 beschrijven we een nieuwe techniek voor het versterken van de signalen in niet-lineaire vibratiespectroscopie van nanoschaal volumes. Hiertoe maken we gebruik van gouden nano-antennes met een antenneresonantie in het infrarood. De kracht van deze methode wordt gedemonstreerd door het uitvoeren van polarisatie-opgeloste lineaire en pomp-probe metingen van een 5 nm polymethylmethacrylaat (PMMA) laagje op de gouden antennes. Exciteren en proben van dit systeem met pulsen gepolariseerd langs de lengte-as van de antennes resulteert in een versterking van het niet-lineaire vibratiesignaal met 4 ordes van grootte. De vergelijking van de meetresultaten met metingen van een gewone dikke PMMA-laag laat zien dat de tijdsdynamiek hetzelfde is in de twee systemen. De geobserveerde lijnvormen en het versterkingsmechanisme worden verklaard door middel van een gekoppeld punt-dipool-model. Verder demonstreren we ook dat de methode van nano-antenne versterkte niet-lineaire vibratiespectroscopie gebruikt kan worden om de signalen in 2DIR te versterken.

LOKAAL-VELDEFFECT IN NANO-ANTENNE VERSTERKTE INFRAROODSPECTROSCOPIE In hoofdstuk 6 beschrijven we een analytisch model dat de interactie tussen moleculaire vibraties en metalen nano-antennes verklaart. In een eerste benadering beschrijven we de moleculaire vibraties en nano-antennes als gekoppelde punt-dipolen, en gebruiken we een pertubatieve benadering om hun interactie te beschrijven. De oorsprong van de signaalversterking wordt geïdentificeerd als de terugkoppeling van de geëxciteerde vibratie op het dipoolmoment van de antenne. Vervolgens wordt het dipoolmodel uitgebreid om de aanwezigheid van een substraat en de geometrie van de antenne mee te rekenen. Ten slotte laten we zien dat lokale-veldeffecten, die bepaald worden door de geometrie en de diëlektrische functie van de gedetecteerde lagen, een verassend sterke invloed hebben op de vorm van de geobserveerde spectroscopische signalen en daarom in de omschrijving moeten worden opgenomen. De resultaten berekend met het model zijn in uitstekende overeenkomst met numerieke eindige-differentie tijdsdomeinsimulaties.

REORIËNTATIE DYNAMICA VAN HET ORGANISCHE KATION IN METHYLAMMONIUM LOODJODIDE PEROVSKIET Organometaalhalogenide persovskieten zijn een nieuwe klasse van zonnecelmaterialen die een foton conversieratio kan behalen van meer dan 20%. In hoofdstuk 7 bestuderen we de reoriëntatiedynamica van het methylammonium (MA) kation in loodjodide perovskieten. We gebruiken 2DIR spectroscopie voor het volgen van de oriëntatiedynamica van de symmetrische $NH_3{}^+$-buigvibratie, waarvan het transitiedipoolmoment georiënteerd is langs de moleculaire as van het methylammonium kation. Er werd een levensduur van 3 ps voor deze vibratie

gevonden en de anisotropie vertoont een bi-exponentieel verval bestaande uit een snelle 300 fs en langzame 3 ps component. Ab initio moleculaire dynamicasimulaties zijn gebruikt om de twee tijdschalen aan moleculaire bewegingen toe te wijzen. Wij vinden dat het organische kation een voorkeur heeft uitgelijnd te zijn langs een van de jodide rooster-assen, en we associëren de snelle tijdschaal met een 'wiebelen-in-een-kegel'-beweging met een semi-kegel hoek van 31°rond een rooster-as. The langzame tijdschaal correspondeert met 90°hoeksprongen tussen verschillende jodide rooster-assen. De meetresultaten geven meer inzicht in de bijdrage van het organische kation aan de diëlektrische functie, en ze weerleggen de voorheen voorgestelde aanwezigheid van lange-afstand, langzaam onderling omzettende ferro-elektrische domeinen in organometaalhalogenide-perovskieten.

HALOGENIDE-AFHANKELIJKE KATION REORIËNTATIE IN METHYLAMMONIUM LOOD-HALOGENIDE PEROVSKIETEN Een van de meest opmerkelijke eigenschappen van lood-halogenide perovskieten is hun eenvoudige band gap-afstelbaarheid door het aanpassen van de halogenidesamenstelling. In hoofdstuk 8 breiden we de studie van het vorige hoofdstuk uit en onderzoeken we de invloed van het halogenide-ion op de reoriëntatiedynamica van het organisch kation in lood-halogenide perovskieten. Hiertoe zijn 2DIR metingen uitgevoerd op de drie meest bestudeerde pure halogenide perovskieten $MAPbX_3$ (X=I, Br, Cl) en op de gemengde halogenides $MAPb(Cl_xBr_{1-x})_3$, $MAPb(Br_xI_{1-x})_3$. We observeren een anisotropie verval op twee verschillende tijdschalen voor alle perovskieten. De snelle dynamica, geassocieerd met een 'wiebelen-in-een-kegel'-beweging, vinden plaats op een vergelijkbare tijdschaal voor alle monsters, terwijl de tijdsconstante van de langzame dynamica, toegewezen aan grote hoeksprongen, een duidelijke variatie vertonen. In de pure halogenide serie vertraagt de anisotropie dynamica bij een toenemende grootte van het halogenide. We verklaren deze vertraging door een toename in de activatie-energie voor het reoriënteren van het organische kation tussen twee energetisch gelijke vlakken van de eenheidscel. De gemenge halogenides vertonen een significant langzamere reoriëntatiedynamica en zelfs een gedeeltelijke immobilisatie. Met behulp van grote-schaal, klassieke polariseerbare moleculaire dynamicasimulaties, wijzen we deze langzame reoriëntatiedynamica toe aan symmetriebreking van deeenheidscel. Omdat de waterstofbrugsterkte tussen het kation en de anorganische kooi afhankelijk is van de halogenide, leidt de asymmetrie tot minima in het rotatiepotentiaal van het organische kation, resulterende in relatief stabiele oriëntaties en een vertraging van de sprongen tussen verschillende rooster-assen.

Acknowledgments

Thank you, dear reader, for showing interest in this thesis and making it to the last pages. It took several years to complete the work that you now hold in your hands and this task would have been unthinkable without the assistance of many wonderful people.

First of all, I would like to express my sincere gratitude to my supervisor Yves Rezus for providing me with the opportunity to be part of his group. You always took the time to share your immensely detailed knowledge about the fundamentals of physics and were eager to inspect the latest experimental results. Our discussions taught me a lot about nonlinear infrared spectroscopy, the significance of the given data and how to properly communicate my results. Thank you for your continuous support and patience.

I would like to thank my promotor Huib Bakker for helping me till the very last minute with the endeavor of writing this thesis. You have the amazing ability to quickly grasp the essence and weakness of the presented information and immediately provide invaluable feedback.

My appreciation also goes to Artem Bakulin for introducing me to new parts of physics, performing awesome experiments together, and sharing and discussing world views during lunch.

The presented experimental work was made possible by the incredible technical support in AMOLF. Special thanks goes to Jan for teaching me how to work with and maintain an ultrafast laser system and his continuous assistance. Thanks also goes to Niels and Hinco for their extremely efficient and fast help even with weird and obscure mechanical requests. Thank you Sjoerd, Marco, Idsart, and Duncan for providing the electronics and software support which allowed for a fast and smooth initialization of the new experimental setup.

One daily joy of a scientist is the possibility to have conversations about state of the art research and life in general with incredibly smart colleagues. Thanks to all current and former members of the Rezus and Bakker groups: Andrea, Alexandr, Bart, Biplab, Eliane, Harmen, Jiri, Johannes, Konrad, Liyuan, Niklas, Roel, Simona, Stefanie, Stephan, and Sietse for not only providing productive feedback but making work a fun place to be at.

During my time I had the pleasure of sharing my office with some indescribably interesting people and their personal passions. Thank you Wilbert for sharing your theoretical knowledge and always filling the room with more energy and good spirit. Thank you Lutz for the extended conversations about plasmonics, stuff that fluoresces and the wonder of the Tentacle. Thank you Moritz for explaining the current trends in the field of PV.

Thanks also goes to Lianne and Giulia for their moral and scientific support and the

hours of entertaining conversation. You are two of the most kind-hearted people I know.
Ein rießengroßer Dank geht an meine Eltern. Vielen Dank für euer stetiges Interesse und die permanente Unterstützung über Jahrzehnte hinweg.
Last but definitely not least, I would like to thank Franzi. Your are the reason I made it and meanwhile had the best five years so far. Thank you!